DISSERTATION

submitted to the

Combined Faculties for the Natural Sciences and for Mathematics
of the Ruperto-Carola University of Heidelberg, Germany

for the degree of

Doctor of Natural Sciences

Put forward by

Johannes Amadeus Schwinn

born in Darmstadt

Oral Examination: 12.01.2021

NON-LINEAR STRUCTURES AS PROBES OF THE COSMOLOGICAL STANDARD MODEL

Referees:

Prof. Dr. Matthias Bartelmann
Prof. Dr. Björn Malte Schäfer

ABSTRACT

Non-linear structures provide an important test of the cosmological standard model. In this thesis, we investigate both analytic approaches to describing statistical properties of cosmic non-linear structures and a comparison of observational with simulated data.

In the first part, we focus on analytic derivations in the framework of kinetic field theory (KFT), a novel theory to cosmic structure formation based on statistical field theory of classical particles. We investigate ways to derive the probability density function (PDF) of the cosmic density field within this framework. For this purpose, we introduce different models and explore approaches to derive the density PDF from the generating functional of KFT directly.

We then use parts of these results in order to obtain an analytic derivation of the halo mass function. Unlike the standard approach, we derive the halo mass function from the present day non-linear density field directly. We use two models of the density PDF for this purpose, the lognormal and the generalised normal distribution, and fix their parameters by the predictions of KFT. We then derive the halo mass function using excursion set theory with correlated random walks. We obtain a closed form expression for the halo mass function, with only one free parameter, i.e. the halo overdensity Δ. For a choice of $\Delta = 2.9$, our results agree well with those of simulations.

In the last part, we investigate a concrete example of non-linear structure, i.e. the substructure distribution in the massive galaxy cluster Abell 2744. We compare it to that of haloes of the Millennium XXL simulation in order to test its compatibility with the cosmological standard model ΛCDM. We identify structures in both the mass map of Abell 2744 and comparable mass maps of the MXXL haloes by a method based on the wavelet transform. This allows us to find three haloes in the MXXL simulation with a substructure distribution similar to Abell 2744 thus corroborating its concordance with ΛCDM. We add a thorough discussion of our results and put them into context with the findings of other recent works.

ZUSAMMENFASSUNG

Nichtlineare Strukturen stellen einen wichtigen Test des kosmologischen Standardmodells dar. Aus diesem Grund untersuchen wir in dieser Dissertation sowohl analytische Ansätze, um statistische Eigenschaften kosmischer nichtlinearer Strukturen zu beschreiben, als auch einen Vergleich zwischen Beobachtungs- und Simulationsdaten.

Im ersten Teil der Arbeit stehen analytische Berechnungen im Vordergrund, welche im Rahmen der kinetischen Feldtheorie (KFT), einer neuen Theorie basierend auf der statistischen Feldtheorie klassischer Teilchen, hergeleitet werden. Wir untersuchen Wege, um die Wahrscheinlichkeitsverteilung (PDF) des kosmischen Dichtefeldes innerhalb dieser Theorie zu berechnen. Dazu führen wir verschiedene Modelle ein und ergründen Möglichkeiten, um die PDF direkt aus den Erzeugendenfunktional der KFT zu bestimmen.

Wir nutzen anschließend Teile dieser Ergebnisse, um eine analytische Herleitung der Halo-Massenfunktion zu erhalten. Im Gegensatz zur Standardvorgehensweise versuchen wir, die Halo-Massenfunktion direkt mithilfe des heutigen nichtlinearen Dichtefeldes herzuleiten. Zu diesem Zweck benutzen wir die Log-Normal- und die generalisierte Normalverteilung in Kombination mit KFT aus dem ersten Teil der Arbeit. Wir leiten anschließend die Halo-Massenfunktion mithilfe von Exkursionsmengen-Theorie mit korrelierten Zufallsschritten her. Dies resultiert in einer geschlossenen Form für die Halo-Massenfunktion, die nur von einem freien Parameter abhängt, der Halo-Überdichte Δ. Für eine Wahl von $\Delta = 2.9$ erhalten wir eine gute Übereinstimmung unserer Halo-Massenfunktion mit Ergebnissen aus Simulationen.

Im letzten Teil untersuchen wir ein konkretes Beispiel der nichtlinearen Struktur, die Substrukturverteilung des massereichen Galaxienhaufens Abell 2744. Wir vergleichen diese mit Halos gleicher Masse aus der MXXL-Simulation, um die Übereinstimmung mit dem kosmologischen Standardmodell ΛCDM zu testen. Wir identifizieren Substrukturen sowohl in der Massekarte von Abell 2744 als auch in vergleichbaren Karten der MXXL-Halos mithilfe einer Methode, die auf der Wavelet-Transformation basiert. Dadurch können drei Halos in der MXXL-Simulation gefunden werden, welche eine ähnliche Substrukturverteilung zu der in Abell 2744 aufweisen. Auf dieser Grundlage kann daher kein Konflikt zu ΛCDM behauptet werden. Daran anschließend folgt eine detaillierte Diskussion unserer Ergebnisse und deren Zusammenhangs mit den Resultaten anderer kürzlich veröffentlichter Arbeiten.

CONTENTS

LIST OF FIGURES

LIST OF TABLES

ACRONYMS

CDM	cold dark matter
CMB	cosmic microwave background
EdS	Einstein-de Sitter
FoF	friends-of-friends
KFT	kinetic field theory
LPT	Lagrangian perturbation theory
MXXL	Millennium XXL
NFW	Navarro-Frenk-White
PDF	probability density function
PS	Press-Schechter
SPT	standard perturbation theory
SCGF	scaled cumulant generating function
WT	wavelet transform

Fourier convention:

$$\tilde{f}(\vec{k}) = \int \mathrm{d}^3\vec{q}\, f(\vec{q})\, \mathrm{e}^{-\mathrm{i}\vec{k}\cdot\vec{q}}, \quad f(\vec{q}) = \int \frac{\mathrm{d}^3\vec{k}}{(2\pi)^3}\, \tilde{f}(\vec{k})\, \mathrm{e}^{\mathrm{i}\vec{k}\cdot\vec{q}}$$

1 INTRODUCTION

The Universe contains a large variety of different structures. There are stellar systems with planets orbiting their stars, galaxies typically of spiral or elliptical shape and finally clusters of galaxies that are enormous gravitationally bound structures, which can reach masses of several 10^{15} $M_\odot$. In a more general sense these structures can be seen as patterns of overdense and underdense regions in space. It is one of the key aims of cosmology to find out where these patterns come from, what their statistical properties are and how they evolve over time. Central to cosmic structure formation is the idea that the Universe was in an almost homogeneous state at very early times (e.g. at the release of the cosmic microwave background (CMB) at redshift $z \approx 1100$). The cosmic microwave background shows, however, that there have been very small density fluctuations at that time already. It is currently assumed that these are rooted in quantum fluctuations, which is a prediction by the theory of inflation. The evolution of these small over- and underdensities is governed by the action of gravity. This leads to overdensities attracting more matter and therefore becoming even denser, whereas underdensities become less and less dense. This process leads to the formation of dense "pancake-like" walls, which further collapse to form filaments and finally haloes. These haloes are finally assumed to be sites in which galaxies and galaxy clusters form and reside today.

The theoretical description of structure formation is located within the framework of the cosmological standard model ΛCDM. This by now well established theory (see Chapter 2 for an introduction) assumes that gravity is the main driver for cosmic evolution, that 80 per cent of the matter is made up by cold dark matter (CDM), which is of unknown composition so far, and that the accelerated expansion of the Universe is caused by the cosmological constant Λ. It was realised by Peebles (1965) that cosmic structures grow in a hierarchical fashion, i.e. overdense regions on small scales collapse first, whereas larger objects form later. Moreover, Peebles and Yu (1970) proposed that the origins of today's rich cosmic structure left an imprint in the CMB in form of small temperature fluctuations. However, it was realised later in Peebles (1982) that the matter content of the Universe must be dominated by dark matter in order to explain the amplitude of the CMB temperature fluctuations to be two orders of magnitude lower than first expected.

Since gravity is a highly non-linear theory, the analytical description of the process of structure formation is very difficult. A first approach in early years was therefore to linearise the equations, which should be valid in the case of very small density fluctuations (see e.g. Lifshitz, 1946; Bonnor, 1957). Due to the hierarchical nature of structure formation, the validity of this description depends on both the considered length scale and the considered time. At the present time, the linear description should be valid

on length scales of $\gtrsim 20$ Mpc. However, the majority of cosmic structures as for example filaments or haloes can only be described by the full non-linear equations. Substantial progress in describing the mildly non-linear regime has been made by Zel'dovich (1970), who provided an approximate description in terms of the initial deformation tensor. It resulted in the notion that structures first collapse to form "pancake-like" walls as mentioned above, before they collapse further to form filaments and then haloes. At a similar time, Gunn and Gott (1972) introduced their model of spherical collapse, describing the evolution of a spherical halo in an expanding space. Finally, Press and Schechter (1974) presented the first analytic derivation of the halo mass function, i.e. the comoving number density of haloes of a given mass, combining the ideas of spherical collapse with a linear extrapolation.

In the last three decades, cosmic structure formation has been described increasingly by the help of simulations. These solve the non-linear equations numerically and allow simulating the formation of cosmic structures for a given cosmological model. The constant improvement of computational power allowed to simulate larger and larger simulation volumes with increasing resolution as well as to include baryonic effects. Milestones were for example the *Millennium* simulation (Springel et al., 2005), which simulates the dark matter distribution in a box with a side length of 739 Mpc, or the *Illustris* simulation (Vogelsberger et al., 2014), which also includes baryonic effects like radiative cooling, stellar feedback, etc. in a box with side length of 111 Mpc.[1]

Non-linear cosmic structures are of interest for several reasons. On the one hand, they are simple in the sense that they can be classified into only a few categories (haloes, filaments, etc.) and that baryonic effects can usually be neglected. On the other hand, their non-linear formation is complicated enough to provide an important test for the cosmological standard model. Furthermore, they can be observed in large numbers such that their statistical properties can be measured to a precision that allows the determination of cosmological parameters. This has become in particular true in recent years with several ongoing large galaxy surveys that provide an enormous amount of observational data. The amount of data will even increase in the years to come with planned survey programmes that will measure the cosmic large-scale structure with an unprecedented precision. Current programmes are for example the Dark Energy Survey (DES, Abbott et al., 2018) and the Kilo Degree Survey (KiDS, de Jong, J. T. A. et al., 2017), which are mapping large fractions of the sky. In the future, these data will be complemented by the even more detailed observations of the Euclid satellite (Laureijs et al., 2011), the Legacy Survey of Space and Time (LSST, Ivezić et al., 2019) at the Vera C. Rubin Observatory in the optical wavebands and by SKA (Maartens et al., 2015) in the radio wavebands. These will provide an enormous amount of data, which will allow determining statistical quantities of the non-linear large-scale structure and cosmological

1 The box lengths are typically given in units of h^{-1}Mpc, where the dimensionless Hubble parameter h (defined in Eq. 2.8) has been factored out. We absorbed here h into the units by using $h = 0.6766$ (Planck Collaboration, 2020a).

parameters with per cent precision or better. For this reason, it is important to advance as well the theoretical understanding of structure formation.

In this thesis, we investigate several aspects of non-linear structures using both analytic approaches and a comparison of observations with the predictions of a cosmological simulation. The analytic calculations are mainly based on kinetic field theory (KFT), which is a recently introduced theory to describe cosmic structure formation using statistical field theory for an ensemble of classical point particles (see Bartelmann et al., 2019, for a review). There are several reasons for why it is worthwhile trying to advance the analytical description of cosmic structure formation. While cosmic simulations seem to provide easy to interpret results at first sight, they can be affected by numerical errors and systematic biases, which can alter the results substantially without being noticed. This is connected to the limits to the information gain through simulations. Usually, simulations are used in the form that one inserts a number of parameters and then "runs the machine", without reaching the fundamental processes happening inside the machine. Analytic descriptions instead help to better understand these fundamental laws governing the formation of structures in the Universe. Moreover, high-resolution cosmic N-body simulations take a long time and require large computational power and storage capacities. In contrast, an analytic description for some of the quantities of interest, e.g. higher order spectra or the halo mass function, allows a computation in a small fraction of the time a simulation takes. Once an analytical description is found, it can furthermore be adapted easily to changes of the model such as the modification of the laws of gravity. In the case of a simulation this would require a completely new run of the simulation. Therefore, precise parameter studies on the basis of simulations turn out to be very challenging. For these reasons, we will explore ways to obtain analytic derivations for two statistical quantities of non-linear cosmic structures: (*i*) the probability density function (PDF) of the cosmic matter density field and (*ii*) the halo mass function. We will base our calculations on the KFT framework already developed.

N-body simulations, however, allow for solutions of the non-linear equations in regimes, which are not accessible or only difficult to access by analytical calculations. As a concrete example for the structure in the highly non-linear regime, we will consider the substructure of a massive galaxy cluster Abell 2744. Since the cosmological standard model needs to make valid predictions also in this regime, we will take the substructure distribution of Abell 2744 as a test for ΛCDM. To this end, we use the data of the N-body simulation Millennium XXL (Angulo et al., 2012) as the prediction of ΛCDM. We will put special emphasis on treating observational and simulated data alike.

This thesis is structured as follows. We will start with an introduction to cosmology in Chapter 2, where we introduce the most important concepts relevant for our further derivations. We continue with an overview of KFT in Chapter 3. Here, we will make the reader familiar with its central object, i.e. the generating functional, and a reformulation in terms of macroscopic fields the so called resummed kinetic field theory (RKFT). The first main part of this thesis concerns the density PDF in Chapter 4. We will introduce

models that are currently used in the literature and use the predictions of KFT to fix the parameters of two of these models, i.e. the lognormal model and the generalised normal model. We will furthermore try to derive the PDF from the generating functional directly. We then focus on the halo mass function in the second main part of the thesis. We review the current approaches to deriving the halo mass function in Chapter 5 and add a critical discussion of some conceptual shortcomings. We then present an alternative based on the present day non-linear density field including excursion set theory with correlated random walks in Chapter 6. Subsequently, we turn towards a more explicit investigation of non-linear structure in the last part of this thesis. We use observational data of Abell 2744 in order to compare its substructure to the predictions of ΛCDM in Chapter 7. To this end, we introduce an algorithm based on the wavelet transform which is then applied to the observational and simulated data. Finally, we conclude with a summary of our results in Chapter 8.

Parts of this thesis have already been published in the following papers:

- Jauzac, M., Eckert, D., Schaller, M., Schwinn, J., Massey, R., Bahé, Y., Baugh, C., Barnes, D., Dalla Vecchia, C., Ebeling, H., Harvey, D., Jullo, E., Kay, S. T., Kneib, J. -P., Limousin, M., Medezinski, E., Natarajan, P., Nonino, M., Robertson, A., Tam, S. I., Umetsu, K. (2017): *Growing a 'cosmic beast': observations and simulations of MACS J0717.5+3745*. MNRAS, **481** 3, 2901
- Schwinn, J., Baugh, C. M., Jauzac, M., Bartelmann, M., Eckert, D. (2018): *Uncovering substructure with wavelets: proof of concept using Abell 2744* . MNRAS, **481** 4, 4300

2 COSMOLOGY

The field of cosmology seeks to describe the evolution of the Universe as a whole. It therefore tries to find a consistent description from the earliest times – potentially the Universe's origin, if it has one – until today. It is especially concerned with the creation of structures in the Universe and their evolution over time. In this chapter, we will give a brief overview over the most important cosmological concepts and quantities. Since modern cosmology is a rather wide field, we will focus on only those concepts that will be important later in this thesis. We will start in Section 2.1 with a summary of the evolution of the Universe smoothed over large scales, where it can be assumed to be homogeneous. This will lead us to the introduction of the cosmological standard model in Section 2.2. We continue with the description of the evolution of small structures on top of the homogeneous background field in Section 2.3. Finally, we conclude with the introduction of the power spectrum in Section 2.4.

2.1 THE HOMOGENEOUS UNIVERSE

The theoretical base of cosmology lies in the description of the evolution of the Universe through the effects of gravity. All other forces can be neglected on cosmological scales. The weak and strong force are extremely short ranged (weak force < 1 fm, strong force ~ 1 fm). They therefore only play a role in the earliest times of the Universe and have no effect on the later evolution. Electromagnetic forces play an important role for galaxy formation and the intergalactic medium. However, the range of electric forces is limited by Debye-shielding of the free charges in the cosmic plasma to scales $\lesssim 1$ m. The effect of magnetic fields in cosmology is still not completely understood. There seem to exist magnetic fields on cosmological length scales, i.e. several Mpc. However, they usually reach field strengths of only $\lesssim 1$ μG (Han, 2017). They therefore do not contain enough energy to play a role in the evolution of the Universe.

The current theory of gravity is general relativity. It describes gravity via a geometric theory based on the idea that space and time are two parts of one and the same mathematical object – a four dimensional manifold called *spacetime*. While the mass of objects – or more generally energy and momentum – causes the spacetime to be curved, it is exactly this curvature of spacetime that governs the trajectories of matter

and energy. It therefore causes the effect, which we call the gravitational acceleration. The interplay between energy and curvature is described by the field equations[1]

$$G_{\mu\nu} + \Lambda g_{\mu\nu} = \frac{8\pi G}{c^4} T_{\mu\nu} \,, \tag{2.1}$$

where $g_{\mu\nu}$ is the metric tensor describing the *spacetime* manifold, $G_{\mu\nu}$ the Einstein tensor, which contains second derivatives of the metric tensor and hence describes its curvature of spacetime, Λ is the cosmological constant, G Newton's gravitational constant, c the speed of light in vacuum and finally $T_{\mu\nu}$ is the energy-momentum tensor describing the distribution of matter and energy. Since the introduction of the field equations in Einstein (1915), they have been confirmed impressively well by a large number of experiments over the last century (e.g. Dyson et al., 1920; Lemaître, 1931; Pound and Rebka, 1959; Shapiro, 1964; LIGO-Collaboration et al., 2016). The equations are non-linear, coupled partial differential equations and therefore they cannot be solved for general systems. It is, however, possible to find solutions for special cases where the equations can be simplified due to the symmetries of the system.

In the case of cosmology, one is first of all interested in the evolution of the Universe as a whole. For this reason, considering only very large scales (we will discuss in the paragraph below, what *very large* means in this context), two assumptions can be made in order to simplify the field equations for a freely falling observer considerably:

1. *The Universe is isotropic.*
2. *No point in the Universe is preferred to any other (Copernican principle).*

The combination of both assumptions implies that the Universe must be spatially homogeneous on large scales, since it must be isotropic around each point in space. These two symmetry assumptions are often referred to as the *cosmological principle*.

The assumption of isotropy is well supported by observations of the cosmic microwave background (CMB, see e.g. Bennett et al., 1994; Planck Collaboration, 2020b). These show that after foreground cleaning and correcting for the motion with respect to the CMB rest frame, the Universe is isotropic with a precision better than 10^{-4}. It is way harder to find evidence for the second assumption, since a test of homogeneity would require observing the Universe from different points in space. Observations, however, only test our own backward light-cone. Thus, a time-evolving homogeneous universe cannot be distinguished from an inhomogeneous universe with a different time evolution. While it is not possible at the moment to directly proof the validity of the homogeneity assumption, it is still possible to perform in a sense null hypothesis tests and constrain if the observational data would at least be compatible with a homogeneous universe. If scales $\gtrsim 100$ Mpc are considered, there does not seem to be evidence for inhomogeneities

1 Note that the Λ- and the $T_{\mu\nu}$-term appear in the literature sometimes with a negative sign. This depends on the choice of metric signature and the definition of the Ricci tensor. We adopt here the sign convention of Misner et al. (1973) that uses the metric signature (-,+,+,+).

(Bull et al., 2012; Redlich et al., 2014a). Moreover, also large galaxy surveys reach the same conclusion, i.e. that the Universe appears homogeneous on scales $\gtrsim 100$ Mpc (e.g. Hogg et al., 2005; Ntelis, 2016). The cosmological principle is therefore a valid assumption, when the Universe smoothed over scales of ~ 100 Mpc is considered.

On smaller scales, however, the Universe is obviously inhomogeneous with a large variety of structures (e.g. voids, walls, filaments and nodes). The standard cosmological description assumes that the background solution (i.e. where the cosmological principle holds) can be treated as a solution of the field equations decoupled of the small scale evolution; in other words that backreaction effects can be neglected[2] (Baumann et al., 2012; Adamek et al., 2013; Green and Wald, 2014).

Under the assumption of the cosmological principle, the metric takes a particularly simple form. Due to isotropy, the spatial part can be expressed in spherical coordinates (χ, θ, φ). The only entry in the spatial part of the metric, which is allowed by the symmetries of the system, is a function $a(t)$ scaling the spatial part as a whole. It can only depend on time due to homogeneity. The so called *Robertson-Walker* metric then takes the form

$$\mathrm{d}s^2 = -c^2\mathrm{d}t^2 + a^2(t)\left[\mathrm{d}\chi^2 + f_K^2(\chi)\mathrm{d}\Omega^2\right] , \tag{2.2}$$

where $\mathrm{d}\Omega$ is the solid angle element and $f_K^2(\chi)$ contains the dependence of the angular part of the metric on spatial curvature K

$$f_K(\chi) = \begin{cases} K^{-1/2}\sin\left(K^{1/2}\chi\right) & (K > 0) \\ \chi & (K = 0) \\ |K|^{-1/2}\sinh\left(|K|^{1/2}\chi\right) & (K < 0) \, . \end{cases} \tag{2.3}$$

The scale factor is typically normalised to be $a(t_0) = 1$ at present time t_0 and in the following text all quantities with a subscript zero shall denote present day values. With the metric at hand, the left side of the field equation (Eq. 2.1) is determined. The symmetries of the cosmological principle allow furthermore to write the energy-momentum tensor in a simple form. When viscosity and matter decay are neglected, it can be assumed to have the form of a perfect fluid

$$T^{\mu\nu} = \left(\rho + \frac{p}{c^2}\right) u^\mu u^\nu + p g^{\mu\nu} , \tag{2.4}$$

2 It should be noted, however, that the topic of backreaction is still under debate (see e.g. for a review of the current status Bolejko and Korzyński, 2017) and that there is a number of scholars who doubt the validity of this assumption that backreaction can be neglected (Räsänen, 2006; Buchert et al., 2015).

where ρc^2 denotes the fluid's energy density, p its pressure and u^μ the four velocity of the fluid. Choosing the frame of reference of a freely falling observer (i.e. $u^\mu = (c, 0, 0, 0)$) and inserting the energy momentum tensor (Eq. 2.4) and the metric (Eq. 2.2) into the field equations (Eq. 2.1), they simplify considerably and can be written as two equations

$$\left(\frac{\dot{a}}{a}\right)^2 = \frac{8\pi G}{3}\rho - \frac{Kc^2}{a^2} + \frac{\Lambda c^2}{3}\,, \tag{2.5}$$

$$\frac{\ddot{a}}{a} = -\frac{4\pi G}{3}\left(\rho + \frac{3p}{c^2}\right) + \frac{\Lambda c^2}{3}\,, \tag{2.6}$$

called the *Friedmann equations*. Furthermore, we define the Hubble-Lemaître function

$$H(a) := \frac{\dot{a}}{a}\,, \tag{2.7}$$

which quantifies the expansion rate of the Universe. Today's value of the Hubble-Lemaître function (i.e. the Hubble-Lemaître parameter) is typically expressed in units of 100 km s^{-1} Mpc^{-1} and therefore the dimensionless parameter h is defined via

$$H_0 =: 100h \text{ km s}^{-1}\,\text{Mpc}^{-1}\,. \tag{2.8}$$

The expansion of space causes a stretch of the photons' wavelengths, the *cosmological redshift*. It is related to the scale factor via

$$z := \frac{\lambda_\text{o} - \lambda_\text{e}}{\lambda_\text{e}} = \frac{1}{a} - 1\,, \tag{2.9}$$

where λ_e denotes the photon's wavelength at emission and λ_o the observed wavelength.

In order to simplify the first Friedmann equation even further, we will assume the fluid to consist of two components, a non-relativistic component, which scales as $\rho_m \propto a^{-3}$, and a relativistic component, which scales as $\rho_r \propto a^{-4}$. The additional factor of a^{-1} for relativistic matter can be understood as follows. For relativistic particles, the rest-mass is zero (photons) or negligible and the energy of each particle is determined by its wavelength. The particle's wavelength gets stretched as $\propto a$ (see redshift, Eq. 2.9) in addition to the scaling of the number density as $\propto a^{-3}$ and the combination of both effects leads to a scaling with a^{-4}. We wish to express the different energy components as dimensionless quantities. We therefore identify the typical energy density scale occurring in the equation and define it as the critical density

$$\rho_\text{crit} := \frac{3H^2}{8\pi G}\,. \tag{2.10}$$

This allows us to define the dimensionless density parameters

$$\Omega_\text{m}(a) := \frac{\rho_\text{m}(a)}{\rho_\text{crit}(a)}, \qquad \Omega_\text{r}(a) := \frac{\rho_\text{r}(a)}{\rho_\text{crit}(a)}\,. \tag{2.11}$$

Also the curvature and cosmological constant terms in the first Friedmann equation can be expressed in terms of dimensionless parameters

$$\Omega_K(a) := -\frac{Kc^2}{H^2a^2}, \qquad \Omega_\Lambda(a) := \frac{\Lambda c^2}{3H^2}\,. \tag{2.12}$$

Inserting the definition of $H(a)$ and the density parameters Ω_i into Eq. (2.5) while expressing them through their scaling with a, we obtain the particularly simple expression for the first Friedmann equation

$$H^2(a) = H_0\left[\Omega_{r0}a^{-4} + \Omega_{m0}a^{-3} + \Omega_{K0}a^{-2} + \Omega_{\Lambda 0}\right]\,. \tag{2.13}$$

2.2 THE COSMOLOGICAL STANDARD MODEL

The first Friedmann equation in the form of Eq. (2.13) forms the base of the current standard model of cosmology, which is called the ΛCDM *model*. Its name derives from its two main ingredients, i.e. the cosmological constant Λ and cold dark matter (CDM). We will summarise the origin and impact of these assumptions as well as observational evidence below.

2.2.1 *Dark matter*

The observational evidence for the need for a dark (i.e. a non-luminous) matter component dates back to the early 20$^{\text{th}}$ century. The observations of the velocity dispersion of galaxy clusters indicated that these clusters must contain much more mass than could be explained through the matter visible in form of the stars of the member galaxies (Zwicky, 1933). This additional matter component was named *dark matter*. A similar problem was observed four decades later when galaxy rotation curves were used to determine the mass of spiral galaxies (Rubin et al., 1978). The measured flat rotation curves could only be explained with the existence of a massive dark halo surrounding each galaxy and extending to radii way larger than the galactic disc.

The strongest indication, that this dark matter needs to be a completely new form of matter, came with the discovery of the cosmic microwave background (CMB) and the investigation of its temperature fluctuations. In the 1970s, it was assumed that the CMB must contain temperature fluctuations of order 10^{-3}, simply by scaling back today's density fluctuations (making the conservative choice that fluctuations today are at least $\delta \sim 1$) to the redshift of the CMB and assuming the coupling between matter and radiation leads to an imprint of the density fluctuations in the CMB. It came as a surprise when no fluctuations of this order were observed (Boughn et al., 1981; Melchiorri et al., 1981). Peebles (1982) suggested that the smaller amplitude of the temperature fluctuations could be explained if there existed an unknown form of matter that does not or only extremely weakly interact with electromagnetic radiation.

Finally, further evidence for the existence of dark matter is provided by the reconstruction of cluster masses through gravitational lensing (e.g. Taylor et al., 1998; Refregier, 2003) and most prominently the separation of matter and gas in the so called *bullet cluster* (Clowe et al., 2006). Today, a large variety of different explanations for dark matter exist ranging from massive dark objects like black holes, to a unknown particle species or modifications of the theory of gravity. The most common theory is that dark matter is explained by a novel particle species. If thermally produced, such a particle needs to be heavy (i.e. $\gtrsim 3$ keV) in order to be in agreement with the observed amount of substructure in the Universe[3]. Since a heavy particle would have a small velocity dispersion, it is usually called *cold dark matter* (CDM). The standard model of cosmology assumes that dark matter is in the form of such cold dark matter.

2.2.2 *Dark energy*

The second ingredient to the ΛCDM model is the cosmological constant. In 1998 and 1999, the teams of Riess and Perlmutter used supernovae of type Ia as standardisable candles in order to determine the relation between distance and redshift in the Universe. This led to the surprising result that the expansion of the Universe is accelerating (Riess et al., 1998; Perlmutter et al., 1999). This behaviour can be explained by an additional energy component with a negative pressure, which is typically called *dark energy*. A positive cosmological constant Λ provides the simplest explanation for the accelerated expansion. It can be absorbed in the energy momentum tensor and therefore be seen as an energy component whose density does not change with time.

Additional evidence for the accelerated expansion of the Universe is provided by the CMB (Planck Collaboration, 2020a) in combination with the clustering of galaxies (eBOSS Collaboration, 2020) and gravitational lensing (Joudaki et al., 2017; Köhlinger et al., 2017; Troxel et al., 2018). There exists an overwhelming variety of possible theories explaining the accelerated expansion either through modifications of the gravitational laws (modified gravity) or an additional component in the energy momentum tensor (dark energy), like for example a scalar field. However, all of the measurements are consistent with the accelerated expansion being caused by the cosmological constant Λ.

2.2.3 *The ΛCDM-model*

These two ingredients, (*i*) assuming the existence of a cold dark matter component and (*ii*) that the cosmological constant is the reason for the accelerated expansion of

3 A light particle would have a large velocity dispersion (for this reason also called *hot dark matter*), which would lead to small scale structures (e.g. satellite galaxies) being washed out. Comparing the amount substructure observed in the Universe to that observed in hot dark matter simulations, leads to conflicting results. A hypothetical dark matter candidate, which is not produced thermally, would for example be an axion-like particle (e.g. Hu et al., 2000).

Table 2.1: Cosmological paramters determined via the combination of measurements of the Planck satellite, lensing and baryonic acoustic oscillations (last column in Table 2 of Planck Collaboration, 2020a).

A_s	2.105 ± 0.030
n_s	0.9665 ± 0.0038
$100\theta_{MC}$	1.04101 ± 0.00029
τ	0.056 ± 0.014
Ω_b	0.04858 ± 0.00068
Ω_c	0.2607 ± 0.0038
Ω_Λ	0.6889 ± 0.0056
σ_8	0.8102 ± 0.0060
h	0.6766 ± 0.0042

the Universe, form in combination with the Friedmann equations the current standard model of cosmology, ΛCDM. In its simplest form, it depends on only six parameters: the amplitude of the primordial power spectrum[4] A_s and the exponent of its power law n_s, the observed angular size of the sound horizon at recombination θ_{MC}, the reionisation optical depth τ, the baryon density Ω_b and that of dark matter[5] Ω_c. All other parameters like for example the Hubble-Lemaître constant H_0 or the normalisation of the matter power spectrum σ_8 can be derived from these six parameters[6]. Starting from the formation of the first elements in the early Universe until the present day with the Universe being filled with a large variety of structures, the ΛCDM-model gives a coherent model of the cosmic evolution. It is able to explain a variety of observations impressively well, such as the fluctuations in the cosmic microwave background (Planck Collaboration, 2020a), the large-scale clustering of galaxies (Cole et al., 2005; eBOSS Collaboration, 2020), weak gravitational lensing (Joudaki et al., 2017; Köhlinger et al., 2017; Troxel et al., 2018) and the accelerated expansion of the Universe measured by supernovae of type Ia (Riess et al., 1998; Perlmutter et al., 1999). The combination of these cosmological probes allows determining the six ΛCDM-parameters to percent precision (see Table 2.1).

Due to the non-linear nature of gravity, it is very hard to obtain analytical predictions for the formation of cosmic structures in a ΛCDM-universe. While it is possible to linearise the equations for early times (which will be introduced in Section 2.3), these

4 See introduction of the power spectrum in Section 2.4.
5 These two densities add up to the total matter density as $\Omega_m = \Omega_b + \Omega_c$.
6 In order to derive σ_8, an additional assumption on the shape for the evolved density-fluctuation power spectrum has to be made.

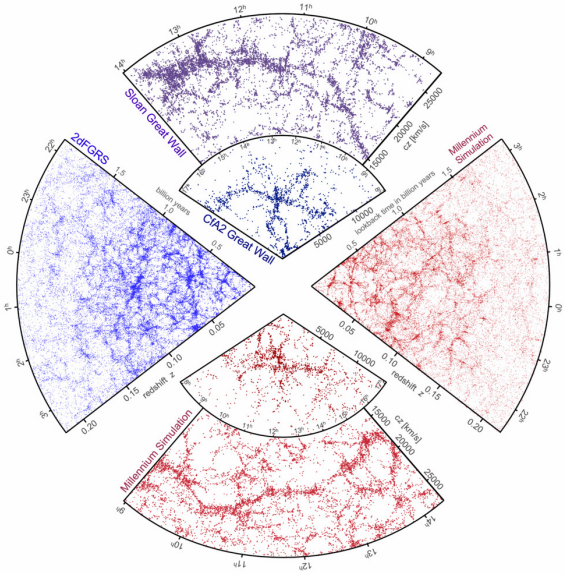

Figure 2.1: Galaxy distribution observed in large galaxy redshift surveys, e.g. SDSS or 2dFGRS in comparison to the ΛCDM prediction as obtained by the Millennium simulation. The figure was taken with kind permission from Springel et al. (2006), Fig. 1.

approximations break down when the density fluctuations grow non-linearly over time. For this reason, numerical simulations play an important role to obtain theoretical predictions of ΛCDM that can be tested against observations. Such simulations evolve a realisation of the initial density field forward in time to the present day. By now, there exist a large number of numerical simulations modelling different cosmologies on various scales, while containing either dark matter only or baryons additionally. The Millennium simulations (Springel et al., 2005; Boylan-Kolchin et al., 2009; Angulo et al., 2012) are a renowned set of dark matter only simulations. It was possible to use these to show that the ΛCDM prediction of the large-scale structure corresponds well with that obtained from observations (see Fig. 2.1). We will make use of one of these simulations, the Millennium XXL simulation, in Chapter 7. An alternative, analytical approach to non-linear structure formation based on kinetic field theory will be described and used in Chapters 3 and 4.

2.3 LINEAR STRUCTURE FORMATION

While the Friedmann equations describe the background evolution of the Universe, we now would like to proceed to the formation of structures in terms of fluctuations in the density field. We will quantify the density fluctuations in terms of the density contrast

$$\delta(\vec{x}) = \frac{\rho(\vec{x}) - \bar{\rho}}{\bar{\rho}}\,, \tag{2.14}$$

where $\bar{\rho}$ denotes the mean cosmic density, or in terms of its Fourier transform

$$\delta(\vec{k}) = \int \mathrm{d}^3\vec{x}\; \delta(\vec{x})\; e^{-\mathrm{i}\vec{x}\cdot\vec{k}}. \tag{2.15}$$

The analytical description of structure formation in full generality is a very complicated task due to the non-linear nature of gravity. During the earliest epoch of the Universe, however, the fluctuations are still small as can be seen in the CMB ($\delta \sim 10^{-5}$). We can therefore linearise the equations to describe structure formation in the early Universe. We will use the non-relativistic fluid equations[7] to link the density ρ, the velocity $\vec{v}$, the pressure p and the gravitational potential ϕ (see e.g. Peebles, 1993 pp. 112 or Mo et al., 2011, pp. 163 for the details of the calculation). The non-relativistic fluid equations are given by the continuity equation

$$\frac{\partial\rho}{\partial t} + \vec{\nabla}\cdot(\rho\vec{v}) = 0\,, \tag{2.16}$$

the Euler equation

$$\frac{\partial\vec{v}}{\partial t} + (\vec{v}\cdot\vec{\nabla})\vec{v} = -\frac{\vec{\nabla}p}{\rho} - \vec{\nabla}\phi \tag{2.17}$$

and the Poisson equation[8]

$$\Delta\phi = 4\pi G\rho\,. \tag{2.18}$$

In order to linearise these equations, we consider the values of all fields as small perturbations on top of the background field, e.g. $\rho = \bar{\rho} + \delta\rho$, $\vec{v} = \vec{\bar{v}} + \delta\vec{v}$, etc. We furthermore

7 Since we describe structure formation on spatial scales $r \ll c/H(t)$, time scales $t \ll 1/H(t)$, the velocities are small $v \ll c$ and the potentials are weak $\Phi \ll c^2$ we can neglect relativistic effects.

8 It is interesting to note that from the Newtonian limit of Einstein's field equations we would obtain the Poisson equation including the cosmological constant Λ. However, since we describe structure formation on scales $r \ll c/H(t)$ and moreover the Λ-term in $H(t)$ is just becoming relevant in the present era, we can neglect Λ here.

express the equations in terms of comoving coordinates $\vec{x}$ instead of the physical coordinates[9], $\vec{r} = a(t)\vec{x}$, and define the peculiar velocity in comoving units, $\vec{u} := \delta\vec{v}/a$. This leads to the perturbation equations

$$\frac{\partial\delta}{\partial t} + \vec{\nabla}\cdot\vec{u} = 0\,, \tag{2.19}$$

$$\frac{\partial\vec{u}}{\partial t} + 2H\vec{u} = -\frac{c_s^2\vec{\nabla}\delta}{a^2} - \frac{\vec{\nabla}\delta\phi}{a^2}\,, \tag{2.20}$$

$$\Delta\delta\phi = 4\pi G\bar{\rho}a^2\delta\,, \tag{2.21}$$

where we introduced the sound speed $c_s^2 := \delta p/\delta\rho$ to express the pressure perturbations in terms of density perturbations. By taking the divergence of Eq. (2.20) and inserting it into the time derivative of Eq. (2.19), we obtain the *linear growth equation*

$$\ddot{\delta} + 2H\dot{\delta} = \frac{c_s^2}{a^2}\nabla^2\delta + 4\pi G\bar{\rho}\delta\,. \tag{2.22}$$

Since the growth equation is a homogeneous differential equation, we use the separation of variables to factor out the time evolution and write the density field $\delta(\vec{x},t)$ as a product of the initial density $\delta_{\rm i}(\vec{x})$ and a factor $D_+(t)$,

$$\delta(\vec{x},t) = D_+(t)\delta_{\rm i}(\vec{x})\,. \tag{2.23}$$

The factor $D_+(t)$ is typically called the *linear growth factor*, since it describes the growth of density modes with time. It should be noted that since the growth equation (Eq. 2.22) is of second order, it has two solutions, i.e. a growing and a decaying solution. Since the decaying solution will play no role in the formation of structures, we only consider the growing solution. For now, we will also only consider the evolution of dark matter structures. Since dark matter is pressureless, we can neglect the pressure term in Eq. (2.22) and insert Eq. (2.23) to obtain

$$\ddot{D}_+ + 2H\dot{D}_+ = 4\pi G\bar{\rho}D_+\,. \tag{2.24}$$

A good approximation to the solution of this differential equation has been found by Carroll et al. (1992)

$$D_+(z) = \frac{5a}{2}\Omega_{\rm m}(z)\left[\Omega_{\rm m}^{4/7}(z) - \Omega_\Lambda(z) + \left(1+\frac{1}{2}\Omega_{\rm m}(z)\right)\left(1+\frac{1}{70}\Omega_\Lambda(z)\right)\right]^{-1}\,. \tag{2.25}$$

This approximation, however, is only valid for cosmological-constant models and not for more general models including dynamical dark energy. As mentioned above, this

9 Note that this also leads to $\vec{\nabla}$ now describing the derivative with respect to the comoving coordinates $\vec{\nabla} \to \vec{\nabla} \equiv \vec{\nabla}_x = a\vec{\nabla}_r$ and also the time derivative gets replaced by $\frac{\partial}{\partial t} \to \frac{\partial}{\partial t} - H\vec{x}\cdot\vec{\nabla}$.

linear description only holds for a limited range of time. This can be understood quite easily when considering that the initial density field can be assumed to be Gaussian and that it stays Gaussian under linear evolution. Furthermore, it is obvious that the density contrast cannot take lower values than $\delta = -1$, which corresponds to $\rho = 0$, i.e. empty space and therefore the support of the probability distribution has a lower limit. Hence, it must become non-Gaussian once the density fluctuations become of order $|\delta| \approx 1$, since the probability distribution cannot be symmetric any more as required by the Gaussian. For this reason, it is assumed that the linear description breaks down for values $\delta \gtrsim 1$. The condition of small δ is fulfilled for early times and when the field is smoothed over large scales.

2.4 THE POWER SPECTRUM

Since the exact theoretical description of the evolution and state of every point in space is an impossible task, modern cosmology resorts to a statistical description. It considers the Universe to be one realisation of a random process. We therefore need statistical tools in order to relate theoretical predictions to observations. One of the simplest statistical quantities of a random field is its variance. It is typically useful to investigate the variance of the field's Fourier modes, which is called the power spectrum. For the field of density fluctuations, it is defined as

$$\left\langle \delta(\vec{k})\, \delta^*(\vec{k}') \right\rangle =: (2\pi)^3 \delta_{\mathrm{D}}(\vec{k} - \vec{k}') P(|\vec{k}|)\,. \tag{2.26}$$

Due to statistical isotropy, the power spectrum can only depend on the absolute value $|\vec{k}|$ and the δ_{D}-distribution ensures that modes are uncorrelated as required by homogeneity[10].

The Gaussian probability distribution is defined by only two parameters, the mean μ and the variance σ^2. Since the mean of $\delta(\vec{k})$ is zero by definition, the statistical properties of $\delta(\vec{k})$ are completely specified by the power spectrum as long as $\delta(\vec{k})$ can be described as a Gaussian random field. As soon as the Gaussian description breaks down, all so called higher order spectra, i.e. bispectra, trispectra, etc., become non-zero and therefore relevant[11].

10 It should be noted that throughout this thesis angular brackets denote ensemble averages and in this case an average over an ensemble of density fields. In practise, however, the ergodic principle is assumed and the ensemble average is replaced by an average over statistically independent regions of one realisation, i.e. our Universe.

11 For completeness it shall be mentioned that for a Gaussian random field all even higher moments are also non-zero (i.e. trispectra, etc.). However, they can be expressed via Wick's theorem in terms of the powerspectrum.

We will furthermore define the density field smoothed by a window function $W_R(|\vec{x}|)$, which depends on a smoothing radius R

$$\delta_R(\vec{x}) := \int \mathrm{d}^3\vec{y}\delta(\vec{x})W_R(|\vec{x}-\vec{y}|)\,. \tag{2.27}$$

Typically the field is smoothed using a spherical top hat function. The variance of the smoothed field is related to the power spectrum via

$$\sigma_R^2 = 4\pi \int \frac{\mathrm{d}k\, k^2}{(2\pi)^3} P(k) W_R^2(k)\,, \tag{2.28}$$

where $W_R(k)$ denotes the Fourier transform of the spherical top hat, given by

$$W_R(k) = \frac{j_1(kR)}{kR}\,. \tag{2.29}$$

From theoretical considerations it is found that the power spectrum can be expressed as a power law (e.g Peebles and Yu, 1970; Zel'dovich, 1972)

$$P_{\mathrm{i}}(k) = A_s k^{n_s}\,. \tag{2.30}$$

The parameters n_s and A_s remain free parameters of the ΛCDM model and need to be determined by observations (see Table 2.1). The amplitude A_s is in some cases determined by measuring the variance of the density field smoothed over a sphere with radius $R = 8h^{-1}$Mpc, i.e. σ_8 according to Eq. (2.28). This, however, requires assuming a shape of the evolved power spectrum.

3

KINETIC FIELD THEORY

The quantitative description of the formation of structures in the cosmos is at the core of modern cosmology. On the observational side, the measurement of the statistical distribution of structures has become more and more precise in the last decades. In parallel, there has been a shift towards simulations on the theoretical side. Despite this, the need for an analytical description of cosmic structure formation is now as before very high, since it offers two advantages. First, large cosmological simulations with high spatial resolution require a large amount of computational time, which can reach from several days up to months. Parameter estimations that match the level of precision of the upcoming large-scale surveys, e.g. LSST (Ivezić et al., 2019) or Euclid (Laureijs et al., 2011), require precise predictions for a six- or higher dimensional parameter space. This poses a problem, since running a large number of cosmological simulations, e.g. in order to perform a Monte Carlo Markov Chain analysis, is not feasible. An analytical description in contrast could deliver results within a small fraction of the time and therefore solve this problem. Second, an analytical description usually provides much deeper insight into the underlying physical processes than just a simulation. It would help to single out processes and effects relevant for structure formation and therefore understand its theory better.

In the previous chapter, we already showed an analytical description of structure formation in terms of linear perturbation theory (Section 2.3). The description in the non-linear regime, however, turns out to be a much harder task. A first approach in the mildly non-linear regime is represented by the Zel'dovich approximation (Zel'dovich, 1970). More recently proposed approaches include standard perturbation theory (SPT, see e.g. Bernardeau et al., 2002, for an extensive review), Lagrangian perturbation theory (LPT, e.g. Section 2.7 in Bernardeau et al., 2002) or effective theories (Carrasco et al., 2012; Floerchinger et al., 2017).

A completely different approach has been proposed recently by Bartelmann et al. (2016) by the name *kinetic field theory* (KFT, see Bartelmann et al., 2019, for a review), which is based on the field-theoretical description of classical particles (Penco and Mauro, 2006; Mazenko, 2010; Mazenko, 2011; Das and Mazenko, 2012; Das and Mazenko, 2013). It is a kinetic theory based on classical particle trajectories obeying Hamilton's equations. Stochasticity enters the formalism through the initial conditions of the particles, which are provided in terms of a probability distribution. The theory is formulated in phase space and therefore circumvents the well known *shell-crossing* problem, which is present for example in SPT and LPT approaches like the Zel'dovich approximation. This problem arises whenever the trajectories of two dark matter streams cross. In SPT it is

assumed that particles move as a single coherent flow, typically called the single stream approximation. This allows setting the velocity dispersion to zero. At shell-crossing, however, when multiple streams exist in the same region of space the velocity dispersion will become non-zero and the description breaks down (c.f. Section 2.2 in Bernardeau et al., 2002). This problem also arises in Lagrangian descriptions. In the Zel'dovich approximation for example, collapsing mass shells will cross each other when they form a "pancake". Due to the free streaming assumed in the Zel'dovich approximation, these shells would re-expand forever, while in reality they will obviously remain bound by the gravitational potential. It can be seen also from a mathematical viewpoint that the Lagrangian description breaks down. At shell crossing, two fluid elements originating from different initial positions end up at the same Eulerian position. This causes the mapping between Lagrangian and Eulerian space to lose its bijective property. The Jacobian of this mapping then becomes zero and the density (defined as inverse of the Jacobian) becomes singular (c.f. Section 2.5 in Bernardeau et al., 2002). In phase space, however, Hamilton's equations are unique once their initial conditions are set. For this reason, KFT provides a framework to compute statistical properties of the cosmic density field on scales that are much deeper in the non-linear regime than comparable formulations. For example, it is currently able to predict the non-linear power spectrum of cosmic density fluctuations up to a scale of $k \sim 5\,h\mathrm{Mpc}^{-1}$ with a precision of better than 12 per cent Bartelmann et al. (2019) compared to the N-body fitting formula of Smith et al. (2003).

In this chapter we will give an introduction to the basic concepts of KFT. It is mainly based on the review by Bartelmann et al. (2019) and Lilow et al. (2019). While we will focus on the application of KFT to cosmic structure formation, the applicability of KFT reaches far beyond cosmology. For example, there have been other applications such as systems of Rydberg atoms (Kozlikin, 2018; Bartelmann et al., 2019) or the derivation of a truncation criterion for the BBGKY hierarchy (Viermann et al., 2015). We will start with introducing the central object of KFT, i.e. the generating functional of correlation functions, in Section 3.1. We then introduce operators, which allow extracting correlators from the generating functional, in Section 3.2 and specify the initial conditions in Section 3.3. We continue with defining the propagators, which describe the free motion of particles, in Section 3.4. We will briefly discuss interactions in Section 3.5 and then proceed to calculating statistical quantities like cumulants or the power spectrum in Section 3.6. Finally, we will sketch the macroscopic formulation of KFT first introduced by Lilow et al. (2019) in Section 3.7. This reformulation of KFT will be used in one of our approaches to derive the probability distribution of the cosmic density field, which is described in the subsequent chapter (Chapter 4).

3.1 THE GENERATING FUNCTIONAL

Kinetic field theory is a theory to (not only but most importantly) predict statistical properties of the cosmic structure and their development over time. It is based on a central mathematical object, the *generating functional* Z, which is also known from quantum field theory (QFT). KFT, however, is a statistical field theory describing *classical* particles. As the name suggests, the generating functional can be used to generate correlation functions of arbitrary order and therefore takes a role similar to the partition sum in the statistical physics approach to thermodynamics. In full generality, it can be written as a path integral over all possible states of the system,

$$Z = \int \mathcal{D}\varphi \; P(\varphi)\,, \tag{3.1}$$

where φ denotes a general state of the system, $P(\varphi)$ is the probability distribution of these states and $\mathcal{D}\varphi$ signals that the integral is in fact a path integral. The aim will be now to construct a generating functional such that statistical quantities like the power spectrum of cosmic densities can be obtained by applying the corresponding operators to it. The computation of the power spectrum and higher-order spectra is done analogously to obtaining moments from the moment generating function of a random variable or to obtaining ensemble averages by applying derivative operators to the partition sum in thermodynamics.

Since it is our aim to describe cosmic structure formation, we would like to describe trajectories of classical particles. Let us introduce in this context the notation which will be needed for the calculations in this and the next chapter. KFT is based on the description of particle trajectories in phase space. We will denote the phase space coordinate of the jth particle by a six-dimensional vector $x_j := (\vec{q}_j, \vec{p}_j)$, with position $\vec{q}_j$, momentum $\vec{p}_j$ and $1 \leq j \leq N$. The phase space coordinates of all particles are contained in the tensor

$$\boldsymbol{x} = x_j \otimes e_j\,, \tag{3.2}$$

where summation over j is implied and the vector e_j has components $\left(e_j\right)_i = \delta_{ij}$, with $1 \leq i \leq N$. Furthermore, we define a scalar product for these tensors,

$$\langle \boldsymbol{x}, \boldsymbol{y} \rangle := (x_i \cdot y_j)(e_i \cdot e_j) = x_i \cdot y_i. \tag{3.3}$$

In this context, our system will be a sub-volume of the cosmos sampled by N particles and we will consider that its state is given by the final phase space coordinates of its N particles $\boldsymbol{x}^{(f)}$. We go one step beyond and do not want to express the state of system in terms of the phase space coordinates $\boldsymbol{x}^{(f)}$, but instead in terms of the trajectories starting at the particles' initial coordinates $\boldsymbol{x}^{(\mathrm{i})}$ and ending at $\boldsymbol{x}^{(f)}$. We denote these trajectories by $\boldsymbol{x}(t)$, but we will not write out the time dependence explicitly in the following calculations.

We now express the generating functional (Eq. 3.1) in terms of the particle trajectories,

$$Z = \int \mathcal{D}\boldsymbol{x}\, P(\boldsymbol{x})\,, \tag{3.4}$$

involving a path integral over all N particle trajectories. We only want to consider trajectories that fulfil the classical equations of motion, which will be reflected by the form that the trajectories' probability distribution $P(\boldsymbol{x})$ takes. Let us write the classical equations of motion abstractly as

$$\boldsymbol{E}\big(\boldsymbol{x}, \boldsymbol{x}^{(\mathrm{i})}\big) = 0\,, \tag{3.5}$$

where $\boldsymbol{E} = E_j \otimes e_j$. The particles shall be placed in phase space at an initial time according to a probability distribution $P\big(\boldsymbol{x}^{(\mathrm{i})}\big)$. We can then rewrite the probability of the trajectories as a conditional probability,

$$P(\boldsymbol{x}) = \int \mathrm{d}\boldsymbol{x}^{(\mathrm{i})}\; P\big(\boldsymbol{x}|\boldsymbol{x}^{(\mathrm{i})}\big)\, P\big(\boldsymbol{x}^{(\mathrm{i})}\big)\,, \tag{3.6}$$

with the transition probability $P\big(\boldsymbol{x}|\boldsymbol{x}^{(\mathrm{i})}\big)$ is given by

$$P\big(\boldsymbol{x}|\boldsymbol{x}^{(\mathrm{i})}\big) = \delta_{\mathrm{D}}\big[\boldsymbol{E}\big(\boldsymbol{x}, \boldsymbol{x}^{(\mathrm{i})}\big)\big]\,. \tag{3.7}$$

The delta distribution ensures that only such trajectories are selected that solve the equations of motion.

Since we are considering classical particles, the equation of motion for a single particle is given by the Hamiltonian equation[1],

$$\dot{x} - \mathcal{J}\nabla_x H(x) = 0\,. \tag{3.8}$$

Here, we have chosen the typical notation using the symplectic matrix defined as

$$\mathcal{J} := \begin{pmatrix} 0 & \mathbb{1}_3 \\ -\mathbb{1}_3 & 0 \end{pmatrix}\,, \tag{3.9}$$

where $\mathbb{1}_n$ denotes the unit matrix in n dimensions and $H(x)$ the Hamiltonian function. Formally, we can split the Hamiltonian into a free part H_0 describing the motion of particles without forces and a part H_{I} describing the contribution due to interactions between the particles, i.e. $H = H_0 + H_{\mathrm{I}}$. The solution to the free equations of motion (i.e. inserting $H = H_0$ into Eq. 3.8) can be formulated in terms of the Green's function $G(t, t')$,

$$x^{(0)}(t) = G(t, 0) x^{(\mathrm{i})}\,. \tag{3.10}$$

1 Note that we adopt here the notation of Lilow et al. (2019), which differs from Bartelmann et al. (2019), where H describes only the free Hamiltonian and interactions are introduced as an inhomogeneity in the Hamilton equation. In our case H describes the full Hamiltonian.

We can write the Green's function in terms of its position and momentum components

$$G(t,t') := \begin{pmatrix} g_{qq}(t,t')\mathbb{1}_3 & g_{qp}(t,t')\mathbb{1}_3 \\ 0 & g_{pp}(t,t')\mathbb{1}_3 \end{pmatrix} . \tag{3.11}$$

To demonstrate explicitly the role of the component functions g_{ab} (also called propagators), we plug this form of the Green's function back into Eq. (3.10), which gives

$$\vec{q}_j^{(0)} = g_{qq}(t,t_0)\vec{q}_j^{(\mathrm{i})} + g_{qp}(t,t_0)\vec{p}_j^{(\mathrm{i})} , \tag{3.12}$$

$$\vec{p}_j^{(0)} = g_{pp}(t,t_0)\vec{p}_j^{(\mathrm{i})} . \tag{3.13}$$

In order to make the notation more compact, we summarise the Green's functions of all N particles in the tensor $\boldsymbol{G}(t,t') := G(t,t') \otimes \mathbb{1}_N$.

We now turn back to the full equations of motion including interactions (Eq. 3.8), given by

$$0 = \boldsymbol{E}(\boldsymbol{x}) = \dot{\boldsymbol{x}} - \mathcal{J}\nabla_{\boldsymbol{x}} H(\boldsymbol{x}) . \tag{3.14}$$

Its general solution for a particle starting at initial coordinate $x^{(\mathrm{i})}$ can be expressed for one particle in terms of the Greens function by including the interaction potential V,

$$x(t) = G(t,0)x^{(\mathrm{i})} + \int_0^t \mathrm{d}t' G(t,t') \begin{pmatrix} 0 \\ -\vec{\nabla} V(t') \end{pmatrix} . \tag{3.15}$$

In order to express the generating functional in terms of these particle trajectories, we insert Eqns. (3.6) and (3.7) into Eq. (3.4) to obtain

$$Z = \int \mathcal{D}\boldsymbol{x} \int \mathrm{d}\boldsymbol{x}^{(\mathrm{i})}\, P\big(\boldsymbol{x}^{(\mathrm{i})}\big)\, \delta_{\mathrm{D}}\big[\boldsymbol{E}(\boldsymbol{x})\big] . \tag{3.16}$$

For compactness, we introduce the short-hand notation

$$\mathrm{d}\Gamma := \mathrm{d}\boldsymbol{x}^{(\mathrm{i})}\, P\big(\boldsymbol{x}^{(\mathrm{i})}\big) \tag{3.17}$$

and proceed by expressing the delta distribution in terms of its Fourier transform,

$$Z = \int \mathrm{d}\Gamma \int \mathcal{D}\boldsymbol{x} \int \mathcal{D}\boldsymbol{\chi}\; e^{\mathrm{i}\int \mathrm{d}t\; \langle \boldsymbol{\chi}, \mathrm{E}(\boldsymbol{x})\rangle} , \tag{3.18}$$

where $\boldsymbol{\chi}$ is the field conjugate to $\boldsymbol{x}$. Since the combination of the two fields $\boldsymbol{\chi}$ and $\boldsymbol{x}$ will appear quite often in the following calculations, it turns out useful to introduce the combined field $\boldsymbol{\psi} := (\boldsymbol{x}, \boldsymbol{\chi})$. The microscopic action can then be defined as

$$S[\boldsymbol{\psi}] = \int \mathrm{d}t\; \langle \boldsymbol{\chi}, \boldsymbol{E}(\boldsymbol{x})\rangle . \tag{3.19}$$

As already mentioned within the context of the Hamiltonian, the action can be split into a free part and an interacting part, $S = S_0 + S_\mathrm{I}$, with

$$S_0[\boldsymbol{\psi}] = \int \mathrm{d}t \langle \boldsymbol{\chi}, \dot{\boldsymbol{x}} - \mathcal{J} \nabla_{\boldsymbol{x}} H_0[\boldsymbol{x}] \rangle \,, \tag{3.20}$$

$$S_\mathrm{I}[\boldsymbol{\psi}] = \int \mathrm{d}t \langle \boldsymbol{\chi}_p, \nabla_{\boldsymbol{q}} H_\mathrm{I}[\boldsymbol{q}] \rangle \,. \tag{3.21}$$

We can therefore rewrite Eq. (3.19) in a form that will become beneficial later,

$$Z = \int \mathrm{d}\Gamma \int \mathcal{D}\boldsymbol{\psi}\; e^{\mathrm{i}S[\boldsymbol{\psi}]} = \int \mathrm{d}\Gamma \int \mathcal{D}\boldsymbol{\psi}\; e^{\mathrm{i}S_{\boldsymbol{\psi},I} + \mathrm{i}S_{\boldsymbol{\psi},0}} \,. \tag{3.22}$$

3.2 OPERATORS

The main application of KFT is to describe statistical quantities of the cosmic density field. We are considering point particles as the tracers of the underlying density field. Their number density in position space is given by

$$\rho\left(\vec{x}, t\right) = \sum_{j=1}^{N} \delta_\mathrm{D}\big(\vec{q} - \vec{q}_j(t)\big) \,. \tag{3.23}$$

It should be noted that we focus here on the position space density, whereas other works base their calculations on the *phase space* density which is often denoted by f (e.g. in Lilow et al., 2019). Since we will work in Fourier space, we will use the Fourier convention

$$\tilde{a}(\vec{k}) = \int \mathrm{d}^3\vec{q}\; a(\vec{q})\, e^{-\mathrm{i}\vec{k}\cdot\vec{q}}, \qquad a(\vec{q}) = \int \frac{\mathrm{d}^3\vec{k}}{(2\pi)^3}\; \tilde{a}(\vec{k})\, e^{\mathrm{i}\vec{q}\cdot\vec{k}}, \tag{3.24}$$

to arrive at

$$\tilde{\rho}\left(\vec{k}_1, t_1\right) =: \tilde{\rho}(1) = \sum_{j=1}^{N} e^{-\mathrm{i}\vec{k}_1\cdot\vec{q}_j(t_1)} \,. \tag{3.25}$$

In the first step, we have introduced the short-hand notation $(k_s, t_s) =: (s)$, which will be frequently used throughout the following calculations. For clarity, we will drop the tilde for denoting the Fourier transformed quantities and we introduce the short-hand expressions

$$\int_q := \int \mathrm{d}^3\vec{q}, \qquad \int_k := \int \frac{\mathrm{d}^3\vec{k}}{(2\pi)^3} \,. \tag{3.26}$$

In order to extract cumulants – for example of the density ρ – from the generating functional, we will have to introduce source fields and density operators, just as it is familiar from QFT. These source fields are introduced by hand such that the operators

can act on them to obtain the statistical quantity of interest. Afterwards the source fields are set to zero. Let us introduce the source fields $\boldsymbol{J} := J_j \otimes e_j$ and $\boldsymbol{K} := K_j \otimes e_j$ for the phase space trajectories $\boldsymbol{x}$ and their conjugate field $\boldsymbol{\chi}$, respectively, with $J_j = (\vec{J}_{q_j}, \vec{J}_{p_j})$ and $K_j = (\vec{K}_{q_j}, \vec{K}_{p_j})$. This allows writing the generating functional as

$$Z[\boldsymbol{J}, \boldsymbol{K}] = \int \mathrm{d}\Gamma \int \mathcal{D}\boldsymbol{\psi}\; e^{\mathrm{i}\int_t [\langle \boldsymbol{\chi}, \boldsymbol{E}(\boldsymbol{x})\rangle + \langle \boldsymbol{J}, \boldsymbol{x}\rangle + \langle \boldsymbol{K}, \boldsymbol{\chi}\rangle]}\,. \tag{3.27}$$

where we used the generating functional of the form of Eq. (3.18).

The average phase space coordinate $\langle x_j(t)\rangle$ of particle j at time t can now be calculated by applying a functional derivative with respect to $J_j(t)$,

$$\langle x_j(t)\rangle = -\mathrm{i}\frac{\delta}{\delta J_j(t)} Z[\boldsymbol{J}, \boldsymbol{K}]\,\Big|_{\boldsymbol{J}=0, \boldsymbol{K}=0} =: \hat{x} Z[\boldsymbol{J}, \boldsymbol{K}]\,\Big|_{\boldsymbol{J}=0, \boldsymbol{K}=0}\,, \tag{3.28}$$

where we have introduced the *phase space coordinate operator* $\hat{x}$ in the last step. Note that operators will be denoted by a hat in the subsequent text. Since the Fourier transform of the microscopic density field in Eq. (3.25) is defined via the positions of the particles, we can define the density operator simply by replacing $\vec{q}$ with the position component of $\hat{x}$, yielding

$$\hat{\rho}(1) := \sum_{j=1}^{N} \underbrace{\exp\left[-\mathrm{i}\vec{k}_1 \cdot \hat{x}_{q_j}(t_1)\right]}_{=:\hat{\rho}_j} = \sum_{j=1}^{N} \exp\left[-\vec{k}_1 \cdot \frac{\delta}{\delta J_{q_j}(t_1)}\right]\,. \tag{3.29}$$

Applying this operator once to the logarithm of the generating functional, $W := \ln Z$, with Z from Eq. (3.27), would give the mean cosmic density, applying it twice would lead to the power spectrum and n times yields the nth-order spectrum. Further operators can be defined when needed in a similar manner, such as the response field operator defined in Section 3.5.

3.3 INITIAL CONDITIONS

In order to actually calculate the non-linear power spectrum of the cosmic density field, we need to specify two further elements of the generating functional. First, we need to define the particles' *initial distribution* in phase space, which is contained in $\mathrm{d}\Gamma$. Second, we need to specify the particle *propagators* g_{ab} that determine the particle trajectories. We will focus here on the initial conditions and introduce the propagators in the next section. Since we only show the main steps of the derivation, we refer the reader to Appendix A of Bartelmann et al. (2016) for the details. We will focus in our considerations on universes containing only one sort of matter, i.e. dark matter. However, there exists as well a description that includes a mixture of dark and baryonic matter (Bartelmann et al., 2019; Geiss et al., 2020).

As argued in Section 2.3, the initial density field can be described well by a Gaussian random field. The particle positions can then be obtained by Poisson sampling from the underlying density distribution. The probability distribution of finding particle j at position $\vec{q}_j$ with given density $\rho_j = \rho(\vec{q}_j)$ is therefore

$$P(\vec{q}_j^{\,(\mathrm{i})}|\rho_j) = N^{-1}\rho_j\,. \tag{3.30}$$

In order to obtain the initial distribution of the momenta, we will assume that the initial velocity field can be described as the gradient of a velocity potential Ψ. This assumption can be justified as follows. By applying the Helmholtz theorem, the velocity field can be decomposed into a curl and a gradient. The curl component, however, will quickly decay during the early linear evolution of cosmic structures, so only the gradient part remains. Introducing the notation $\vec{y}_j := \vec{\nabla}\Psi_j$, where $\Psi_j = \Psi(\vec{q}_j^{\,(\mathrm{i})})$ is only defined on the initial spatial section and therefore depends on the initial spatial coordinates $\vec{q}_j^{\,(\mathrm{i})}$ only, and setting the mass of the particles $m = 1$, we obtain for the initial momentum distribution

$$P(\vec{p}_j^{\,(\mathrm{i})}|\vec{y}_j) = \delta_{\mathrm{D}}\left[\vec{p}_j^{\,(\mathrm{i})} - \vec{y}_j\right]\,. \tag{3.31}$$

The initial phase space distribution can therefore be expressed as the joint probability

$$\begin{aligned} P(\vec{q}_j, \vec{p}_j) &= \int \mathrm{d}\delta_j \int \mathrm{d}^3\vec{y}_j P(\vec{q}_j^{\,(\mathrm{i})}|\delta_j) P(\vec{p}_j^{\,(\mathrm{i})}|\vec{y}_j) P(\delta_j, \vec{y}_j) && (3.32)\\ &= \frac{\bar{\rho}}{N}\int \mathrm{d}\delta_j (1+\delta_j) \int \mathrm{d}^3\vec{y}_j \delta_{\mathrm{D}}[\vec{p}_j^{\,(\mathrm{i})} - \vec{y}_j] P(\delta_j, \vec{y}_j) && (3.33)\\ &= \frac{\bar{\rho}}{N}\int \mathrm{d}\delta_j (1+\delta_j) P(\delta_j, \vec{p}_j^{\,(\mathrm{i})})\,, && (3.34) \end{aligned}$$

where we expressed the density ρ_j in terms of the density contrast δ_j which follows a Gaussian distribution with mean $\langle\delta\rangle = 0$.

Taking the continuity equation and expressing the velocity through its potential, leads to a Poisson equation for the initial[2] density contrast $\delta = -\Delta\Psi$. We conclude that the density contrast can only be normally distributed if the velocity potential is normally distributed, since the divergence is a linear operator, which leaves the Gaussian property intact. We know that the normal distribution of the density contrast is determined through its power spectrum $P_\delta(k)$. Using the Poisson equation we can derive the power spectrum of the velocity potential to be

$$P_\Psi(k) = k^{-4}\, P_\delta(k)\,. \tag{3.35}$$

Therefore, the probability distribution $P(\delta_j, \vec{p}_j)$ in Eq. (3.32) is a multivariate Gaussian distribution and the power spectrum P_δ suffices completely to determine its covariance matrix. Inserting the resulting Gaussian distribution for $P(\delta_j, \vec{p}_j)$ into Eq. (3.32) yields

2 keeping in mind that Ψ is only defined for the initial spatial coordinates.

then the initial phase space distribution $P(\boldsymbol{q}^{(\mathrm{i})}, \boldsymbol{p}^{(\mathrm{i})})$. The final result as obtained in Bartelmann et al. (2016) is given by

$$P(\boldsymbol{q}^{(\mathrm{i})}, \boldsymbol{p}^{(\mathrm{i})}) = \frac{V^{-N}}{\sqrt{(2\pi)^{3N} \det C_{pp}}} \mathcal{C}(\boldsymbol{p}^{(\mathrm{i})}) \exp\left(-\frac{1}{2} \boldsymbol{p}^{(\mathrm{i})\mathrm{T}} C_{pp}^{-1} \boldsymbol{p}^{(\mathrm{i})}\right), \tag{3.36}$$

with the factor $\mathcal{C}(\boldsymbol{p}^{(\mathrm{i})})$ which is a polynomial in the momenta. If the propagator is chosen such that it becomes $g_{qp} \gg 1$ for late times, then factor can be approximated by $\mathcal{C}(\boldsymbol{p}^{(\mathrm{i})}) \approx 1$ in for the present time (Bartelmann et al., 2019). We will use, however, a different approach which is analogous to Lilow (2018) when we calculate the free cumulants (Appendix A). We will expand $\mathcal{C}(\boldsymbol{p}^{(\mathrm{i})})$ in the lowest order of the initial density power spectrum $P_\delta^{(\mathrm{i})}(k)$. The momentum correlation matrix is defined via the power spectrum of the velocity potential,

$$C_{p_j p_k} = \int_k (\vec{k} \otimes \vec{k}) P_\Psi(k) e^{\mathrm{i}\vec{k}\cdot\vec{q}_{jk}}. \tag{3.37}$$

It is conveniently split into its diagonal and off-diagonal elements,

$$C_{pp} = \frac{\sigma_1^2}{3} \mathbb{1}_3 \otimes \mathbb{1}_N + \bar{C}_{p_j p_k} \otimes E_{jk}, \tag{3.38}$$

where $\bar{C}_{p_j p_k}$ contains only the off-diagonal terms (i.e. the diagonal is $\bar{C}_{p_j p_j} = 0$) and $E_{jk} := e_j \otimes e_k$. The variance σ_1^2 is given by

$$\sigma_1^2 := \int_k \frac{P_\delta}{k^2}, \qquad \text{with } \sigma_n^2 := \int_k k^{2n} P_\Psi = \int_k k^{2(n-2)} P_\delta. \tag{3.39}$$

3.4 PROPAGATORS

Within the framework of KFT, there are different choices to describe the trajectories of particles in phase space, which are determined through the microscopic propagators g_{ab}. Amongst the possible choices are trajectories derived from (*i*) the Zel'dovich approximation, (*ii*) an improved version of the Zel'dovich approximation (Bartelmann, 2015) that reduces the overshooting of the original Zel'dovich trajectories and (*iii*) Newtonian dynamics in an expanding Universe. We will use the latter in our calculations analogously to Lilow et al. (2019) and will briefly introduce it in this section.

In order to make calculations easier, we will choose the logarithm of the linear growth factor $D_+(t)$ as the time coordinate,

$$\eta(t) := \log \frac{D_+(t)}{D_+(t_\mathrm{i})}, \tag{3.40}$$

where dividing by the D_+ at initial time t_i ensures that $\eta(t_\mathrm{i}) = 0$. Furthermore, we will choose comoving spatial coordinates

$$\vec{q} := \frac{\vec{r}}{a}\,, \tag{3.41}$$

with physical coordinate $\vec{r}$ and scale factor a, and the momentum defined via

$$\vec{p} := \frac{\mathrm{d}\vec{q}}{\mathrm{d}\eta}\,. \tag{3.42}$$

As shown in Appendix D of Lilow et al. (2019), the Newtonian equations of motion for dark matter particles in an expanding space time read

$$\frac{\mathrm{d}\vec{q}}{\mathrm{d}\eta} = \vec{p}\,, \tag{3.43}$$

$$\frac{\mathrm{d}\vec{p}}{\mathrm{d}\eta} = \left(1 - \frac{3}{2}\frac{\Omega_\mathrm{m}}{f_+^2}\right)\vec{p} - \vec{\nabla}_q\tilde{V} \approx -\frac{1}{2}\vec{p} - \vec{\nabla}_q\tilde{V}\,, \tag{3.44}$$

with the linear growth rate $f_+ := \mathrm{d}\ln D_+/\mathrm{d}\ln a$. The canonical conjugate momentum $\vec{p}_\mathrm{can}$ and the Newtonian potential V have been rescaled, $\vec{p} := \vec{p}_\mathrm{can}/(ma^2Hf_+)$ and $\tilde{V} := V/(a^2f_+^2H^2)$, in order to bring the equations in a simpler form.

The components of the Green's function (Eq. 3.11) can then be obtained by solving the free equations of motion, i.e. setting $\tilde{V} = 0$ in Eqns. (3.43) and (3.44), which can be written as

$$\left(\frac{\mathrm{d}}{\mathrm{d}\eta} + \mathcal{E}_0\right)\vec{x} = 0, \qquad \mathcal{E}_0(\eta) = \begin{pmatrix} 0 & -\mathbb{1}_3 \\ 0 & \frac{1}{2}\mathbb{1}_3 \end{pmatrix}. \tag{3.45}$$

This equation is solved by the Green's function (analogously to Bartelmann, 2015)

$$G(\eta,\eta') = \exp\left[-\int_{\eta'}^{\eta}\mathrm{d}\bar{\eta}\,\mathcal{E}_0\right]\theta_\mathrm{H}(\eta-\eta')\,. \tag{3.46}$$

The component functions of this Green's function finally represent the desired propagators, which are given by

$$g_{qq}(\eta,\eta') = \theta_\mathrm{H}(\eta-\eta')\,, \tag{3.47}$$

$$g_{qp}(\eta,\eta') = 2\left(1 - e^{-\frac{1}{2}(\eta-\eta')}\right)\theta_\mathrm{H}(\eta-\eta')\,, \tag{3.48}$$

$$g_{pq}(\eta,\eta') = 0\,, \tag{3.49}$$

$$g_{pp}(\eta,\eta') = e^{-\frac{1}{2}(\eta-\eta')}\theta_\mathrm{H}(\eta-\eta')\,, \tag{3.50}$$

where θ_H denotes the Heaviside step function.

3.5 INTERACTIONS

The above form of the equations of motion (Eqns. 3.43 and 3.44) also leads to the corresponding interaction potential. The rescaled gravitational potential $\tilde{V}$ needs to fulfil

$$\vec{\nabla}_q^2 \tilde{V} = \frac{3}{2}\frac{\Omega_\mathrm{m}}{f_+^2}\frac{\rho - \bar{\rho}}{\bar{\rho}} \approx \frac{3}{2}\frac{\Phi_\rho - \bar{\rho}}{\bar{\rho}} \,. \tag{3.51}$$

According to Lilow et al. (2019), the solution for $\tilde{V}(\vec{q}, t)$ can be written as a sum of the single-particle gravitational potentials $v(|\vec{q} - \vec{q}_j(t)|)$,

$$\tilde{V}(\vec{q}, t) = \sum_{j=1}^{N} v(|\vec{q} - \vec{q}_j(t)|) \,. \tag{3.52}$$

The single-particle gravitational potential can be determined by solving Eq. (3.51) in Fourier space. It results in

$$v(k) = -\frac{3}{2}\frac{1}{\bar{\rho}k^2} \,. \tag{3.53}$$

With this at hand, we would like to write the interaction part of the action (Eq. 3.21) more explicitly. It turns out useful to introduce the response field B for this purpose, defined as

$$B\left(\vec{x}, t\right) := \sum_{j=1}^{N} \vec{\chi}_{p_j}(t) \cdot \vec{\nabla}_q \delta_\mathrm{D}\left(\vec{q} - \vec{q}_j(t)\right) \,, \tag{3.54}$$

where we used the notation $\chi_j := (\chi_{q_j}, \chi_{p_j})$ and we remind the reader that χ_j represents the Fourier conjugate to the trajectory $x_j(t)$ (as introduced in Eq. 3.18). We can now Fourier transform B and define the response field operator in terms of the single-particle density operator $\hat{\rho}_j$

$$\hat{B}\left(\vec{k}, t\right) := \sum_{j=1}^{N} \left(\vec{k} \cdot \frac{\delta}{\delta K_{p_j}}\right) \hat{\rho}_j \,. \tag{3.55}$$

We furthermore define the interaction matrix element

$$\sigma_{\rho B}(1, -2) = -v(k_1, t_1)(2\pi)^3 \delta_\mathrm{D}(\vec{k}_1 - \vec{k}_2)\delta_\mathrm{D}(t_1 - t_2) \,. \tag{3.56}$$

The interaction part of the action (Eq. 3.21) can then be rewritten as

$$S_{\boldsymbol{\psi},\mathrm{I}} = \int \mathrm{d}1 \int \mathrm{d}2 \, \rho(-1) \, \sigma_{\rho B}(1, -2) \, B(2) \,. \tag{3.57}$$

Since the following calculations contain numerous integrals over Fourier space, we will use the notation

$$\int \mathrm{d}1 := \int \frac{\mathrm{d}^3\vec{k}_1}{(2\pi)^3} \int \mathrm{d}t_1 \tag{3.58}$$

and introduce the dot product

$$A \cdot B := \int \mathrm{d}1 \, A(-1)B(1) \tag{3.59}$$

as a short hand-notation for the integration. We can then write

$$S_{\boldsymbol{\psi},\mathrm{I}} = \rho \cdot \sigma_{\rho B} \cdot B \,. \tag{3.60}$$

In order to further ease the notation we introduce the dressed response field $\mathcal{F} := \sigma_{\rho B} \cdot B$ with the corresponding dressed response field operator

$$\hat{\mathcal{F}} := \sigma_{\rho B} \cdot \hat{B} \,. \tag{3.61}$$

We thus can write the interaction part of the action as

$$S_{\boldsymbol{\psi},\mathrm{I}} = \rho \cdot \mathcal{F} \,. \tag{3.62}$$

This represents our final form of $S_{\boldsymbol{\psi},\mathrm{I}}$ which will be used throughout the text. It shall be mentioned that there exist alternative ways to include interactions in KFT, e.g. when using the improved Zel'dovich trajectories (as described in the review Bartelmann et al., 2019).

3.6 STATISTICAL QUANTITIES FROM THE GENERATING FUNCTIONAL

We now have all the ingredients to calculate statistical quantities from the generating functional (Eq. 3.27). We will summarise in this section the results for cumulants in the free (i.e. non-interacting) case, then the power spectrum including interactions and finally the free bispectrum.

3.6.1 *The free cumulants*

For deriving the cumulants in the non-interacting case, we introduce the free generating functional. We use the formulation of the generating functional in terms of the action $S_{\boldsymbol{\psi}} = S_{\boldsymbol{\psi},0} + S_{\boldsymbol{\psi},\mathrm{I}}$ (c.f. Eq. 3.22) and set the interaction part to zero, $S_{\boldsymbol{\psi},\mathrm{I}} = 0$. Since we are interested in cumulants of the density and the dressed response field, we introduce two source fields H_ρ and $H_\mathcal{F}$, and write the free generating functional as

$$Z_0^{\rho,\mathcal{F}}[H_\rho, H_\mathcal{F}] := \int \mathrm{d}\Gamma \int \boldsymbol{\psi} \; e^{\mathrm{i}S_{\boldsymbol{\psi},0} + \mathrm{i}H_\rho \cdot \rho + \mathrm{i}H_\mathcal{F} \cdot \mathcal{F}} \,. \tag{3.63}$$

Furthermore, we define the logarithmic free generating functional

$$W_0^{\rho,\mathcal{F}}[H_\rho, H_\mathcal{F}] := \ln Z_0^{\rho,\mathcal{F}}[H_\rho, H_\mathcal{F}]\,. \tag{3.64}$$

We would like to emphasise that in contrast to the generating functional in Eq. (3.27), we introduced here source terms for the density ρ and the dressed response field $\mathcal{F}$ directly instead of those for the particle phase space trajectories x and their conjugate field χ. This eases the following calculations, where we are interested in cumulants of exactly these collective fields ρ and $\mathcal{F}$. We highlighted the changed source fields by the superscript $\rho, \mathcal{F}$. The density operator can now be formulated as a functional derivative with respect to H_ρ,

$$\hat{\rho}(1) = -\mathrm{i}\frac{\delta}{\delta H_\rho(1)} \quad \text{equivalent to} \quad \hat{\rho}(1) = \sum_{j=1}^{N} \exp\left[-\vec{k}_1 \cdot \frac{\delta}{\delta J_{q_j}(t_1)}\right], \tag{3.65}$$

which can be easily translated into its corresponding form in terms of $\delta J_{q_j}(t_1)$ by inserting the definition of ρ into Eq. (3.63). The dressed response field operator is in this case given by

$$\hat{\mathcal{F}}(1) = -\mathrm{i}\frac{\delta}{\delta H_\mathcal{F}(1)}\,. \tag{3.66}$$

The cumulants for the non-interacting case are then obtained by applying j density operators $\hat{\rho}$ and k dressed response field operators $\hat{\mathcal{F}}$ to the logarithmic free generating functional $W_0^{\rho,\mathcal{F}}$ which yields the cumulant $G_{\rho_1\ldots\rho_j\mathcal{F}_1\ldots\mathcal{F}_k}$.[3] Their general form has been calculated in Fabis (2015) for a statistically homogeneous and isotropic Hamiltonian system with Gaussian initial conditions. These results were then applied in Appendix B of Lilow (2018) in order to give specific expressions for the cumulants. We will state here the results of Lilow (2018) with two modifications. First, we consider the position space density $\rho(\vec{q})$ in contrast to the phase space density $f(\vec{q}, \vec{p})$ used in Lilow (2018). We therefore have to integrate out the phase space cumulants' momentum information. This is equivalent to setting all appearances of the Fourier conjugate of the momentum to zero, i.e. $\vec{l}_r = 0$, where r runs from 1 to the number of phase space density operators applied. Second, we take only the lowest order in initial correlations, $P_\delta^{(\mathrm{i})}$, into account. This means for example terms linear in $P_\delta^{(\mathrm{i})}$ for $G_{\rho\rho}$ and $G_{\rho\rho\mathcal{F}}$ and terms quadratic in $P_\delta^{(\mathrm{i})}$ for $G_{\rho\rho\rho}$. We can therefore also neglect the damping term which does not appear in this approximation. We show here the 1- and 2-point cumulants (for more details of the calculations and the lengthier expressions for the 3-point cumulants see Appendix A),

3 We would like to emphasise that G with subscript ρ and $\mathcal{F}$ denotes the respective cumulant and should not be confused with the propagator $G(t, t')$.

$$G_{\mathcal{F}}(1) = 0\,, \tag{3.67}$$

$$G_{\rho}(1) = (2\pi)^3\delta_{\mathrm{D}}(\vec{k}_1)\bar{\rho}\,, \tag{3.68}$$

$$G_{\mathcal{F}\mathcal{F}}(1,2) = 0\,, \tag{3.69}$$

$$G_{\rho\mathcal{F}}(1,2) \approx \mathrm{i}(2\pi)^3\delta_{\mathrm{D}}(\vec{k}_1+\vec{k}_2)\vec{k}_1^2\, g_{qp}(t_1,t_2)\bar{\rho}v_{(k_1,t_1)}\,, \tag{3.70}$$

$$G_{\mathcal{F}\rho}(1,2) = G_{\rho\mathcal{F}}(2,1)\,, \tag{3.71}$$

$$G_{\rho\rho}(1,2) \approx (2\pi)^3\delta_{\mathrm{D}}(\vec{k}_1+\vec{k}_2)(1+g_{qp}(t_1,0))(1+g_{qp}(t_2,0))\bar{\rho}^2P_{\delta}^{(\mathrm{i})}(\vec{k}_1)\,. \tag{3.72}$$

In Eqns. (3.67) and (3.69), it was used that pure dressed response field cumulants $G_{\mathcal{F}\ldots\mathcal{F}}$ vanish. It was shown in Appendix A of Fabis (2015) that the pure response field cumulants $G_{B\ldots B}$ vanish, which implies that the dressed response field cumulants are zero as well.

3.6.2 *The density power spectrum with mean field interactions*

Besides these results for the non-interacting case, the power spectrum of the cosmic density field has been derived in the most recent formulation of KFT (Bartelmann et al., 2019) taking interactions into account via a mean field approach using the improved Zel'dovich propagator. They obtain for the free power spectrum the expression

$$\mathcal{P}(k,t) = \int_q \left(e^{Q}-1\right)e^{\mathrm{i}kq}\,, \tag{3.73}$$

with

$$Q := -\,g_{qp}^2(t)k^2a_{||}(q)\,, \tag{3.74}$$

and the correlation function of the parallel momentum components

$$a_{||}(q) := a_1(q) + \mu^2 a_2(q)\,, \tag{3.75}$$

where the functions a_1 and a_2 are given as

$$a_1 = -\,\frac{1}{2\pi}\int_0^\infty \mathrm{d}kP_{\delta}^{(\mathrm{i})}(k)\frac{j_1(kq)}{kq} \quad \text{and} \tag{3.76}$$

$$a_2 = \frac{1}{2\pi}\int_0^\infty \mathrm{d}kP_{\delta}^{(\mathrm{i})}(k)j_2(kq)\,. \tag{3.77}$$

These functions contain the spherical Bessel functions $j_{1,2}(kq)$ and depend on the cosine of the angle θ_{kq} enclosed by $\vec{k}$ and $\vec{q}$, i.e. $\mu := \cos\theta_{kq}$.

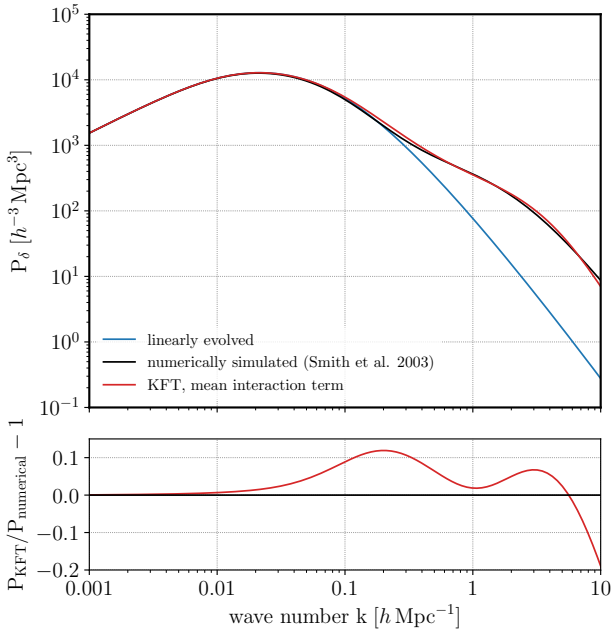

Figure 3.1: Upper panel: The non-linear density power spectrum as predicted by KFT including interactions through a mean field approach (*red*). For comparison the linearly evolved power spectrum is shown in *blue* and a prediction from N-body simulations by Smith et al. (2003) in *black*. Lower panel: Relative deviation of the KFT prediction from the N-body fitting formula of Smith et al. (2003). The figure was taken with kind permission from Bartelmann et al. (2019), Fig. 4.

The power spectrum including interactions can then be expressed in terms of the free power spectrum by applying a mean field approach (see Bartelmann et al., 2019, Section 4 for details), yielding

$$\bar{\mathcal{P}}(k,t) = e^{-Q_0 + \mathrm{i}\langle S_\mathrm{I}\rangle}\mathcal{P}(k,t)\,, \tag{3.78}$$

with

$$Q_0 := \frac{\sigma_1^2}{3} g_{qp}^2(t) k^2 \tag{3.79}$$

and the mean interaction part of the action

$$\langle S_\mathrm{I}\rangle = -2k\int_0^t \mathrm{d}t' g_{qp}(t,t')\langle f_{12}\rangle(k,t')\,, \tag{3.80}$$

where $\langle f_{12}\rangle$ is the projection of the force between two particles on the wave vector k. The angular brackets denote taking the average over all particle pairs. A comparison between the KFT prediction, the results from N-body simulations (Smith et al., 2003) and the linear power spectrum is shown in Fig. 3.1.

3.6.3 *The free density bispectrum*

The analytical prediction of the density bispectrum, i.e. the Fourier transform of connected three-point correlation function, is a much harder task and up to now there exist only approximations either based on perturbation theory (Bernardeau et al., 2002; McCullagh et al., 2016; Lazanu and Liguori, 2018) or based on effective field theory (Angulo et al., 2015). A first order approximation of the bispectrum similar to that known for SPT (c.f. Eq. 43 in Bernardeau et al., 2002) can be derived from KFT in the interaction-free case as shown in Bartelmann et al. (2016). The result is given by

$$P^{(3)}\left(\vec{k}_1,\vec{k}_2,\vec{k}_3\right) = \delta_{\mathrm{D}}\Big(\vec{k}_1+\vec{k}_2+\vec{k}_3\Big) \times \Big[P_\delta(k_1)P_\delta(k_2)F(\vec{k}_1,\vec{k}_2) + \mathrm{cyc.}\Big]\,, \tag{3.81}$$

with

$$F\left(\vec{k}_1,\vec{k}_2\right) = 1 + \frac{\vec{k}_1\cdot\vec{k}_2}{k_1^2} + \frac{\vec{k}_1\cdot\vec{k}_2}{k_2^2} + \frac{(\vec{k}_1\cdot\vec{k}_2)^2}{k_1^2k_2^2}.$$

The similarity to the result from SPT becomes even more apparent when comparing the predictions for the third cumulants obtained from the bispectra, which will be shown in Section 4.2.

3.7 MACROSCOPIC FORMULATION

The framework of KFT has been extended by an approach introducing macroscopic fields, dubbed resummed KFT (RKFT), which was proposed by Lilow et al. (2019). While the original version of RKFT is based on the density in phase space (Klimontovich density), we will introduce the formalism more adapted to our calculations in Section 4.3 and consider therefore the density in position space only. The macroscopic position space density ϕ_ρ is introduced in the generating functional (Eq. 3.22 with Eq. 3.62) by setting it exactly to the microscopic density ρ via a δ_{D}-distribution,

$$\begin{aligned} Z &= \int \mathcal{D}\phi_\rho \int \mathrm{d}\Gamma \int \mathcal{D}\boldsymbol{\psi}\; e^{\mathrm{i}S_{\boldsymbol{\psi},0}+\mathrm{i}\phi_\rho\cdot\mathcal{F}}\;\delta_{\mathrm{D}}\left[\phi_\rho-\rho\right] \\ &= \int \mathcal{D}\phi_\rho \int \mathcal{D}\phi_\beta\; e^{-\mathrm{i}\phi_\beta\cdot\phi_\rho} \int \mathrm{d}\Gamma \int \mathcal{D}\boldsymbol{\psi}\; e^{\mathrm{i}S_{\boldsymbol{\psi},0}+\mathrm{i}\phi_\rho\cdot\mathcal{F}+\mathrm{i}\phi_\beta\cdot\rho}\,. \end{aligned} \tag{3.82}$$

In the second line we have Fourier transformed the δ_{D}-distribution by introducing the macroscopic auxiliary field ϕ_β, which is the Fourier conjugate to ϕ_ρ. In the expression for the generating functional above, we can interpret the macroscopic fields ϕ_ρ and ϕ_β as the source fields for the microscopic density ρ and dressed response field $\mathcal{F}$, respectively. We

can therefore express the last two integrals as the free generating functional (Eq. 3.63), with source fields ϕ_ρ and ϕ_β, which leads to

$$\begin{aligned} Z &= \int \mathcal{D}\phi_\rho \int \mathcal{D}\phi_\beta \; e^{-\mathrm{i}\phi_\beta\cdot\phi_\rho} \underbrace{\int \mathrm{d}\Gamma \int \mathcal{D}\boldsymbol{\psi} \; e^{\mathrm{i}S_{\psi,0}+\mathrm{i}\phi_\rho\cdot\mathcal{F}+\mathrm{i}\phi_\beta\cdot\rho}}_{=Z_0^{\rho,\mathcal{F}}[\phi_\beta,\phi_\rho]} \\ &= \int \mathcal{D}\phi_\rho \int \mathcal{D}\phi_\beta \; e^{-\mathrm{i}\phi_\beta\cdot\phi_\rho} \; Z_0^{\rho,\mathcal{F}}[\phi_\beta,\phi_\rho] \\ &= \int \mathcal{D}\phi \; e^{-\mathrm{i}\phi_\rho\cdot\phi_\beta+W_0^{\rho,\mathcal{F}}[\phi_\beta,\phi_\rho]} \\ &= \int \mathcal{D}\phi \; e^{\mathrm{i}S_\phi} \,, \end{aligned} \tag{3.83}$$

where we combined the two macroscopic fields into $\phi := (\phi_\rho, \phi_\beta)$ in the third line and defined the logarithm of the free generating functional (Eq. 3.64). In the fourth line, we defined the macroscopic action

$$S_\phi := -\phi_\rho \cdot \phi_\beta - \mathrm{i}W_0^{\rho,\mathcal{F}}[\phi_\beta,\phi_\rho] \,. \tag{3.84}$$

As emphasised by Lilow et al. (2019), this description is still exact and the macroscopic action contains therefore the complete information on the microscopic dynamics. All of the microscopic information is encoded in the free generating functional $W_0^{\rho,\mathcal{F}}[\phi_\beta,\phi_\rho]$. Statistical quantities like for example the power spectrum can now be obtained by introducing source fields for the macroscopic fields and applying functional derivatives to the generating functional with respect to these source fields. The resulting expressions can then be solved in a perturbative approach by Taylor expanding $W_0^{\rho,\mathcal{F}}[\phi_\beta,\phi_\rho]$ and inserting the free microscopic cumulants obtained in Section 3.6.1. The full details of this calculation are presented in Lilow et al. (2019). We use an analogous approach when we apply the macroscopic formulation in order to calculate the PDF of the cosmic density field in Section 4.3.

4

THE ONE-POINT DISTRIBUTION FROM KFT

The cosmic density contrast is a correlated random field and therefore the probability to obtain a density at one-point in space is conditional on the field values at other points. To fully describe the density field, this conditional density distribution needs to be known, which contains the information of all n-point spectra. We consider here the so called one-point distribution, i.e. the conditional distribution marginalised over the field values at all other points. We will call this distribution for brevity simply the probability distribution function (PDF) of the cosmic density contrast[1]. It is a key quantity of modern cosmology, since it summarises important information about the statistical properties of the density field. It is needed for deriving further observables such as the halo mass function (which we will consider in Chapters 5 and 6) or in the prediction of the halo merger rate.

In the early Universe, the density contrast is well described by a Gaussian random field as observations of the CMB (Planck Collaboration, 2020a) show. The corresponding PDF of the density contrast at early times is therefore given by a normal distribution. As explained in Section 2.3, the PDF then evolves away from a normal distribution due to cosmic structure formation and the non-linearity of gravity. The description of the PDF of today's non-linearly evolved density field is a very hard task which has no satisfying solution yet. One reason for this is that in principle infinitely many moments of the PDF are required to describe the PDF of the non-linear field. As an alternative, the current approach has been either to work on the basis of the initial density field as in the Press-Schechter approach to the halo mass function (Press and Schechter, 1974) or to assume a suitable model for the PDF of the evolved (over-)density field. It should be noted that usually not the PDF of the actual overdensity field δ is considered, but instead that of the field δ_R smoothed with a spherical filter of variable radius. To avoid confusion, we would like to warn the reader that we will use the term density field synonymously for the smoothed overdensity field. However, the meaning should become clear, since we use δ_R with subscript R in the respective equations to signal that the smoothed overdensity field is considered.

We will start with an overview of different models for the PDF that are currently being used in the literature, which we will introduce in Section 4.1. We then present a first approach to obtaining the density PDF from KFT in Section 4.2. Here, we will take two of the models discussed in the preceding section, i.e. the *lognormal* model and the *generalised normal model*, and fix their parameters by predictions of KFT. This section is

1 As mentioned in the previous chapter, we will focus only on dark matter in our considerations due to its simple properties and since it represents the majority of the cosmic matter content.

based on Linke (2017) and unpublished work by M. Feix[2]. In the last sections, we will present a more fundamental approach, where we aim at deriving an approximation to the density PDF directly from the generating functional of RKFT. We obtain the PDF using perturbation theory up to second order in Section 4.3. A third-order approximation is investigated in Section 4.4. Finally, we sketch an alternative ansatz based on the large deviation principle in Section 4.5. We will consider in this chapter a dark matter only universe, with parameters corresponding to those measured by (Planck Collaboration, 2020b), i.e. $H_0 = 67.66\ \mathrm{km\,s^{-1}\,Mpc^{-1}}$, $\Omega_\Lambda = 0.6889$, $\Omega_\mathrm{m} = 0.3111$, $\sigma_8 = 0.8102$ and $n_s = 0.9665$.

4.1 MODELS OF THE COSMIC DENSITY PDF

4.1.1 *Lognormal distribution*

Already in the 1930s, it was observed by Hubble (1934) that the galaxy distribution can be described reasonably well by a *lognormal distribution*. Several decades later the theoretical implications for the cosmic density field were investigated by Coles and Jones (1991). It was then shown by Kayo et al. (2001) that the predictions of a lognormal distribution also compare well to the predictions of cosmological N-body simulations.

By definition the mean of the density contrast needs to vanish, $\langle \delta_R \rangle = 0$. We furthermore introduce a scaling parameter $\tilde{\sigma}_R > 0$ which is related to the variance of the cosmic overdensity field σ_R^2 through $\tilde{\sigma}_R^2 = \ln(1+\sigma_R^2)$. The lognormal distribution is then given by

$$p_\mathrm{LN}(\delta_R) = \frac{1}{\sqrt{2\pi}\tilde{\sigma}_R\,(1+\delta_R)} \exp\left[-\frac{\left(\ln(1+\delta_R) + \tilde{\sigma}_R^2/2\right)^2}{2\tilde{\sigma}_R^2}\right] \tag{4.1}$$

and it is defined for values $-1 < \delta_R < \infty$. The lognormal distribution shares all the advantageous analytical properties of the normal distribution, since it can be seen as a normal distribution after a change of variables $x \to \ln(x)$ has been applied. Therefore, it is described by just one parameter in the case of the cosmic overdensity field, since the second parameter is fixed by $\langle \delta_R \rangle = 0$.

4.1.2 *Generalised normal distribution*

A more accurate model for the density PDF has been proposed by Shin et al. (2017). Based on the measurement of the density PDF from N-body simulations, they propose to use

2 These two works led to a paper draft including contributions by the author of this dissertation. Parts of this unpublished manuscript have been adopted verbatim in Section 4.2 and Chapter 6.

the *generalised normal distribution*. This distribution is a generalisation of the lognormal distribution which depends on three parameters. It takes the form

$$p_{\mathrm{GN}}(\delta_R) = \frac{1}{\sqrt{2\pi}} \frac{1}{\alpha - \beta(\delta_R - \mu)} \times \exp\left[-\frac{1}{2\beta^2}\left(\ln\left[1 - \frac{\beta(\delta_R - \mu)}{\alpha}\right]\right)^2\right], \tag{4.2}$$

with a location parameter μ, a scaling parameter $\alpha > 0$ and a shape parameter β. We will require the PDF to be positively skewed in order to allow the tail to extend to high densities while the PDF is bounded from below by $\delta > -1$.The shape parameter therefore needs to fulfil $\beta < 0$. The PDF is defined for the range $\mu + \alpha/\beta < \delta_R < \infty$.

Shin et al. (2017) show that the generalised normal distribution provides a fit to simulation results that is significantly better than the lognormal distribution for smoothing radii in the range of 2 to 25 h^{-1}Mpc. The generalised normal model is able to describe the density PDF with a precision of less than 20 per cent in this range of smoothing radii. The lognormal distribution in contrast describes the N-body with precision of less than 40 per cent.

We show an example of a Gaussian, lognormal and generalised normal distribution in Fig. 4.1. The parameters were chosen such that the variance and the skewness match the KFT prediction for the density field smoothed at 20 h^{-1}Mpc (see Section 4.2). While the Gaussian distribution is by definition symmetric around its mean, the other two distributions are noticeably skewed. For the smoothing radius shown in the figure, their large density tails roughly coincide. The lognormal distribution, however, is more concentrated around its centre and therefore its low density tail decreases faster for smaller densities.

4.1.3 *Edgeworth approximation*

An alternative approach, which has been used to describe the weakly non-Gaussian regime, is the *Edgeworth expansion* (see e.g. Juszkiewicz et al., 1995). It approximates the PDF by a series expansion which perturbs a Gaussian distribution with the help of Hermite polynomials. The expansion coefficient of the nth polynomial is set by the nth cumulant of the distribution that is to be approximated. However, the Edgeworth expansion suffers from several conceptual shortcomings, which have been pointed out recently by Sellentin et al. (2017) and Linke (2017).

The most severe problem is that the series only describes the PDF asymptotically. It typically does not converge. Therefore, expansion coefficients "explode" as the next-order term is even larger than the previous. The terms typically have alternating signs in order to overcompensate the error of the previous expansion order. The asymptotic nature of the series implies a second problem. There exists no clear measure to decide how well the expansion matches the true PDF. Third and last, the Edgeworth approximation can have negative values and therefore it does not represent a valid PDF. However, as stated in Sellentin et al. (2017), this presents the smallest of its problems as it could be easily

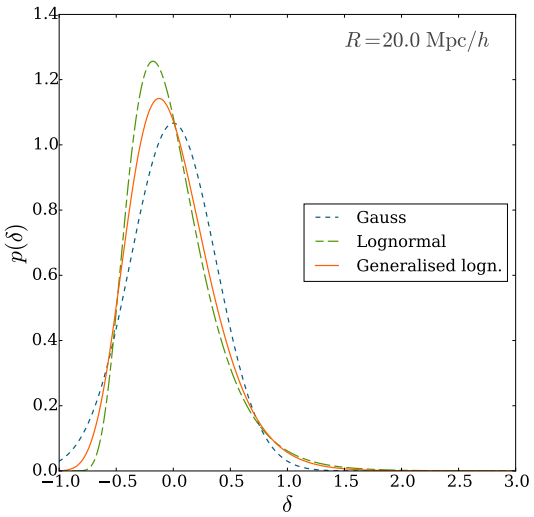

Figure 4.1: Examples of three different PDF models for the density field smoothed at 20 h^{-1}Mpc. The *blue, short dashed* line shows a Gaussian, the *green, long dashed* a lognormal distribution (Eq. 4.1) and the *orange, solid* line a generalised normal distribution (Eq. 4.2). The parameters were chosen such that the variance and the skewness match the KFT prediction (see Section 4.2) and the mean is set to $\delta = 0$.

circumvented. For example, these values could be set to zero while renormalising the PDF afterwards. For these reasons, we will not use the Edgeworth expansion in this work and mention it only for completeness.

4.1.4 *Large deviation principle*

A recent approach to deriving the PDF of the cosmic density field in the mildly non-linear regime ($R \sim 10$ to 20 h^{-1}Mpc) is based on the *large deviation principle*. This principle represents a generalisation of the central limit theorem (see e.g. Touchette, 2009, for a nicely written introduction). It is fulfilled, if the asymptotic limit of the PDF, for a *driving parameter* n going to infinity, is described by

$$P(x) \sim e^{-n\psi(x)} \qquad \text{for } n \to \infty\,, \tag{4.3}$$

where the function $\psi(x)$ is called the *rate function*. In the case that $\psi(x)$ has a global minimum of value zero, a Taylor expansion up to second order around this minimum would recover the central limit theorem. It furthermore predicts the exponential suppression of large deviations from the distribution's most likely value.

We will introduce very briefly the most important concepts and theorems of large deviation theory, which will become important in our subsequent discussion. A central

quantity in large deviation theory is the scaled cumulant generating function (SCGF), $\varphi(k)$. It is defined for a real random variable A_n as

$$\varphi(k) := \lim_{n\to\infty} \frac{1}{n} \ln \left\langle e^{nkA_n} \right\rangle , \tag{4.4}$$

where $k \in \mathbb{R}$ and

$$\left\langle e^{nkA_n} \right\rangle = \int_{\mathbb{R}} e^{nka} P(A_n \in \mathrm{d}a) . \tag{4.5}$$

The *Gärtner-Ellis theorem* then states that if the SCGF exists and if it is differentiable for all $k \in \mathbb{R}$, then A_n satisfies the large deviation principle. It furthermore states that the SCGF is connected to the rate function via the Legendre-Fenchel transformation, which is a generalisation of the Legendre transformation for non-convex functions,

$$\psi(x) = \sup_{k\in\mathbb{R}} \{kx - \varphi(k)\} . \tag{4.6}$$

The second important theorem we will need is the *contraction principle*. Consider a second random variable B_n that is a function of another random variable, $B_n = f(A_n)$. The contraction principle then states, if A_n fulfils the large deviation principle, then the large deviation principle also holds for B_n and the rate functions are connected via the infimum,

$$\psi_B(b) = \inf_{a:f(a)=b} \psi_A(a) . \tag{4.7}$$

The large deviation principle can now be applied to derive the PDF of the cosmic density field (Valageas, 2002; Bernardeau et al., 2014; Bernardeau and Reimberg, 2016; Uhlemann et al., 2016). The linearly evolved density contrast, which shall be denoted by τ, is described by a Gaussian random field. It can be shown, that the SCGF of a Gaussian distribution exists and is differentiable for all $k \in \mathbb{R}$ with the inverse variance, $1/\sigma^2$, being the driving parameter (c.f. Schilder's theorem, Eq. 215 in Touchette, 2009). The Gärtner-Ellis theorem thus states that τ fulfils the large deviation principle. If the real density contrast $\rho := \frac{\rho_{\mathrm{phys}}}{\bar{\rho}}$ can now be expressed in terms of the linearly evolved density contrast τ, the contraction principle can be used to derive the rate function of ρ from that of τ. This has been done by Bernardeau et al. (2014) using the spherical collapse model, where they obtain

$$\rho = \left(1 - \frac{\tau}{\nu}\right)^{-\nu} , \qquad \text{with } \nu = \frac{21}{13} . \tag{4.8}$$

However, Uhlemann et al. (2016) suggest applying the contraction principle to the logarithmic density $\mu = \ln\rho$ instead of ρ. They state that this cures some shortcomings of the original approach presented in Bernardeau et al. (2014), benefiting from the fact that μ cannot become negative. The contraction principle then gives

$$\psi_\mu = \inf_{\tau:f(\tau)=\mu} \psi_\tau(\tau) . \tag{4.9}$$

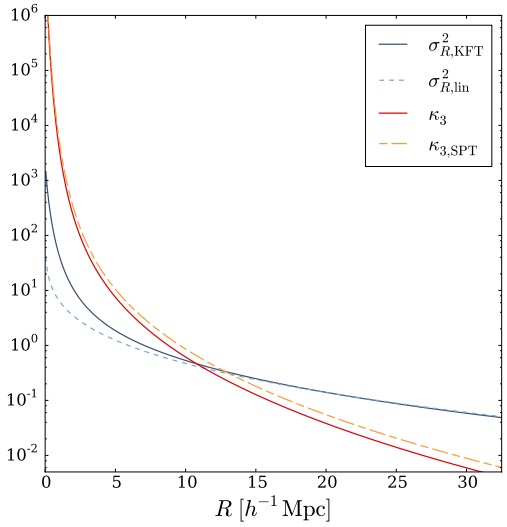

Figure 4.2: Comparison of the KFT prediction of the variance σ^2_{KFT} (*blue, solid line*) with the variance calculated from the linear power spectrum σ^2_{lin} (*light blue, dashed line*) and the third cumulant from KFT κ_3 (*red, solid line*) with the prediction by SPT $\kappa_{3,\mathrm{SPT}}$ (*orange, long dashed line*). All quantities are predictions for the cosmic density field smoothed by a spherical top-hat filter as a function of filter scale R.

This rate function can then be transformed into the scaled cumulant generating function φ via a Legendre-Fenchel transformation. Subsequently, Uhlemann et al. (2016) make the ansatz that the cumulant generating function $\tilde{\varphi}$ is connected to the scaled cumulant generating function via $\tilde{\varphi} = \frac{1}{\sigma^2}\varphi(\lambda\sigma^2)$, where $\lambda = \mathrm{d}\psi/\mathrm{d}\rho$ is the Legendre conjugate variable and σ is a free parameter. The PDF can be obtained by a Laplace transform of $\tilde{\varphi}$ using the saddle-point approximation. Expressing the result in terms of ρ, Uhlemann et al. (2016) obtain

$$P(\rho) = \sqrt{\frac{\psi''(\rho) + \frac{1}{\rho}\psi'(\rho)}{2\pi\sigma^2}}\,\exp\left[-\frac{\psi(\rho)}{\sigma^2}\right]. \tag{4.10}$$

They demonstrate that this expression describes the PDF of the cosmic density field in the mildly non-linear regime considerably better than for example a lognormal distribution. A connection between the parameter σ^2 and the variance of the non-linearly evolved density field as predicted by KFT has been recently investigated by Bieringer (2018).

4.2 PREDICTING MODEL PARAMETERS WITH KFT

Our first approach to describe the PDF of the density field with predictions from KFT will employ two of the models introduced in the previous section. We will use KFT to

obtain the parameters of the lognormal and the generalised normal distributions. These parameters are fixed by the KFT results for the variance and the skewness of the density field smoothed on a radius R.

The variance can be easily obtained from the KFT prediction of the non-linear power spectrum (Fig. 3.1). The most recent development of KFT (Bartelmann et al., 2019) provides the power spectrum of the non-linearly evolved cosmic density field $P_\delta(k)$ with a precision of better than 20 per cent on scales up to $k \sim 10\ h\mathrm{Mpc}^{-1}$, which is already deeply in the non-linear regime. It includes interactions between the dark matter particles by a mean field approach. The variance is then simply given by

$$\sigma_R^2 = \int \frac{\mathrm{d}^3k}{(2\pi)^3}\ P_\delta(k)\hat{W}_R^2(k)\,, \tag{4.11}$$

where $\hat{W}_R$ is the Fourier transform of the top-hat filter with radius R, which has been used to smooth the density field.

The third cumulant can be obtained in a similar way by integrating over the bispectrum. Using the KFT prediction of the bispectrum in the non-interacting case (see Section 3.6.3), the third cumulant κ_3 can be calculated via

$$\begin{aligned}\kappa_3(R) &= \int \frac{\mathrm{d}^3k_1}{(2\pi)^3}\frac{\mathrm{d}^3k_2}{(2\pi)^3}\frac{\mathrm{d}^3k_3}{(2\pi)^3}\,P^{(3)}(\vec{k}_1,\vec{k}_2,\vec{k}_3)\ \hat{W}_R(k_1)\hat{W}_R(k_2)\hat{W}_R(k_3)\\ &= \sigma_R^4\left(4+\frac{R}{\sigma_R^2}\frac{\mathrm{d}\sigma_R^2}{\mathrm{d}R}\right),\end{aligned} \tag{4.12}$$

which has been first derived in Linke (2017). It only depends on the variance σ_R^2 and its derivative with respect to R. The form of Eq. (4.12) is very similar to the result from SPT for an Einstein-de Sitter universe (Eq. 60 in Bernardeau, 1994a), i.e.

$$\kappa_{3,\mathrm{SPT}} = \sigma_R^4\left(\frac{34}{7}+\frac{R}{\sigma_R^2}\frac{\mathrm{d}\sigma_R^2}{\mathrm{d}R}\right). \tag{4.13}$$

The two equations differ only in the numerical value of the first summand in the bracket. We show a comparison of the KFT-prediction for the variance σ_R^2, the linear variance from the Bardeen power spectrum $\sigma_{R,\mathrm{lin}}^2$, the third cumulant κ_3 from KFT and the SPT-prediction $\kappa_{3,\mathrm{SPT}}$ in Fig. 4.2. Since KFT includes the non-linear evolution of density fluctuations (see Fig. 3.1) the KFT prediction for the variance is on all scales larger than the linear prediction. The non-linear effects become especially important on small scales, which is reflected in an increasing discrepancy when smoothed over smaller and smaller scales. The third cumulant κ_3, which reflects the skewness of the distribution, decreases considerably faster than the variance for increasing smoothing radii. The predictions of SPT deviate from those of KFT by 20 to 30 per cent. However, it is important to mention, that the values for κ_3 for SPT are not a pure SPT result, since we only took the functional form of Eq. (4.13), but we inserted the KFT values for the variance and its derivative, in order to just compare the difference in the functional forms.

We now use these KFT predictions to fix the parameters of the models for the density PDF presented in Section 4.1. In case of the lognormal distribution (Eq. 4.1) this is particularly easy. Since it only depends on one parameter $\tilde{\sigma}_R$, we simply insert the KFT prediction for the variance into

$$\tilde{\sigma}_R^2 = \ln(1+\sigma_R^2)\,. \tag{4.14}$$

This fully specifies the lognormal distribution at each radius.

The generalised normal distribution (Eq. 4.2) depends on three parameters, where the first constraint is given by using $\langle\delta_R\rangle = 0$. Calculating the mean $\langle\delta_R\rangle$ from Eq. (4.2) then leads to the condition

$$\frac{\tilde{\mu}\beta}{\alpha} = e^{\beta^2/2} - 1. \tag{4.15}$$

Furthermore, we can similarly calculate the variance $\sigma_R^2 = \langle\delta_R\delta_R\rangle$ and third cumulant $\kappa_3 = \langle\delta_R\delta_R\delta_R\rangle$ for the generalised normal distribution Eq. (4.2). This leads to the conditions

$$\sigma_R^2 = \frac{\alpha^2}{\beta^2} e^{\beta^2}\left(e^{\beta^2}-1\right) \tag{4.16}$$

and

$$\kappa_3 = \frac{2 + e^{3\beta^2} - 3e^{\beta^2}}{\left(e^{\beta^2}-1\right)^{3/2}}\,\sigma^3\,. \tag{4.17}$$

To further ease the notation, we define $\tilde{\kappa}_3 := \kappa_3/\sigma_R^3$ and

$$y := 1 + \frac{\tilde{\kappa}_3^2}{2} - \frac{\sqrt{4\tilde{\kappa}_3^2 + \tilde{\kappa}_3^4}}{2}\,. \tag{4.18}$$

Eq. (4.17) can then be solved for β to get an explicit relation with respect to $\tilde{\kappa}_3$

$$\beta^2 = \ln\left(-1 + y^{1/3} + y^{-1/3}\right)\,. \tag{4.19}$$

Moreover, we obtain the remaining two parameters by solving Eqns. (4.15) and (4.16), which leads to

$$\alpha^2 = \sigma_R^2\beta^2\, e^{-\beta^2}\left(e^{\beta^2}-1\right)^{-1} \tag{4.20}$$

and

$$\tilde{\mu} = \frac{\alpha}{\beta} e^{\beta^2/2} - 1. \tag{4.21}$$

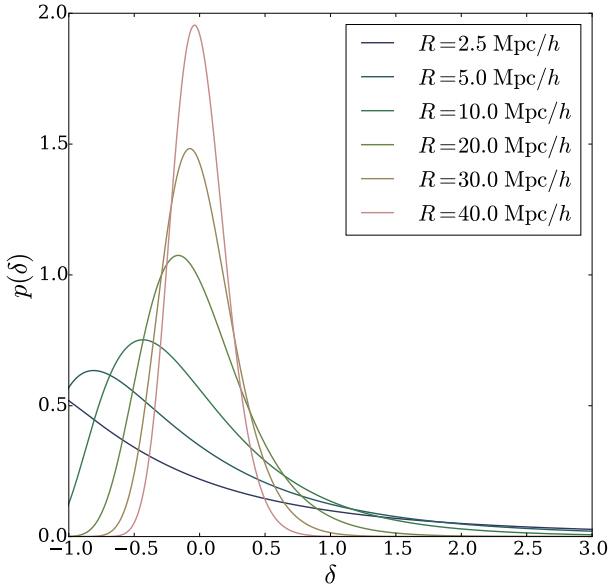

Figure 4.3: PDF of the cosmic density field smoothed with a spherical top-hat filter based on a generalised normal distribution (Eq. 4.2) as described in the text. Variance and skewness are fixed by KFT predictions. The colours encode different smoothing radii ranging from $R = 2.5$ to 40 h^{-1}Mpc.

This allows to fully determine the generalised normal distribution by plugging in the KFT predictions for σ_R^2 and κ_3.

A comparison of the resulting lognormal distribution, generalised normal distribution and a Gaussian can be seen for a smoothing radius of $R = 20\ h^{-1}$Mpc in Fig. 4.1. The generalised normal distribution for six different smoothing radii is shown in Fig. 4.3. For large smoothing radii, the PDF is still almost symmetric and has a shape close to a Gaussian distribution. As the smoothing radius gets smaller, the variance and skewness increase considerably. This leads to a shift of the maximum to more and more negative values and a long tail extending to ever higher densities.

4.3 THE DENSITY PDF FROM THE GENERATING FUNCTIONAL

We will now explore a second path, which aims at deriving the density PDF from the generating functional of KFT directly without assuming any PDF model. For this purpose, we will use the framework of resummed KFT (RKFT, Lilow et al., 2019), which has been summarised in Section 3.7. To extract the PDF from the generating functional, we will introduce an indicator function $I_{\tilde{\rho}}$. The purpose of this function is to filter out only those field configurations in the macroscopic generating functional (Eq. 3.83), for which the macroscopic density ϕ_ρ (evaluated at the origin) has a value in a range of $\Delta\tilde{\rho}$ around a fiducial density $\tilde{\rho}$. It results in a probability distribution of the density $\tilde{\rho}$ represented

by bins of width $\Delta\tilde{\rho}$, which we denote as $P(\tilde{\rho})\Delta\tilde{\rho} = P(\tilde{\rho} - \Delta\tilde{\rho}/2 \lesssim \phi_\rho \lesssim \tilde{\rho} + \Delta\tilde{\rho}/2)$. The indicator function is then formally introduced in the generating functional (Eq. 3.83) as

$$P(\tilde{\rho})\Delta\tilde{\rho} = \mathcal{N} \int \mathcal{D}\phi \; e^{\mathrm{i}S_\phi} \; I_{\tilde{\rho}}(\phi_\rho)\,, \tag{4.22}$$

where $\mathcal{N}$ is a normalisation constant. The most natural choice for the indicator function would be a box function which returns one when the density is within the interval $\Delta\tilde{\rho}$ around $\tilde{\rho}$ and zero otherwise. In our approach, we choose a Gaussian indicator function instead, since its Fourier transform is particularly easy and it allows us to perform the calculations analytically. The indicator function for the macroscopic density evaluated at a position $\vec{q}_0$ and time t is given by

$$I_{\tilde{\rho}}\left(\phi_\rho(\vec{q}_0, t)\right) = e^{-\frac{\left(\phi_\rho(\vec{q}_0,t)-\tilde{\rho}\right)^2}{2\sigma^2}}\,, \tag{4.23}$$

where we assumed that the normalisation factor of the Gaussian will be contained in the normalisation factor $\mathcal{N}$ in Eq. (4.22). It will now be our aim to rewrite Eq. (4.22) such that we absorb the indicator function into the action. We can then perform a perturbation theory approach analogously to that presented in Lilow et al. (2019) in order to approximate the integral. For simplicity, we choose $\vec{q}_0 = 0$, since the point at which the field is evaluated is arbitrary due to the homogeneity assumption of cosmology.

We need to bring the indicator function into a form that uses the same structure as the macroscopic action of RKFT. We will show here only the most important steps, while the detailed calculations are presented in Appendix B. To bring the indicator function into a RKFT-compatible notation, we rewrite the products in the exponent as the dot product defined in Eq. (3.59). This requires to express the indicator function in dependency of wave vectors $\vec{k}$ instead of positions $\vec{q}_0$ and to introduce integrals over $\vec{k}$ and t. As detailed in Appendix B.1, the indicator function expressed in Fourier space, denoted by $\tilde{I}_{\tilde{\rho}}(\phi_\rho(\vec{k}, t))$, then takes the form

$$\tilde{I}_{\tilde{\rho}}\left(\phi_\rho\right) = e^{-\frac{1}{2\sigma^2}\left(\iint \mathrm{d}1\,\mathrm{d}2\;\phi_\rho(1)\phi_\rho(2)\delta_\mathrm{D}(t_1-t)\delta_\mathrm{D}(t_2-t) - 2\int \mathrm{d}1\;\tilde{\rho}\phi_\rho(1))\delta_\mathrm{D}(t_1-t)\right)} e^{-\frac{\tilde{\rho}^2}{2\sigma^2}}\,. \tag{4.24}$$

In order to be able to introduce the dot product in the exponent, we define the two auxiliary functions

$$\mathcal{W}_1(1) := \frac{\tilde{\rho}\delta_\mathrm{D}(t_1 - t)}{\sigma^2}\,, \tag{4.25}$$

$$\mathcal{W}_2(1,2) := \frac{\delta_\mathrm{D}(t_1 - t)\delta_\mathrm{D}(t_2 - t)}{\sigma^2}\,, \tag{4.26}$$

which depend on the arguments 1 and 2 only formally[3], allowing us to write the linear and the quadratic term of the exponent in the desired form of the dot product,

$$\tilde{I}_{\tilde{\rho}}\left(\phi_\rho\right) = e^{\mathcal{W}_1\cdot\phi_\rho - \frac{\phi_\rho\cdot\mathcal{W}_2\cdot\phi_\rho}{2}} e^{-\frac{\tilde{\rho}^2}{2\sigma^2}}\,. \tag{4.27}$$

We now insert it into the generating functional (Eq. 3.83) and obtain

$$\begin{aligned} P(\tilde{\rho})\Delta\tilde{\rho} &= \mathcal{N}\int \mathcal{D}\phi\; e^{\mathrm{i}S_\phi}\,\tilde{I}_{\tilde{\rho}}(\phi_\rho) \\ &= \mathcal{N}\int \mathcal{D}\phi\; e^{\mathrm{i}S_\phi}\; e^{\mathcal{W}_1\cdot\phi_\rho - \frac{\phi_\rho\cdot\mathcal{W}_2\cdot\phi_\rho}{2}} e^{-\frac{\tilde{\rho}^2}{2\sigma^2}} \\ &=: \mathcal{N}\, e^{-\frac{\tilde{\rho}^2}{2\sigma^2}}\int \mathcal{D}\phi\; e^{\mathrm{i}S_\phi^{\mathrm{pdf}}}\,. \end{aligned} \tag{4.28}$$

In the last step, we have defined the action $S_{\boldsymbol{\phi}}^{\mathrm{pdf}}$, which contains those parts of the indicator function that depend on the field ϕ_ρ,

$$S_\phi^{\mathrm{pdf}} := -\phi_\rho\cdot\phi_\beta - \mathrm{i}W_0^{\rho,\mathcal{F}}[\phi_\beta,\phi_\rho] - \mathrm{i}\mathcal{W}_1\cdot\phi_\rho + \mathrm{i}\frac{\phi_\rho\cdot\mathcal{W}_2\cdot\phi_\rho}{2}\,. \tag{4.29}$$

We now solve the path integral of Eq. (4.28) in a procedure analogous to the perturbation theory approach proposed by Lilow et al. (2019). We will expand the free generating functional $W_0^{\rho,\mathcal{F}}[\phi_\beta,\phi_\rho]$ contained in the action S_ϕ^{pdf} up to second order. The third-order expansion will be investigated in Section 4.4. Since all other summands in the action are of quadratic order or less, the path integral can easily be solved by a Gaussian integration. We write the quadratic form of the action in terms of the field ϕ, the one-point vertex $\mathcal{V}$ and the macroscopic propagator Δ, which are yet to be defined. We need to emphasise that $\mathcal{V}$ and Δ are in this case *not* the same as in the standard RKFT formulation but will have a slightly modified shape, since they will contain also the indicator function. We thus assume the action to be of the form

$$\begin{aligned} \mathrm{i}S_\phi^{\mathrm{pdf}} &= \int \mathrm{d}1\;\left(\mathcal{V}_\rho,\mathcal{V}_\beta\right)(1)\begin{pmatrix}\phi_\rho\\ \phi_\beta\end{pmatrix}(-1) \\ &\quad - \frac{1}{2}\int \mathrm{d}1\int \mathrm{d}2\;\left(\phi_\rho,\phi_\beta\right)(-1)\begin{pmatrix}(\Delta^{-1})_{\rho\rho} & (\Delta^{-1})_{\rho\beta}\\ (\Delta^{-1})_{\beta\rho} & (\Delta^{-1})_{\beta\beta}\end{pmatrix}(1,2)\begin{pmatrix}\phi_\rho\\ \phi_\beta\end{pmatrix}(-2) \\ &= \mathcal{V}\cdot\phi - \frac{1}{2}\phi^{\mathrm{T}}\cdot\Delta^{-1}\cdot\phi\,, \end{aligned} \tag{4.30}$$

3 Note also that we used $\mathcal{W}_1(1) = \mathcal{W}_1(-1)$ and $\mathcal{W}_2(1,2) = \mathcal{W}_2(-1,-2)$, since neither $\mathcal{W}_1$ nor $\mathcal{W}_2$ depends on $\vec{k}$. In principle, the definition would require a minus sign in front of all of the arguments, according to the definition of the dot product in Eq. (3.59).

where $\mathcal{V}$ and Δ are still to be specified. Sparing the identification of $\mathcal{V}$ and Δ for a second step, we can solve Eq. (4.28)

$$\begin{aligned} P(\tilde{\rho})\Delta\tilde{\rho} &= \mathcal{N}\, e^{-\frac{\tilde{\rho}^2}{2\sigma^2}} \int \mathcal{D}\phi\; e^{-\frac{1}{2}\phi^{\mathrm{T}}\cdot\Delta^{-1}\cdot\phi+\mathcal{V}\cdot\phi} \\ &= \tilde{\mathcal{N}}\, e^{\frac{1}{2}\mathcal{V}\cdot\Delta\cdot\mathcal{V}-\frac{\tilde{\rho}^2}{2\sigma^2}}\,, \end{aligned} \tag{4.31}$$

where we absorbed in the second line all constant factors from the path integral into the normalisation constant $\tilde{\mathcal{N}}$.

We now proceed with specifying the actual form of $\mathcal{V}$ and Δ, where especially the inversion of Δ^{-1} will require some involved calculations. To bring Eq. (4.29) into quadratic form, we need to Taylor expand the logarithm of the free generating functional $W_0^{\rho,\mathcal{F}}[\phi_\beta,\phi_\rho]$ up to second order. The Taylor expansion in terms of the source fields ϕ_β and ϕ_ρ is given by

$$\begin{aligned} W[\phi] &= \sum_{n_\rho,n_\beta} \frac{1}{n_\rho! n_\beta!} \prod_{u=1}^{n_\beta} \left(\int \mathrm{d}u\; \phi_\beta(-u) \frac{\delta}{\delta\phi_\beta(u)} \right) \prod_{r=1}^{n_\rho} \left(\int \mathrm{d}r'\; \phi_\rho(-r') \frac{\delta}{\delta\phi_\rho(r')} \right) W[\tilde{\phi}]|_{\phi=0} \\ &= \sum_{n_\rho,n_\beta} \frac{\mathrm{i}^{n_\rho+n_\beta}}{n_\rho! n_\beta!} \prod_{u=1}^{n_\beta} \left(\int \mathrm{d}u\; \phi_\beta(-u) \right) \dots \\ &\qquad\qquad \times \prod_{r=1}^{n_\rho} \left(\int \mathrm{d}r'\; \phi_\rho(-r') \right) G_{\rho\cdots\rho\mathcal{F}\cdots\mathcal{F}}(1,\dots,n_\beta,1',\dots,n_\rho)\,, \end{aligned} \tag{4.32}$$

where we have used in the second step that ϕ_ρ and ϕ_β are in our picture the source fields of the dressed response field $\mathcal{F}$ and the microscopic density field ρ, respectively. Applying functional derivatives with respect to ϕ_ρ and ϕ_β to the logarithm of the free generating functional therefore simply yields the corresponding free cumulant up to a constant prefactor. These cumulants have been summarised in Section 3.6.1.

Multiplying Eq. (4.29) by a factor of i and inserting the Taylor expansion up to second order leads to

$$\begin{aligned}
\mathrm{i}S_\phi^{\mathrm{pdf}} &= -\mathrm{i}\phi_\beta\cdot\phi_\rho + \mathcal{W}_1\cdot\phi_\rho - \frac{\phi_\rho\cdot\mathcal{W}_2\cdot\phi_\rho}{2} + \mathrm{i}G_\rho\cdot\phi_\beta + \mathrm{i}G_\mathcal{F}\cdot\phi_\rho \\
&\quad - \frac{1}{2}\phi_\beta\cdot G_{\rho\rho}\cdot\phi_\beta - \frac{1}{2}\phi_\rho\cdot G_{\mathcal{F}\mathcal{F}}\cdot\phi_\rho - \phi_\beta\cdot G_{\rho\mathcal{F}}\cdot\phi_\rho \\
&= (\mathrm{i}G_\mathcal{F} + \mathcal{W}_1)\cdot\phi_\rho + \mathrm{i}G_\rho\cdot\phi_\beta - \phi_\rho\cdot\frac{1}{2}\left(\mathcal{W}_2 + G_{\mathcal{F}\mathcal{F}}\right)\cdot\phi_\rho \\
&\quad - \frac{1}{2}\phi_\beta\cdot G_{\rho\rho}\cdot\phi_\beta - \phi_\beta\cdot\left(G_{\rho\mathcal{F}} + \mathrm{i}\mathcal{I}\right)\cdot\phi_\rho \\
&= \left((\mathrm{i}G_\mathcal{F} + \mathcal{W}_1),\ \mathrm{i}G_\rho\right)\cdot\begin{pmatrix}\phi_\rho\\ \phi_\beta\end{pmatrix} \\
&\quad - \frac{1}{2}\left(\phi_\rho, \phi_\beta\right)\cdot\begin{pmatrix}\mathcal{W}_2 + G_{\mathcal{F}\mathcal{F}} & \mathrm{i}\mathcal{I} + G_{\mathcal{F}\rho}\\ \mathrm{i}\mathcal{I} + G_{\rho\mathcal{F}} & G_{\rho\rho}\end{pmatrix}\cdot\begin{pmatrix}\phi_\rho\\ \phi_\beta\end{pmatrix},
\end{aligned} \tag{4.33}$$

with the 2-point identity function $\mathcal{I}$ defined as

$$\mathcal{I}(1,2) := (2\pi)^3\delta_\mathrm{D}(\vec{k}_1 + \vec{k}_2)\delta_\mathrm{D}(t_1 - t_2). \tag{4.34}$$

In the second step, we collected summands according to their powers in ϕ_ρ and ϕ_β, respectively, and used vector/matrix-notation in the third step. Comparing this form of the action with Eq. (4.30), the vertex $\mathcal{V}$ and the inverse macroscopic propagator Δ^{-1} can easily be identified as

$$\mathcal{V} \equiv \left((\mathrm{i}G_\mathcal{F} + \mathcal{W}_1),\ \mathrm{i}G_\rho\right) \tag{4.35}$$

and

$$\Delta^{-1} \equiv \begin{pmatrix}(\mathcal{W}_2 + G_{\mathcal{F}\mathcal{F}}) & (\mathrm{i}\mathcal{I} + G_{\mathcal{F}\rho})\\ (\mathrm{i}\mathcal{I} + G_{\rho\mathcal{F}}) & G_{\rho\rho}\end{pmatrix}. \tag{4.36}$$

Taking the free cumulants introduced in the previous chapter, i.e. Eqns. (3.67) – (3.72), we see that the pure dressed response field cumulants are zero, which leads to

$$\mathcal{V} = \left(\mathcal{W}_1,\ \mathrm{i}G_\rho\right) = \left(\frac{\tilde{\rho}}{\sigma^2}\delta_\mathrm{D}(t_1 - t),\ \mathrm{i}G_\rho\right) \tag{4.37}$$

and

$$\Delta^{-1} = \begin{pmatrix}\mathcal{W}_2 & \mathrm{i}\mathcal{I} + G_{\mathcal{F}\rho}\\ \mathrm{i}\mathcal{I} + G_{\rho\mathcal{F}} & G_{\rho\rho}\end{pmatrix} \tag{4.38}$$

$$:= \begin{pmatrix}A & B\\ C & D\end{pmatrix}. \tag{4.39}$$

We defined in the last step A, B, C and D to ease notation for deriving the inverse of Δ^{-1}. They can be interpreted as block matrices in the following way. Discretising the time evolution into n time steps, the fields ϕ_ρ and ϕ_β can be seen as n-dimensional vectors. In this picture, components of the inverse propagator take the shape of $n \times n$ matrices. Their full functional form is recovered in the limit $n \to \infty$.

4.3.1 *Calculating the propagator*

In this section, it will be our task to calculate the propagator

$$\Delta =: \begin{pmatrix} \Delta_{11} & \Delta_{12} \\ \Delta_{21} & \Delta_{22} \end{pmatrix}, \tag{4.40}$$

i.e. to invert Eq. (4.38) such that we can insert it into Eq. (4.31). Using matrix inversion with block matrices known from linear algebra, we obtain

$$\Delta_{11} = (A - B \cdot D^{-1} \cdot C)^{-1} = -C^{-1} \cdot D \cdot (B - A \cdot C^{-1} \cdot D)^{-1}, \tag{4.41}$$

$$\Delta_{12} = (C - D \cdot B^{-1} \cdot A)^{-1}, \tag{4.42}$$

$$\Delta_{21} = (B - A \cdot C^{-1} \cdot D)^{-1}, \tag{4.43}$$

$$\Delta_{22} = (D - C \cdot A^{-1} \cdot B)^{-1} = -B^{-1} \cdot A \cdot (C - D \cdot B^{-1} \cdot A)^{-1}, \tag{4.44}$$

where we have rewritten Eqns. (4.41) and (4.44) such that they can be expressed in terms of Δ_{12} and Δ_{21}. We will therefore start with calculating Δ_{12}.

In order to make the following calculations more readable and to highlight that the δ_D-distributions are the crucial point, we absorb all functional dependences that are not δ_D-distributions into the functions $\tilde{G}_{\rho\mathcal{F}(k_1;t_1,t_2)}$ and $\tilde{G}_{\rho\rho(k_1;t_1,t_2)}$, i.e.

$$\begin{aligned} G_{\rho\mathcal{F}}(1,2) &=: (2\pi)^3 \delta_\mathrm{D}(\vec{k}_1 + \vec{k}_2) \tilde{G}_{\rho\mathcal{F}(k_1;t_1,t_2)} \\ &\approx \mathrm{i}(2\pi)^3 \delta_\mathrm{D}(\vec{k}_1 + \vec{k}_2) \vec{k}_1^2 \, g_{qp}(t_1,t_2) \bar{\rho} v_{(k_1,t_1)}, \end{aligned} \tag{4.45}$$

$$\begin{aligned} G_{\rho\rho}(1,2) &=: (2\pi)^3 \delta_\mathrm{D}(\vec{k}_1 + \vec{k}_2) \tilde{G}_{\rho\rho(k_1;t_1,t_2)} \\ &\approx (2\pi)^3 \delta_\mathrm{D}(\vec{k}_1 + \vec{k}_2)(1 + g_{qp}(t_1,0))(1 + g_{qp}(t_2,0)) \bar{\rho}^2 P_{\delta\delta}^\mathrm{ini}(\vec{k}_1). \end{aligned} \tag{4.46}$$

(*i*) *Calculating* Δ_{12}:

By definition of the inverse and the 2-point identity function (Eq. 4.34), we have

$$\Delta_{12}(1,\bar{1}) \cdot (C - D \cdot B^{-1} \cdot A)_{(-\bar{1},2)} \stackrel{!}{=} \mathcal{I}(1,2), \tag{4.47}$$

where the variable with a bar is the variable which is integrated over in the dot product (defined in Eq. 3.59). Inserting the matrix components A, B, C and D leads to

$$\Delta_{12}(1,\bar{1}) \cdot \Big[\mathrm{i}\mathcal{I}(-\bar{1},2) + (2\pi)^3\delta_\mathrm{D}(-\vec{k}_{\bar{1}} + \vec{k}_2)\tilde{G}_{\rho\mathcal{F}}(-k_{\bar{1}};t_{\bar{1}},t_2) - (2\pi)^3 \ldots$$
$$\delta_\mathrm{D}(-\vec{k}_{\bar{1}} + \vec{k}_{\bar{1}'})\tilde{G}_{\rho\rho}(-k_{\bar{1}};t_{\bar{1}},t_{\bar{1}'}) \cdot B^{-1}(-\bar{1}',\bar{1}'') \cdot \frac{\delta_\mathrm{D}(t_{\bar{1}''} - t)\delta_\mathrm{D}(t_2 - t)}{\sigma^2}\Big] \stackrel{!}{=} \mathcal{I}(1,2)\,. \tag{4.48}$$

In order to solve this equation, we will proceed analogously to Lilow et al. (2019) and assume that Δ_{12} can be decomposed into summands that contain various combinations of δ_D-distributions. We guess the form of Δ_{12} on the basis of the structure of Δ^{-1}, i.e. by recognising the different combinations of δ_D-distributions contained in A, B, C and D. We therefore assume that we can decompose Δ_{12} into

$$\begin{aligned}\Delta_{12}(1,\bar{1}) = -\mathrm{i}\Big(&\mathcal{I}(1,\bar{1}) + (2\pi)^3\delta_\mathrm{D}(\vec{k}_1 + \vec{k}_{\bar{1}})\tilde{\Delta}_{12}^{(1)}(k_1;t_1,t_{\bar{1}}) \ldots \\ &+ \delta_\mathrm{D}(t_{\bar{1}} - t)\tilde{\Delta}_{12}^{(2)}(k_1,k_{\bar{1}};t_1;t) + \tilde{\Delta}_{12}^{(3)}(k_1,k_{\bar{1}};t_1,t_{\bar{1}};t)\Big)\,,\end{aligned} \tag{4.49}$$

where the functions $\tilde{\Delta}_{12}^{(1)}$, $\tilde{\Delta}_{12}^{(2)}$ and $\tilde{\Delta}_{12}^{(3)}$ contain the remaining unknown functional dependences belonging to each δ_D-distribution and they are now to be determined.

We furthermore notice that B^{-1} equals exactly the off-diagonal entry in the propagator of Lilow et al. (2019), which was used to calculate the non-linear power spectrum. We can therefore simply use their solution for B^{-1}, which they named the *advanced propagator* Δ_A after factoring out a factor of $-\mathrm{i}$. It is given by

$$B^{-1}(-\bar{1}',\bar{1}'') = -\mathrm{i}\left[\mathcal{I} - \mathrm{i}G_{\mathcal{F}\rho}\right]^{-1}(-\bar{1}',\bar{1}'') = -\mathrm{i}\Delta_\mathrm{A}(-\bar{1}',\bar{1}'') \tag{4.50}$$

$$= -\mathrm{i}\left(\mathcal{I}(-\bar{1}',\bar{1}'') + (2\pi)^3\delta_\mathrm{D}(-\vec{k}_{\bar{1}'} + \vec{k}_{\bar{1}''})\tilde{\Delta}_\mathrm{A}(-k_{\bar{1}'};t_{\bar{1}'},t_{\bar{1}''})\right)\,, \tag{4.51}$$

where – in the same spirit as above – it was assumed in the second line that the advanced propagator can be decomposed into a summand equal to the identity function and another proportional to $\delta_\mathrm{D}(-\vec{k}_{\bar{1}'} + \vec{k}_{\bar{1}''})$. Lilow et al. (2019) describe the computation of $\tilde{\Delta}_\mathrm{A}$ in their Appendix B.[4] They also introduce the retarded propagator Δ_R, which is related to the advanced propagator simply by exchanging the arguments, $\Delta_\mathrm{A}(1,2) = \Delta_\mathrm{R}(2,1)$.

Inserting our ansatz for Δ_{12} (Eq. 4.49) and the result for B^{-1} (Eq. 4.51) into Eq. (4.48) leads us to the constraint equation which should allow us to determine the three functions $\tilde{\Delta}_{12}^{(1)}$, $\tilde{\Delta}_{12}^{(1)}$ and $\tilde{\Delta}_{12}^{(3)}$. Carrying out all resulting integrations in Eq. (4.48) leads

4 They show that for certain functional forms of $\tilde{G}_{\rho\mathcal{F}}$ an exact analytic expression can be obtained using Laplace transforms. In the general case, an approximate numerical result can be computed using the discretisation of the time argument mentioned in the paragraph below Eq. (4.39).

then to the lengthy expression (see Appendix B.2 for the details of the calculation)

$$
\begin{aligned}
&(2\pi)^3\delta_{\mathrm{D}}(\vec{k}_1+\vec{k}_2)\left[-\mathrm{i}\tilde{G}_{\rho\mathcal{F}}(k_1;t_1,t_2)+\tilde{\Delta}^{(1)}_{12}(k_1;t_1,t_2)-\mathrm{i}\int_{t_{\bar{1}}}\underline{\tilde{\Delta}^{(1)}_{12}(k_1;t_1,t_{\bar{1}})}\,\tilde{G}_{\rho\mathcal{F}}(k_1;t_{\bar{1}},t_2)\right]\dots\\
&\quad+\tfrac{\delta_{\mathrm{D}}(t_2-t)}{\sigma^2}\left[\tilde{G}_{\rho\rho}(k_1;t_1,t)+\int_{t_{\bar{1}'}}\tilde{G}_{\rho\rho}(k_1;t_1,t_{\bar{1}'})\tilde{\Delta}_{\mathrm{A}}(k_1;t_{\bar{1}'},t)+\int_{t_{\bar{1}}}\underline{\tilde{\Delta}^{(1)}_{12}(k_1;t_1,t_{\bar{1}})}\,\tilde{G}_{\rho\rho}(k_1;t_{\bar{1}},t)\dots\right.\\
&\qquad+\int_{t_{\bar{1}}}\int_{t_{\bar{1}'}}\underline{\tilde{\Delta}^{(1)}_{12}(k_1;t_1,t_{\bar{1}})}\,\tilde{G}_{\rho\rho}(k_1;t_{\bar{1}},t_{\bar{1}'})\tilde{\Delta}_{\mathrm{A}}(k_1;t_{\bar{1}'},t)+\sigma^2\underline{\tilde{\Delta}^{(2)}_{12}(k_1,k_2;t_1;t)}\dots\\
&\qquad+\int_{k_{\bar{1}}}\underline{\tilde{\Delta}^{(2)}_{12}(k_1,k_{\bar{1}};t_1;t)}\,\tilde{G}_{\rho\rho}(-k_{\bar{1}};t,t)+\int_{k_{\bar{1}}}\underline{\tilde{\Delta}^{(2)}_{12}(k_1,k_{\bar{1}};t_1;t)}\int_{t_{\bar{1}'}}\tilde{G}_{\rho\rho}(-k_{\bar{1}};t,t_{\bar{1}'})\tilde{\Delta}_{\mathrm{A}}(-k_{\bar{1}};t_{\bar{1}'},t)\dots\\
&\qquad+\int_{k_{\bar{1}}}\int_{t_{\bar{1}}}\underline{\tilde{\Delta}^{(3)}_{12}(k_1,k_{\bar{1}};t_1,t_{\bar{1}};t)}\,\tilde{G}_{\rho\rho}(-k_{\bar{1}};t_{\bar{1}},t)\dots\\
&\qquad\left.+\int_{k_{\bar{1}}}\int_{t_{\bar{1}}}\underline{\tilde{\Delta}^{(3)}_{12}(k_1,k_{\bar{1}};t_1,t_{\bar{1}};t)}\int_{t_{\bar{1}'}}\tilde{G}_{\rho\rho}(-k_{\bar{1}};t_{\bar{1}},t_{\bar{1}'})\tilde{\Delta}_{\mathrm{A}}(-k_{\bar{1}};t_{\bar{1}'},t)\right]\dots\\
&-\mathrm{i}\underline{\tilde{\Delta}^{(2)}_{12}(k_1,k_2;t_1;t)}\,\tilde{G}_{\rho\mathcal{F}}(-k_2;t,t_2)+\underline{\tilde{\Delta}^{(3)}_{12}(k_1,k_2;t_1,t_2;t)}-\mathrm{i}(2\pi)^3\underline{\tilde{\Delta}^{(3)}_{12}(k_1,k_{\bar{1}};t_1,t_{\bar{1}};t)}\cdot\delta_{\mathrm{D}}(-\vec{k}_{\bar{1}}+\vec{k}_2)\tilde{G}_{\rho\mathcal{F}}(-k_{\bar{1}};t_{\bar{1}},t_2)\quad\stackrel{!}{=}0\,,
\end{aligned}
\tag{4.52}
$$

where we regrouped the summands according to the contained δ_{D}-distribution. In order to make it easier to match equal terms, we highlight them by the same line style. Each of the three summands is proportional to a different δ_{D}-distribution and therefore each of the summands has to be zero individually. We end up with three constraining equations that will allow us to determine the three functions $\tilde{\Delta}^{(1)}_{12}$, $\tilde{\Delta}^{(1)}_{12}$ and $\tilde{\Delta}^{(3)}_{12}$. These read

$$
\underline{\tilde{\Delta}^{(1)}_{12}(k_1;t_1,t_2)}=\mathrm{i}\tilde{G}_{\rho\mathcal{F}}(k_1;t_1,t_2)+\mathrm{i}\int_{t_{\bar{1}}}\underline{\tilde{\Delta}^{(1)}_{12}(k_1;t_1,t_{\bar{1}})}\,\tilde{G}_{\rho\mathcal{F}}(k_1;t_{\bar{1}},t_2)\,,
\tag{4.53}
$$

$$
\begin{aligned}
\underline{\tilde{\Delta}^{(2)}_{12}(k_1,k_2;t_1;t)}=-\frac{1}{\sigma^2}\Bigg[&\tilde{G}_{\rho\rho}(k_1;t_1,t)+\int_{t_{\bar{1}'}}\tilde{G}_{\rho\rho}(k_1;t_1,t_{\bar{1}'})\tilde{\Delta}_{\mathrm{A}}(k_1;t_{\bar{1}'},t)+\int_{t_{\bar{1}}}\underline{\tilde{\Delta}^{(1)}_{12}(k_1;t_1,t_{\bar{1}})}\,\tilde{G}_{\rho\rho}(k_1;t_{\bar{1}},t)\dots\\
&+\int_{t_{\bar{1}}}\int_{t_{\bar{1}'}}\underline{\tilde{\Delta}^{(1)}_{12}(k_1;t_1,t_{\bar{1}})}\,\tilde{G}_{\rho\rho}(k_1;t_{\bar{1}},t_{\bar{1}'})\tilde{\Delta}_{\mathrm{A}}(k_1;t_{\bar{1}'},t)+\int_{k_{\bar{1}}}\underline{\tilde{\Delta}^{(2)}_{12}(k_1,k_{\bar{1}};t_1;t)}\,\tilde{G}_{\rho\rho}(-k_{\bar{1}};t,t)\dots\\
&+\int_{k_{\bar{1}}}\underline{\tilde{\Delta}^{(2)}_{12}(k_1,k_{\bar{1}};t_1;t)}\int_{t_{\bar{1}'}}\tilde{G}_{\rho\rho}(-k_{\bar{1}};t,t_{\bar{1}'})\tilde{\Delta}_{\mathrm{A}}(-k_{\bar{1}};t_{\bar{1}'},t)+\int_{k_{\bar{1}}}\int_{t_{\bar{1}}}\underline{\tilde{\Delta}^{(3)}_{12}(k_1,k_{\bar{1}};t_1,t_{\bar{1}};t)}\,\tilde{G}_{\rho\rho}(-k_{\bar{1}};t_{\bar{1}},t)\dots\\
&+\int_{k_{\bar{1}}}\int_{t_{\bar{1}}}\underline{\tilde{\Delta}^{(3)}_{12}(k_1,k_{\bar{1}};t_1,t_{\bar{1}};t)}\int_{t_{\bar{1}'}}\tilde{G}_{\rho\rho}(-k_{\bar{1}};t_{\bar{1}},t_{\bar{1}'})\tilde{\Delta}_{\mathrm{A}}(-k_{\bar{1}};t_{\bar{1}'},t)\Bigg]\,,
\end{aligned}
\tag{4.54}
$$

$$
\underline{\tilde{\Delta}^{(3)}_{12}(k_1,k_2;t_1,t_2;t)}=\mathrm{i}\underline{\tilde{\Delta}^{(2)}_{12}(k_1,k_2;t_1;t)}\,\tilde{G}_{\rho\mathcal{F}}(-k_2;t,t_2)+\mathrm{i}(2\pi)^3\underline{\tilde{\Delta}^{(3)}_{12}(k_1,k_{\bar{1}};t_1,t_{\bar{1}};t)}\cdot\delta_{\mathrm{D}}(-\vec{k}_{\bar{1}}+\vec{k}_2)\tilde{G}_{\rho\mathcal{F}}(-k_{\bar{1}};t_{\bar{1}},t_2)\,,
\tag{4.55}
$$

The first equation (Eq. 4.53) provides an easy solution to $\tilde{\Delta}^{(1)}_{12}$ after one realises that it is almost identical to Eq. (B.5) in Lilow et al. (2019), i.e. the constraint equation for $\tilde{\Delta}_{\mathrm{R}}$. The only difference is in the order of the time arguments of the functions appearing under the integral and which are integrated over. Despite this difference, the result will be exactly the same as can be seen as follows. Recursively inserting the right-hand side of Eq. (4.53)

for $\tilde{\Delta}_{12}^{(1)}$ under the integral leads to a recursive series, which is a so called Neumann series. This leads to integrals of arbitrarily many factors of $\tilde{G}_{\rho\mathcal{F}}$. In this representation it becomes obvious that Eq. (4.53) is in fact identical to Eq. B.5 in Lilow et al. (2019) despite the different order of time variables under the integral. We therefore get

$$\underline{\tilde{\Delta}_{12}^{(1)}(k_1;t_1,t_2)} = \tilde{\Delta}_{\mathrm{R}}(k_1;t_1,t_2)\,, \tag{4.56}$$

where we can consider $\tilde{\Delta}_{\mathrm{R}}$ as known by adopting the results of Lilow et al. (2019).

We now continue with the third equation (Eq. 4.55), since it can be inserted into Eq. (4.54) to obtain a solution for $\tilde{\Delta}_{12}^{(2)}$. Also here we can obtain a simple form by identifying $\tilde{\Delta}_{\mathrm{R}}$ as shown in Appendix B.3. We end up with

$$\underline{\tilde{\Delta}_{12}^{(3)}(k_1,k_2;t_1,t_2;t)} = \underline{\tilde{\Delta}_{12}^{(2)}(k_1,k_2;t_1;t)}\,\tilde{\Delta}_{\mathrm{R}}(-k_2;t,t_2)\,. \tag{4.57}$$

We can obtain $\tilde{\Delta}_{12}^{(2)}$ by inserting Eqns. (4.56) and (4.57) into the second constraint equation (Eq. 4.54), which leads to

$$\begin{aligned}
\underline{\tilde{\Delta}_{12}^{(2)}(k_1,k_2;t_1;t)} = -\frac{1}{\sigma^2}\Bigg[& \underbrace{\tilde{G}_{\rho\rho}(k_1;t_1,t) + \int_{t_{\bar{1}'}} \tilde{G}_{\rho\rho}(k_1;t_1,t_{\bar{1}'})\left(\tilde{\Delta}_{\mathrm{A}}(k_1;t_{\bar{1}'},t) + \tilde{\Delta}_{\mathrm{R}}(k_1;t_1,t_{\bar{1}'})\right)\ldots}_{\ldots} \\
& \underbrace{+ \int_{t_{\bar{1}}}\int_{t_{\bar{1}'}} \tilde{\Delta}_{\mathrm{R}}(k_1;t_1,t_{\bar{1}})\tilde{G}_{\rho\rho}(k_1;t_{\bar{1}},t_{\bar{1}'})\tilde{\Delta}_{\mathrm{A}}(k_1;t_{\bar{1}'},t)\ \ldots}_{\ldots} \\
& \qquad\qquad =:\tilde{\Delta}_{\rho\rho}(k_1;t_1,t) \\
& + \int_{k_{\bar{1}}} \underline{\tilde{\Delta}_{12}^{(2)}(k_1,k_{\bar{1}};t_1;t)}\left[\tilde{G}_{\rho\rho}(-k_{\bar{1}};t,t) + \int_{t_{\bar{1}}} \tilde{G}_{\rho\rho}(-k_{\bar{1}};t,t_{\bar{1}})\tilde{\Delta}_{\mathrm{A}}(-k_{\bar{1}};t_{\bar{1}},t)\right]\ldots \\
& + \int_{k_{\bar{1}}}\int_{t_{\bar{1}}} \underline{\tilde{\Delta}_{12}^{(2)}(k_1,k_{\bar{1}};t_1;t)}\,\tilde{\Delta}_{\mathrm{R}}(-k_{\bar{1}};t,t_{\bar{1}})\left[\tilde{G}_{\rho\rho}(-k_{\bar{1}};t_{\bar{1}},t) + \int_{t_{\bar{1}'}} \tilde{G}_{\rho\rho}(-k_{\bar{1}};t_{\bar{1}},t_{\bar{1}'})\tilde{\Delta}_{\mathrm{A}}(-k_{\bar{1}};t_{\bar{1}'},t)\right]\Bigg]\,.
\end{aligned} \tag{4.58}$$

Also here we can identify an expression that occurred already in Lilow et al. (2019). The first three terms in the bracket correspond to the density-density propagator $\Delta_{\rho\rho}$, defined for the phase space density f in Eq. (B.11) of Lilow et al. (2019), where the tilde signals that the δ_{D}-distribution has been factored out. We furthermore see that the right-hand side of the equation does not depend on k_2. Therefore, $\tilde{\Delta}_{12}^{(2)}$ cannot depend on k_2 either, which we drop from now on,

$$\underline{\tilde{\Delta}_{12}^{(2)}(k_1,k_2;t_1;t)} \equiv \underline{\tilde{\Delta}_{12}^{(2)}(k_1;t_1;t)}\,. \tag{4.59}$$

This allows us to pull $\tilde{\Delta}^{(2)}_{12}$ out of those integrals where the second k-argument is the integration variable,

$$\begin{aligned}\underline{\underline{\tilde{\Delta}^{(2)}_{12}}}(k_1;t_1;t) = -\frac{1}{\sigma^2}\Bigg[\tilde{\Delta}_{\rho\rho}(k_1;t_1,t) + \underline{\underline{\tilde{\Delta}^{(2)}_{12}}}(k_1;t_1;t)\int_{k_{\bar{1}}}\Bigg[\tilde{G}_{\rho\rho}(-k_{\bar{1}};t,t)\ \ldots \\ + \int_{t_{\bar{1}}}\tilde{G}_{\rho\rho}(-k_{\bar{1}};t,t_{\bar{1}})\left(\tilde{\Delta}_{\mathrm{A}}(-k_{\bar{1}};t_{\bar{1}},t) + \tilde{\Delta}_{\mathrm{R}}(-k_{\bar{1}};t,t_{\bar{1}})\right)\ldots \\ + \int_{t_{\bar{1}}}\int_{t_{\bar{1}'}}\tilde{\Delta}_{\mathrm{R}}(-k_{\bar{1}};t,t_{\bar{1}})\tilde{G}_{\rho\rho}(-k_{\bar{1}};t_{\bar{1}},t_{\bar{1}'})\tilde{\Delta}_{\mathrm{A}}(-k_{\bar{1}};t_{\bar{1}'},t)\Bigg]\Bigg] \\ = -\frac{1}{\sigma^2}\left[\tilde{\Delta}_{\rho\rho}(k_1;t_1,t) + \underline{\underline{\tilde{\Delta}^{(2)}_{12}}}(k_1;t_1;t)\int_{k_{\bar{1}}}\tilde{\Delta}_{\rho\rho}(-k_{\bar{1}};t,t)\right],\end{aligned} \tag{4.60}$$

where we used in the second step that we can write the bracket as well as $\tilde{\Delta}_{\rho\rho}$. We now solve the equation for $\tilde{\Delta}^{(2)}_{12}$ and obtain

$$\begin{aligned}\underline{\underline{\tilde{\Delta}^{(2)}_{12}}}(k_1;t_1;t) &= -\frac{1}{\sigma^2}\tilde{\Delta}_{\rho\rho}(k_1;t_1,t)\left(1 + \frac{1}{\sigma^2}\int_{k_{\bar{1}}}\tilde{\Delta}_{\rho\rho}(-k_{\bar{1}};t,t)\right)^{-1} \\ &= -\tilde{\Delta}_{\rho\rho}(k_1;t_1,t)\left(\sigma^2 + \int_{k_{\bar{1}}}\tilde{\Delta}_{\rho\rho}(-k_{\bar{1}};t,t)\right)^{-1}.\end{aligned} \tag{4.61}$$

According to its definition in Lilow et al. (2019), the density-density propagator $\Delta_{\rho\rho}(1,2) = (2\pi)^3\delta_{\mathrm{D}}(\vec{k}_1+\vec{k}_2)\tilde{\Delta}_{\rho\rho k_1;t_1,t_2)}$ corresponds to the 2-point density cumulant, however without terms involving vertices. Integrating $\tilde{\Delta}_{\rho\rho}$ over all k-values therefore results in a linearly evolved density variance[5], which we define as $\sigma^2_{\mathrm{lin}} := \int_{k_{\bar{1}}}\tilde{\Delta}_{\rho\rho}(k_{\bar{1}};t,t)$. Hence, we obtain the result

$$\underline{\underline{\tilde{\Delta}^{(2)}_{12}}}(k_1;t_1;t) = -\frac{1}{\sigma^2+\sigma^2_{\mathrm{lin}}}\tilde{\Delta}_{\rho\rho}(k_1;t_1,t)\,. \tag{4.62}$$

We have now determined all three of the component functions and, taking the results for $\tilde{\Delta}_{\mathrm{R}}$ and $\tilde{\Delta}_{\rho\rho}$ from Lilow et al. (2019), we obtain a solution for Δ_{12}.

(*ii*) *Calculating* Δ_{21}:

The solution for Δ_{12} leaves us at the same time with a simple result for Δ_{21}, realising that Δ_{21} is simply the transposed of Δ_{12}, i.e. interchanging first and second argument.

5 In general, the integral over $\tilde{\Delta}_{\rho\rho}$ does not correspond exactly to the linearly evolved density variance, since the free $G_{\rho\rho}$-cumulants contain also non-linear $P^{(\mathrm{i})}_{\delta}$-terms. However, this deviation should be very small. Since we employ an approximation of $G_{\rho\rho}$ up to linear order in $P^{(\mathrm{i})}{}_{\delta}$ (c.f. Eq. 3.72), it is in our case exactly the linear variance.

This is because Δ_{12} and Δ_{21} take a role similar to the advanced propagator Δ_A and the retarded Δ_R in Lilow et al. (2019), which are related by exchanging their first and second arguments. We can therefore directly express Δ_{21} as

$$\Delta_{21}(1,2) = \Delta_{12}^\mathrm{T}(1,2) = \Delta_{12}(2,1)\,. \tag{4.63}$$

(*iii*) *Calculating* Δ_{11}:

We start with Eq. (4.41) and identify the inverse of the bracket with Δ_{21}, which leads to

$$\Delta_{11}(1,2) = -C^{-1}(1,\bar{1})\cdot D(-\bar{1},\bar{1}')\cdot\Delta_{21}(-\bar{1}',2)\,. \tag{4.64}$$

Furthermore, we can identify C^{-1} with the definition of the retarded propagator Δ_R from Lilow et al. (2019), as it was done above analogously for B^{-1} with the advanced propagator. The only difference between B and C is the order of the arguments, since $\mathcal{F}$ and ρ are interchanged in the cumulant. This is the reason why now the retarded propagator Δ_R is involved. We can therefore write

$$C^{-1}(-\bar{1}',\bar{1}'') = -\mathrm{i}\left[\mathcal{I} - \mathrm{i}G_{\rho\mathcal{F}}\right]^{-1}(-\bar{1}',\bar{1}'') = -\mathrm{i}\Delta_\mathrm{R}(-\bar{1}',\bar{1}'') \tag{4.65}$$

$$= -\mathrm{i}\left(\mathcal{I}(-\bar{1}',\bar{1}'') + (2\pi)^3\delta_\mathrm{D}(-\vec{k}_{\bar{1}'}+\vec{k}_{\bar{1}''})\tilde{\Delta}_\mathrm{R}(-k_{\bar{1}'};t_{\bar{1}'},t_{\bar{1}''})\right)\,. \tag{4.66}$$

Inserting this result together with D (Eq. 4.38) and Δ_{21} (Eq. 4.63) into Eq. (4.64) leads to

$$\begin{aligned}\Delta_{11}(1,2) = \int_{t_{\bar{1}}}\Big[&\left(\delta_\mathrm{D}(t_{\bar{1}}-t_1)+\tilde{\Delta}_\mathrm{R}(k_1;t_1,t_{\bar{1}})\right)\Big((2\pi)^3\delta_\mathrm{D}(\vec{k}_1+\vec{k}_2)\tilde{G}_{\rho\rho}(k_2;t_{\bar{1}},t_2)\ldots\\
&+(2\pi)^3\delta_\mathrm{D}(\vec{k}_1+\vec{k}_2)\int_{t_{\bar{1}'}}\tilde{G}_{\rho\rho}(k_2;t_{\bar{1}},t_{\bar{1}'})\tilde{\Delta}_{12}^{(1)}(k_2;t_2,t_{\bar{1}'})\ldots\\
&+\tilde{G}_{\rho\rho}(-k_1;t_{\bar{1}},t)\tilde{\Delta}_{12}^{(2)}(k_2,k_1;t_2;t)+\int_{t_{\bar{1}'}}\tilde{G}_{\rho\rho}(-k_1;t_{\bar{1}},t_{\bar{1}'})\tilde{\Delta}_{12}^{(3)}(k_2,k_1;t_2,t_{\bar{1}'};t)\Big)\Big]\,,\end{aligned} \tag{4.67}$$

where the integrations have been carried out already. The detailed steps are shown in Appendix B.4.

(*iv*) *Calculating* Δ_{22}:

Finally, we can obtain Δ_{22} in a similar way from Eq. (4.44), leading to

$$\Delta_{22}(1,2) = -B^{-1}(1,\bar{1})\cdot A(-\bar{1},\bar{1}')\cdot\Delta_{12}(-\bar{1}',2)\,, \tag{4.68}$$

where we have identified the inverse of the bracket with Δ_{12}. We can again use the solution for B^{-1} from Lilow et al. (2019), i.e. Eq. (4.51), and insert A (Eq. 4.38) as well as Δ_{21} (Eq. 4.42) to obtain

$$\Delta_{22}(1,2) = \frac{\delta_\mathrm{D}(t_1-t)+\tilde{\Delta}_\mathrm{A}(k_1;t_1,t)}{\sigma^2}\left[\delta_\mathrm{D}(t_2-t)+\tilde{\Delta}_{12}^{(1)}(-k_2;t,t_2)\ldots\right.$$
$$\left.+\delta_\mathrm{D}(t_2-t)\int_{k_{\bar{1}'}}\tilde{\Delta}_{12}^{(2)}(-k_{\bar{1}'},k_2;t;t)+\int_{k_{\bar{1}'}}\tilde{\Delta}_{12}^{(3)}(-k_{\bar{1}'},k_2;t,t_2;t)\right]. \tag{4.69}$$

Also here we have carried out the integrations where possible. The details of the calculation can be found in Appendix B.5.

4.3.2 *Calculating the PDF*

This puts us in the position to actually calculate the PDF as given in Eq. (4.31) by inserting our results for the one-point vertex $\mathcal{V}$ and the propagator Δ. The one-point distribution can then be calculated as

$$\begin{aligned}P(\tilde{\rho})\Delta\tilde{\rho} &= \tilde{\mathcal{N}}\, e^{-\frac{\tilde{\rho}^2}{2\sigma^2}+\frac{1}{2}\mathcal{V}\cdot\Delta\cdot\mathcal{V}}\\ &= \tilde{\mathcal{N}}\,\exp\left[-\frac{\tilde{\rho}^2}{2\sigma^2}+\frac{1}{2}\left(\mathcal{V}_1\cdot\Delta_{11}\cdot\mathcal{V}_1+\mathcal{V}_2\cdot\Delta_{21}\cdot\mathcal{V}_1+\mathcal{V}_1\cdot\Delta_{12}\cdot\mathcal{V}_2+\mathcal{V}_2\cdot\Delta_{22}\cdot\mathcal{V}_2\right)\right]\\ &=: \tilde{\mathcal{N}}\,\exp\left[-\frac{\tilde{\rho}^2}{2\sigma^2}+\frac{1}{2}\left(\mathrm{I}+\mathrm{II}+\mathrm{III}-\mathrm{IV}\right)\right].\end{aligned} \tag{4.70}$$

Since the steps to carry out the dot products for each of the terms I to IV do not bear any deeper insights but involve only straightforward calculus, we will give just the final results here and refer the reader to Appendix B.6 for the details. We obtain

$$\mathrm{I} = \frac{\tilde{\rho}^2\sigma_\mathrm{lin}^2}{\sigma^4}\frac{\sigma^2}{\sigma^2+\sigma_\mathrm{lin}^2}, \tag{4.71}$$

$$\mathrm{II} = \frac{\tilde{\rho}\bar{\rho}}{\sigma^2}\frac{\sigma^2}{\sigma^2+\sigma_\mathrm{lin}^2}, \tag{4.72}$$

$$\mathrm{III} = \mathrm{II}, \tag{4.73}$$

$$\mathrm{IV} = \frac{\bar{\rho}^2}{\sigma^2}\frac{\sigma^2}{\sigma^2+\sigma_\mathrm{lin}^2}. \tag{4.74}$$

Inserting these into Eq. (4.70) gives

$$\begin{aligned} P(\tilde{\rho})\Delta\tilde{\rho} &= \tilde{\mathcal{N}} \exp\left[-\frac{\tilde{\rho}^2}{2\sigma^2} + \frac{1}{2}\left(\frac{\tilde{\rho}^2}{\sigma^4}\sigma_{\rm lin}^2 + 2\frac{\tilde{\rho}\bar{\rho}}{\sigma^2} - \frac{\bar{\rho}^2}{\sigma^2}\right)\frac{\sigma^2}{\sigma^2+\sigma_{\rm lin}^2}\right] \\ &= \tilde{\mathcal{N}} \exp\left[\frac{1}{2}\left(-\frac{\tilde{\rho}^2}{\sigma^2} + 2\frac{\tilde{\rho}\bar{\rho}}{\sigma^2} - \frac{\bar{\rho}^2}{\sigma^2}\right)\frac{\sigma^2}{\sigma^2+\sigma_{\rm lin}^2}\right] \\ &= \tilde{\mathcal{N}} \exp\left[-\frac{(\tilde{\rho}-\bar{\rho})^2}{\sigma^2+\sigma_{\rm lin}^2}\right]. \end{aligned} \tag{4.75}$$

This form already represents a Gaussian distribution as expected from a second-order approximation. However, we can go one step beyond and evaluate the PDF in the limit of vanishing width of the indicator function ($\sigma \to 0$). We are then left with the Gaussian approximation of the PDF itself and eliminated the influence of the indicator function,

$$P(\tilde{\rho})\mathrm{d}\tilde{\rho} = \lim_{\sigma\to 0} P(\tilde{\rho})\Delta\tilde{\rho} = \tilde{\mathcal{N}} \exp\left[-\frac{(\tilde{\rho}-\bar{\rho})^2}{\sigma_{\rm lin}^2}\right]. \tag{4.76}$$

We thus indeed managed to obtain a Gaussian distribution. This is of course the expected result, since we required a quadratic form of the exponent of the generating functional in order to be able to solve the path integral in Eq. (4.28).

This result is of course not useful when one wishes to calculate the non-linear cosmic density field. As we argued above, the present day density field is indeed non-Gaussian. However, the exercise shown above can be interpreted as a first step. We succeeded in deriving a PDF from the generating functional using an indicator function and the result matches the expectations. It therefore represents an encouraging first result from which we can proceed towards deriving a non-Gaussian PDF from the generating functional.

4.4 BEYOND QUADRATIC APPROXIMATIONS

In the next step, we extend this approach by expanding the generating functional beyond second order. This, however, leads to the problem that the path integral in Eq. (4.31) cannot be solved in a straightforward manner, since it is not a Gaussian integral any longer. This problem is also known from QFT, where a frequently used solution is to approximate the path integral by an effective action (see e.g. Weigand, 2013; Ch. 11.3 in Peskin and Schroeder, 1997). In this section, it is our aim to explore if a similar approach can be applied in our case as well.

In the spirit of its definition in QFT, we define the *effective logarithmic generating functional* W as the logarithmic generating functional that contains the information of the path integral

$$P(\tilde{\rho})\Delta\tilde{\rho} = \mathcal{N}e^{W[\mathcal{V}_1]} := \mathcal{N}\int \mathcal{D}\phi\; e^{\mathrm{i}S_\phi} \tag{4.77}$$

and it is a functional of our source fields $\mathcal{V}_1$ only[6]. However, it is usually more convenient to use instead of $W[\mathcal{V}_1]$ its Legendre transform (or rather the Legendre transform of $-\mathrm{i}W[\mathcal{V}_1]$)[7], which is called the *effective action*. The Legendre transform is a functional of $-\mathrm{i}\frac{\delta W}{\delta \mathcal{V}_1}$, which is the expectation value of ϕ while the sources are still present, i.e.

$$-\mathrm{i}\frac{\delta W}{\delta \mathcal{V}_1} = \frac{\int \mathcal{D}\phi\; \phi\; e^{\mathrm{i}S_\phi}}{\int \mathcal{D}\phi\; e^{\mathrm{i}S_\phi}} =: \bar{\phi}\,. \tag{4.78}$$

Performing the Legendre transformation and multiplying with i, we obtain the effective action as

$$\mathrm{i}\Gamma[\bar{\phi}] = W[\mathcal{V}_1[\bar{\phi}]] - \mathrm{i}\mathcal{V}_1\cdot\bar{\phi}\,. \tag{4.79}$$

However, since calculating $\bar{\phi}$ also requires solving the path integral, it poses the same problem as calculating $P(\tilde{\rho})$ directly. We will therefore express the expectation value of ϕ by its lowest-order approximation

$$\bar{\phi} \approx \Delta\cdot\mathcal{V}_1\,. \tag{4.80}$$

Since we are not interested in the effective action, but in W expressed in terms of $\bar{\phi}$, we will reformulate Eq. (4.79) as $W[\mathcal{V}_1[\bar{\phi}]] = \mathrm{i}\Gamma[\bar{\phi}] + \mathrm{i}\mathcal{V}_1\cdot\bar{\phi}$. Hence, we can calculate the probability distribution of $\tilde{\rho}$ as

$$P(\tilde{\rho})\Delta\tilde{\rho} = e^{W[\mathcal{V}_1[\bar{\phi}]]}\,. \tag{4.81}$$

We will neglect any loops and take the effective action at tree-level,

$$\Gamma[\bar{\phi}] \approx S_\phi|_{\phi=\bar{\phi}}\,. \tag{4.82}$$

6 W can be seen as the generating functional of connected correlation functions, see e.g. Peskin and Schroeder (1997) p. 380.

7 This is due to the fact that in our notation a factor i has been absorbed into W to make the connection to statistical physics more obvious. However, in the standard QFT formalism the i is usually factored out. We therefore have to perform the Legendre transformation of $-\mathrm{i}W[\mathcal{V}_1]$.

Combining Eqns. (4.78), (4.79) and (4.82) leads to

$$
\begin{aligned}
W[\bar{\phi}] &\approx \mathrm{i}S_{\phi}|_{\phi=\bar{\phi}} + \mathrm{i}\mathcal{V}_1 \cdot \bar{\phi} \\
&\approx \Bigg[-\mathrm{i}\mathcal{V}_1 \cdot \phi - \frac{1}{2}\phi \cdot \Delta^{-1} \cdot \phi - \mathrm{i}\left(\frac{1}{3!}\phi_\beta \cdot \phi_\beta \cdot \phi_\beta \cdot G_{\rho\rho\rho} + \frac{1}{2}\phi_\beta \cdot \phi_\beta \cdot \phi_\rho \cdot G_{\rho\rho\mathcal{F}} \ldots \right. \\
&\qquad \left. + \frac{1}{2}\phi_\beta \cdot \phi_\rho \cdot \phi_\rho \cdot G_{\rho\mathcal{F}\mathcal{F}} + \frac{1}{3!}\phi_\rho \cdot \phi_\rho \cdot \phi_\rho \cdot \underbrace{G_{\mathcal{F}\mathcal{F}\mathcal{F}}}_{=0} \right) \Bigg] \Bigg|_{\phi=\bar{\phi}} + \mathrm{i}\mathcal{V}_1 \cdot \bar{\phi}\,,
\end{aligned}
\tag{4.83}
$$

where we have approximated W_0 up to third order in the second step, introducing the 3-point cumulants which are explicitly given in Appendix A.

Unfortunately, it quickly turns out that this approach does not lead to sensible results. Inserting Eq. (4.83) into Eq. (4.81) shows that the odd orders will lead to a diverging PDF. For negative values of δ, the exponent becomes positive and grows therefore exponentially. Hence, the PDF is not normalisable. These findings are in line with Sellentin (2015), where the same result was obtained in the context of likelihood estimations. As pointed out by Sellentin (2015), this problem arises due to the slow convergence of the Taylor expansion of the logarithm, since we expand the logarithmic generating functional W. They state further that an expansion well beyond the fourth order would be needed in order to expect the PDF to be normalisable. Considering that already the third cumulants can only be obtained as a rough first-order approximation, an approximation in terms of sixth-, seventh- or higher-order cumulants does not seem feasible at this stage. Furthermore, Carron and Neyrinck (2012) suggest that even the full hierarchy of correlation functions could be insufficient to describe a correlated lognormal field due to the long tail of the lognormal distribution. This would imply that also the analogous description after marginalising over all other points, i.e. describing the one-point distribution in terms of all cumulants, would not be unique for a long-tailed distribution.

4.5 LARGE DEVIATION PRINCIPLE

For this reason, we would like to sketch an alternative approach here, which is based on the large deviation principle. As shown in the review by Touchette (2009), the large deviation principle can be connected to statistical physics. This allows identifying the SCGF with the Helmholtz free energy times the scaling parameter N. Since also KFT has a deep link to statistical physics, e.g. the generating functional fulfils the same role as a partition sum, it seems plausible to find a connection of KFT with the large deviation principle. If it is possible to find a rate function from KFT, this would then allow obtaining an asymptotic description of the density PDF.

As is known from quantum field theory, the Schwinger functional (i.e. the logarithm of the generating functional[8]) takes the same role as the Helmholtz free energy (see Peskin and Schroeder, 1997, p. 365) and it therefore also corresponds to the SCGF divided by the particle number φ/N. The rate function is connected to the SCGF by a Legendre-Fenchel transformation and the Legendre-Fenchel transformation of the Schwinger functional results in an effective action Γ (times a factor of i due to the definition of the Schwinger functional in KFT). This finally gives us the link between the rate function and the effective action

$$N\psi = \mathrm{i}\Gamma\,. \tag{4.84}$$

We would like to emphasise that in this section we turn away from the RKFT formulation used in the previous sections and base our considerations on the formulation of the generating functional derived in Eq. (3.27).[9] A recent calculation by Schmidt (2020) has shown that an effective action for the KFT generating functional can be written as

$$\begin{aligned}\Gamma[X,\tilde{\phi}] &= W_0 + W_K - J\cdot X - K\cdot\tilde{\phi}\\ &= \tilde{\phi}\cdot G^{-1}\cdot X - \mathrm{i}\ln\int \mathrm{d}q\exp\left[-\frac{1}{2}\tilde{\phi}_p(0)C_{pp}(q)\tilde{\phi}_p(0) - \mathrm{i}\left\langle\tilde{\phi}_q(0),q\right\rangle\right]\,,\end{aligned} \tag{4.85}$$

where the first equality simply reproduces the definition of the effective action as the Legendre transform of the Schwinger functional $W = -\mathrm{i}\ln Z[J,K]$ with respect to the phase space-position source field J and the response source field K. This implies the definition of the Legendre conjugate variables as

$$\tilde{\phi} := \frac{\delta W}{\delta K} = \langle\chi\rangle\,, \tag{4.86}$$

$$X := \frac{\delta W}{\delta J} = \langle x\rangle\,, \tag{4.87}$$

which both correspond to macroscopic fields in the sense that both the initial phase-space coordinates and the final field configurations have been integrated out. It implies furthermore that the effective action Γ contains corrections to the action S appearing inside the generating functional (Eq. 3.22), since the fluctuations of the initial conditions have been taken into account by performing the integral. The second line of Eq. (4.85) is the effective action derived by Schmidt (2020), which includes the matrix of initial momentum correlations C_{pp} (see Eq. 3.38). Note that we furthermore added a tilde to the Legendre conjugate to J, i.e. $\tilde{\phi}$, in contrast to the original ϕ used in Schmidt (2020), since we already used ϕ to denote the macroscopic fields in the previous sections.

It is now our aim to extract the rate function from

$$\mathrm{i}\Gamma[X,\tilde{\phi}] = \mathrm{i}\tilde{\phi}\cdot G^{-1}\cdot X + \ln\int \mathrm{d}q\exp\left[-\frac{1}{2}\tilde{\phi}_p(0)C_{pp}(q)\tilde{\phi}_p(0) - \mathrm{i}\left\langle\tilde{\phi}_q(0),q\right\rangle\right]\,. \tag{4.88}$$

8 in some cases up to a prefactor of i or $-\mathrm{i}$

9 Note that the form of the generating functional used in Schmidt (2020) also uses the approximation $\mathcal{C}\approx 1$; see also the discussion in the paragraph below Eq. (3.36).

To do so, we need to identify a scaling $i\Gamma \propto N$, which would then allow us to determine the rate function ψ by comparing with Eq. (4.84). We will ignore the first term, $i\tilde{\phi} \cdot G^{-1} \cdot X$, since it should be purely imaginary and thus just adds a phase, which should average out while $N \to \infty$.[10] Instead we consider the second term, but can only sketch a potential route to extract the rate function from it. Since C_{pp} is symmetric, positive definite and real, we know that it can be diagonalised with an orthogonal matrix $R \in \mathrm{SO}(3N)$ and has real eigenvalues. For $N = 2$, these eigenvalues are

$$\lambda_i = \frac{\sigma_1^2}{3} \pm \begin{cases} \frac{\zeta'_\Psi(q)}{q} \\ \zeta''_\Psi(q) \end{cases}, \qquad \text{with } i \in [1,6]\,. \tag{4.89}$$

The eigenvalues depending on $\frac{\zeta'_\Psi(q)}{q}$ have multiplicity two, while those depending on $\zeta''_\Psi(q)$ multiplicity one as stated in Linke (2017). Applying the orthogonal matrix R, however, will also rotate the vectors $\tilde{\phi}_p(0)$, which results in $\tilde{\phi}'_p(0) = R\tilde{\phi}_p(0)$. These will be the arguments of our rate function in the end. We write the diagonalised C_{pp} matrix as

$$\Lambda := R^{-1} C_{pp} R = \mathrm{diag}(\lambda_1, ..., \lambda_{3N})\,, \tag{4.90}$$

which leads to

$$i\Gamma[X, \tilde{\phi}'] = \ln \int \mathrm{d}q \exp\left[-\frac{1}{2}\tilde{\phi}'_p(0)\Lambda(q)\tilde{\phi}'_p(0) - i\left\langle \tilde{\phi}_q(0), q\right\rangle\right] \tag{4.91}$$

$$= \ln \int \mathrm{d}q \exp\left[-\frac{1}{2}\sum_{i=1}^{3N} \tilde{\phi}'_{p_i}(0)\lambda_i(q)\tilde{\phi}'_{p_i}(0) - i\left\langle \tilde{\phi}_q(0), q\right\rangle\right]. \tag{4.92}$$

If we could now solve the integral by a saddle-point approximation and ignore the second imaginary term, we would end up with

$$i\Gamma[X, \tilde{\phi}] \approx \ln \exp\left[-\frac{1}{2}\sum_{i=1}^{3N} \tilde{\phi}'_{p_i}(0)\tilde{\lambda}_i\tilde{\phi}'_{p_i}(0)\right], \tag{4.93}$$

where $\tilde{\lambda}_i = \inf_{q_i} \lambda(q_i)$. Since we are interested in the limit $N \to \infty$, we furthermore approximate the sum via the average $\left\langle \tilde{\lambda}_i \right\rangle_{i\in[1,3N]}$ and arrive at

$$i\Gamma[X, \tilde{\phi}] \approx -\frac{3N}{2}\tilde{\phi}'_{p_i}(0)\left\langle \tilde{\lambda}_i \right\rangle_{i\in[1,3N]} \tilde{\phi}'_{p_i}(0)\,, \tag{4.94}$$

where we can set $\phi'_{p_i}(0) =: k$, since it corresponds to a wave number and it is the argument of our rate function. This leaves us with the rate function

$$\psi(k) = -\frac{3}{2}k^2 \left\langle \tilde{\lambda}_i \right\rangle_{i\in[1,3N]}. \tag{4.95}$$

This, however, should merely sketch the idea rather than present a rigorous deduction, since it is unclear at the moment how the $\left\langle \tilde{\lambda}_i \right\rangle_{i\in[1,3N]}$ could be obtained. We leave this calculation for further investigation.

10 Note that $\tilde{\phi}$ and X are vectors with $6N$ entries and G^{-1} is a $6N \times 6N$-matrix, so $\tilde{\phi} \cdot G^{-1} \cdot X$ consists of $(6N)^2$ terms.

5 THE HALO MASS FUNCTION

Every reasonably comprehensive cosmological model must be equipped with a theory of the formation and evolution of structures and objects within the Universe. This theory should be able to predict the abundance of cosmological objects (i.e. dark matter haloes) at a given time, which then can be tested against observations. This can be seen as a test of both the underlying cosmological model and the method used to predict the number of objects in the Universe. One of these testable predictions for the abundance of cosmological objects is provided by the *halo mass function*, which describes the comoving number density of dark matter haloes with a given mass M at redshift z. The limitation of this function to dark matter haloes makes the theoretical description much easier and therefore especially the high mass end of the halo mass function is of interest, where baryonic effects can be neglected (see also Castro et al., 2020).

In this chapter, we will give a short overview of the most important results for the calculation of the halo mass function. We will confine this summary to only those works which will be important for our new approach in the next chapter. We will introduce the pioneering work of Press and Schechter (1974) and Bond et al. (1991), who extended the Press-Schechter ansatz by combining it with random walk statistics. In this context, we will also need the results of the spherical collapse model. We end this chapter with a critical discussion of the (extended) Press-Schechter (PS) approach. We will list several shortcomings as a motivation for our approach and we will briefly summarise some alternative ideas presented in other works.

5.1 THE ASSUMPTIONS OF THE PRESS-SCHECHTER APPROACH

The first ansatz for an analytic prediction of the halo mass function was proposed by Press and Schechter (1974). It builds essentially on three ideas (see e.g. Zentner, 2007 and Desjacques et al., 2018 for nicely written, extended reviews):

(*i*) the origin of today's haloes can already be found in the density field at reasonably early times,

(*ii*) the evolution of these regions can be extrapolated linearly to define a criterion determining if this region will collapse to form a halo and

(*iii*) the threshold used to define this criterion can be calculated using spherical collapse.

The first assumption, working on the level of the initial density field, provides the advantage that it can be described as a Gaussian random field[1]. The restriction to linear theory only (i.e. assumption (*ii*)) assures that the field stays Gaussian, since linear transformations leave the Gaussian property unchanged. Working with a Gaussian random field makes the analytical calculation way easier and allows the derivation of a closed form halo mass function. The assumption of linear evolution might seem misplaced, since the interiors of clusters are highly non-linear (see discussion of the applicability of linear evolution in Section 2.3). However, it is assumed here that in particular the field smoothed over *large scales* will be decisive if the halo collapses or not. It is assumed that the field at these scales can be reasonably well described by linear theory. The Press-Schechter approach therefore neglects what the interior of the halo looks like, which is governed by highly non-linear processes. The third assumption, finally, is needed to be able to find a numerical value for the threshold that identifies collapsing regions. We will comment on the scope of validity of these assumptions in Section 5.5.

5.2 SPHERICAL COLLAPSE

The PS approach is founded on the idea that only those regions in space can form collapsed objects whose densities are high enough, i.e. that exceed a critical density δ_c. Therefore, haloes can be identified in the smoothed density field by searching for such regions. One possible threshold can be derived on the basis of spherical collapse in combination with linear perturbation theory (Gunn and Gott, 1972; Peebles, 1980). Let us consider a sphere of radius R and mass M. Its evolution is governed exclusively by its interior (see e.g. *Birkhoff's theorem* or Einstein and Straus, 1946). Due to this decoupling from the cosmological background, we can approximate the evolution of the sphere by Newtonian gravity (see e.g. Peebles, 1980, pp. 79 or Weinberg, 2008, Section 11.7 for a detailed derivation). The equation of motion for a test particle at radius R is then given by

$$\frac{\mathrm{d}^2 R}{\mathrm{d}t^2} = -\frac{GM}{R^2}\,, \tag{5.1}$$

where M is the mass enclosed of the sphere with radius R. Integrating once yields

$$\frac{1}{2}\left(\frac{\mathrm{d}R}{\mathrm{d}t}\right)^2 - \frac{GM}{R} = \mathcal{E}, \tag{5.2}$$

1 Primordial non-Gaussianities are measured to be small enough that they can be neglected for our purposes at early times like e.g. $z \approx 1000$ (Planck Collaboration, 2020a).

with the energy per unit mass $\mathcal{E}$. Considering the gravitationally bound case ($\mathcal{E} < 0$), this equation has the following parametric solution.

$$R = A(1 - \cos\theta), \qquad \text{with} \quad A = \frac{GM}{2|\mathcal{E}|}, \tag{5.3}$$

$$t = B(\theta - \sin\theta), \qquad \text{with} \quad B = \frac{GM}{(2|\mathcal{E}|)^{3/2}}. \tag{5.4}$$

The parameter θ describes the time evolution and runs from $\theta = 0$ (i.e. $t_{\rm ini} = 0$ and $R_{\rm ini} = 0$) to 2π, where the sphere collapsed again to a point (i.e. $t_{\rm coll} = 2\pi B$ and $R_{\rm coll} = 0$). At half of the collapse time or equally at $\theta = \pi$, the radius reaches its maximum, which is called the turn-around point (i.e. $t_{\rm ta} = t_{\rm coll}/2 = \pi B$ and $R_{\rm ta} = 2A$).

Since we are interested in the time evolution of the halo's density contrast, we can use mass conservation in order to express the density in terms of our parametric solution

$$\rho = \frac{M}{4\pi/3R^3} = \frac{3M}{4\pi}\frac{1}{A^3(1-\cos\theta)^3}. \tag{5.5}$$

To obtain the density contrast, we have to consider that the mean matter density changes with time as well. Using Eq. (2.11) and that $H = 2/3t$ for an Einstein-de Sitter (EdS) universe ($\Omega_{\rm m0} = 1$), we get

$$\bar{\rho} = \frac{3H^2}{8\pi G} = \frac{1}{6\pi G t^2} = \frac{1}{6\pi G}\frac{1}{B^2(\theta - \sin\theta)^2}. \tag{5.6}$$

The evolution of the density contrast δ as predicted by the spherical collapse model is then given by

$$1 + \delta = \frac{\rho}{\bar{\rho}} = \frac{9}{2}\frac{(\theta - \sin\theta)^2}{(1-\cos\theta)^3}. \tag{5.7}$$

This description breaks down of course for late times, since the spherical collapse model predicts the sphere to collapse to a single point and the density to become infinite. We therefore use linear perturbation theory instead to predict the density evolution, while combining it with spherical collapse result for the collapse time $t_{\rm coll}$. We assume that the lowest order Taylor expansion of Eqns. (5.4) and (5.7) can be extrapolated to the times where the spherical collapse equations themselves would lead to unphysical results.[2] This approach is furthermore justified by the fact that the result (Eq. 5.10) corresponds

2 Also the linear prediction leads of course to a result for $\delta_{\rm c}$ that is way lower than the real overdensity of a collapsed halo. We will discuss the effects of virialisation and the calculation of a more physical collapse overdensity below. The linear result, however, is important, since the Press-Schechter approach is based on the *linearly* evolved density field.

precisely to the result obtained by linear perturbation theory. The Taylor expansions to lowest order give

$$1 + \delta = 1 + \frac{3}{20}\theta^2 + \mathcal{O}(\theta^4)\,, \tag{5.8}$$

$$t = \frac{B}{6}\theta^3 + \mathcal{O}(\theta^5)\,. \tag{5.9}$$

Solving Eq. (5.9) for θ and plugging it into Eq. (5.8) gives

$$\delta(t) = \frac{3}{20}(6\pi)^{2/3}\left(\frac{t}{t_{\rm ta}}\right)^{2/3}\,, \tag{5.10}$$

where we used $t_{\rm ta} = \pi B$ and that turn-around happens at $\theta = \pi$. This reproduces the result known from linear perturbation for the EdS model (i.e. $\delta_{\rm EdS} \propto t^{2/3}$). Plugging the collapse time from the spherical model ($t_{\rm coll} \equiv t(\theta = 2\pi) = 2t_{\rm ta}$) into Eq. (5.10) gives for the overdensity of a collapsed halo as predicted by *linear* theory (Bardeen et al., 1986)

$$\delta_{\rm c} = \frac{3}{5}\left(\frac{3\pi}{2}\right)^{2/3} \approx 1.686\,. \tag{5.11}$$

As mentioned above, we have assumed an EdS universe in the derivation of this value. There exist also more general versions of Eq. (5.11) that calculate $\delta_{\rm c}$ depending on the cosmological parameters (Lahav et al., 1991; Lacey and Cole, 1993; Mo et al., 2011). Since the dependence of $\delta_{\rm c}$ on $\Omega_{\rm m}$ and Ω_Λ is found to be weak, the value $\delta_{\rm c} = 1.686$ is typically used for ΛCDM universes nevertheless.

A more realistic value for the overdensity of collapsed haloes can be obtained by considering spherical collapse without linear perturbation theory, but assuming that the halo is virialised when the halo collapsed to half of the value at turn-around[3], $R_{\rm vir} = R_{\rm ta}/2$. Solving Eq. (5.3) for the cosine term, we obtain $1 - \cos\theta = 1$. Since the sine term, however, parameterises the time evolution and we assume the virialisation still to happen at $t_{\rm vir} = 2t_{\rm ta}$, we obtain with Eq. (5.4) that $(\theta - \sin\theta)^2 = (2\pi)^2$. Inserting both into Eq. (5.7) leads to

$$1 + \Delta_{\rm vir} = \frac{9}{2}(2\pi)^2 \approx 178\,. \tag{5.12}$$

Due to the number of simplifying assumptions made on the way towards this result, it can only give a rough estimate for the overdensity of real haloes. In order to reflect the lack of accuracy, this value is usually set to $\Delta_{\rm vir} = 200$.

3 The virial theorem predicts $E = T + V = V(R_{\rm vir})/2$, with kinetic energy $T = -V(R_{\rm vir})/2$ and potential energy V. At turn-around $T = 0$ and therefore $E = V(R_{\rm ta})$, which leads to $R_{\rm vir} = R_{\rm ta}/2$, since $V \propto 1/R$

5.3 THE PRESS-SCHECHTER HALO MASS FUNCTION

We will use the critical density of Eq. (5.11) to identify collapsed regions in the linearly evolved density field. The size of these regions is introduced by considering the smoothed density contrast[4] δ_R as a function of the smoothing scale R (as introduced in Eq. 2.27). It should be noted that R describes the radius of the *Lagrangian* volume throughout the calculation, so it is a comoving radius that is always centred on the central peak. The probability distribution of the smoothed field is given by a Gaussian

$$p(\delta_R) = \frac{1}{\sqrt{2\pi\sigma_R^2}}\, e^{-\delta_R^2/(2\sigma_R^2)}\,. \tag{5.13}$$

The probability of the smoothed density contrast to exceed δ_c is then given by

$$p(\delta_R \geq \delta_c) = \int_{\delta_c}^{\infty} \mathrm{d}\delta_R\; p(\delta_R) = \frac{1}{2}\,\mathrm{erfc}\left(\frac{\delta_c}{\sqrt{2}\sigma_R}\right)\,. \tag{5.14}$$

This cumulative probability corresponds to the fraction of volume that is occupied by haloes of size defined by the smoothing scale R.

For the next step, we need to add a quite crucial assumption, i.e. that we can assign a mass $M(R)$ to each region smoothed with a filter of size R. This sounds quite straight forward for a real space top-hat filter. It is not clear, however, for a sharp-k filter as we will discuss in Section 5.4. Doing so, we can denote the volume fraction occupied by haloes of mass $m > M$ by $F(>M)$ and rewrite Eq. (5.14)

$$F(>M) = \frac{1}{2}\,\mathrm{erfc}\left(\frac{\delta_c}{\sqrt{2}\sigma_{R(M)}}\right)\,. \tag{5.15}$$

Since $F(>M)$ is a cumulative quantity, but the halo mass function quantifies the differential probability in a mass interval $[M, M+\mathrm{d}M]$, we need to take the derivative with respect to M

$$\frac{\mathrm{d}F(>M)}{\mathrm{d}M} = \frac{\mathrm{d}F(>M(R))}{\mathrm{d}R}\frac{\mathrm{d}R}{\mathrm{d}M} = f(R)\frac{\mathrm{d}R}{\mathrm{d}M}\,. \tag{5.16}$$

This quantity gives us the volume fraction of haloes in the mass interval $[M, M+\mathrm{d}M]$, while we are interested in the number density of haloes per volume. We therefore have to

4 The adequate choice for the filter function would be a spherical top-hat here, since δ_c was calculated with the spherical collapse model.

divide Eq. (5.16) by the average volume of a halo of mass M, which is given by $\bar{V} = \bar{\rho}/M$.[5] The *halo mass function* is then given by[6]

$$n(M)\mathrm{d}M = \frac{\bar{\rho}}{M}\left|\frac{\mathrm{d}F}{\mathrm{d}R}\right|\frac{\mathrm{d}R}{\mathrm{d}M}\,\mathrm{d}M\,. \tag{5.17}$$

Note that we need to take the absolute value of $\frac{\mathrm{d}F}{\mathrm{d}R}$, since there are fewer large than small haloes and therefore the volume fraction decreases with increasing radius R, so $\frac{\mathrm{d}F}{\mathrm{d}R} < 0$. The final form of the Press-Schechter mass function is obtained by plugging Eq. (5.15) into Eq. (5.17) and multiplying it by a fudge factor of 2

$$n(M)\mathrm{d}M = \sqrt{\frac{2}{\pi}}\frac{\bar{\rho}}{M}\frac{\delta_\mathrm{c}}{\sigma_R}\frac{\mathrm{d}\ln\sigma_R}{\mathrm{d}M}\exp\left(-\frac{\delta_\mathrm{c}^2}{2\sigma_R^2}\right)\mathrm{d}M\,. \tag{5.18}$$

This additional factor of 2 needs to be introduced by hand, since otherwise only half of the mass of the Universe would be bound in haloes. This can be easily verified by integrating Eq. (5.16) over all masses.

5.4 THE HALO MASS FUNCTION WITH EXCURSION SET STATISTICS

While the above description was based on the spherical top hat filter, Bond et al. (1991) proposed to filter the field instead with a sharp filter in k-space

$$W_R(k) = \begin{cases} 1 & (kR \leq 1) \\ 0 & (kR > 1)\,. \end{cases} \tag{5.19}$$

As we have seen in the definition of the power spectrum (Eq. 2.26), the modes of a statistically homogeneous Gaussian random field are uncorrelated. Smoothing with a sharp k-filter therefore corresponds to adding independent modes, or in other words it represents a Markov process. Thus, the smoothed field as a function of k can be described by an uncorrelated random walk. Smoothing around every point in space provides us then with an ensemble of uncorrelated random walks. Since $k = 0$ corresponds to smoothing over the whole space, the smoothed density at $k = 0$ will be the mean density and therefore $\delta_R(k = 0) = 0$. Hence, all random walks will start at zero. Note that in the literature typically the fact is used that the variance of the smoothed field $S(R) := \sigma^2(R)$ is a monotonous function of the smoothing scale R or wave number k, respectively. For

5 One might wonder why the density of the halo's region is assumed to be $\bar{\rho}$ in this step although haloes are defined via their linear overdensity δ_c. The standard reasoning is that in the Press-Schechter approach haloes are identified in fact in the initial density field as proto-haloes where overdensities are still negligible. The linear extrapolation solely helps to identify these regions. Since gravitational collapse is a non-linear process, the overdensity δ_c has no physical reality anyway. Using Lagrangian coordinates, the halo's volume is then simply given by $M/\bar{\rho}$.

6 At times, the different notation $\mathrm{d}n(M)/\mathrm{d}M$ is used to denote the halo mass function in order to emphasise that the halo mass function is a differential quantity. The notation $n(M)$ is more common, however.

this reason, the random walk is often described as a function of S instead of k. We will make use of this notation at times in this thesis, when summarising some results of the literature.

The key idea of the excursion set ansatz of Bond et al. (1991), is to identify $\mathrm{d}F(>M(R))/\mathrm{d}R$ with the so called *first crossing rate* $f(R)$, i.e. the rate of random walks that cross the density threshold δ_c in the interval $[M, M+\mathrm{d}M]$ for the first time. This quantity can be predicted for an uncorrelated random walk treating δ_c as an absorbing barrier. The result for this problem has been known for quite some time (Chandrasekhar, 1943) and reads

$$f(S) = \frac{\delta_\mathrm{c}}{\sqrt{2\pi S^3}} \exp\left(-\frac{\delta_\mathrm{c}^2}{2S}\right) . \tag{5.20}$$

It provides exactly the additional factor of two, which had to be plugged in by hand in the original Press-Schechter approach (compare Eq. 5.20 with the derivative of Eq. 5.15 with respect to S). On the basis of this result, there exists also a justification of why the original approach is missing this factor of two. From the random walk point of view, it is easy to see that a walk could cross the barrier at some scale k_1, but then drop again below the threshold for higher k. This corresponds to an underdense region that lies within a larger, collapsed overdensity. Since it is part of the parent halo this region would certainly be needed to count for the volume fraction of the parent halo. However, the original Press-Schechter approach ignored all these walks, since they are below the threshold. This is called the "*cloud in cloud*" problem. The probability for an uncorrelated random walk to continue at the threshold in upward direction is exactly the same as the probability to continue downwards. Therefore only half of the random walks will have stayed above the threshold when integrating over all k, which then leads exactly to the missing factor of two[7].

However, smoothing with a sharp-k filter comes at the price that this filter has no well defined volume in real space. Therefore, it is not possible anymore to relate a mass $M(R)$ to the smoothing scale R. In Bond et al. (1991), the choice for the specific value of $V(R)$ is left open and the first crossing rate is simply plugged into Eq. (5.18) to obtain the final Press-Schechter result. The extended Press-Schechter approach therefore solves the cloud in cloud problem at the cost of introducing a (minor) inconsistency. Usually, the volume is fixed by using that of a real space top-hat with the same filter scale $V = 4/3\pi R^3$ instead or $V = 6\pi R^3$ (Lacey and Cole, 1993), respectively.

5.5 SHORTCOMINGS OF THE PRESS-SCHECHTER APPROACH

The Press-Schechter approach and more so its extension in Bond et al. (1991) provided an important step in the analytical description and quantification of structures in the

7 We would like to caution the reader that also this excursion set approach comes with some conceptual problems, as we will discuss in Section 5.5. So, this argumentation should be taken with a grain of salt.

Universe. Its result for the halo mass function describes numerical and observational data surprisingly well, given the simplifying nature of the underlying assumptions. Due to this fact, it remained over several decades the most established analytic description of the halo mass function, which is not dependent on any fits to numerical simulations.

However, there are several problems with the assumptions underlying the (extended) Press-Schechter approach, which causes the theory to rest on shaky ground. While it is totally justified to employ simplifying assumptions for a first approach, it remains unsatisfying for a theory being widely considered (and taught) as the standard approach to the halo mass function. This has been commented on in many works (see e.g. Zentner, 2007; Robertson et al., 2009; Maggiore and Riotto, 2010a; Maggiore and Riotto, 2010b; Maggiore and Riotto, 2010c; Corasaniti and Achitouv, 2011; Hagstotz et al., 2019). In the following, we will summarise these problematic assumptions and highlight alternative approaches where possible.

1. Linear extrapolation

Basing the theory on the linearly evolved density field comes with one great advantage. Linear evolution ensures that the Gaussian nature of the density field stays untouched. Therefore the form of the density field's PDF is known and calculations become especially easy due to the well behaved nature of the normal distribution. While the assumption of linear evolution seems reasonable at large scales (i.e. $k \lesssim 0.1$ Mpc$/h$ for $z = 0$, see e.g. the power spectrum in Bartelmann et al., 2019, Fig. 3), it appears rather unsuited for the description of collapsed objects due to the highly non-linear nature of gravity. As described above, spherical collapse predicts an overdensity for virialised objects of $\Delta_{\mathrm{vir}} \approx 178$, well above the linear regime (i.e. $\delta \ll 1$). It therefore appears surprising that the Press-Schechter approach nevertheless gives reasonable results. It can also be added that even the result obtained by linear extrapolation ($\delta_{\mathrm{c}} = 1.686$) is not in the linear regime anymore.

2. Spherical collapse

The Press-Schechter approach uses spherical collapse to predict the linear density threshold for collapsed objects δ_{c}. In Doroshkevich (1970), however, it has in fact been shown that the probability for the spherically symmetric collapse of a halo is identical to zero. Calculating the eigenvalues ($\lambda_i, i \in \{1, 2, 3\}$) of the deformation tensor introduced in Zel'dovich (1970), one can show that only points in space with three positive eigenvalues will collapse to form haloes. Since the probability of all three of the eigenvalues to be the same (as required for spherical collapse) is zero, the collapse will happen in an ellipsoidal fashion.

On the one hand, isotropy of the Universe requires that there is no preferred orientation of the ellipsoidal collapse and therefore stacking the images of a large number of observed

clusters would indeed lead to a spherical result. However, the ellipsoidal collapse requires an overdensity larger than the spherical prediction in order to counteract the occurring tidal forces. This is the case in each individual collapsing halo regardless of its orientation and therefore ellipsoidal collapse has to be taken into account when the density threshold is determined. It seems reasonable to assume that this effect is most visible on small scales, where the influence of the local gravitational field will lead to strong tidal forces. Hence, the assumption of spherical collapse should at most be valid in the regime of highest mass peaks, since these are affected the least by the distortions of smaller scale overdensities (Robertson et al., 2009). Sheth et al. (2001) therefore incorporated ellipsoidal collapse by introducing an excursion set approach with a moving barrier, i.e. a density threshold that decreases as a function of scale R.

3. Excursion set approach

The excursion set approach in Bond et al. (1991) provides an elegant resolution to the "fudge factor" and cloud in cloud problem in Press and Schechter (1974). However, it poses new problems and requires additional unsatisfactory assumptions. In order to apply the theory of uncorrelated random walks, we need to filter the random field with a sharp filter in k-space. This filter, however, has no well defined volume in real space and therefore does not allow assigning a mass to the halo. In other words, we can calculate the volume fraction of haloes at a certain filter scale R, but not a mass fraction. This leads to a contradiction within the model, since a spherical top-hat is used to obtain $\delta_c = 1.686$, but the field is smoothed with a sharp k-filter when this threshold is applied.

Using a Gaussian or a spherical top hat filter in the excursion set statistics instead, would introduce correlations between the steps of the random walk and therefore poses a much more complicated problem to solve analytically. Correlated random walks can be caused by two effects. First, the unfiltered random field can possess coupled modes through non-Gaussianities either in the primordial or the evolved field. Secondly, correlations can be caused by the filter function. The excursion set approach has been extended to correlated random walks by Peacock and Heavens (1990) and more recently by Musso and Sheth (2012). Peacock and Heavens (1990) derived an approximation by realising that an uncorrelated random walk can be recovered by increasing the step size of the random walk to a value larger than the correlation length. The correlations are then included in the additional parameter that describes the correlation length. Musso and Sheth (2012) use the joint probability distribution of the density field and its derivative with respect to the smoothing scale in order to describe the excursion set statistics of strongly correlated steps.

The excursion set approach, however, faces a much more fundamental problem. The notion of a halo is very unclear conceptually in this approach and does not harmonise with the way haloes are defined in simulations or observations (Zentner, 2007, pp. 40). The excursion set approach assigns each point in space that exceeds the threshold at a

filter scale R to the volume of a halo of mass $M(R)$. It is quite obvious, however, that a neighbouring point will not be counted for the same mass halo, but either for a higher mass halo if it is more central or a lower mass halo if it is located towards the outskirts. As stressed by Zentner (2007), the excursion set approach leads to a continuous "halo mass field" in contrast to an identification of distinct haloes with particular masses, which would be needed for a conceptually sound comparison with simulations or observations[8]. This inconsistency has also been investigated numerically in simulations (Robertson et al., 2009). They determine the overdensity threshold in dependence of scale by measuring the overdensity of those patches in the simulation's initial density field that are found to form a halo at $z = 0$. They find good agreement with the moving threshold proposed in Sheth et al. (2001) from ellipsoidal collapse. However, after inserting this barrier into the excursion set formalism, the resulting halo mass function does not agree with that measured in the simulation. This therefore shows that the excursion set approach does not lead to a correct prediction of the halo mass function. A similar result has been obtained by Geiger (2020) (see Section 5.7).

Alternative concepts have been proposed quite early, e.g. Bardeen et al. (1986) proposed an approach which is based on predicting the abundance of peaks in the density field instead of the abundance of haloes of a given mass. This approach has been extended to predict the distribution of potential depths Angrick and Bartelmann (2009) and it has been combined with excursion set statistics of correlated random walks in Paranjape et al. (2012). Furthermore, Maggiore and Riotto (2010a) used a path integral approach, which takes into account correlated steps caused by both the non-Gaussianities of the density field and its filtering and it assumes a stochastic barrier reflecting that haloes in simulations identified through e.g. the Friends-of-Friends[9] (FoF) algorithm (Davis et al., 1985) can be of quite irregular shape.

4. Mass as an observable

The alternative approaches proposed by Bardeen et al. (1986) and Angrick and Bartelmann (2009) additionally bypass a fourth problem, which lies at the core of the halo mass function itself. It is a long standing problem that there exists no clear definition of a halo and its mass. A variety of different halo mass definitions have been developed, depending on which branch of cosmology, i.e. theory, observations or simulations, is considered[10]. A possibility to remedy the different halo notions in simulations and theory was proposed by Maggiore and Riotto (2010b). They incorporate the irregular shape of haloes in simulations into the halo mass function by applying a stochastic barrier to their path integral approach. Bardeen et al. (1986) and Angrick and Bartelmann (2009)

8 It could be argued, however, that the description in terms of a continuous halo mass field may be more realistic than the description in terms of distinct haloes. Nevertheless, it leads to a conflict when the results are to be compared with haloes from simulations.

9 See Section 7.1 for an introduction of the FoF code.

10 See Section 7.1 for a discussion of halo mass definitions in observations, simulations and theory.

drop the halo mass quantity altogether. Their approaches are based on peaks in the density field and potential minima instead. Being local quantities, these are well defined in observations, simulations and theory alike and could therefore be advantageous over an approach based on halo masses.

5.6 BEYOND PRESS-SCHECHTER

Motivated by the success of the extended Press-Schechter approach in qualitatively describing the simulation results, a large variety of different halo mass function shapes have been proposed in order to improve the quantitative description. The extended Press-Schechter approach, however, remains the only completely analytical prediction of the halo mass function, since all other forms contain free parameters that need to be fitted to numerical simulations. As a representative for the large variety of fit functions, we will shortly present the result of Tinker et al. (2008), which will be used in the next chapter. We furthermore summarise an analytical approach by Musso and Sheth (2012), which considers random walks with correlated steps.

At this point, it also should be mentioned that the halo mass function is often expressed in the form

$$n(M)\mathrm{d}M = \frac{\bar{\rho}}{M^2} S f(S) \left| \frac{\mathrm{d}\ln S}{\mathrm{d}\ln M} \right| \mathrm{d}M\,, \tag{5.21}$$

in the literature. This form is handy, since most halo mass functions only differ in the quantity $Sf(S)$, which is called the *multiplicity function*. It quantifies the number of first crossings per logarithmic variance interval, i.e. $Sf(S) = \mathrm{d}F(S)/\mathrm{d}\ln S$.

5.6.1 *Functions fitted to simulations*

By now, there exists a plethora of fitting functions, whose parameters are optimised by fitting to N-body simulations (see e.g. Murray et al., 2013b, for a list). We will make use of the fitting formula proposed by Tinker et al. (2008) in order to compare the results of our novel approach presented in the next chapter (Chapter 6) to the predictions of simulations. Tinker et al. introduce a form for $f(\sigma)$ that is similar to the first crossing distribution proposed in Sheth and Tormen (1999)

$$f(\sigma) = A \left[\left(\frac{\sigma}{b} \right)^{-a} + 1 \right] e^{-c/\sigma^2}\,. \tag{5.22}$$

It depends on four parameters: a normalisation constant A, a and b, which specify the slope and amplitude of the low-mass power law, and c, which determines the exponential cut-off of the halo mass function. Fitting their halo mass function to all haloes found in a sample of 18 N-body simulations, they obtain the parameters as $A = 0.186, a = 1.47, b = 2.57$ and $c = 1.19$. We chose particularly this fitting function

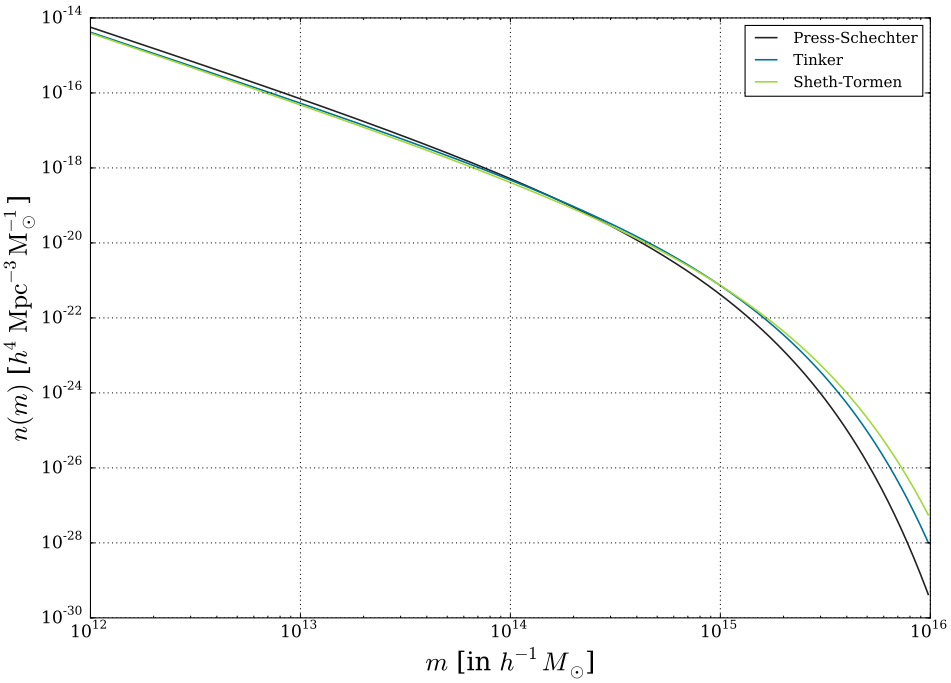

Figure 5.1: Comparison of three different halo mass function models, i.e. Press-Schechter (*black*), Tinker (*blue*) and Sheth-Tormen (*green*).

for the comparison to our results, since haloes in their simulations were found with a spherical over density finder with $\Delta = 200$. This corresponds well to our theoretical derivation, where we likewise use the spherical overdensity as the criterion to identify haloes.

A comparison of the Press-Schechter, the Sheth-Tormen and the Tinker halo mass functions is shown in Fig. 5.1. While all models show the same qualitative behaviour, the Press-Schechter clearly predicts too many low mass haloes and underpredicts the high mass tail. The Sheth-Tormen as well as the Tinker mass functions are fits to cosmological simulations and therefore reflect the theoretical ΛCDM predictions by N-body simulations. However, also these two functions show a considerable discrepancy in the high mass regime. This demonstrates that the functional form of the halo mass function is by no means uniquely determined by simulations and there still exists a considerable uncertainty in the theoretical description (see also Murray et al., 2013a).

5.6.2 *First crossing rate with correlated steps*

As mentioned above, the assumption of uncorrelated steps in the extended Press-Schechter approach seems quite problematic. Musso and Sheth (2012) therefore proposed a formalism to predict the first crossing rate of a random walk with correlated steps. As

they point out, the first crossing rate for completely correlated (cc) walks, i.e. when δ_R is a deterministic function of smoothing scale R, is given by

$$\begin{aligned} f_{\rm cc} &= \frac{{\rm d}F_{\rm cc}}{{\rm d}R} = \frac{\rm d}{{\rm d}R}\left(\int_{\delta_c}^{\infty} p(\delta_R){\rm d}\delta_R\right) \\ &= \frac{\rm d}{{\rm d}R}\left[\frac{1}{2}\,{\rm erfc}\left(\frac{\delta_{\rm c}}{\sqrt{2S}}\right)\right] = \frac{1}{\sqrt{2\pi}}\exp\left(-\frac{\delta_{\rm c}^2}{2S}\right), \end{aligned} \tag{5.23}$$

which exactly represents the Press-Schechter result without the fudge factor of two. Musso and Sheth (2012) argue therefore, that the first crossing rate of a random walk with somewhat correlated steps must lie in between the fully correlated result of Eq. (5.23) and the uncorrelated result, i.e. Eq. (5.23) times a factor of two as obtained in Bond et al. (1991).

Musso and Sheth (2012) derive the first crossing rate in the strongly (but not completely) correlated (sc) regime (see also Musso and Sheth, 2014a; Musso and Sheth, 2014b). This means that walks that are in an upward direction are very likely to continue in an upward direction and vice-versa. If such a random walk crosses the barrier in an upward direction it can therefore be assumed that it crossed never before. The first crossing distribution can then be estimated by counting only those walks which cross the barrier in an upward direction. For conditioning the first crossing distribution on upward walks, the probability of the derivative of the density field with respect to S is needed in addition to the probability of the field value itself. The first crossing distribution can be derived from the joint distribution $p(\delta, \delta')$ via

$$f_{\rm sc}(S)\Delta S = \int_0^{\infty}{\rm d}\delta' \int_{\delta_{\rm c}}^{\delta_{\rm c}+\delta'\Delta S}{\rm d}\delta\; p(\delta,\delta') \approx \Delta S\int_0^{\infty}{\rm d}\delta'\delta' p(\delta=\delta_{\rm c},\delta')\,, \tag{5.24}$$

where the prime denotes a derivative with respect to S, i.e. $\delta' = {\rm d}\delta/{\rm d}S$. In the second step, the density integral was approximated by the trapezoidal rule and by using $p(\delta = \delta_{\rm c} + \delta'\Delta S, \delta') \approx p(\delta = \delta_{\rm c}, \delta')$.

The joint probability distribution can only be written down for a small number of distributions $p(\delta)$. For a generic random variable X, there is no way to deduce what type of distribution their derivative X' follows. Since taking the derivative is a linear operation, however, the derivative of a Gaussian distributed random variable must be Gaussian distributed as well. Hence, assuming that δ follows a Gaussian distribution, it is possible to write down the joint probability distribution as

$$p(\delta,\delta') = \frac{\gamma}{\pi\sqrt{1-\gamma^2}}\exp\left[-\frac{2\gamma^2}{1-\gamma^2}\left(\frac{\delta^2}{4S\gamma^2} - \delta\delta' + S\delta'^2\right)\right], \tag{5.25}$$

where the Pearson-correlation coefficient γ^2 is defined by

$$\gamma^2 := \frac{\langle\delta\delta'\rangle^2}{\langle\delta\delta\rangle\,\langle\delta'\delta'\rangle}\,. \tag{5.26}$$

Plugging the joint PDF (Eq. 5.25) into Eq. (5.24) finally leads to the first crossing rate

$$f_{\mathrm{sc}}(S)\Delta S = \frac{e^{-\delta_{\mathrm{c}}^2/2S}}{2\sqrt{2\pi S^3}}\left[\frac{1+\mathrm{erf}(\Gamma\delta_{\mathrm{c}}/\sqrt{2S})}{2} + \sqrt{\frac{S}{2\pi}}\frac{e^{-\Gamma^2\delta_{\mathrm{c}}^2/2S}}{\Gamma\delta_{\mathrm{c}}}\right]\Delta S\,, \tag{5.27}$$

with

$$\Gamma := \frac{\gamma^2}{1-\gamma^2}\,. \tag{5.28}$$

A comparison of Eq. (5.27) to Monte Carlo predictions of walks with correlated steps (Musso and Sheth, 2012, Fig. 1) showed a very good agreement. However, when compared to the first crossing distribution measured in N-body simulations the results of Eq. (5.27) as well as a number of other predictions (e.g. those by Peacock and Heavens, 1990; Bond et al., 1991 or Maggiore and Riotto, 2010a) show large discrepancies (Lapi and Danese, 2014, Fig. 2 and Hiotelis and Popolo, 2017, Fig. 4).

The halo mass function can finally be obtained by inserting the first crossing rate (Eq. 5.27) into Eq. (5.21). In this context, Musso and Sheth (2014a) make a further remark concerning the comparison with N-body simulations. They argue that the random walks described with Eq. (5.27) would not correspond to those found in simulations, since these will always be centred on a simulation particle. To take this bias into account, they suggest to mass weight the random walks, i.e. to multiply $p(\delta)$ by a factor of δ. We will comment on this ad hoc modification in Section 6.1.

5.7 INVESTIGATING THE EXCURSION SET APPROACH

The applicability of the excursion set statistics has furthermore been investigated in a recent study by Geiger (2020). Their analysis was based on Gaussian random fields[11] in order to investigate the excursion set statistic on a fundamental level. Using Gaussian random fields in contrast to a more realistic density field, e.g. from a cosmological simulation, allowed to make use of the Gaussian field's convenient analytical properties. The halo mass function was determined from the random field in two ways: (*i*) applying the excursion set approach and (*ii*) using a spherical overdensity finder (as e.g. in Tinker et al., 2008). As a proof of concept, the excursion set statistics was first determined directly from the generated field and then compared to the analytical description. The extended Press-Schechter prediction could be perfectly recovered as expected. In a second step, a spherical overdensity finder similar to that of Tinker et al. (2008) was used to identify haloes according to the halo-definition employed in simulations. The halo mass function found by this procedure is in strong disagreement with the excursion set prediction. This goes in line with the results of Robertson et al. (2009) and shows once more that the excursion set approach does not provide a sound description of the halo mass function.

11 The Gaussian random fields were generated such that they have the same power spectrum as predicted for cosmic structure formation (Bardeen et al., 1986; Eisenstein and Hu, 1998).

They furthermore investigated the influence of the filter function on the results of the excursion set formalism. This was done by smoothing the simulated field with: (*i*) a sharp-*k* filter as in the extended Press-Schechter approach and (*ii*) with a top-hat filter in real space. Afterwards, the excursion set statistic was determined by counting random walks in the simulated field for each filter that exceed a threshold δ_c. This showed that the choice of filter function in the excursion set approach has a significant influence on the halo mass function, especially in the high-mass end. It was shown that the sharp-*k* filter predicts more than an order of magnitude less haloes of masses $M \gtrsim 5 \times 10^{14} \mathrm{M}_\odot$. As explained above, using the sharp-*k* filter in the extended Press-Schechter approach leads to an inconsistency in the formalism. The derivation of the density threshold δ_c and the identification of haloes in simulations are both based on spherical overdensities in real space, while the sharp-*k* random walks do not reflect any physical object. The results obtained with the top-hat filter in real space should therefore reflect much better the halo mass function as it would be determined in a simulation. Hence, this result corresponds well with the finding that the Press-Schechter halo mass function underpredicts the high mass tail in comparison to simulations.

6

A KFT APPROACH TO THE HALO MASS FUNCTION

As explained in the last chapter, the current analytical derivation of the halo mass function has several conceptual short comings and the most recent proposals consist of fitting functions only. However, the halo mass function remains an important cosmological probe. It is interesting not only for conceptual reasons. It also can be used to determine cosmological parameters, since its high mass tail in particular is very sensitive to the matter density Ω_m and the normalisation of the power spectrum σ_8. The determination of the halo mass function is therefore the goal of current and future cosmological surveys, such as DES (Abbott et al., 2018), KiDS (de Jong, J. T. A. et al., 2017), Euclid (Laureijs et al., 2011) and LSST (Ivezić et al., 2019). For this reason, it seems desirable to gain a deep understanding of the halo mass function in form of an analytical approach that goes beyond fitting functions.

We make an attempt at improving the derivation of the halo mass function by applying excursion set statistics directly to the present day non-linear density field. This avoids the problematic detour via the linearly extrapolated density field. In exchange, random walks cannot be assumed to be uncorrelated anymore in our approach. We will therefore base our analysis on the work of Musso and Sheth (2012) presented in Section 5.6.2. The rough outline of our approach is as follows: We will use KFT to predict the second and third moment of the present day density field. With these at hand, we can fix the parameters of our model for the density PDF. From the PDF, we then derive the first crossing rate for a fixed density threshold Δ, where Δ is assumed to be constant throughout the calculations. We do not derive this parameter from spherical collapse. It is rather treated as a free parameter, which would be the analytic analogue to setting the overdensity parameter in spherical overdensity halo finders used in cosmological simulations (e.g. by Lacey and Cole, 1994; Sheth and Tormen, 1999; Tinker et al., 2008). After all, the halo mass function is calculated by inserting the first crossing distribution into Eq. (5.17).

The approach presented in this chapter builds upon work by Linke (2017) and unpublished work by M. Feix[1]. We start with explaining the mass weighting of random walks and deriving the first crossing distributions of two different models for the density PDF in two different correlation regimes in Section 6.1. We will then derive the halo mass function in Section 6.2. We will finally discuss our results in Section 6.3.

1 These two works led to a paper draft including contributions by the author of this dissertation. Parts of this unpublished manuscript have been adopted verbatim in Section 4.2 and Chapter 6.

6.1 THE FIRST-CROSSING RATE

As discussed above, Musso and Sheth (2012) provide a first crossing rate for random walks with correlated steps. We will apply their approach while investigating two regimes in particular: (*i*) the *completely correlated limit*, where δ_R is a deterministic function of R,[2] and (*ii*) the regime of *strongly correlated random walks*. We will perform each of the calculations with two models for the density field's probability distribution: (*a*) a lognormal distribution (Eq. 4.1), which is used for illustrative purposes to present our method, and (*b*) the generalised normal distribution (Eq. 4.2), which should represent a more realistic model of the PDF.

6.1.1 *Weighted random walks*

Before we calculate the first crossing rates in the respective regimes, we need to slightly modify the models of our density PDFs. This is necessary, since a direct application of the excursion set approach to the gravitationally evolved, non-Gaussian density field would result in an underestimation of the halo number density. As discussed in Musso and Sheth (2014b) this becomes apparent when the PDF is transformed to a Gaussian distribution, where the threshold has to be transformed accordingly, which consequently leads to it not being constant any more. Taking the lognormal distribution as an example, a constant threshold becomes a linearly increasing barrier after being mapped to Gaussian walks. Hence, not all walks cross the barrier any more and only a small fraction of the total mass is predicted to be bound in haloes. Musso and Sheth (2014b) suggest a solution to this issue in a different context. They argue that there exists another problem when their results are compared to those obtained from simulations. When haloes are identified in simulations, only such random walks are considered that are centred on a mass particle of the simulation. This argument views the halo finding process as the closest numerical equivalent to performing the excursion set approach. Musso and Sheth (2014b) mention that a crude way to account for this fact would be to weight every random walk by its mass when estimating the crossing rate (see also Sheth, 1998). This corresponds to introducing a factor of $(1 + \delta_R)$ in the case of the lognormal PDF (introduced in Section 4.1.1)

$$\tilde{p}_{\mathrm{LN}}(\delta_R) = (1 + \delta_R) p_{\mathrm{LN}}(\delta_R)\,. \tag{6.1}$$

2 This is expected to be a good approximation for very massive haloes, which should be affected only little by noise. These very massive haloes would naturally appear, when the density field is smoothed over large scales.

We can furthermore absorb the weighting factor into the lognormal model through a redefinition of its parameters. It just amounts to a sign flip of the mean parameter $\tilde{\mu} = -\tilde{\sigma}_R^2/2$, i.e.

$$\tilde{\mu} \to \tilde{\nu} = -\tilde{\mu} = \frac{\tilde{\sigma}_R^2}{2}. \tag{6.2}$$

We can therefore write the weighted lognormal distribution as

$$\tilde{p}_{\mathrm{LN}}(\delta_R) = \frac{1}{\sqrt{2\pi}\tilde{\sigma}_R\,(1+\delta_R)} \exp\left[-\frac{\left(\ln\left(1+\delta_R\right) - \tilde{\sigma}_R^2/2\right)^2}{2\tilde{\sigma}_R^2}\right]. \tag{6.3}$$

At the same time, the additional weighting factor turns the increasing threshold, which was obtained after the mapping to a Gaussian distribution, into a linearly decreasing one. Thus, all random walks are guaranteed to cross at some scale, which also solves the first problem of underpredicting the total mass bound in haloes.

We generalise this idea, by applying a similar weighting also to the generalised normal distribution (see Section 4.1.2)

$$\tilde{p}_{\mathrm{GN}}(\delta_R) = \left(\left|\tilde{\mu} + \frac{\alpha}{\beta}\right| + \delta_R\right) p_{\mathrm{GN}}(\delta_R). \tag{6.4}$$

Analogously to the lognormal distribution, the weighting factor has been determined from the Jacobian associated with the mapping of the generalised normal distribution into a Gaussian. It ensures as well that all random walks cross the threshold. Also for the generalised normal distribution, we can absorb the weighting factor into a redefinition of the model's parameters

$$\alpha \to \tilde{\alpha} = \alpha e^{\beta^2}, \tag{6.5}$$

$$\tilde{\mu} \to \tilde{\nu} = \tilde{\mu} - \frac{\alpha}{\beta}\left(e^{\beta^2} - 1\right), \tag{6.6}$$

while β remains the same. Therefore the weighted distribution for the generalised normal case can be written as

$$\tilde{p}_{\mathrm{GN}}(\delta_R) = \frac{1}{\sqrt{2\pi}} \frac{1}{\tilde{\alpha} - \beta(\delta_R - \tilde{\nu})} \exp\left[-\frac{1}{2\beta^2}\left(\ln\left[1 - \frac{\beta(\delta_R - \tilde{\nu})}{\tilde{\alpha}}\right]\right)^2\right]. \tag{6.7}$$

6.1.2 *Completely correlated random walks*

We will now calculate the first crossing distribution for the lognormal distribution in the limit of completely correlated steps. As shown in Section 5.6.2, the first crossing distribution is given by Eq. (5.23), i.e.

$$f_{\mathrm{cc}} = \frac{\mathrm{d}}{\mathrm{d}R}\left(\int_\Delta^\infty \tilde{p}(\delta_R)\mathrm{d}\delta_R\right) = \frac{\mathrm{d}\tilde{\sigma}_R^2}{\mathrm{d}R}\frac{\mathrm{d}}{\mathrm{d}\tilde{\sigma}_R^2}\left(\int_\Delta^\infty \tilde{p}(\delta_R)\mathrm{d}\delta_R\right). \tag{6.8}$$

Calculating the above integral for the weighted lognormal distribution (Eq. 6.3) yields

$$\int_{\Delta}^{\infty} \tilde{p}_{\mathrm{LN}}(\delta_R)\mathrm{d}\delta_R = \frac{1}{2}\,\mathrm{erfc}\left[\frac{\ln\left(1+\Delta\right)-\tilde{\sigma}_R^2/2}{\sqrt{2}\tilde{\sigma}_R}\right], \tag{6.9}$$

which leads to the result

$$f_{\mathrm{cc,LN}} = \frac{1}{\sqrt{8\pi}\tilde{\sigma}_R}\left(1+\frac{2\ln\left(1+\Delta\right)}{\tilde{\sigma}_R^2}\right)\exp\left[-\frac{\left(\ln\left(1+\Delta\right)-\tilde{\sigma}_R^2/2\right)^2}{2\tilde{\sigma}_R^2}\right]\frac{\mathrm{d}\tilde{\sigma}_R^2}{\mathrm{d}R}. \tag{6.10}$$

For the generalised normal distribution, the integral in Eq. (6.8) is evaluated as

$$\int_{\Delta}^{\infty} \tilde{p}_{\mathrm{GN}}(\delta_R)\mathrm{d}\delta_R = \frac{1}{2}\,\mathrm{erfc}\left[\frac{\ln\left(1-\beta\left(\Delta-\tilde{\nu}\right)/\tilde{\alpha}\right)}{\sqrt{2}\beta}\right]. \tag{6.11}$$

We would like to introduce a slight notational change from that used in the previous chapter for the following calculations. From now on, primes denote derivatives with respect to R, i.e. $A' = \mathrm{d}A/\mathrm{d}R$. Thus the first-crossing distribution in the limit of completely correlated steps is given by

$$\begin{aligned} f_{\mathrm{cc,GN}} = &-\frac{1}{\sqrt{2\pi}\beta}\exp\left[-\frac{\left(\ln\left[1-\beta\left(\Delta-\tilde{\nu}\right)/\tilde{\alpha}\right]\right)^2}{2\beta^2}\right] \\ &\times\left[\frac{\left(\beta\tilde{\nu}/\tilde{\alpha}\right)'-\Delta\left(\beta/\tilde{\alpha}\right)'}{1-\beta\left(\Delta-\tilde{\nu}\right)/\tilde{\alpha}}-\frac{\ln\left(1-\beta\left(\Delta-\tilde{\nu}\right)/\tilde{\alpha}\right)}{\beta}\frac{\mathrm{d}\beta}{\mathrm{d}R}\right], \end{aligned} \tag{6.12}$$

with

$$\frac{\beta\tilde{\nu}}{\tilde{\alpha}} = e^{-\beta^2/2}-1, \quad \frac{\beta}{\tilde{\alpha}} = \frac{e^{-\beta^2}-1}{\sigma_R^2}. \tag{6.13}$$

6.1.3 *Strongly correlated random walks*

We now continue with the strongly (but not completely) correlated regime following Musso and Sheth (2012). As shown in Eq. (5.24), they obtain the first crossing distribution by only selecting trajectories that cross the barrier in an upward direction at scale $S(R)$, which leads to

$$f_{\mathrm{sc}} = -\int_{-\infty}^{0}\mathrm{d}\delta_R'\tilde{p}\left(\Delta,\delta_R'\right)\delta_R'. \tag{6.14}$$

Note once again that primes denote here derivatives with respect to R. Since S is monotonously decreasing with R, we have to consider downward crossing walks in contrast to Eq. 5.24 and therefore the integration boundaries are changed. For clarity, we will apply this approach here only to the lognormal distribution. The corresponding

calculations for the generalised normal distribution can be found in Appendix C.3. In order to derive the joint distribution $p(\delta_R, \delta'_R)$ we will transform the lognormal distribution into a Gauss distribution. Since the derivative of a normally distributed variable also follows a normal distribution, the joint distribution is given by a bivariate normal distribution and $p(\delta_R, \delta'_R)$ can be obtained by reversing the transformation afterwards.

Considering the weighted lognormal distribution specified by Eq. (6.3), we introduce the new random variables

$$\begin{aligned} x &= \ln(1+\delta_R)\,, \\ x' &= \frac{\mathrm{d}x}{\mathrm{d}R} = \frac{\delta'_R}{1+\delta_R}. \end{aligned} \tag{6.15}$$

The joint PDF $\tilde{p}_x(x, x')$ then takes the form of a bivariate Gaussian with its mean and covariance matrix characterised by (see Appendix C.1 for the detailed calculation)

$$\begin{aligned} \langle x \rangle &= \frac{1}{2}\tilde{\sigma}_R^2, & \langle x' \rangle &= 0, \\ \langle x^2 \rangle &= \tilde{\sigma}_R^2, & \langle x x' \rangle &= \frac{\langle \delta_R \delta'_R \rangle}{1+\sigma_R^2}, \\ \langle x'^2 \rangle &= \frac{\langle \delta'^2_R \rangle}{1+\sigma_R^2} - \left(\frac{\langle \delta_R \delta'_R \rangle}{1+\sigma_R^2} \right)^2. \end{aligned} \tag{6.16}$$

Transforming back to variables δ_R and δ'_R yields the joint PDF $\tilde{p}(\delta_R, \delta'_R)$ as

$$\begin{aligned} \tilde{p}(\delta_R, \delta'_R) &= \frac{1}{(1+\delta_R)^2} \tilde{p}_x(x, x') \\ &= \frac{1}{(1+\delta_R)^2} \frac{1}{2\pi \sqrt{\langle x^2 \rangle \langle x'^2 \rangle (1-\gamma^2)}} \exp\left[-\frac{z}{2(1-\gamma^2)} \right], \end{aligned} \tag{6.17}$$

where x and x' need to be expressed through their definition in Eq. (6.15) in terms of δ_R and δ'_R. Furthermore, we defined

$$z := \left(\frac{(x - \langle x \rangle)^2}{\langle x^2 \rangle} + \frac{(x' - \langle x' \rangle)^2}{\langle x'^2 \rangle} - 2\gamma \frac{(x - \langle x \rangle)(x' - \langle x' \rangle)}{\sqrt{\langle x^2 \rangle \langle x'^2 \rangle}} \right), \tag{6.18}$$

(6.19)

and used $\gamma = \langle xx' \rangle / \sqrt{\langle x^2 \rangle \langle x'^2 \rangle}$. Finally, Eq. (6.17) can be inserted into Eq. (6.14). The final result for the first crossing distribution reads then

$$\begin{aligned} f_{\mathrm{sc,LN}} = \frac{1}{2\pi\tilde{\sigma}_R^2} \sqrt{\langle x'^2 \rangle} \exp\left[-\frac{\left(x_\Delta - \tilde{\sigma}_R^2/2\right)^2}{2\tilde{\sigma}_R^2} \right] \\ \times \left(\sqrt{1-\gamma^2}\tilde{\sigma}_R \exp\left[-\frac{\gamma^2 \left(x_\Delta - \tilde{\sigma}_R^2/2\right)^2}{2\left(1-\gamma^2\right)\tilde{\sigma}_R^2} \right] \right. \\ \left. - \sqrt{\frac{\pi}{2}} \gamma \left(x_\Delta - \tilde{\sigma}_R^2/2\right) \operatorname{erfc}\left[\frac{\gamma \left(x_\Delta - \tilde{\sigma}_R^2/2\right)}{\sqrt{2\left(1-\gamma^2\right)}\tilde{\sigma}_R} \right] \right), \end{aligned} \tag{6.20}$$

with $x_\Delta := \ln(1+\Delta)$. The resulting crossing rate for the generalised normal distribution is given by an analogous calculation resulting in Eq. (C.42).

6.2 CALCULATING THE HALO MASS FUNCTION

The first crossing rates $f(R)$ can now be inserted into Eq. (5.18), i.e.

$$n(M)\mathrm{d}M = \frac{\bar{\rho}}{M} \frac{\Delta}{\sigma_R} f(R) \frac{\mathrm{d}\ln\sigma_R}{\mathrm{d}M} \mathrm{d}M\,. \tag{6.21}$$

This leads to an analytic estimate of the halo mass function from the non-linear density field. While all parameters of the underlying PDF model are fixed by KFT predictions, the only free parameter in our model is the barrier Δ. It determines the threshold above which an overdense region is considered to be a collapsed halo. The choice of this value, however, is unspecified. As we are considering the non-linear density field, the linear critical density of spherical collapse ($\Delta_{\mathrm{lin\_sc}} = \delta_{\mathrm{c}} = 1.686$), used by Press and Schechter (1974), is not applicable. The other extreme would be that the PDF of the non-linear density field is perfectly known. In this case a value close to the result obtained from spherical collapse ($\Delta_{\mathrm{nonlin\_sc}} = \Delta_{\mathrm{vir}} = 177$) would be expected. However, the problem of an accurate, analytical description of the PDF down to small scales remains unsolved. Inaccuracies in the PDF model should also lead to values of Δ deviating from the spherical collapse prediction. Therefore, Δ stays a free parameter in our approach. We expect its value to be higher than the prediction of the linear extrapolation, $\Delta_{\mathrm{lin\_sc}}$, but still significantly lower than the non-linear spherical collapse prediction, $\Delta_{\mathrm{nonlin\_sc}}$, since our PDF model becomes more and more inaccurate on small scales.

We discuss here the results obtained using the generalised normal distribution for the *completely correlated* case (i.e. $f_{\mathrm{cc,GN}}$) and the *strongly correlated random walk* (i.e. $f_{\mathrm{sc,GN}}$), which have been calculated in Appendix C.3. We compare these results to the Press-Schechter and Tinker mass functions. The Tinker mass function is especially suitable for our purposes, since a spherical overdensity halo finder was used in their simulations to identify collapsed objects. This is equivalent to the definition of a halo in our approach.

In Fig. 6.1, we show the corresponding halo mass functions for four different density thresholds in the range from $\Delta = 2.0$ to 10.0. These choices are only representative choices to show the overall dependence of the resulting halo mass functions on the threshold. The corresponding results for the lognormal distribution can be found in Appendix D. Fig. 6.1a shows the result of the completely correlated case (see Eq. (6.12)). It can be seen that for $\Delta = 2.9$, our results are in very good agreement with the Tinker halo mass function over six orders of magnitude. It should be emphasised, that this value of Δ is not a fit, but a plausible choice. It is therefore not meant to be a precise measurement of Δ, but should rather show that for a suitable choice of Δ, our analytic approach is capable of producing results that agree closely with those from numerical simulations. To highlight our agreement with the Tinker halo mass function, also the Press-Schechter mass function is shown in contrast. Since it is based on linear evolution, it underpredicts the high mass tail, whereas the completely correlated case with $\Delta = 2.9$ shows a very good agreement with the Tinker halo mass function. Changing the threshold to higher values leads to a severe underprediction of massive haloes. Selecting a threshold of $\Delta = 10$ leads to an underprediction of haloes of mass $M = 10^{15}\ h^{-1}\mathrm{M}_\odot$ of more than three orders of magnitude. The low mass haloes, in contrast, are slightly overpredicted. The halo mass function for a threshold of $\Delta = 10$ is even slightly higher than the Press-Schechter prediction for the mass range between 10^{10} and $10^{11}\ h^{-1}\mathrm{M}_\odot$. For values of Δ smaller than 2.9, massive haloes are significantly overpredicted, but the halo mass function agrees well with the Tinker prediction in the low mass regime.

The results obtained by using strongly correlated random walks (i.e. using Eq. C.42) are plotted in Fig. 6.1b. Choosing $\Delta = 2.9$ leads also in this case to a very good agreement with the Tinker halo mass function. The high mass tail agrees slightly better with the Tinker halo mass function, but fine-tuning Δ to a slightly lower value would have led to a similar agreement in the completely correlated case. It is, however, not our aim to give a precise value for Δ, but to highlight the differences between both results. Despite a very similar overall behaviour, the strongly correlated random walk shifts all halo mass functions to slightly higher values. Therefore, all curves apart from the halo mass function with $\Delta = 2.0$ lie slightly above the Press-Schechter result. The relative difference between our results for $\Delta = 2.9$ and the predictions of the Tinker prediction can as well be seen in Fig. 6.2.

To test the predictions for redshifts higher than $z = 0$, we calculate the results of our halo mass function for redshift $z = 1$, by inserting the corresponding KFT predictions into the density PDF model. Also in this case (see Fig. 6.3), we obtain results that agree very well with the predictions of the Tinker halo mass function. However, to obtain a better agreement in the high-mass tail the threshold would be needed to be chosen slightly lower ($\Delta = 2.7$). It can also be seen that the slope of the high mass tail is slightly steeper than that of the Tinker halo mass function but the discrepancy is of the same order as that between the Tinker fit and their simulation results. This shows that our approach provides reasonable results also for redshifts different from today's $z = 0$.

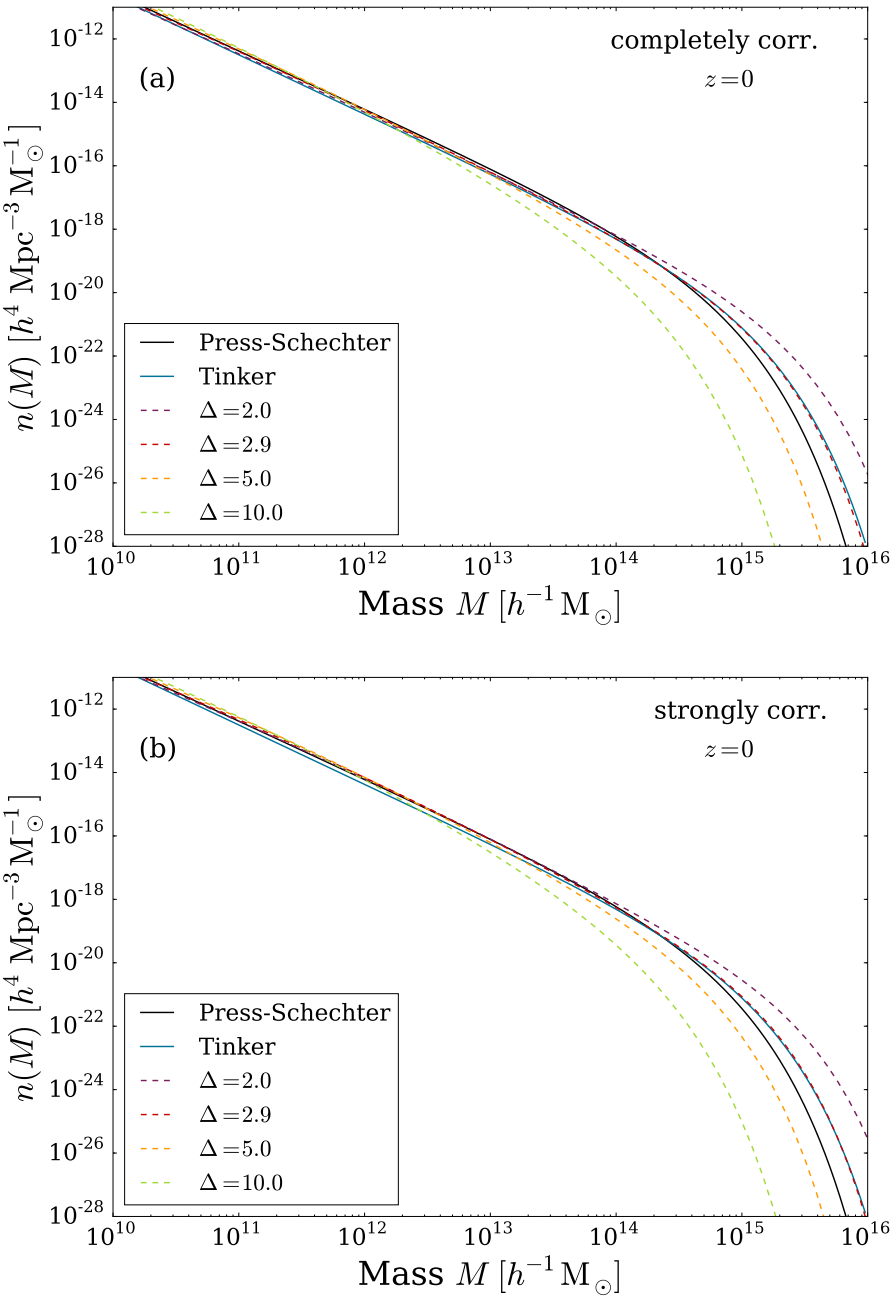

Figure 6.1: Halo mass functions predicted analytically from the non-linear density field using a generalised normal distribution (*dashed lines*). The four different density thresholds in the range $\Delta = 2.0 - 10.0$ are coded by colours as given in the legend. The Press-Schechter prediction is shown in *black* and the Tinker fit in *blue*. The upper panel (a) shows the completely correlated case (Eq. 6.12). The lower panel (b) shows the results for a strongly correlated random walk (Eq. C.42).

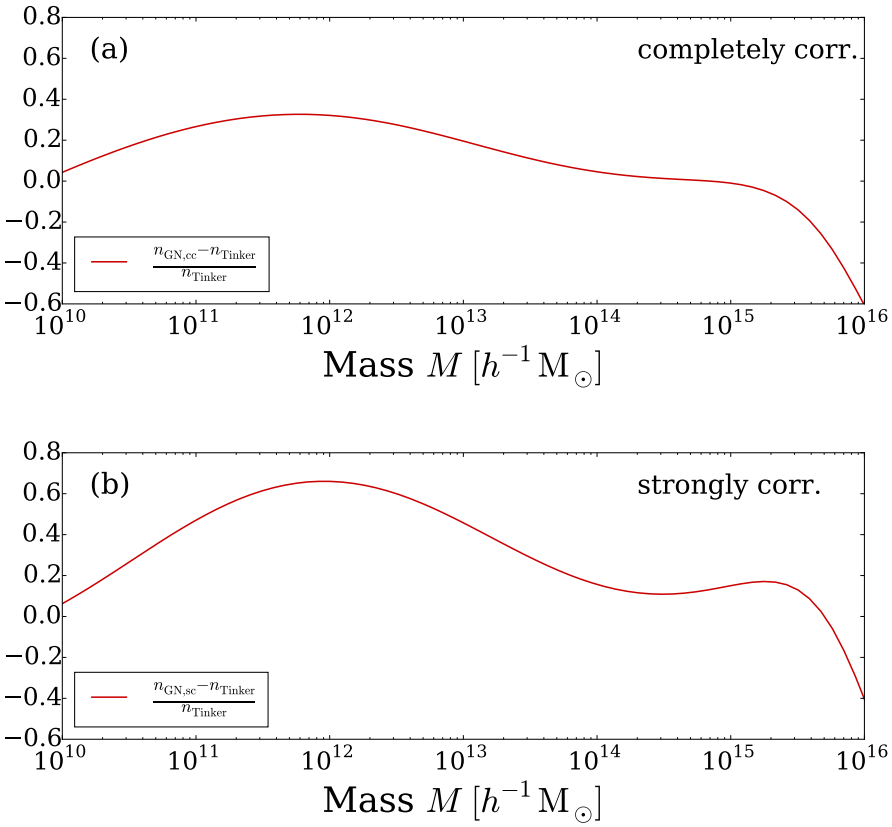

Figure 6.2: The relative deviation of our halo mass function based on the generalised normal model as compared to the Tinker fit. The density threshold was set in our model to $\Delta = 2.9$ (corresponding to the *red dashed* line in Fig. 6.1). The upper panel (a) shows the completely correlated case and the lower panel (b) the a strongly correlated regime.

6.3 DISCUSSION

The approach presented above represents a first step towards an analytical derivation of the halo mass function from the non-linear cosmic density field. It is a purely analytic derivation of the halo mass function, since the free parameters of the PDF model are fixed by the predictions of KFT. The only remaining free parameter of our model is the density threshold Δ above which a halo is considered to be collapsed. This leaves us with a closed form for the halo mass function. In both of the regimes tested, i.e. the *completely correlated* and the *strongly correlated regime*, we obtain very good agreement for a choice of $\Delta = 2.9$ with the predictions of the Tinker halo mass function. Being a fit to numerical simulations, the Tinker halo mass function serves as a proxy for the direct comparison to cosmological N-body simulations. The results agree in particular well with the high

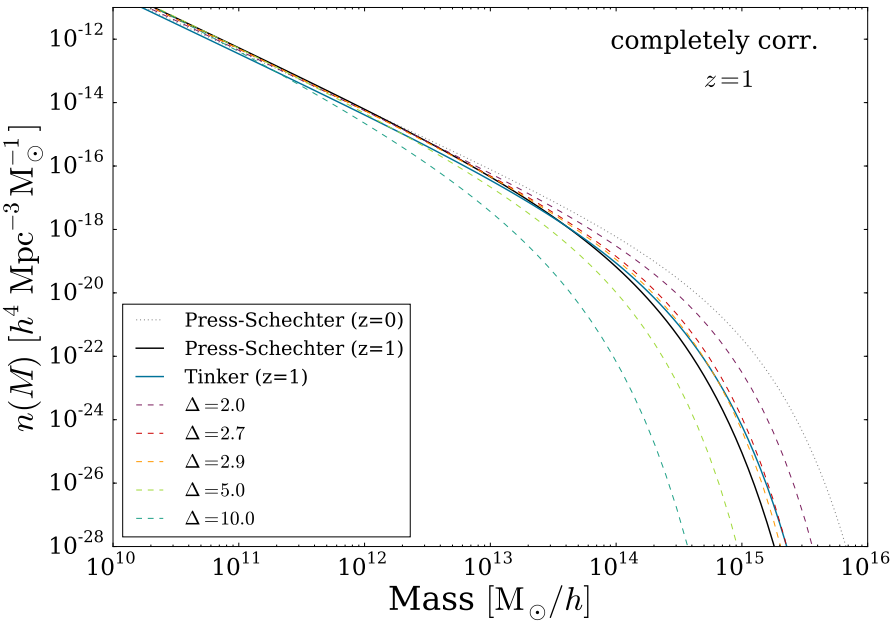

Figure 6.3: Halo mass functions at redshift $z = 1$, predicted using a generalised normal distribution (*dashed lines*). The colour coding was chosen analogously to Fig. 6.1. Additionally the Press-Schechter halo mass function for redshift $z = 0$ is plotted as *dotted line*.

mass tail of the halo mass function, where the Press-Schechter model deviates from the results found in simulations.

However, the chosen value for Δ does not correspond to the virial overdensity obtained from spherical collapse ($\Delta_{\text{nonlin\_sc}} = 177$), but is two orders of magnitude lower. Since our PDF model breaks down on small scales, it is expected that our threshold Δ lies below $\Delta_{\text{nonlin\_sc}} = 177$, but still in the non-linear regime and therefore above $\Delta_{\text{lin\_sc}} = 1.686$. In order to improve our results and obtain a value closer to the overdensity measured in virialised objects, a more accurate PDF would be necessary. A step in this direction has been presented in Chapter 4. However, continuing work needs to be done in this direction. Moreover, in case the strongly correlated regime is considered and the Musso-Sheth approach is to be applied, the PDF of the density field alone would not be sufficient, but the joint PDF $p(\delta_R, \delta'_R)$ would be needed.

For completeness, we would like to mention that there is a slightly different interpretation of the low value of Δ when formulating our approach taking a Lagrangian perspective[3]. The mass weighting of random walks in Eqns. (6.1) and 6.4 can also be seen as transforming the Eulerian PDF (e.g. our unweighted lognormal model) into the corresponding Langrangian PDF as argued in Musso and Sheth (2014b). This is necessary since the Lagrangian volume is considerably larger than the Eulerian and it is thereby

3 This was pointed out by the anonymous referee of a paper draft submitted to the Monthly Notices of the Royal Astronomical Society.

changing the densities in the Lagrangian picture. This can be accounted for by multiplying the lognormal distribution exactly by the weighting factor $(1 + \delta_R)$ (Bernardeau, 1994b; Bernardeau et al., 2002; Lam and Sheth, 2008). Mapping the weighted lognormal distribution to the Gaussian distribution then requires adapting the density threshold accordingly. This results in $\delta = \ln(1 + \Delta) \approx 1.55$,[4] which corresponds to a value similar to $\delta_c = 1.686$ used in the original Press-Schechter description[5]. It is understandable to draw therefore the conclusion that our approach simply represents a mapping of the non-Gaussian density field to the Lagrangian initial density field and subsequently performing the standard Press-Schechter approach. However, this is not quite the case. On the one hand, the viewpoint presented above indeed could help to understand why our approach predicts too many haloes at lower masses, where it agrees well with the predictions of the Press-Schechter mass function. Furthermore, the connection of our approach to the Press-Schechter approach in terms of the mapping between the density thresholds gives somewhat more substance to the answer to why the original Press-Schechter approach works comparably well despite its conceptual shortcomings[6]. A similar result was obtained by Valageas (2009) aiming at deriving a more realistic value for δ_c, where $\delta_c \approx 1.59$ was found. This value is close to our value stated above, $\delta = \ln(1 + \Delta) \approx 1.55$, obtained from mapping the lognormal distribution to the Gaussian distribution (see Appendix D).

On the other hand, this way of reasoning does not explain why we arrive at our result using strongly or even completely correlated random walks. This crucial difference does not allow interpreting our approach simply as a complicated way of performing the standard Press-Schechter approach. Furthermore, our approach agrees well with the high mass tail predicted by the Tinker halo mass function (see Fig. 6.1). It should be mentioned, however, that the tail of extremely large masses (i.e. $M \gtrsim 10^{15}\,\mathrm{M}_\odot$) is only poorly constrained by simulations due to the rarity of the objects.

4 This results from the threshold $\Delta = 3.7$ found for the lognormal case (Appendix D). The generalised normal distribution yields a slightly lower value of $\delta = \ln(1 + \Delta) \approx 1.36$.

5 Note that the value $\delta_c = 1.686$ was derived for an EdS universe (see Section 5.2) and a more realistic value should be closer to the value we obtained here.

6 A very interesting alternative derivation of the Press-Schechter result has been proposed recently by Lapi and Danese (2020). Their approach is not based on excursion set statistics but on describing clustering via a stochastic differential equation with respect to time.

7

SUBSTRUCTURES OF GALAXY CLUSTERS

We have mentioned in the previous chapter that the high mass tail of the halo mass function is highly sensitive to σ_8 and Ω_m due to its exponential decrease. It is populated by the most massive gravitationally bound structures that can be found in the Universe today, which are clusters of hundreds to thousands of galaxies. For this reason, galaxy clusters represent an important cosmological probe, which allow to measure cosmological parameters with exponential sensitivity. A further important reason for the interest in galaxy clusters is that their formation processes take place on scales up to a few Mpc, due to their enormous masses ($\gtrsim 10^{14}\,M_\odot$). At such large scales, baryonic affects can be assumed to play only a minor to negligible role (Munari et al., 2016; Shirasaki et al., 2018). They therefore represent an excellent testbed for the standard model of cosmology. Several cluster properties can be used for this purpose, such as their mass distribution, number density or their extreme value distribution. In this chapter, we will focus on the distribution of substructures within the cluster and their masses, which has been of interest in a number of recent studies (Knebe and Mueller, 2000; Natarajan et al., 2007; Jauzac et al., 2016; Jauzac et al., 2018; Natarajan et al., 2017; Mao et al., 2018).

We will investigate the massive galaxy cluster Abell 2744, since a recent analysis has revealed that it contains a large number of very massive substructures and thus it represents one of the most complex clusters known (Jauzac et al., 2016). We will test the compatibility of its substructure distribution with ΛCDM by comparing it to clusters of similar mass in the cosmological simulation Millennium XXL (MXXL, Angulo et al., 2012). In order to allow a quantitative analysis that treats simulation data and observational data alike, we introduce an algorithm based on wavelets.

We will start with a brief introduction of different mass definitions in Section 7.1 highlighting the different quantities used in observations, simulations and theory. We then introduce the cluster Abell 2744 and its observational data in Section 7.2, followed by the introduction of the Millennium XXL (MXXL) simulation in Section 7.3. We give a brief summary of the wavelet transform in Section 7.4 and define how we use it to find substructures in Section 7.5. The results of the comparison of observational and simulated data are presented in Section 7.6. In Section 7.7, we investigate thoroughly potential errors due to the fact that we analyse the particle data at a somewhat different redshift than that of Abell 2744. We put our results into context with the findings of Schwinn et al. (2017) and Mao et al. (2018) in Section 7.8. We finish with some concluding remarks in Section 7.9, emphasising the importance of being aware of the differences between the mass definitions used in simulations and observations. The content of this

chapter is to a large extent based on Schwinn et al. (2018) from which several passages have been included verbatim.

7.1 MASS DEFINITIONS

Substructures of galaxy clusters are often compared to those in ΛCDM haloes based on their masses. However, as already mentioned in Section 5.5, mass is a problematic observable as there exists no unique definition for the mass of a cluster. For this reason, we deem it helpful to provide here a short list of the different mass observables used in the different branches of cosmology, i.e. theory, observations and simulations.

7.1.1 *Masses in theoretical considerations*

In theoretical considerations, the mass of a halo is usually defined via the so called virial radius. We have discussed in Section 5.2 that spherical collapse predicts that virialised objects enclose a mean overdensity of roughly $\rho_{200} = 200 \times \bar{\rho}$. Hence, the virial radius is typically estimated by the radius of a sphere enclosing ρ_{200}, denoted by $R_{200,\mathrm{mean}}$. For preciseness, we differentiate here between $R_{200,\mathrm{mean}}$, which encloses a density of 200 times the *mean density*, and an alternative definition, $R_{200,\mathrm{crit}}$, which encloses a density of 200 times the *critical density* ρ_{cr} (Eq. 2.10), which is also frequently used. The virial mass is defined accordingly as

$$M_{200,\mathrm{crit}} = \frac{4\pi}{3} R^3_{200,\mathrm{crit}} \times 200 \rho_{\mathrm{cr}} \,. \tag{7.1}$$

Throughout the rest of this chapter, we will approximate the virial mass by $M_{200,\mathrm{crit}}$, since this convention was used by Neto et al. (2007), in which the concentration-mass relation is introduced, which will be used in Section 7.8. Furthermore, we drop the subscript "crit" for brevity.

7.1.2 *Masses in observations*

The results of imaging observations are typically two-dimensional maps. When it comes to cluster potential reconstructions through gravitational lensing, for example, the end product will be a potential- or mass map of the cluster. It seems therefore natural to characterise the mass of clusters simply by placing a circular aperture of a specified radius on the cluster centre and measure the enclosed mass, denoted by M_{ap}. Ideally, neglecting line-of-sight projections, this mass estimate would coincide with M_{200}, if the aperture radius was taken as R_{200}. However, first of all, the virial radius R_{200} has to be estimated from the potential map as well and can have quite a large error. Secondly, since we are dealing with the real Universe of course, there will be line-of-sight projections and mergers, such that other structures can contaminate the mass within the aperture

around the cluster of interest. Hence, it is often useful to choose a radius smaller than R_{200} in order to exclude such contaminations, especially when a second structure is clearly visible in the vicinity.

7.1.3 *Masses in simulations*

Halo masses in simulations typically depend on the method used to identify haloes. This is done usually by the help of structure finding algorithms. We will here focus on the algorithms used in the MXXL simulation introduced in Section 7.3. Structures are identified in the MXXL simulation using the well-known Friends-of-Friends (FoF) algorithm (Davis et al., 1985). It finds haloes by connecting all particles that are separated by less than a given linking length, b. The linking length is typically given in units of the mean interparticle separation and it was set to $b = 0.2$ in the MXXL simulation. This value is typically regarded to ensure that the mean density of FoF haloes corresponds to ~ 200 times the critical density ($\rho_{\mathrm{crit}} := 3H^2/(8\pi G)$)[1]. The mass of such a FoF halo is then given consequently as the summed mass of all particles assigned to the halo, which we will denote by M_{FoF}. In addition, also the R_{200}-radius has been determined for each FoF halo in the MXXL simulation and therefore also M_{200} is known. This allows for a more unbiased comparison with theoretical results.

Within these FoF haloes, substructures are identified in the MXXL simulation using the `SUBFIND` (Springel et al., 2001) algorithm. It identifies substructures by detecting saddle points in the halo's density distribution. It then assigns all particles to the subhalo that are within the isodensity contour that traverses a saddle point and it only assigns those particles to the substructure that are actually gravitationally bound to it. All other particles are assigned to the main halo. The summed mass of all particles assigned to the subhalo then gives the `SUBFIND` mass, which we will denote by M_{sub}.

7.2 ABELL 2744 – OBSERVATIONAL DATA

Abell 2744 is one of the most massive and most complex galaxy clusters in the Universe. It is located at a redshift of $z = 0.308$ and has a total mass of $\sim 3 \times 10^{15}\,\mathrm{M}_\odot$. At least seven massive substructures with masses $\gtrsim 5 \times 10^{13}\,\mathrm{M}_\odot$ have been found to reside in the cluster (Jauzac et al., 2016). Due to these distinctive properties, it has been the subject of a large number of investigations and observations in various wavebands (e.g. Merten et al., 2011; Owers et al., 2011; Eckert et al., 2015; Medezinski et al., 2016; Jauzac et al., 2016).

The analysis performed in this chapter is based on the reconstruction of the cluster's mass distribution obtained in Jauzac et al. (2016). The observational data sets used for this reconstruction comprise observations from the *Hubble Space Telescope* (HST), which

1 However, More et al. (2011) show that setting the linking length to $b = 0.2$ could in fact lead to haloes that enclose a significantly higher overdensity in the range ~ 250 to ~ 600.

Table 7.1: The eight substructures of Abell 2744. Column 1 gives the ID of the substructure, columns 2 and 3 give the position on the sky, column 4 gives the mass within a circular aperture of radius 150 kpc, column 5 gives the significance level of the detection in units of the variance (σ) in the mass map and column 6 gives the distance of the substructure from the Core's brightest cluster galaxy (BCG). The BCG is located at right ascension $\alpha = 3.586\,259°$ and declination $\delta = -30.400\,174°$. This table is based on Table 2 from Jauzac et al. (2016).

ID	R.A. (deg)	Dec. (deg)	$M(r < 150\,\mathrm{kpc})$ ($10^{13}\,\mathrm{M}_\odot$)	σ	D_{C-S} (kpc)
Core	3.58626	-30.40017	13.55 ± 0.09	150	-
N	3.57666	-30.35759	6.10 ± 0.50	12	708.4
NW	3.55310	-30.37676	7.90 ± 0.60	13	603.6
W_{bis}	3.54629	-30.40332	5.20 ± 0.60	9	565.3
S1	3.60412	-30.37465	5.00 ± 0.40	13	486.9
S2	3.59895	-30.35693	5.40 ± 0.50	11	728.5
S3	3.54151	-30.37378	6.50 ± 0.60	11	763.7
S4	3.52473	-30.36958	5.50 ± 1.20	5	1000.5

probe especially the inner region of the cluster for the strong lensing analysis, the *Canada-France-Hawaii Telescope* (CFHT) for the large-scale weak lensing analysis and the Wide Field Imager (WFI) at La Silla Observatory, Chile for photometric redshifts. The redshift data was supplemented by spectroscopic data from Owers et al. (2011). All these data were compiled to perform a combined strong and weak lensing analysis, which resulted in a map of Abell 2744's gravitational potential (see Fig. E.1 in Appendix E). The details of this reconstruction, including the selection of background galaxies, shape measurements and noise estimation, can be found in Jauzac et al. (2016).

The mass distribution given by the potential map allows determining Abell 2744's mass within a circular aperture of $R = 1.3$ Mpc, which is obtained to be $M(R < 1.3\,\mathrm{Mpc}) = (2.3 \pm 0.1) \times 10^{15}\,\mathrm{M}_\odot$.[2] Furthermore, the potential map reveals eight massive substructures within a distance of 1 Mpc from the cluster centre. All these substructures have masses $\gtrsim 5 \times 10^{13}\,\mathrm{M}_\odot$. We list the ID, position on the sky, mass, significance and distance of all eight substructures in Table 7.1, which was taken from Jauzac et al. (2016). However, Jauzac et al. (2016) caution that one of these substructures (W_{bis}) is probably a background structure projected onto the cluster, since it has a relatively high mass-to-light ratio and the spectroscopic redshifts of galaxies in its vicinity place it behind the cluster.

2 Note that this corresponds in fact to the mass contained in a cylinder of radius $R = 1.3$ Mpc, since it is inferred from the line-of-sight projected 2D-map. To infer the proper three-dimensional mass of the cluster itself, further assumptions about the shape and symmetry of the cluster need to be made.

We therefore make the conservative assumption that Abell 2744 contains at least seven massive substructures. We test the compatibility of Abell 2744 with the cosmological standard model by investigating if haloes of similar total mass taken from a large ΛCDM simulation contain a similar number of substructures as massive and as close to the centre as in Abell 2744.

7.3 THE MILLENNIUM XXL – SIMULATED DATA

7.3.1 *Simulation properties*

For this purpose, we use the Millennium XXL (MXXL) simulation (Angulo et al., 2012). The MXXL simulation is the third in the family of Millennium simulations. These simulate the content of a ΛCDM universe (dark matter only) with parameters chosen as $H_0 = 73\,\mathrm{km\,s^{-1}Mpc^{-1}}$, $\Omega_\Lambda = 0.75$, $\Omega_\mathrm{m} = \Omega_\mathrm{dm} + \Omega_\mathrm{b} = 0.25$, $\Omega_\mathrm{b} = 0.045$ and $\sigma_8 = 0.9$ (Springel et al., 2005; Boylan-Kolchin et al., 2009). The only difference between the simulations is given by the simulated volume and therefore their mass- and spatial resolution. The MXXL simulation, being the largest of the three, comprises a box of side length 4.3 Gpc. It is therefore large enough to contain multiple haloes of the mass of Abell 2744 at redshift $z \approx 0.3$. The dark matter fluid is sampled by 303 billion particles each having a mass of $m_\mathrm{p} = 8.80 \times 10^9\,\mathrm{M_\odot}$.[3]

During the simulation run, gravitationally bound structures were found by using the FoF algorithm and substructures within these haloes were identified by `SUBFIND`. The properties of the FoF and `SUBFIND` haloes were stored for 64 snapshots ranging from $z = 63$ to 0. The full information of all dark matter particles, i.e. their position and velocities, were stored only for four snapshots at redshifts $z = 0, 0.24, 1$ and 3. This data reduction was necessary, since storing the full particle data of all snapshots would have required an enormous storage space of about 700 TB. We will base our analysis on the FoF data sets as well as the full particle data at snapshot 54 ($z = 0.24$), which is the snapshot closest to the redshift of Abell 2744 for which the full particle data are available. We aim to use the particle data of the simulation to create cluster mass maps that are comparable to those obtained from observations. Using the same method when analysing observational and simulated mass maps allows us to perform a comparison in an as unbiased way as possible. In a second step, we then compare our findings with the `SUBFIND` data sets in Section 7.8.

3 Note that quantities from simulations are in the literature typically given in units with the dimensionless Hubble constant factored out (e.g. $h^{-1}\mathrm{Mpc}$, $h^{-1}\mathrm{M_\odot}$, …). In order to guarantee comparability of our results with the observational results, we do not follow this choice in this chapter, but we absorb factors of h into the units and adopt a value of $h = 0.7$ as in Jauzac et al. (2016).

7.3.2 *Mass maps from the MXXL simulation*

The projected mass maps for all MXXL haloes with a mass similar to Abell 2744 are obtained as follows. First, we select all FoF-haloes at redshift $z = 0.28$ with a mass of $M_{200} \geq 2.0 \times 10^{15}\,\mathrm{M}_\odot$. This represents a rather conservative mass cut, since it corresponds to the lower 3σ-bound of Abell 2744's mass within an aperture of 1.3 Mpc obtained in Jauzac et al. (2016). This radius, however, is smaller than the R_{200}-radius and therefore the M_{200}-mass of Abell 2744 can be assumed to be way larger. An extrapolation by Schwinn et al. (2017) in order to estimate Abell 2744's virial mass (M_{200}), led to $M_{200} = 3.3 \pm 0.2 \times 10^{15}\,\mathrm{M}_\odot$, which lies well above our lower threshold. The mass criterion defined above is fulfilled by 209 haloes in the MXXL simulation.

The particle data of the MXXL simulation can now be used to create projected mass maps of each halo. We use the snapshot closest to the redshift of Abell 2744 for which full particle data is available, i.e. the snapshot at $z = 0.24$. Mass maps are then generated by projecting all particles over a length of 30 Mpc on a 3×3 Mpc map and binning them into pixels of side length 4.55 kpc. This choice corresponds to the resolution of the mass map obtained for Abell 2744 in Jauzac et al. (2016). By varying the projection length, we found that the results of our analysis are fairly insensitive to the choice of 30 Mpc. A projection over 15 Mpc, for example, would not alter the conclusions of our analysis. We obtain for each halo three mass maps using either the x-, y- or z-axis as the line-of-sight. Due to the limited mass resolution of the MXXL simulation with a particle mass of $m_p = 8.80 \times 10^9\,\mathrm{M}_\odot$, the mass maps from the simulation are much more coarse-grained than those obtained from observations. In order to correct for this effect, we smooth all mass maps (that of Abell 2744 as well) with a Gaussian filter with a standard deviation of 1.5 pixels ($\sim$ 6.8 kpc). With these mass maps we can perform a comparison of simulated clusters and Abell 2744 on equal footing. For this purpose, we will use an algorithm based on the wavelet transform, which is introduced in the next section.

7.4 THE WAVELET TRANSFORM

In signal and data processing, typically the Fourier transform is used to isolate frequencies of interest, i.e. signal contributions of certain length or time scales. This, however, is done at the cost of losing any time or position information about the signal. An analysis in Fourier space is therefore most useful for stationary signals, but has only limited advantage for signals changing with time or position in a nonperiodic way. An alternative combining the best of both worlds is provided by the *wavelet transform* (WT) (Morlet et al., 1982; Daubechies, 1988; Mallat, 1989; Meyer, 1989). This transform allows filtering out specific frequencies of a signal without losing positional information (see e.g. the overviews by Rioul and Vetterli, 1991, and Jones, 2009, or the books of Daubechies, 1992, and Mallat, 2009 for a detailed introduction).

The wavelet decomposition can be used for both discrete signals, using the wavelet series expansion, and continuous signals using the continuous wavelet transform. The continuous wavelet transform of a signal $s(x)$ is defined via

$$W_s(a,b) = \frac{1}{\sqrt{a}} \int_{-\infty}^{+\infty} \psi\left(\frac{x-b}{a}\right) s(x)\,\mathrm{d}x, \tag{7.2}$$

where $\psi(x)$ represents the *mother wavelet function*, which is scaled by a parameter a and shifted by a parameter b. In other words, the wavelet transform is given by the convolution of a window function $\psi(x)$ with the signal function $s(x)$. By shifting this window function using the parameter b, the positional information of the original signal is preserved. Furthermore, the width of the filter governed by the scaling parameter a introduces a filter scale. The wavelet functions $\psi_{a,b}(x) = \psi\left(\frac{x-b}{a}\right)$ are chosen such that they form an orthonormal basis of L^2 (i.e. the space of square integrable functions). Furthermore, the mother wavelet function $\psi(x)$ needs to fulfil two conditions:

(*i*) it needs to have zero mean

$$\int_{-\infty}^{\infty} \psi(x)\,\mathrm{d}x = 0, \tag{7.3}$$

(*ii*) it needs to be normalised

$$||\psi(x)|| = \left[\int_{-\infty}^{\infty} |\psi(x)|^2\,\mathrm{d}x\right]^{1/2} = 1. \tag{7.4}$$

The combination of conditions (*i*) and (*ii*) requires $\psi(x)$ to be a localised, oscillatory function. Furthermore, it can be seen that the prefactor of $1/\sqrt{a}$ in Eq. (7.2) ensures that the scaled wavelet remains normalised according to condition (*ii*).

There exist many different choices for the mother wavelet in the literature. The most common ones are the Haar wavelet, the Mexican Hat wavelet, the Morlet wavelet, which is a complex valued wavelet, and the family of Daubechies wavelets (see e.g. Daubechies, 1992; Jones, 2009; Mallat, 2009). We show examples of these four wavelets in Fig. 7.1. The choice of the mother wavelet depends mainly on the signal to be analysed. The mother wavelet is chosen such that it best describes the signal that is to be isolated.

7.5 FINDING SUBSTRUCTURES USING THE WAVELET TRANSFORM

We can use this wavelet transform to devise an algorithm to identify the positions of all peaks on sub-cluster scales in the mass maps. This method would allow treating simulated and observed data alike. Hence, it prevents the results from being biased by the substructure finding algorithm used in the simulation, since these algorithms identify substructures on the basis of different criteria than those used in the observations. The

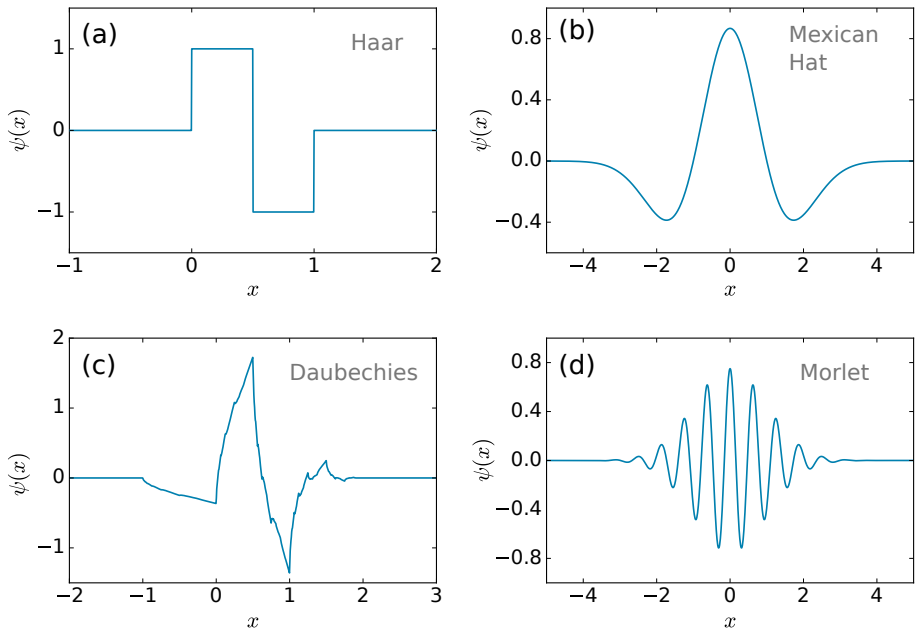

Figure 7.1: Examples of four of the most common mother wavelet functions: (a) Haar wavelet, (b) Mexican Hat wavelet, (c) Daubechies wavelet (with two vanishing moments) and (d) real part of the Morlet wavelet.

wavelet transform provides a convenient tool in this case, since it allows extracting the mass signal at the scale of interest, without losing the positional information as would be the case with a Fourier transform. It has been applied already in a number of studies to investigate cluster substructures (see e.g. Escalera and Mazure, 1992; Krywult et al., 1999; Flin and Krywult, 2006; Livermore et al., 2017). It is therefore our aim to use the coefficients of the wavelet transform (WT) to identify significant mass peaks in each mass map. We will then define a set of criteria including the scale of the WT and a threshold in the WT coefficients, which is tailored such that it selects only substructures that are as significant as those of Abell 2744.

In doing so, it is important to keep in mind that the projected substructure mass in the mass map actually consists of two components: (*i*) the mass gravitationally bound to the substructure and (*ii*) the background mass distribution of the host halo in which the substructure resides. The WT coefficients depend on both of these components and the host halo boosts the coefficients of the substructures. Hence, a small fluctuation close to the centre can have a higher coefficient than a substructure further away with a higher density peak in comparison to the local background. To avoid this, we fit the mass distribution of the main halo with an NFW density profile (Navarro et al., 1996) and subtract its contribution from the mass map before performing the wavelet transform. Although we fit the cluster by a spherically symmetric mass distribution, which gives only a rough estimate for a cluster undergoing a merger, it still minimizes the contamination

by the background halo. Due to the subsequent filtering with the wavelet transform, the remaining residuals do not play an important role, since they appear on larger length scales and have a smaller amplitude than the subhaloes that are to be extracted. A more precise modelling of the background halo could, however, even increase the sensitivity with which subhaloes can be detected.

To perform the wavelet transform, we use the publicly available 1D continuous wavelet transform module of the `PyWavelet` package[4]. We adopt the Mexican Hat wavelet as the mother wavelet function, since it matches best the shape expected for a density peak of a subhalo in comparison to other wavelets (see Fig. 7.1). In contrast, if a function closer to the actual density profile was chosen, the wavelet-conditions (Eqns. 7.3 and 7.4) would not be fulfilled. Since the 1D wavelet transform is used to analyse a 2D map, we apply the 1D wavelet transform row-wise and column-wise. The final WT coefficients are then obtained by taking the arithmetic mean of the row-wise and column-wise coefficients. We chose this approach, since it was comparably simple to implement and led to satisfactory results. It could be improved, however, by implementing a 2D wavelet transform. This should not alter the qualitative results we obtain, but it should increase the sensitivity to weak signals, since subhaloes can be filtered out better the more precisely they are modelled. It would, for example, prevent the striped patterns visible in Fig. 7.2.

With this map of WT coefficients at hand, substructures can be detected automatically. Based on the WT coefficients, we can define a quantitative criterion that determines which of the identified substructures can be considered to be equally significant as those of Abell 2744. This criterion consists of two parameters: the scale of the wavelet transform and the threshold for its coefficients, marking the threshold for the significance of the substructure. The values of these parameters are set such that our method recovers as many of the eight substructures of Abell 2744 found in Jauzac et al. (2016) as possible[5]. We adopt the following choice of parameters:

- a WT scale of 40 pixels, corresponding to 182 kpc and

- a threshold for WT coefficients of $W \geq 2.6 \times 10^{10}\,\mathrm{M}_{\odot}\mathrm{pc}^{-1}$.

The scale of the WT is set such that it maximises the coefficients of the peaks corresponding to Abell 2744's substructures. The threshold was set to the lowest WT coefficient value of these peaks. Applying this criterion to the mass maps obtained from the MXXL haloes ensures that the substructures found in the simulated mass maps are at least as significant as the substructures found in Abell 2744 and we do not include random fluctuations in our analysis.

In order to detect peaks in the mass maps using as little computational time as possible, we apply the following procedure. First, we select only those pixels that are at least 5

4 http://pywavelets.readthedocs.io

5 As discussed in Section 7.6.1, this choice recovers seven substructures and only fails to recover the *S1* substructure, which also does not show up as a prominent peak in the mass map.

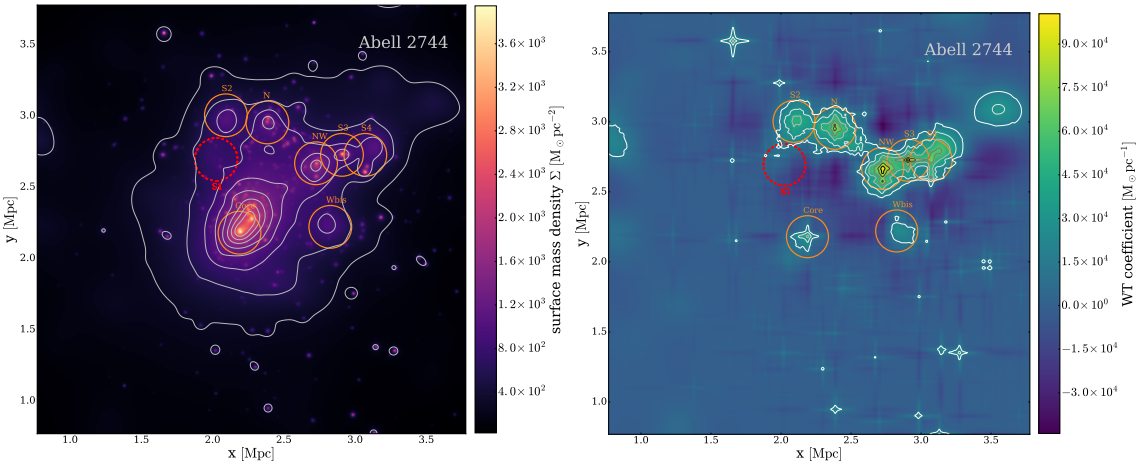

(a) (b)

Figure 7.2: Substructures of Abell 2744 identified automatically by using the wavelet transform. The *left* panel shows the mass map of Abell 2744 where the colour map and contours show the surface density. The *right* panel shows the wavelet transform coefficients computed as described in the text. Substructures fulfilling the defined threshold criteria are marked as orange circles with radius corresponding to $R = 150$ kpc. The *S1* substructure found in Jauzac et al. (2016) is highlighted as a red dashed circle.

times above the average WT coefficient of the map. We then select 20 per cent of these pixels randomly. This further helps us to save computational time and does not pose a problem, since we expect each subhalo to have ten or more pixels that are at least 5 times above the average WT coefficient. We then draw a circular aperture around the selected pixels with a radius of 100 kpc. Since this radius is smaller than the aperture used to determine the mass of the substructures (i.e. $R = 150$ kpc), it allows us to have slightly overlapping subhalo apertures. In each aperture around the randomly selected pixels, we select the pixel with the largest WT coefficient and change the centre of the aperture to this pixel. Since the local maximum could lie outside of the circle, i.e. when several circles were placed in the vicinity of the same subhalo, it is well possible that the maximal pixel lies at the edge of the aperture. We therefore perform this procedure iteratively ten times. This ensures that all peaks are found and that peaks have a minimal distance of 100 kpc to each other. We do not aim to find peaks closer than that, since they would have significantly overlapping apertures, preventing their masses from being determined independently. As a last step we discard all substructures with an aperture mass $M(R < 150 \text{ kpc}) < 3 \times 10^{13}\,\mathrm{M}_\odot$ or which are at a distance $R > 1.25$ Mpc from the halo centre, since they do not match the properties of the substructures found in Abell 2744.

7.6 RESULTS

7.6.1 *Abell 2744*

We apply the method specified above to the mass map obtained in Jauzac et al. (2016). As highlighted in Fig. 7.2, we are able to recover seven of the eight substructures they report. Our algorithm does not identify the *S1* substructure identified in both Medezinski et al. (2016) (where it was named *NE*) and Jauzac et al. (2016). Although this substructure produces a lensing signal with a high significance (13σ in Jauzac et al., 2016), it does not show up as a clearly visible peak in the mass map (see Fig. 7.2). Since our detection algorithm is based on the mass of substructures and their scale, it fails to identify this substructure. For this reason, we consider a cluster to be Abell 2744-like in terms of its substructure distribution, if at least six substructures[6] are found that:

(*i*) are identified by our wavelet transform algorithm with the above defined thresholds,

(*ii*) have an aperture mass of at least $M(R < 150\ \mathrm{kpc}) \geq 3 \times 10^{13}\,\mathrm{M}_{\odot}$,

(*iii*) have a projected distance not larger than 1.25 Mpc from the cluster centre.

7.6.2 *MXXL*

Exactly the same method is then applied to the mass maps obtained for the 209 MXXL haloes with a mass similar to Abell 2744 (as described in Section 7.3.2). We find three haloes that can be considered similar to Abell 2744 according to the criteria (*i*) - (*iii*). The mass maps of these three haloes are shown in Fig. 7.3 together with the maps of the corresponding WT coefficients. We list the properties (i.e. aperture mass, distance from the centre and WT coefficient) of all identified substructures in Table 7.2.

The first halo (*halo 37*) resembles the properties of Abell 2744 remarkably closely. The cluster has a mass of $M_{37}(R < 1.3\mathrm{Mpc}) = 2.61 \times 10^{15}\,\mathrm{M}_{\odot}$, similar to that of Abell 2744. Our wavelet transform algorithm identifies nine substructures within a projected distance of 1.2 Mpc. Sorting the subhaloes by descending projected mass and comparing the mass of each rank to its equivalent in Abell 2744 shows a maximal discrepancy of 23 per cent between their aperture masses. Furthermore, the central substructure seems to consist of two separate density peaks, very similar to the bimodal mass distribution of the core of Abell 2744 (Jauzac et al., 2015).

The second halo, *halo 95*, has a mass of $M_{95}(R < 1.3\mathrm{Mpc}) = 2.00 \times 10^{15}\,\mathrm{M}_{\odot}$ and is therefore the least massive of the three MXXL haloes. Also this cluster consists of nine substructures with an aperture mass higher than $3 \times 10^{13}\,\mathrm{M}_{\odot}$ within a distance of 1.0 Mpc from the centre. Comparing the substructures' aperture masses to those of Abell 2744

6 keeping in mind that W_{bis} is potentially a line-of-sight projection

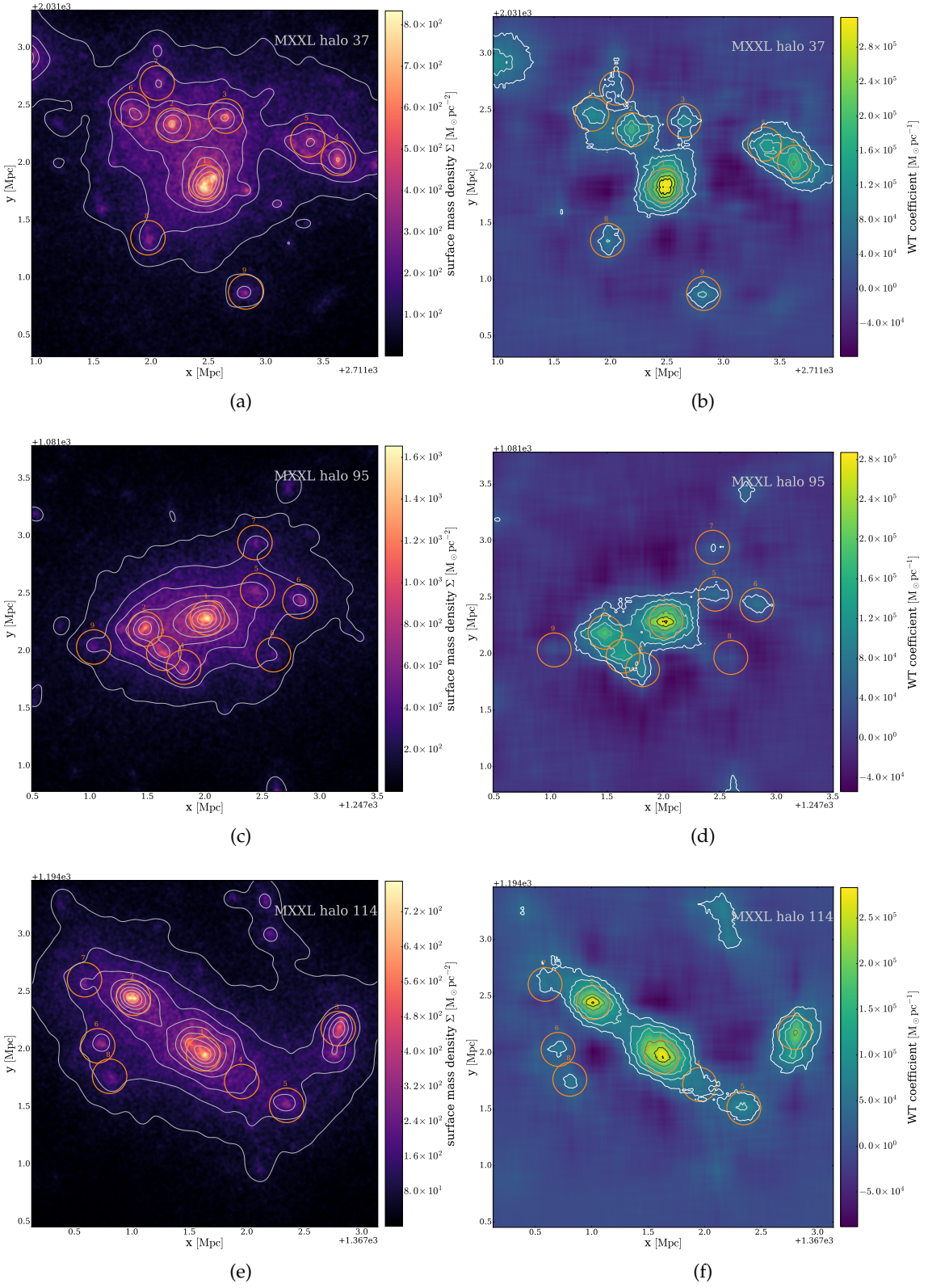

Figure 7.3: MXXL haloes 37, 95 and 114 which show a substructure distribution similar to that of Abell 2744. The panels on the *left* side show the mass maps of all haloes where the colour map and contours show the surface density. The contours show the map after being smoothed by a Gaussian with standard deviation of 8 pixels ($\sim$ 36.4 kpc). The *right* panels show the wavelet transform coefficients used to identify the substructures. Substructures fulfilling the threshold criteria are marked as orange circles with radius corresponding to $R = 150$ kpc.

Table 7.2: Properties of substructures found in Abell 2744 and in three MXXL clusters. For all clusters the mass within an aperture of 150 kpc, the distance from the cluster centre and the WT coefficient (wtc) of the centre pixel is given. The mass and distance from the centre for Abell 2744's substructures represent the values found by Jauzac et al. (2016).

	Abell 2744				*halo 37*			*halo 95*			*halo 114*		
ID	M_{150} [$10^{13}\,M_\odot$]	D_{C-S} [kpc]	wtc [$10^{10}\,M_\odot pc^{-1}$]	*ID*	M_{150} [$10^{13}\,M_\odot$]	D_{C-S} [kpc]	wtc [$10^{10}\,M_\odot pc^{-1}$]	M_{150} [$10^{13}\,M_\odot$]	D_{C-S} [kpc]	wtc [$10^{10}\,M_\odot pc^{-1}$]	M_{150} [$10^{13}\,M_\odot$]	D_{C-S} [kpc]	wtc [$10^{10}\,M_\odot pc^{-1}$]
Core	13.55 ± 0.09	-	4.88	1	12.90	-	31.50	11.30	-	28.70	10.70	-	28.30
NW	7.90 ± 0.60	604	10.00	2	8.85	576	18.00	8.49	525	19.40	9.50	787	28.30
S3	6.50 ± 0.60	764	9.75	3	7.28	615	11.80	7.22	466	15.10	6.05	1182	20.80
N	6.10 ± 0.50	708	8.04	4	6.97	1182	20.40	5.85	459	10.30	4.84	402	6.93
S4	5.50 ± 1.20	1001	6.99	5	6.73	974	14.20	5.13	522	6.86	4.24	842	8.94
S2	5.40 ± 0.50	729	2.61	6	6.37	902	11.20	4.11	841	7.68	4.09	934	6.77
W_{bis}	5.20 ± 0.60	565	4.91	7	5.00	967	5.94	3.25	793	4.75	4.00	1229	6.06
*S1**	5.00 ± 0.40	487	-	8	4.08	683	8.24	3.04	675	3.10	3.54	851	5.85
-	-	-	-	9	3.08	1008	9.12	3.03	997	3.01	-	-	-

* The substructure *S1* is not identified by the WT algorithm.

by sorting them in the same way as for *halo 37* shows a discrepancy of at most 40 per cent. The higher discrepancy in comparison to that of *halo 37* is due to the low masses of subhaloes *6* to *9*. These are somewhat less massive than the least massive substructures of Abell 2744. The masses of the six most massive substructures differ by less than 17 per cent from those of Abell 2744.

Finally, *halo 114* has a mass of $M_{114}(R < 1.3\text{Mpc}) = 2.10 \times 10^{15}\,\mathrm{M}_\odot$, which is slightly lower than the mass of Abell 2744. We found eight massive substructures within a radius of 1.25 Mpc from the centre. The substructures' masses differ by at most 30 per cent from those of Abell 2744's substructures. Especially the lower mass subhaloes, i.e. all apart from the two most massive ones, contain less mass than the substructures of Abell 2744.

It should be noted that the WT coefficients of almost all substructures in the MXXL simulation are considerably higher than those of Abell 2744. These values could be slightly overestimated due to the finite mass resolution of the MXXL simulation. Since the dark matter distribution of the MXXL simulation is traced by particles of mass $m_p = 8.80 \times 10^9\,\mathrm{M}_\odot$, the cluster mass maps are not as smooth as in the observational case. As described in Section 7.3.2, we correct for this effect by applying a Gaussian filter with a standard deviation of 1.5 pixels to each mass map from the MXXL simulation. This value was chosen such that the smoothing is gently enough to not remove any substructures.

In addition, we can use the mass maps to draw conclusions about Abell 2744's virial mass. In Schwinn et al. (2017), the virial mass was predicted to be $M_{200} = 3.3 \pm 0.2 \times 10^{15}\,\mathrm{M}_\odot$ by using the projection of a corresponding NFW-profile. We compare this prediction with the M_{200} masses of the three MXXL haloes listed above. The first halo (*halo 37*) has a mass of $M_{200,37} = 3.67 \times 10^{15}\,\mathrm{M}_\odot$, which is 40 per cent higher than its aperture mass within 1.3 Mpc. This agrees well with the prediction of Schwinn et al. (2017). However, the masses of both of the other clusters, $M_{200,95} = 2.55 \times 10^{15}\,\mathrm{M}_\odot$ and $M_{200,114} = 2.41 \times 10^{15}\,\mathrm{M}_\odot$, are 11 per cent and 12 per cent, respectively, lower than expected from an extrapolation using an NFW profile. Since all of these clusters are undergoing a merger, the cluster is far from being relaxed, which explains the deviation from the extrapolation using an NFW-profile. This suggests that also the virial mass of Abell 2744 is potentially lower than the value estimated in Schwinn et al. (2017) and should lie in the range of $M_{200,\mathrm{A2744}} \sim 2.5 - 3 \times 10^{15}\,\mathrm{M}_\odot$.

7.7 TIME EVOLUTION AND PROJECTION EFFECTS

An inevitable shortcoming of our work is the analysis of the simulation data at redshift $z = 0.24$, while Abell 2744 is located at $z = 0.306$, which corresponds to a time difference of roughly 600 Myr. This gap in the cluster evolution cannot be avoided, since the particle data of the MXXL simulation is not available for the redshift of Abell 2744. The only possibility to investigate the behaviour of the substructures in between these redshifts is

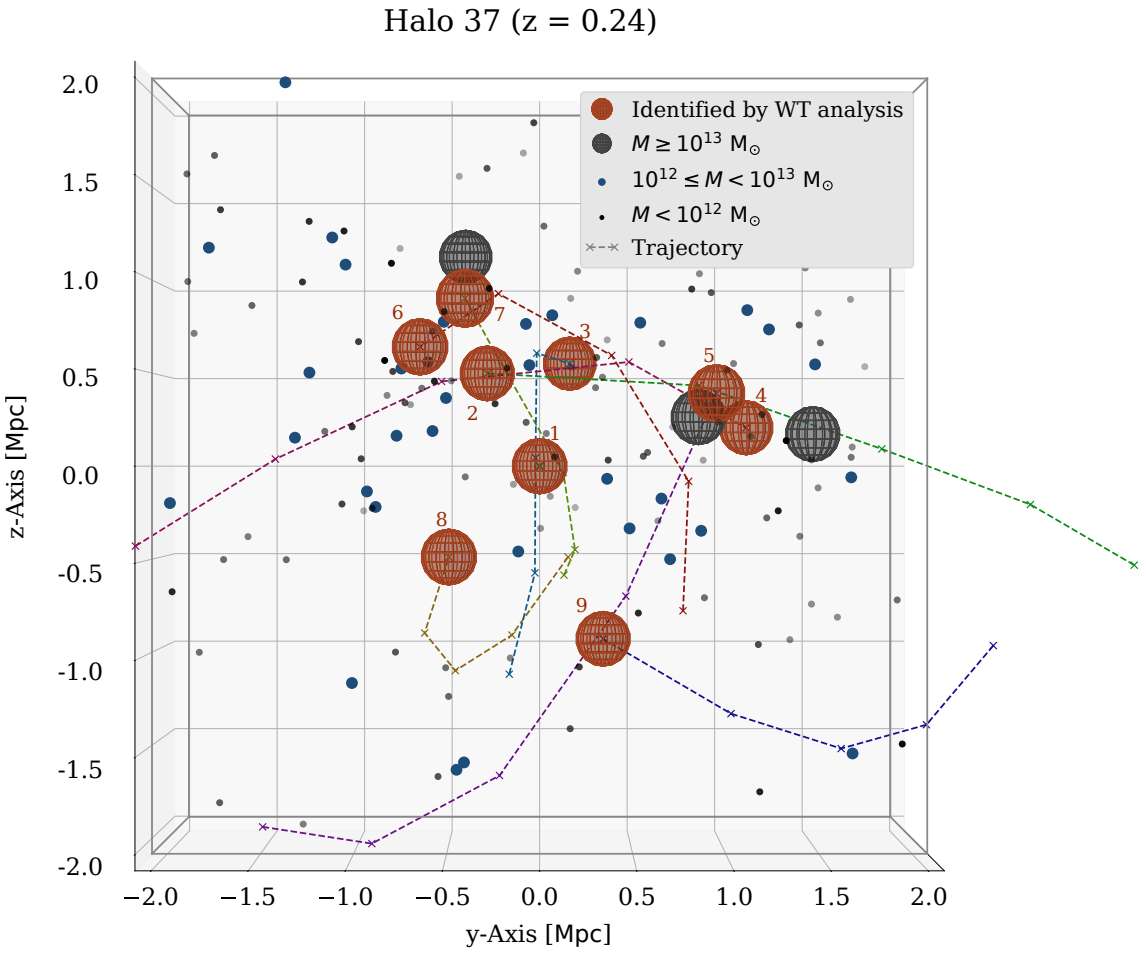

Figure 7.4: Time evolution of the substructures in MXXL *halo 37*. The SUBFIND-haloes corresponding to the nine substructures found by the WT algorithm are shown as red spheres with $R = 150\,\mathrm{kpc}$. Their trajectories between snapshot 50 ($z = 0.41$) and 54 ($z = 0.24$) are shown as dashed lines. The crosses highlight the positions at the corresponding snapshots. All other haloes are shown depending on their mass either as grey spheres, blue or black dots.

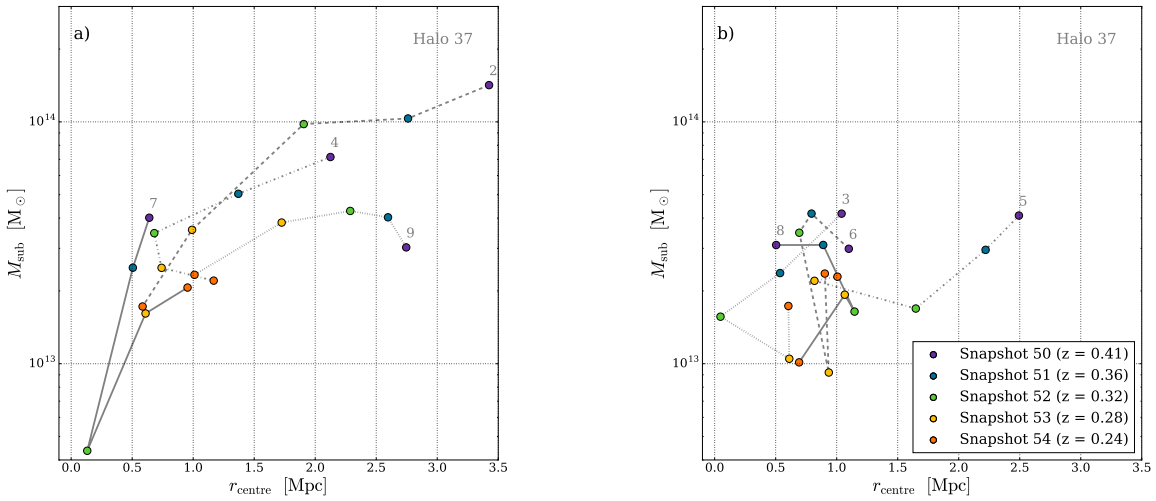

(a) (b)

Figure 7.5: Time evolution of the mass and radial distance of the subhaloes of *halo 37*. The *left* panel shows subhaloes *2*, *4*, *7* and *9*. The *right* panel shows subhaloes *3*, *5*, *6* and *8*. The five different snapshots (50-54) are colour coded as given in the legend. The radius is given as the distance from the position of the central halo.

to trace the substructures back in time using the merger trees available for the SUBFIND haloes. For this reason, we identify the closest SUBFIND halo for each substructure found by the wavelet transform algorithm. In cases where this leads to more than one possible candidate, we select the most massive subhalo. This allows us to predict the positions and masses of the substructures at $z = 0.3$.

We find for all substructures identified in *halo 37* the corresponding SUBFIND haloes. In case of *halo 95*, however, we find that only seven of the nine substructures have SUBFIND haloes at the position of the substructures in the mass map. There are no SUBFIND haloes for substructures *6* and *7*. The substructures with no corresponding SUBFIND halo are very likely line-of-sight projections. For *halo 114* we find SUBFIND haloes for 6 of 8 substructures. For substructures *3* and *4* there is no close SUBFIND halo.

7.7.1 *Change of distance during the infall*

Using these SUBFIND haloes, we track the movement of the substructures during their infall and investigate if they are already within a radius of 1.2 Mpc at $z = 0.3$. The time evolution of the SUBFIND haloes of MXXL *halo 37* is shown in Fig. 7.4. The trajectories of the infalling substructures are heavily affected by the ongoing merger and move by up to 1.9 Mpc between two snapshots. In order to determine the subhaloes' positions at $z = 0.3$ we interpolate the trajectories between the snapshots. At least seven of the

identified substructures can be found within a radius of 1.2 Mpc from the main halo at $z = 0.3$. In case of *halo 95*, the trajectories of the six identified subhaloes describe a merger similar to that of *halo 37*. In this case, only 4 of the 6 SUBFIND haloes are already within a radius of 1.2 Mpc at $z = 0.3$. Since there are no corresponding SUBFIND haloes for substructures *6* and *7*, there is no way to predict the position of these substructures at $z = 0.3$, unfortunately. The trajectories of the subhaloes of *halo 114* differ from the other two haloes. They do not have as perturbed trajectories, but they simply fall into the cluster. For this reason, the substructures are already close to the centre at $z = 0.3$. The maximum distance of the substructures from the central halo at $z = 0.3$ is 1.6 Mpc.

7.7.2 *Change of mass during the infall*

The identification of the SUBFIND haloes also allows us to investigate the mass evolution of the substructures. We can therefore test if any drastic mass changes occurred, such that they would not have been considered to be Abell 2744-like at $z = 0.3$. We show the mass evolution of the subhaloes of *halo 37* in Fig. 7.5 as an example. We consider the subhalo masses from five snapshots in the range from $z = 0.41$ to 0.24. For clarity, these are plotted in two panels each showing the evolution of four subhaloes. The subhaloes show a mixture of mass growth and mass being stripped away due to the infall. While some substructures (subhaloes 2, 4 and 9) are purely affected by tidal stripping during their infall, others (i.e. subhaloes 3, 5, 6, 7 and 8) also gain mass between one or two snapshots. The mass evolution of subhalo 7 reveals clearly the difficulties faced by SUBFIND to identify subhaloes that are very close to the cluster centre. It loses 90 per cent of its mass between snapshot 50 and 52 when it is very close to the centre. Being more distant again in snapshot 53, its mass is restored from 10 per cent back to 40 per cent of its initial mass at snapshot 50. This emphasises the problems of analysing masses of substructures close to the centre based on the SUBFIND data. These findings are in line with the recent results of Mao et al. (2018) and Han et al. (2017). The high fluctuations in the substructures' masses make it difficult to predict the mass change of the substructures between $z = 0.3$ and $z = 0.24$. Since the mass of 4 subhaloes decreased from $z = 0.3$ to 0.24, they have been most likely Abell 2744-like already at $z = 0.3$. In contrast, the masses of the central halo and subhalo 6 increased from $z = 0.3$ to 0.24. However, they increase only by 10 percent and 7 percent, respectively, which does not result in a tension with Abell 2744. Furthermore, the projected mass of subhalo 7 is not very likely to be affected as dramatically as the change in SUBFIND-mass suggests. Since it is much closer to the centre at $z = 0.3$, it is more likely that the projected aperture mass is even higher due to the additional contribution of the host halo. We therefore argue that it is likely to find at least seven substructures with similar aperture masses in *halo 37* at redshift $z = 0.3$.

7.7.3 *Projection effects*

Using the 3D information of the SUBFIND haloes, we can furthermore test the effect of line-of-sight projections on the formation of apparent 2D groups. Investigating the 3D positions of *halo 37*'s substructures shows that the identified substructures are distributed over a distance of almost 4 Mpc centred on the main halo. As expected, subhaloes appearing close to each other on the 2D map can be quite distant in 3D. While subhaloes *2*, *3*, *6* and *7* form a group in projection, they are distributed over a line-of-sight distance of 3.4 Mpc. We test as well, if the 2D map is influenced by another effect, i.e. the projection of multiple subhaloes onto one substructure on the map. Fig. 7.4 shows, however, that this effect is negligible in our case. Only subhalo 5 is affected by another close massive subhalo which appears as separate peak in the mass map in Fig. 7.3.

7.8 COMPARISON TO OTHER RECENT STUDIES – THE ROLE OF MASS ESTIMATES

Our results are in contrast to the recent analysis presented in Jauzac et al. (2016) and Schwinn et al. (2017), which suggested a potential tension between the substructure distribution of Abell 2744 and the predictions for a ΛCDM universe. This initial study, however, was based on FoF- and SUBFIND-haloes alone and did not use the full particle data of the MXXL simulation. The apparent tension was taken up by Mao et al. (2018) searching for haloes similar to Abell 2744 in a different simulation, i.e. the high resolution Phoenix cluster simulations (Gao et al., 2012). Investigating the particle data of the simulation directly, they found one halo with a similar substructure distribution to Abell 2744. Interestingly, they showed that a significant contribution to the subhalo masses, measured by an 150 kpc aperture around the substructure centres, comes in fact by the background mass distribution of the host halo. Additionally, a study by Han et al. (2017) found that the substructure masses can be significantly underpredicted by SUBFIND and thus be in part responsible for the apparent tension with ΛCDM that is found using subhalo masses alone.

We therefore put the results obtained with our wavelet algorithm in contrast to the results of Schwinn et al. (2017), where only the MXXL FoF- and SUBFIND-haloes were used. We focus especially on the role of the different mass estimates either from substructure finding algorithms like SUBFIND or from the particle data directly. We investigate if it is possible to find a relation between these estimates, which would allow translating one into the other.

7.8.1 *Comparison of aperture masses with SUBFIND masses*

We first compare the subhalo masses obtained by SUBFIND with the aperture masses of the substructures identified in the 2D-maps. These masses are listed for all substructures

Table 7.3: Comparison of different mass estimates for all substructures of *halo 37* apart from the central halo. The table lists subhalo ID (column 1), distance from the central halo (column 2), the mass measured within a 150 kpc aperture from the projected mass map (column 3), the mass provided by SUBFIND for the closest SUBFIND-halo (column 4), the mass of the host halo at the position of the substructure estimated assuming an NFW-profile (column 5) and the expected aperture mass assuming two NFW-profiles for the main halo and the SUBFIND subhalo (column 6).

ID	D_{C-S} (kpc)	$M(r < 150\,\mathrm{kpc})$ ($10^{13}\,\mathrm{M}_\odot$)	M_{sub} ($10^{13}\,\mathrm{M}_\odot$)	M_{host} ($10^{13}\,\mathrm{M}_\odot$)	M_{extr} ($10^{13}\mathrm{M}_\odot$)
2	576	8.85	1.72	3.80	4.79
3	615	7.28	1.73	3.35	4.35
4	1182	6.97	2.21	1.61	2.80
5	974	6.73	2.29	2.13	3.36
6	902	6.37	2.36	2.35	3.60
7	967	5.00	2.06	2.19	3.33
8	683	4.08	1.01	2.88	3.54
9	1008	3.08	2.33	2.03	3.27

of *halo 37* in Table 7.3. Similar to the analysis in Mao et al. (2018), we find that the aperture mass of the substructures can reach values up to five times their corresponding SUBFIND mass. Comparing the subhalo masses obtained by SUBFIND (Table 7.3, column 4) to those obtained in the mass map (Table 7.3, column 3) leads to up to 80 per cent lower SUBFIND masses than the masses measured within a 150 kpc-aperture. This additional mass comes most likely from line-of-sight projection of the background mass distribution of the main halo. It explains why no cluster with the same number of massive substructures as Abell 2744 was found in the study of Schwinn et al. (2017). Assuming that substructures have SUBFIND masses similar to their aperture masses led to setting a too high mass threshold when searching for substructures.

We now try to estimate if a relation between SUBFIND mass and aperture mass can be found. This would be extremely helpful, since many simulation snapshots consist only of FoF- and SUBFIND data for reasons of data compression. For this purpose, we model the aperture mass by considering two components, the background halo and the subhalo. We assume that both mass distributions are given by NFW profiles. The mass of the main halo is assumed to be $M_{200} = 3.67 \times 10^{15}\,\mathrm{M}_\odot$ and subhalo mass is estimated by setting $M_{200} = M_{\mathrm{sub}}$, where M_{sub} denotes the mass provided by SUBFIND. The NFW profiles are fixed through the respective masses by adopting the c-M_{200} relation presented in Neto et al. (2007). We then obtain the projected mass by integrating the sum of the subhalo

and host halo density profiles within a cylinder of length 30 Mpc (corresponding to the line-of-sight) and radius 150 kpc (corresponding to the radius of the aperture).

First, we are interested in how much this model predicts the host halo to contribute to the total aperture mass. The contribution of the host halo to the aperture mass is shown in Table 7.3, column 5. This estimate shows that it can contribute between 23 and 71 per cent of the aperture masses measured from the mass maps directly (column 3). Also this result corresponds to the conclusion that a substantial fraction of the aperture mass is due to the background mass distribution of the host halo.

We then compare the predictions of our model for the total aperture masses (i.e. the contributions of host halo and subhalo combined, see column 6 in Table 7.3) to the results from the actual mass maps. The extrapolated masses of all subhaloes apart from subhaloes 8 and 9 are considerably lower than the actual masses measured from the mass map directly. The extrapolation underestimates the projected mass by up to 60 per cent. This shows that the translation from subhalo masses measured with `SUBFIND` to projected masses within a 2D mass map is not possible. This is most likely due to the fact that the cluster is far from being relaxed and thus assuming spherical symmetry and an NFW-profile leads to incorrect results. Additionally an overprediction of tidal stripping by `SUBFIND` as reported in Muldrew et al. (2011) and Han et al. (2017) would as well lead to lower expected masses. We therefore conclude that only an analysis based on the particle data directly can lead to mass estimates that are comparable to those obtained from observations.

7.8.2 *Substructure finding based on SUBFIND*

We furthermore would like to put our results into context with those of Mao et al. (2018), which were based on the particle data of the Phoenix simulations. Their approach consisted of investigating the most massive halo in the simulation, which is the only halo in the simulation as massive as Abell 2744. They first identified all `SUBFIND` haloes with mass $M_{\rm sub} \geq 2.3 \times 10^{11}\,\mathrm{M}_{\odot}$. Then they used the particle data to compute aperture masses centred on these `SUBFIND` haloes for 24 different projections of the halo. By doing so they found at least three projections with eight and another one with nine substructures with properties comparable to Abell 2744.

While the first analysis presented in Schwinn et al. (2017) neglected the contribution of the host halo on the subhalo apertures, the method presented in Mao et al. (2018) could in fact exaggerate the influence of the host halo due to centring apertures on all `SUBFIND` halos above their mass threshold. As they state correctly, their method does not ensure that a halo found by `SUBFIND` is actually significant enough to be detected as a substructure in a weak lensing mass map. Since the host halo contributes such a large fraction to the total mass, Mao et al. (2018) are prone to picking up light subhaloes, to which the necessary aperture mass is provided mainly by the diffuse host halo mass. However, such a subhalo would not correspond to the substructures found in

the observation of Abell 2744. Furthermore, using only SUBFIND haloes can also lead to missing substructures. As discussed in Section 7.7, we find a number of substructures that show up as significant substructures in the mass map, but do not have a corresponding SUBFIND counterpart (e.g. because they are not gravitationally bound). Combining these results it seems advisable not to rely on SUBFIND data at all in this kind of comparison with observations, but to identify structures in a way that is as similar as possible to the observational approach.

7.8.3 *Artificial disruption of substructure*

Finally, we would like to address an additional, unrelated numerical issue. When investigating substructures in N-body simulations, it is important to keep in mind that not only their identification but also their evolution on particle data level can be altered by numerical effects. A very detailed investigation of the influence of parameter choices in the N-body simulation on the tidal disruption of subhaloes has been performed recently by van den Bosch, Frank C and Ogiya, Go (2018). Using the simplified setting of a subhalo on a circular orbit in a static, analytic host halo, they addressed the question of whether the tidal disruption of subhaloes has a physical or numerical origin. They find that mainly two effects have an important influence and cause a spurious disruption of subhaloes.

The first is due to the force softening parameter which is commonly introduced by hand in N-body simulations. It is set to prevent that the gravitational potential between two particles diverges when two particles approach each other. For this reason, a minimal distance ϵ is added quadratically to the separation of the two particles. Several studies exist on the optimal choice of this parameter (Kampen, 2000; Dehnen, 2001; Power et al., 2003). However, van den Bosch, Frank C and Ogiya, Go (2018) find that the commonly chosen values lead to a spurious disruption of subhaloes on orbits close to the centre.

The second effect is the amplification of discreteness noise by a runaway instability. Since the subhalo is represented by discrete particles, there exist different equivalent realisations of the same subhalo. If one of the realisations loses more mass through tidal stripping than the average, it expands more than average due to revirialisation. Thus, again more particles than average are beyond the subhalo's virial radius and get stripped away. This runaway instability leads to a large variance of the time it takes to disrupt the subhalo.

These effects also have the potential to influence the findings of our work. The severity of these effects depend mainly on the radial distance from the centre and how much mass has already been stripped away, i.e. how long the merging already has been going on. van den Bosch, Frank C and Ogiya, Go (2018) show drastic numerical effects for orbits close to the host halo centre (i.e. $R_{\rm orb} = 0.1 R_{\rm vir}$) for the later stages of the infall where the subhalo has already lost more than 90 per cent of its original mass. In our case, the majority of subhaloes are on orbits with $R_{\rm orb} > 400$ kpc. Since Abell 2744 has a virial radius of 2.8

Mpc, this corresponds to $R_{\rm orb} > 0.2R_{200}$. For these larger orbits, van den Bosch, Frank C and Ogiya, Go (2018) show that the numerical bias is still present, but less drastic, especially for the earlier phases of the infall where at least 10 per cent of the original subhalo mass is still gravitationally bound to the subhalo. In order to quantify their findings, van den Bosch, Frank C and Ogiya, Go (2018) give two equations to evaluate up to which bound mass fractions stripped subhaloes can be deemed trustworthy (their Eqns. 20 and 21). We evaluate these equations with the parameters of the MXXL simulation, i.e. particle mass $m_{\rm p} = 8.80 \times 10^9\,{\rm M}_\odot$ and softening length $\epsilon = 13.7$ kpc, and estimate the concentration of the subhaloes with the c-M relation of Neto et al. (2007). This allows us to assess if the substructures identified in the MXXL haloes are significantly influenced by numerical effects.

For this purpose, we need to assume the original mass of the subhaloes in order to assess how much of the subhalo mass has been stripped away already. However, this assumption has no effect on the qualitative nature of the result in our case. If we assume that the infalling subhaloes had an original mass of $M_{\rm orig} = 10^{14}\,{\rm M}_\odot$, we find that numerical processes become important when they are stripped down to a mass of $\sim 5 \times 10^{12}\,{\rm M}_\odot$. Choosing instead an even more conservative value, i.e. a considerably higher original mass of $M_{\rm orig} = 10^{15}\,{\rm M}_\odot$, we find that numerical effects begin to influence the subhalo's disruption significantly when the remaining mass is below $\sim 7.5 \times 10^{12}\,{\rm M}_\odot$. Since the substructures we are analysing still have considerably higher masses ($M_{\rm sub} \gtrsim 10^{13}\,{\rm M}_\odot$), i.e. they have not been stripped to this extend, we may assume that they are not significantly affected by numerical processes. However, it is worth having in mind on the basis of this discussion that substructures close to the centre of clusters are by no means exact representations of the true mass distribution, even if the particle data are analysed. It leaves the possibility that the subhalo masses in our analysis may be slightly underpredicted. It is therefore possible that in a simulation with smaller numerical effect, we would find even more substructures fulfilling our criteria.

7.9 CONCLUDING REMARKS

We have presented here a thorough investigation of the question if the high number of massive substructures in Abell 2744 is in conflict with the predictions of ΛCDM. We addressed this issue by analysing the MXXL simulation on the basis of its particle data. This allowed us to create projected mass maps similar to those available for Abell 2744, which we then analysed using a method based on the wavelet transform. In doing so, we attached great importance to treating observational and simulated data the same way in order to exclude systematic errors. We assessed the similarity to Abell 2744 on the basis of three criteria: (i) the substructure's distance from the centre, (ii) their projected mass within an aperture of 150 kpc radius and (iii) their significance in the mass map based on wavelet filtering. Based on this approach we were able to recover seven of

the eight substructures of Abell 2744 and we find three haloes in the MXXL simulation, that have both a total mass and a substructure distribution similar to that of Abell 2744. Since the simulation volume is ten times bigger than the volume out to z=0.306 and we find three similar clusters, the probability of finding Abell 2744 can be estimated to be approximately 30 per cent.

However, we would like to emphasise that we analysed the simulation at the redshift $z = 0.24$, which is different to that of Abell 2744 ($z = 0.3$). This simulation snapshot was that closest to $z = 0.3$ for which the full particle data is available. Since the difference between these redshifts corresponds to a timespan of roughly 600 Myr, it was important to make plausibility checks, if it is likely that the substructure distribution already had a similar configuration at the redshift of Abell 2744. To do so, we identified the SUBFIND halo corresponding to each substructure where possible. By tracing these back in time, we checked if their masses and positions changed in that period in a way that they would not be compatible with the substructure distribution of Abell 2744 at $z = 0.3$. We were able to demonstrate that this is not the case for at least one halo, *halo 37*, which was analysed exemplarily.

We furthermore put our results into the context of the findings of Schwinn et al. (2017), Mao et al. (2018) and van den Bosch, Frank C and Ogiya, Go (2018). We conclude that the apparent discrepancy discovered in Schwinn et al. (2017) can be traced back to the different mass definitions used in the observations (aperture mass) and the MXXL simulation (SUBFIND mass). We find that the aperture mass contains a large contribution by the mass of the host halo, which ranged from 23 to 71 per cent of the aperture mass. This also confirms the results of Mao et al. (2018). We furthermore showed that it is not possible to estimate the aperture mass on the basis of the SUBFIND mass and the host halo mass. This is most likely due to the perturbed state of the cluster, which does not allow describing the mass distribution on the basis of NFW profiles. We furthermore showed that the SUBFIND masses can show up a dramatic drop when the subhalo gets close to the halo centre, which was also discovered in Han et al. (2017). This can be explained by the method used by SUBFIND to identify substructures based on saddle points in the density distribution. This method breaks down as the main halo gets too dense in the centre to allow the identification of the subhalo. We therefore highly recommend using particle data directly to compare simulations to observations. We furthermore point out that it is important to analyse both observational and simulated data in the same way. We show that the analysis of Mao et al. (2018), which uses the particle data to obtain aperture masses, but SUBFIND data to identify substructures, could also be influenced by systematic effects. First, they do not know if their SUBFIND haloes would show up as a significant structure in the mass map and second they might miss a substructure if it does not have a SUBFIND counterpart. One possibility to avoid these issues is represented by the wavelet approach presented in this chapter.

8

CONCLUSION

Non-linear cosmic structures make up the majority of structures we can observe in the Universe today. While structure formation in the linear regime has been well-understood for several decades now, non-linear cosmic structures still harbour a rich, unexplored well of information, but are at the same time much harder to describe analytically. In this thesis, we investigated various aspects of non-linear cosmic structures with a focus on analytical descriptions and with the aim to use them for testing the cosmological standard model ΛCDM. In the first two parts, we focussed mainly on the analytic derivation of statistical properties of the cosmic density field in the non-linear regime, such as the probability distribution function (PDF) and the halo mass function. The third and last part focussed on the observed substructure distribution in the massive galaxy cluster Abell 2744. Here, we tested if the predictions of ΛCDM from the cosmological N-body simulation Millennium XXL are compatible with the observational data.

The first main part considered the one-point distribution of the cosmic density field, which corresponds to the PDF of density values at one point after it was marginalised over all field values at other points. It is a fundamental probe of the statistical properties of cosmic structures. It is furthermore required for deriving other theoretical predictions such as for example the halo mass function or merger rates. Deriving an analytical description of the density PDF promises a better understanding of the processes relevant to structure formation. At the same time, it would provide a test of ΛCDM with minimized systematic effects in comparison to simulations. We started with introducing the main concepts of cosmology and kinetic field theory (KFT), which is a novel analytic theory to describe cosmic structure formation on the basis of a generating functional. With the theoretical foundation at hand, we focussed on different ways to derive an analytic formula for the density PDF. As a first approach, we employed two models, i.e. the lognormal distribution and the generalised normal distribution, and fixed their free parameters with predictions of KFT. The lognormal model for the smoothed cosmic density contrast δ_R, for example, has only one free parameter. This parameter can be fixed by predicting the variance of the field (depending on the smoothing scale R), which can be obtained from the non-linear power spectrum of KFT. The generalised normal model for δ_R depends on two parameters, which can be fixed through the non-linear variance and the third cumulant. We introduce a first order approximation for the third cumulant in the framework of KFT, which is very similar to a result from standard perturbation theory and should be valid at least at mildly non-linear scales.

Subsequently, we explored a path to extract the density PDF from the generating functional of KFT directly. For this purpose, we used the resummed KFT (RKFT) approach of Lilow (2018) and introduced an indicator function in order to extract the PDF from the generating functional. Using the framework of RKFT and approximating the logarithmic action of the generating functional by a Taylor approximation up to second order, we are able to recover a Gaussian distribution for the PDF. This meets of course our expectations for an approximation of the exponent to second order. However, it is of limited use, since the non-linear regime we are interested in is highly non-Gaussian. We therefore see this approach only as the first step on the path towards a more realistic extraction of the non-linear density PDF from the generating functional. We extended this approach by including the next order of the Taylor expansion. Since in this case we cannot solve the path integral of the generating functional analytically any more, we approximate its result using an effective action. The results, however, are somewhat discouraging. It turns out quickly that the approximation to third order in the exponent leads to a diverging PDF. These findings are in line with the results of Sellentin (2015), who find that this can in fact be traced back to the slow convergence of the Taylor expansion of the logarithm. In order to correct for the problematic results of the low expansion orders, it would be necessary to expand well beyond the fourth order. This, however, does not seem feasible at the current stage, since already the third cumulant can only be obtained as a rough first order approximation. Furthermore, Carron and Neyrinck (2012) find that even all higher-order cumulants might be insufficient to describe a long-tailed distribution. This problem is also related to the Stieltjes moment problem (e.g. Stieltjes, 1894; Novi Inverardi et al., 2005). It states that the reconstruction of the PDF from its moments is only possible if further conditions are fulfilled. There exists a variety of necessary and sufficient conditions in the literature (Lin, 2017), such as the criterion $m_{k+1}/m_k = \mathcal{O}(k^2)$ as $k \to \infty$ just as one example, where m_k denotes the kth moment. In order to avoid these problems, we finally turned to yet another approach. We sketched an idea to describe the PDF asymptotically on the basis of the large deviation principle. We outlined a first ansatz, but we were not yet able to find a solution for the average $\langle \tilde{\lambda}_i \rangle_{i\in[1,3N]}$ appearing in the calculation, where $\tilde{\lambda}_i = \inf_{q_i} \lambda(q_i)$ and $\lambda(q_i)$ are the eigenvalues of the initial momentum-correlation matrix C_{pp}. We leave the continuation of this approach for future work.

In general, the extraction of the PDF from the generating functional remains a desirable target for the future. It seems that this should be possible at least in principle, since theoretically all higher-order cumulants can be derived from the generating functional. It therefore must also contain the information of the PDF itself. Since the path integral can only be solved for approximations of second order, it appears essential to build the approach on an effective action like that derived in Schmidt (2020), which was presented in Section 4.5. A very interesting path, i.e. that involving the large deviation principle, could only be covered very briefly. The large deviation principle can be applied to a surprisingly large variety of physical problems and can as well be linked to statistical

physics. It could therefore be a promising path to also find a link to KFT in the future, which could allow deriving the density PDF from the generating functional.

It should be added as well that in the framework of KFT deriving the density PDF represents an analogous problem to calculating the extrema of the density field. An extremum corresponds to those positions in the field where the response field (see Eq. 3.54) becomes $B = 0$ or $\phi_\beta = 0$ for the macroscopic dressed response field. Therefore, extracting from the generating functional the probability of the field having a density $\rho \in [\rho_0, \rho_0 + \mathrm{d}\rho]$ should make no difference mathematically to extracting the probability of the field having a response field in the range $B \in [-\epsilon, \epsilon]$ for ϵ being small. Therefore, finding a solution to the former problem, could lead to an analogous solution for the density of extrema from which the peak density might be deduced.

In the second part, we focussed on the halo mass function. The halo mass function is a frequently used quantity, since especially its high mass tail is exponentially sensitive to the cosmological parameters Ω_m and σ_8. Since its derivation includes the density PDF, we made use of some of the results of the preceding chapter. We started with an introduction of the current standard derivation of the halo mass function, i.e. the approach by Press and Schechter (1974) with its extension by Bond et al. (1991). This was followed by an in depth discussion of several assumptions in the derivation, which are known to be problematic. These are mainly the following four: (*i*) the assumption of spherical collapse, (*ii*) basing the derivation on linear extrapolation, (*iii*) using the excursion set approach and (*iv*) using mass as the observable of interest. For this reason, we aimed at deriving the halo mass function in an alternative way that overcomes some of these shortcomings. We therefore proposed an approach that discards assumptions (*i*) and (*ii*). Being based on the present day non-linear density field directly, our approach did not include linear evolution. Furthermore, we leave the overdensity threshold of haloes as a free parameter and do not need spherical collapse for this reason. Our approach was based on two of the non-linear PDF models introduced in the first part, i.e. the lognormal and the generalised normal model. It turned out advantageous that both of these models belong to the family of Gaussian distributions, which implies favourable analytic properties. We fixed the model parameters by the KFT predictions for the variance $\sigma^2(R)$ and third cumulant $\kappa_3(R)$.

Since we work on the level of the non-linear density field, the steps of the random walk in the excursion set approach cannot be assumed to be uncorrelated any more. For this reason we applied an approach based on correlated random walks, which was recently proposed in Musso and Sheth (2012). We calculated the halo mass function in two different regimes of correlated steps: (*i*) the *completely correlated limit* and (*ii*) the regime of *strongly correlated random walks*. Following the argument of Musso and Sheth (2014b), we furthermore had to mass-weight the walks to correct for the known fact that the lognormal model leads to a severe underestimation of the halo number density. These calculations were performed for each of the two PDF models separately. We obtained

for the generalised normal model in both of the correlation regimes, i.e. the completely correlated and the strongly correlated case, very good agreement with the Tinker mass function (a fit to N-body simulations), when a threshold of $\Delta = 2.9$ was chosen. The result agrees in particular well with the high mass tail of the halo mass function, where the Press-Schechter model deviates from the results found in simulations. Similar results were obtained with the lognormal model in both regimes. However, the agreement in the high mass tail is slightly worse than with the generalised normal model. While our value for Δ is still way smaller than the overdensity of real galaxy clusters, it is still further in the non-linear regime than the corresponding value of the Press-Schechter mass function. Furthermore, our improvement is of conceptual nature. We were able to present a fully analytic approach that is based on the present day non-linear density field and does not include spherical collapse, thus overcoming two of the shortcomings of the standard Press-Schechter approach. Our ansatz led to a closed form expression for the halo mass function with only one free parameter, i.e. the overdensity threshold Δ.

The discrepancy of the value of our parameter Δ and the real overdensity measured in virialised objects is somewhat expected, since the PDF models used in this approach are known to become inaccurate on small scales. This is in particular the case, since we use only a first order approximation for the third cumulant κ_3. A first step to improve on our result would therefore be a more precise prediction of κ_3. More generally, it would be desirable to find a better analytic description of the density PDF, in the best case from the generating functional of KFT directly. However, the obstacles on this route have been highlighted in the first part of the thesis. Moreover, it remains unclear if an approach based on excursion set statistics is the right way at all to follow, since it has been shown to have substantial deficits (e.g. Robertson et al., 2009). An alternative route would be an approach based on peak theory (Bardeen et al., 1986), which can also be modified such that mass as an observable is abandoned all together (Angrick and Bartelmann, 2009).

Finally we considered a more concrete example of non-linear structures, i.e. the substructure distribution in the massive galaxy cluster Abell 2744. In particular, we tested its compatibility with the predictions of ΛCDM by using the data of the cosmological simulation Millennium XXL (MXXL). Our analysis tied in with the findings of Schwinn et al. (2017), where a potential tension between the substructures of Abell 2744 and ΛCDM was found. However, this initial analysis was based on FoF- and `SUBFIND` haloes of the MXXL simulation alone. To enable a more comparable analysis of the observational and simulated data sets, we resorted to the particle data of the MXXL simulation in order to create 2D mass maps similar to those of Abell 2744. We then applied an approach based on the wavelet transform in order to define criteria to detect significant substructures in the mass maps. This allowed us to identify substructures in the mass map of Abell 2744 and in the MXXL-mass maps by the same method. On this basis, we found three haloes in the MXXL simulation with a substructure distribution similar to that of Abell 2744, therefore refuting a potential tension with ΛCDM.

Since the particle data were taken from a snapshot at $z = 0.24$, which was the snapshot closest to the redshift of Abell 2744 ($z = 0.3$) for which particle data were available, we added an analysis testing if we would expect substantial change in the substructure distribution between these redshifts. For this purpose, we identified (where possible) the corresponding SUBFIND haloes and traced their position and mass back to $z = 0.3$. We found that the substructures of at least one MXXL halo (*halo 37*) can be considered to be similar to those of Abell 2744 already at $z = 0.3$. The other two haloes did not allow such a conclusion, since not for all of their substructures corresponding SUBFIND haloes could be found. Finally, we investigated the reasons for the discrepancy between the results of Schwinn et al. (2017) and the analysis presented here. We found that this is mainly rooted in the incompatibility of SUBFIND masses and the aperture masses inferred from 2D mass maps. A similar result was recently found by Mao et al. (2018) and Han et al. (2017). We therefore concluded with some cautioning remarks concerning the comparison of observational data with SUBFIND haloes, especially with regard to halo masses. We emphasised the importance of analysing simulated and observational data with the same method, such as for example the wavelet method used in that chapter. For the future, it would be interesting to apply the sort of comparison developed in this work also to other massive clusters with substantial substructure, such as for example the *Hubble Frontier Field* clusters (Lotz et al., 2017) or "El Gordo" (Marriage et al., 2011; Menanteau et al., 2012). It could as well be applied to obtain subhalo mass functions from observational and simulated data in order to compare both data sets.

To conclude, we have examined various aspects of cosmic non-linear structures. These contain a great amount of information about the laws governing the evolution of the Universe which is still to be uncovered in the years to come. Still a lot more work is needed to obtain a more precise analytic description of its statistics, e.g. in terms of the PDF and the halo mass function. The interest in improving our understanding of the statistical properties of the cosmic density field is twofold. On the one hand, it is important to make as accurate predictions as possible in order to allow for meaningful tests of the cosmological standard model. On the other hand, a precise model of the statistics of the cosmic density field allows to measure cosmological parameters from observational data. Finally, simulations play a very important role to make cosmological predictions, but it is crucial to be aware of systematic effects that can easily creep into these kinds of analyses. It is therefore important to avoid such biases by analysing observational and simulated data with the same methods.

A

THE FREE CUMULANTS

We reproduce here the calculations of Appendix B of Lilow (2018) in order to calculate the free cumulants of a Hamiltonian system. Please note that we calculate here the cumulants with respect to the position space density ρ unlike the cumulants derived in Lilow (2018), which use the phase space density $f(q,p)$. We therefore need to set the $\vec{l}_r$-vectors appearing in Lilow (2018) to zero. These vectors are the Fourier conjugates to the momentum vectors and the index r runs from 1 to the number of phase space density operators applied. In contrast to Lilow (2018), we take here only the lowest order in initial correlations, $P_\delta^{(\mathrm{i})}$, into account that is not a shot-noise term. This means for example terms linear in $P_\delta^{(\mathrm{i})}$ for $G_{\rho\rho}$ and $G_{\rho\rho\mathcal{F}}$ and terms quadratic in $P_\delta^{(\mathrm{i})}$ for $G_{\rho\rho\rho}$. We can therefore also neglect the damping factor $e^{-\sigma_p^2/2\ \vec{L}^2_{p\{1,\ldots,n_\rho,1',\ldots,n'_\mathcal{F}\}}}$, which does not appear in this approximation. We will calculate here all 1-, 2- and 3-point cumulants.

As shown in Appendix A of Fabis (2015), we can use that the pure response field cumulants $G_{B\ldots B}$ vanish. Keeping in mind that $\hat{\mathcal{F}} = \sigma_{\rho B} \cdot \hat{B}$ and therefore the dressed response field cumulants are obtained by response field cumulants multiplied by factors of $\sigma_{\rho B}$ (Eq. 3.56) according to the number of $\hat{\mathcal{F}}$ operators applied. Hence also the pure dressed response field cumulants vanish,

$$G_\mathcal{F}(1) = 0\,, \tag{A.1}$$

$$G_{\mathcal{F}\mathcal{F}}(1,2) = 0\,, \tag{A.2}$$

$$G_{\mathcal{F}\mathcal{F}\mathcal{F}}(1,2,3) = 0\,. \tag{A.3}$$

We will follow the expressions in Appendix B of Lilow (2018) omitting the damping factor and setting

$$\vec{L}_{p\{1,1'\}}(t_1') = \vec{k}_1 g_{qp}(t_1,t_1')\,, \tag{A.4}$$

since we calculate cumulants for the position space density. We obtain

$$G_\rho(1) = (2\pi)^3 \delta_\mathrm{D}(\vec{k}_1)\bar{\rho}\,, \tag{A.5}$$

$$G_{\rho\rho}(1,2) = (2\pi)^3 \delta_\mathrm{D}(\vec{k}_1+\vec{k}_2)(1+g_{qp}(t_1,0))(1+g_{qp}(t_2,0))\bar{\rho}^2 P_\delta^{(\mathrm{i})}(\vec{k}_1)\,, \tag{A.6}$$

where we combined Eq. B.3 with B.16 of Appendix B in Lilow (2018) taking only those terms linear in $P_\delta^{(\mathrm{i})}$ and neglect all terms $\mathcal{O}\left((P_\delta^{(\mathrm{i})})^2\right)$. Furthermore, we get from Eq. B.2 of Lilow (2018)

$$G_{\rho\mathcal{F}}(1,2) = \mathrm{i}(2\pi)^3\delta_\mathrm{D}(\vec{k}_1+\vec{k}_2)\vec{k}_1^2\, g_{qp}(t_1,t_2)\bar{\rho}v(k_2,t_2)\,, \tag{A.7}$$

$$G_{\mathcal{F}\rho}(1,2) = G_{\rho\mathcal{F}}(2,1) \tag{A.8}$$

and finally

$$\begin{aligned} G_{\rho\mathcal{F}\mathcal{F}}(1,1',2') = -(2\pi)^3\delta_\mathrm{D}(\vec{k}_1+\vec{k}_{1'}+\vec{k}_{2'})\bar{\rho}\vec{k}_{1'}\cdot\left(\vec{k}_1 g_{qp}(t_1,t_{1'})+\vec{k}_{2'}g_{qp}(t_{2'},t_{1'})\right)\dots \\ \vec{k}_{2'}\cdot\left(\vec{k}_1 g_{qp}(t_1,t_{2'})+\vec{k}_{1'}g_{qp}(t_{1'},t_{2'})\right)v(\vec{k}_{1'},t_{1'})v(\vec{k}_{2'},t_{2'})\,, \end{aligned} \tag{A.9}$$

$$\begin{aligned} G_{\rho\rho\mathcal{F}}(1,2,1') = \mathrm{i}(2\pi)^3\delta_\mathrm{D}(\vec{k}_1+\vec{k}_2+\vec{k}_{1'})\bar{\rho}^2 v(k_{1'},t_{1'})\dots \\ \left[\vec{k}_{1'}\cdot\vec{k}_1 g_{qp}(t_1,t_{1'})P_\delta^{(\mathrm{i})}(k_2)\left(1-\frac{\vec{k}_2\cdot\left[\vec{k}_1 g_{qp}(t_1,t)+\vec{k}_{1'}g_{qp}(t_{1'},t)\right]}{\vec{k}_2^2}\right)\left(1+g_{qp}(t_2,t)\right)+\dots\right. \\ \left.\vec{k}_{1'}\cdot\vec{k}_2 g_{qp}(t_2,t_{1'})P_\delta^{(\mathrm{i})}(k_1)\left(1-\frac{\vec{k}_1\cdot\left[\vec{k}_2 g_{qp}(t_2,t)+\vec{k}_{1'}g_{qp}(t_{1'},t)\right]}{\vec{k}_1^2}\right)\left(1+g_{qp}(t_1,t)\right)\right]\,, \end{aligned} \tag{A.10}$$

$$G_{\rho\rho\rho}(1,2,3) = \mathrm{i}(2\pi)^3\delta_\mathrm{D}(\vec{k}_1+\vec{k}_2+\vec{k}_3)\bar{\rho}^3 C_3\left(\vec{L}_{\{1\}},\vec{L}_{\{2\}},\vec{L}_{\{3\}}\right)\,, \tag{A.11}$$

with

$$\begin{aligned} C_3\left(\vec{L}_{\{1\}},\vec{L}_{\{2\}},\vec{L}_{\{3\}}\right) &= P_\delta^{(\mathrm{i})}(k_1)P_\delta^{(\mathrm{i})}(k_2)\left(1+g_{qp}(t_1,t)\right)\left(1+g_{qp}(t_2,t)\right)\dots \\ &\quad\left(\frac{\vec{k}_1\cdot(\vec{k}_1+\vec{k}_2)g_{qp}(t_3,t)}{\vec{k}_1^2}+\frac{\vec{k}_2\cdot(\vec{k}_1+\vec{k}_2)g_{qp}(t_3,t)}{\vec{k}_2^2}+\frac{\vec{k}_1\cdot(\vec{k}_1+\vec{k}_2)\,\vec{k}_2\cdot(\vec{k}_1+\vec{k}_2)g_{qp}^2(t_3,t)}{\vec{k}_1^2\vec{k}_2^2}\right)\dots \\ &\quad+(\{1\}\leftrightarrow\{2\}\leftrightarrow\{3\}) \\ &= P_\delta^{(\mathrm{i})}(k_1)P_\delta^{(\mathrm{i})}(k_2)\left(1+g_{qp}(t_1,t)\right)\left(1+g_{qp}(t_2,t)\right)\dots \\ &\quad\left(2g_{qp}(t_3,t)+\vec{k}_1\cdot\vec{k}_2 g_{qp}(t_3,t)\left(\frac{1}{\vec{k}_1^2}+\frac{1}{\vec{k}_2^2}\right)+\frac{\vec{k}_1\cdot(\vec{k}_1+\vec{k}_2)\,\vec{k}_2\cdot(\vec{k}_1+\vec{k}_2)g_{qp}^2(t_3,t)}{\vec{k}_1^2\vec{k}_2^2}\right)\dots \\ &\quad+(\{1\}\leftrightarrow\{2\}\leftrightarrow\{3\})\,, \end{aligned} \tag{A.12}$$

using Eqns. B.2, B.4, B.6 and B.8 of Lilow (2018), where B.8 is an expansion up to second order in the initial density power spectra and we neglect all terms $\mathcal{O}\left((P_\delta^{(\mathrm{i})})^3\right)$.

B

CALCULATIONS FOR THE DERIVATION OF THE DENSITY PDF FROM THE GENERATING FUNCTIONAL

In this part of the appendix, we add the detailed calculations to the derivation of the density PDF in Chapter 4.3.

B.1 ADAPTING THE INDICATOR FUNCTION TO RKFT NOTATION

We start with rearranging the Gaussian indicator function defined in Eq. (4.23) such that it can be written in terms of the dot product appearing in the RKFT formalism (Eq. 3.59). The indicator function is given by

$$I_{\tilde{\rho}}\left(\phi_\rho(\vec{q}_0,t)\right) = e^{-\frac{\left(\phi_\rho(\vec{q}_0,t)-\tilde{\rho}\right)^2}{2\sigma^2}}\,. \tag{B.1}$$

We set $\vec{q}_0 = 0$ and introduce integrals over the $\vec{q}$ arguments in the exponent

$$I_{\tilde{\rho}}\left(\phi_\rho(0,t)\right) = e^{-\frac{1}{2\sigma^2}\iint \mathrm{d}^3\vec{q}_1\mathrm{d}^3\vec{q}_2\ \left(\phi_\rho(\vec{q}_1,t)-\tilde{\rho}\right)\left(\phi_\rho(\vec{q}_2,t)-\tilde{\rho}\right)\delta_\mathrm{D}(q_1)\delta_\mathrm{D}(q_2)}\,. \tag{B.2}$$

In order to phrase it in the language of the dot product, we express it in Fourier space

$$\tilde{I}_{\tilde{\rho}}\left(\phi_\rho\right) = e^{-\frac{1}{2\sigma^2}\iint \frac{\mathrm{d}^3\vec{k}_1}{(2\pi)^3}\frac{\mathrm{d}^3\vec{k}_2}{(2\pi)^3}\ \left(\phi_\rho(\vec{k}_1,t)-\tilde{\rho}(2\pi)^3\delta_\mathrm{D}(\vec{k}_1)\right)\left(\phi_\rho(\vec{k}_2,t)-\tilde{\rho}(2\pi)^3\delta_\mathrm{D}(\vec{k}_2)\right)} \tag{B.3}$$

and also introduce two time integrals

$$\begin{aligned}
&= e^{-\frac{1}{2\sigma^2}\iint \mathrm{d}1\,\mathrm{d}2\ \left(\phi_\rho(1)-\tilde{\rho}(2\pi)^3\delta_\mathrm{D}(\vec{k}_1)\right)\left(\phi_\rho(2)-\tilde{\rho}(2\pi)^3\delta_\mathrm{D}(\vec{k}_2)\right)\delta_\mathrm{D}(t_1-t)\delta_\mathrm{D}(t_2-t)} \\
&= e^{-\frac{1}{2\sigma^2}\left(\iint \mathrm{d}1\,\mathrm{d}2\ \phi_\rho(1)\phi_\rho(2)\delta_\mathrm{D}(t_1-t)\delta_\mathrm{D}(t_2-t)-2\int \mathrm{d}1\ \tilde{\rho}\phi_\rho(1))\delta_\mathrm{D}(t_1-t)\right)}e^{-\frac{\tilde{\rho}^2}{2\sigma^2}}\,.
\end{aligned} \tag{B.4}$$

We then define two auxiliary functions

$$\mathcal{W}_1(1) := \frac{\tilde{\rho}\delta_\mathrm{D}(t_1-t)}{\sigma^2}\,, \tag{B.5}$$

$$\mathcal{W}_2(1,2) := \frac{\delta_\mathrm{D}(t_1-t)\delta_\mathrm{D}(t_2-t)}{\sigma^2}\,, \tag{B.6}$$

which depend on the arguments 1 and 2 only formally, but allow us to finally write the exponent as a quadratic form in terms of the dot product. Note that we used $\mathcal{W}_1(1) = \mathcal{W}_1(-1)$ and $\mathcal{W}_2(1,2) = \mathcal{W}_2(-1,-2)$, since neither $\mathcal{W}_1$ nor $\mathcal{W}_2$ depends on $\vec{k}$.

In principle, the definition would require a minus sign in front of all of the arguments due to the definition of the dot product in Eq. (3.59). We thus get

$$\int \mathrm{d}1 \, \frac{\tilde{\rho}\delta_\mathrm{D}(t_1 - t)}{\sigma^2}\phi_\rho(1) = \int \mathrm{d}1 \mathcal{W}_1(-1)\phi_\rho(1) = \mathcal{W}_1 \cdot \phi_\rho, \tag{B.7}$$

$$\begin{aligned}\iint \mathrm{d}1\,\mathrm{d}2 \; \phi_\rho(1)\phi_\rho(2)\frac{\delta_\mathrm{D}(t_1 - t)\delta_\mathrm{D}(t_2 - t)}{2\sigma^2} \\ &= \iint \mathrm{d}1\,\mathrm{d}2 \; \frac{\phi_\rho(1)\mathcal{W}_2(-1,-2)\phi_\rho(2)}{2} \\ &= \frac{\phi_\rho \cdot \mathcal{W}_2 \cdot \phi_\rho}{2}\,.\end{aligned} \tag{B.8}$$

With this we can rewrite the indicator function as

$$\tilde{I}_{\tilde{\rho}}\left(\phi_\rho\right) = e^{\mathcal{W}_1 \cdot \phi_\rho - \frac{\phi_\rho \cdot \mathcal{W}_2 \cdot \phi_\rho}{2}} e^{-\frac{\tilde{\rho}^2}{2\sigma^2}}\,, \tag{B.9}$$

which is the form used in Eq. (4.27).

B.2 DETAILS OF THE SOLUTION FOR Δ_{12}

In this section, we show the detailed steps to obtain Eq. (4.52). We start with Eq. (4.48)

$$\begin{aligned}\Delta_{12}(1,\bar{1}) \cdot \Big[\mathrm{i}\mathcal{I}(-\bar{1},2) + (2\pi)^3\delta_\mathrm{D}(-\vec{k}_{\bar{1}} + \vec{k}_2)\tilde{G}_{\rho\mathcal{F}}(-k_{\bar{1}};t_{\bar{1}},t_2) - (2\pi)^3 \ldots \\ \delta_\mathrm{D}(-\vec{k}_{\bar{1}} + \vec{k}_{\bar{1}'})\tilde{G}_{\rho\rho}(-k_{\bar{1}};t_{\bar{1}},t_{\bar{1}'}) \cdot B^{-1}(-\bar{1}',\bar{1}'') \cdot \frac{\delta_\mathrm{D}(t_{\bar{1}''} - t)\delta_\mathrm{D}(t_2 - t)}{\sigma^2}\Big] \stackrel{!}{=} \mathcal{I}(1,2)\,.\end{aligned} \tag{B.10}$$

Plugging in our ansatz for $\Delta_{12}(1,\bar{1})$ from Eq. (4.49) and B^{-1} from Eq. (4.51) we can carry out all of the integrals

$$\begin{aligned}&\Big[-\mathrm{i}\left(\mathcal{I}(1,\bar{1}) + (2\pi)^3\delta_\mathrm{D}(\vec{k}_1 + \vec{k}_{\bar{1}})\tilde{\Delta}^{(1)}_{12}(k_1;t_1,t_{\bar{1}}) + \delta_\mathrm{D}(t_{\bar{1}} - t)\tilde{\Delta}^{(2)}_{12}(k_1,k_{\bar{1}};t_1;t) + \tilde{\Delta}^{(3)}_{12}(k_1,k_{\bar{1}};t_1,t_{\bar{1}};t)\right)\Big] \ldots \\ &\quad \ldots \cdot \Big[\mathrm{i}\left(\mathcal{I}(-\bar{1},2) - \mathrm{i}(2\pi)^3\delta_\mathrm{D}(-\vec{k}_{\bar{1}} + \vec{k}_2)\tilde{G}_{\rho\mathcal{F}}(-k_{\bar{1}};t_{\bar{1}},t_2) + (2\pi)^3\delta_\mathrm{D}(-\vec{k}_{\bar{1}} + \vec{k}_{\bar{1}'}) \ldots \right. \\ &\quad \left. \ldots \tilde{G}_{\rho\rho}(-k_{\bar{1}};t_{\bar{1}},t_{\bar{1}'}) \cdot \left(\mathcal{I}(-\bar{1}',\bar{1}'') + (2\pi)^3\delta_\mathrm{D}(-\vec{k}_{\bar{1}'} + \vec{k}_{\bar{1}''})\tilde{\Delta}_\mathrm{A}(-k_{\bar{1}'};t_{\bar{1}'},t_{\bar{1}''})\right) \cdot \tfrac{\delta_\mathrm{D}(t_{\bar{1}''} - t)\delta_\mathrm{D}(t_2 - t)}{\sigma^2}\right)\Big] \stackrel{!}{=} \mathcal{I}(1,2)\end{aligned}$$

$$\vdots$$

$$\vdots$$

$$\begin{aligned}
&\mathcal{I}(1,2) - \mathrm{i}(2\pi)^3\delta_{\mathrm{D}}(\vec{k}_1+\vec{k}_2)\tilde{G}_{\rho\mathcal{F}}(k_1;t_1,t_2) + (2\pi)^3\delta_{\mathrm{D}}(\vec{k}_1+\vec{k}_{\bar{1}'})\tilde{G}_{\rho\rho}(k_1;t_1,t_{\bar{1}'})\cdot\mathcal{I}(-\bar{1}',\bar{1}'')\cdot\tfrac{\delta_{\mathrm{D}}(t_{\bar{1}''}-t)\delta_{\mathrm{D}}(t_2-t)}{\sigma^2}\dots\\
&\quad\dots + (2\pi)^3\delta_{\mathrm{D}}(\vec{k}_1+\vec{k}_{\bar{1}'})\tilde{G}_{\rho\rho}(k_1;t_1,t_{\bar{1}'})\cdot(2\pi)^3\delta_{\mathrm{D}}(-\vec{k}_{\bar{1}'}+\vec{k}_{\bar{1}''})\tilde{\Delta}_{\mathrm{A}}(-k_{\bar{1}'};t_{\bar{1}'},t_{\bar{1}''})\cdot\tfrac{\delta_{\mathrm{D}}(t_{\bar{1}''}-t)\delta_{\mathrm{D}}(t_2-t)}{\sigma^2}\dots\\
&\quad\dots + (2\pi)^3\delta_{\mathrm{D}}(\vec{k}_1+\vec{k}_{\bar{1}})\tilde{\Delta}^{(1)}_{12}(k_1;t_1,t_{\bar{1}})\cdot\Big[\mathcal{I}(-\bar{1},2) - \mathrm{i}(2\pi)^3\delta_{\mathrm{D}}(-\vec{k}_{\bar{1}}+\vec{k}_2)\tilde{G}_{\rho\mathcal{F}}(-k_{\bar{1}};t_{\bar{1}},t_2) + (2\pi)^3\dots\\
&\qquad\dots\ \delta_{\mathrm{D}}(-\vec{k}_{\bar{1}}+\vec{k}_{\bar{1}'})\tilde{G}_{\rho\rho}(-k_{\bar{1}};t_{\bar{1}},t_{\bar{1}'})\cdot\Big(\mathcal{I}(-\bar{1}',\bar{1}'') + (2\pi)^3\delta_{\mathrm{D}}(-\vec{k}_{\bar{1}'}+\vec{k}_{\bar{1}''})\tilde{\Delta}_{\mathrm{A}}(-k_{\bar{1}'};t_{\bar{1}'},t_{\bar{1}''})\Big)\cdot\tfrac{\delta_{\mathrm{D}}(t_{\bar{1}''}-t)\delta_{\mathrm{D}}(t_2-t)}{\sigma^2}\Big]\\
&\quad\dots + \delta_{\mathrm{D}}(t_{\bar{1}}-t)\tilde{\Delta}^{(2)}_{12}(k_1,k_{\bar{1}};t_1;t)\cdot\Big[\mathcal{I}(-\bar{1},2) - \mathrm{i}(2\pi)^3\delta_{\mathrm{D}}(-\vec{k}_{\bar{1}}\vec{k}_2)\tilde{G}_{\rho\mathcal{F}}(-k_{\bar{1}};t_{\bar{1}},t_2) + (2\pi)^3\dots\\
&\qquad\dots\ \delta_{\mathrm{D}}(-\vec{k}_{\bar{1}}+\vec{k}_{\bar{1}'})\tilde{G}_{\rho\rho}(-k_{\bar{1}};t_{\bar{1}},t_{\bar{1}'})\cdot\Big(\mathcal{I}(-\bar{1}',\bar{1}'') + (2\pi)^3\delta_{\mathrm{D}}(-\vec{k}_{\bar{1}'}+\vec{k}_{\bar{1}''})\tilde{\Delta}_{\mathrm{A}}(-k_{\bar{1}'};t_{\bar{1}'},t_{\bar{1}''})\Big)\cdot\tfrac{\delta_{\mathrm{D}}(t_{\bar{1}''}-t)\delta_{\mathrm{D}}(t_2-t)}{\sigma^2}\Big]\\
&\quad\dots + \tilde{\Delta}^{(3)}_{12}(k_1,k_{\bar{1}};t_1,t_{\bar{1}};t)\cdot\Big[\mathcal{I}(-\bar{1},2) - \mathrm{i}(2\pi)^3\delta_{\mathrm{D}}(-\vec{k}_{\bar{1}}+\vec{k}_2)\tilde{G}_{\rho\mathcal{F}}(-k_{\bar{1}};t_{\bar{1}},t_2) + (2\pi)^3\dots\\
&\qquad\dots\ \delta_{\mathrm{D}}(-\vec{k}_{\bar{1}}+\vec{k}_{\bar{1}'})\tilde{G}_{\rho\rho}(-k_{\bar{1}};t_{\bar{1}},t_{\bar{1}'})\cdot\Big(\mathcal{I}(-\bar{1}',\bar{1}'') + (2\pi)^3\delta_{\mathrm{D}}(-\vec{k}_{\bar{1}'}+\vec{k}_{\bar{1}''})\tilde{\Delta}_{\mathrm{A}}(-k_{\bar{1}'};t_{\bar{1}'},t_{\bar{1}''})\Big)\cdot\tfrac{\delta_{\mathrm{D}}(t_{\bar{1}''}-t)\delta_{\mathrm{D}}(t_2-t)}{\sigma^2}\Big] \quad \stackrel{!}{=} \mathcal{I}(1,2)
\end{aligned}$$

$$\begin{aligned}
&-\mathrm{i}(2\pi)^3\delta_{\mathrm{D}}(\vec{k}_1+\vec{k}_2)\tilde{G}_{\rho\mathcal{F}}(k_1;t_1,t_2) + (2\pi)^3\delta_{\mathrm{D}}(\vec{k}_1+\vec{k}_{\bar{1}'})\tilde{G}_{\rho\rho}(k_1;t_1,t_{\bar{1}'})\cdot\tfrac{\delta_{\mathrm{D}}(t_{\bar{1}'}-t)\delta_{\mathrm{D}}(t_2-t)}{\sigma^2}\dots\\
&\dots + (2\pi)^3\delta_{\mathrm{D}}(\vec{k}_1+\vec{k}_{\bar{1}'})\tilde{G}_{\rho\rho}(k_1;t_1,t_{\bar{1}'})\cdot\tilde{\Delta}_{\mathrm{A}}(-k_{\bar{1}'};t_{\bar{1}'},t)\tfrac{\delta_{\mathrm{D}}(t_2-t)}{\sigma^2} + (2\pi)^3\delta_{\mathrm{D}}(\vec{k}_1+\vec{k}_2)\tilde{\Delta}^{(1)}_{12}(k_1;t_1,t_2)\dots\\
&\dots - \mathrm{i}(2\pi)^6\delta_{\mathrm{D}}(\vec{k}_1+\vec{k}_{\bar{1}})\tilde{\Delta}^{(1)}_{12}(k_1;t_1,t_{\bar{1}})\cdot\delta_{\mathrm{D}}(-\vec{k}_{\bar{1}}+\vec{k}_2)\tilde{G}_{\rho\mathcal{F}}(-k_{\bar{1}};t_{\bar{1}},t_2)\dots\\
&\dots + (2\pi)^3\delta_{\mathrm{D}}(\vec{k}_1+\vec{k}_{\bar{1}})\tilde{\Delta}^{(1)}_{12}(k_1;t_1,t_{\bar{1}})\cdot\Big[(2\pi)^3\delta_{\mathrm{D}}(-\vec{k}_{\bar{1}}+\vec{k}_{\bar{1}'})\tilde{G}_{\rho\rho}(-k_{\bar{1}};t_{\bar{1}},t_{\bar{1}'})\cdot\tfrac{\delta_{\mathrm{D}}(t_{\bar{1}'}-t)\delta_{\mathrm{D}}(t_2-t)}{\sigma^2}\dots\\
&\qquad\dots\ +(2\pi)^3\delta_{\mathrm{D}}(-\vec{k}_{\bar{1}}+\vec{k}_{\bar{1}'})\tilde{G}_{\rho\rho}(-k_{\bar{1}};t_{\bar{1}},t_{\bar{1}'})\cdot\tilde{\Delta}_{\mathrm{A}}(-k_{\bar{1}'};t_{\bar{1}'},t)\tfrac{\delta_{\mathrm{D}}(t_2-t)}{\sigma^2}\Big]\dots\\
&\dots + \delta_{\mathrm{D}}(t_2-t)\tilde{\Delta}^{(2)}_{12}(k_1,k_2;t_1;t) - \mathrm{i}(2\pi)^3\delta_{\mathrm{D}}(t_{\bar{1}}-t)\tilde{\Delta}^{(2)}_{12}(k_1,k_{\bar{1}};t_1;t)\cdot\delta_{\mathrm{D}}(-\vec{k}_{\bar{1}}+\vec{k}_2)\tilde{G}_{\rho\mathcal{F}}(-k_{\bar{1}};t_{\bar{1}},t_2)\dots\\
&\dots + \delta_{\mathrm{D}}(t_{\bar{1}}-t)\tilde{\Delta}^{(2)}_{12}(k_1,k_{\bar{1}};t_1;t)\cdot\Big[(2\pi)^3\delta_{\mathrm{D}}(-\vec{k}_{\bar{1}}+\vec{k}_{\bar{1}'})\tilde{G}_{\rho\rho}(-k_{\bar{1}};t_{\bar{1}},t_{\bar{1}'})\cdot\tfrac{\delta_{\mathrm{D}}(t_{\bar{1}'}-t)\delta_{\mathrm{D}}(t_2-t)}{\sigma^2}\dots\\
&\qquad\dots\ +(2\pi)^3\delta_{\mathrm{D}}(-\vec{k}_{\bar{1}}+\vec{k}_{\bar{1}'})\tilde{G}_{\rho\rho}(-k_{\bar{1}};t_{\bar{1}},t_{\bar{1}'})\cdot\tilde{\Delta}_{\mathrm{A}}(-k_{\bar{1}'};t_{\bar{1}'},t)\tfrac{\delta_{\mathrm{D}}(t_2-t)}{\sigma^2}\Big]\dots\\
&\dots + \tilde{\Delta}^{(3)}_{12}(k_1,k_2;t_1,t_2;t) - \mathrm{i}(2\pi)^3\tilde{\Delta}^{(3)}_{12}(k_1,k_{\bar{1}};t_1,t_{\bar{1}};t)\cdot\delta_{\mathrm{D}}(-\vec{k}_{\bar{1}}+\vec{k}_2)\tilde{G}_{\rho\mathcal{F}}(-k_{\bar{1}};t_{\bar{1}},t_2)\dots\\
&\dots + \tilde{\Delta}^{(3)}_{12}(k_1,k_{\bar{1}};t_1,t_{\bar{1}};t)\cdot\Big[(2\pi)^3\delta_{\mathrm{D}}(-\vec{k}_{\bar{1}}+\vec{k}_{\bar{1}'})\tilde{G}_{\rho\rho}(-k_{\bar{1}};t_{\bar{1}},t_{\bar{1}'})\cdot\tfrac{\delta_{\mathrm{D}}(t_{\bar{1}'}-t)\delta_{\mathrm{D}}(t_2-t)}{\sigma^2}\dots\\
&\qquad\dots\ +(2\pi)^3\delta_{\mathrm{D}}(-\vec{k}_{\bar{1}}+\vec{k}_{\bar{1}'})\tilde{G}_{\rho\rho}(-k_{\bar{1}};t_{\bar{1}},t_{\bar{1}'})\cdot\tilde{\Delta}_{\mathrm{A}}(-k_{\bar{1}'};t_{\bar{1}'},t)\tfrac{\delta_{\mathrm{D}}(t_2-t)}{\sigma^2}\Big] \qquad \stackrel{!}{=} 0\,.
\end{aligned} \tag{B.11}$$

Carry out all remaining integrals where possible

$$
\begin{aligned}
&-\mathrm{i}(2\pi)^3\delta_\mathrm{D}(\vec{k}_1+\vec{k}_2)\tilde{G}_{\rho\mathcal{F}}(k_1;t_1,t_2)+\tilde{G}_{\rho\rho}(k_1;t_1,t)\cdot\tfrac{\delta_\mathrm{D}(t_2-t)}{\sigma^2}\dots\\
&\dots+\int_{t_{\bar{1}'}}\tilde{G}_{\rho\rho}(k_1;t_1,t_{\bar{1}'})\tilde{\Delta}_\mathrm{A}(k_1;t_{\bar{1}'},t)\tfrac{\delta_\mathrm{D}(t_2-t)}{\sigma^2}\dots\\
&\dots+(2\pi)^3\delta_\mathrm{D}(\vec{k}_1+\vec{k}_2)\underline{\tilde{\Delta}^{(1)}_{12}(k_1;t_1,t_2)}-\mathrm{i}(2\pi)^3\delta_\mathrm{D}(\vec{k}_1+\vec{k}_2)\int_{t_{\bar{1}}}\underline{\tilde{\Delta}^{(1)}_{12}(k_1;t_1,t_{\bar{1}})}\tilde{G}_{\rho\mathcal{F}}(k_1;t_{\bar{1}},t_2)\dots\\
&\dots+\int_{t_{\bar{1}}}\underline{\tilde{\Delta}^{(1)}_{12}(k_1;t_1,t_{\bar{1}})}\tilde{G}_{\rho\rho}(k_1;t_{\bar{1}},t)\tfrac{\delta_\mathrm{D}(t_2-t)}{\sigma^2}+\int_{t_{\bar{1}}}\underline{\tilde{\Delta}^{(1)}_{12}(k_1;t_1,t_{\bar{1}})}\int_{t_{\bar{1}'}}\tilde{G}_{\rho\rho}(k_1;t_{\bar{1}},t_{\bar{1}'})\tilde{\Delta}_\mathrm{A}(k_1;t_{\bar{1}'},t)\tfrac{\delta_\mathrm{D}(t_2-t)}{\sigma^2}\\
&\dots+\delta_\mathrm{D}(t_2-t)\underline{\tilde{\Delta}^{(2)}_{12}(k_1,k_2;t_1;t)}-\mathrm{i}\underline{\tilde{\Delta}^{(2)}_{12}(k_1,k_2;t_1;t)}\tilde{G}_{\rho\mathcal{F}}(-k_2;t,t_2)\dots\\
&\dots+\int_{k_{\bar{1}}}\underline{\tilde{\Delta}^{(2)}_{12}(k_1,k_{\bar{1}};t_1;t)}\tilde{G}_{\rho\rho}(-k_{\bar{1}};t,t)\tfrac{\delta_\mathrm{D}(t_2-t)}{\sigma^2}+\int_{k_{\bar{1}}}\underline{\tilde{\Delta}^{(2)}_{12}(k_1,k_{\bar{1}};t_1;t)}\int_{t_{\bar{1}'}}\tilde{G}_{\rho\rho}(-k_{\bar{1}};t,t_{\bar{1}'})\tilde{\Delta}_\mathrm{A}(-k_{\bar{1}};t_{\bar{1}'},t)\tfrac{\delta_\mathrm{D}(t_2-t)}{\sigma^2}\\
&\dots+\underline{\tilde{\Delta}^{(3)}_{12}(k_1,k_2;t_1,t_2;t)}-\mathrm{i}(2\pi)^3\underline{\tilde{\Delta}^{(3)}_{12}(k_1,k_{\bar{1}};t_1,t_{\bar{1}};t)}\cdot\delta_\mathrm{D}(-\vec{k}_{\bar{1}}+\vec{k}_2)\tilde{G}_{\rho\mathcal{F}}(-k_{\bar{1}};t_{\bar{1}},t_2)^1\dots\\
&\dots+\int_{k_{\bar{1}}}\int_{t_{\bar{1}}}\underline{\tilde{\Delta}^{(3)}_{12}(k_1,k_{\bar{1}};t_1,t_{\bar{1}};t)}\tilde{G}_{\rho\rho}(-k_{\bar{1}};t_{\bar{1}},t)\tfrac{\delta_\mathrm{D}(t_2-t)}{\sigma^2}+\int_{k_{\bar{1}}}\int_{t_{\bar{1}}}\underline{\tilde{\Delta}^{(3)}_{12}(k_1,k_{\bar{1}};t_1,t_{\bar{1}};t)}\int_{t_{\bar{1}'}}\tilde{G}_{\rho\rho}(-k_{\bar{1}};t_{\bar{1}},t_{\bar{1}'})\tilde{\Delta}_\mathrm{A}(-k_{\bar{1}};t_{\bar{1}'},t)\tfrac{\delta_\mathrm{D}(t_2-t)}{\sigma^2}\overset{!}{=}0\,.
\end{aligned}
\tag{B.12}
$$

Note that we do not carry out the integrals containing $\tilde{\Delta}^{(3)}_{12}$ for reasons that become obvious in Eq. (B.14). In order to make it easier to match equal terms, we adopted the highlighting by different line styles from Eq. (4.52). We finally regroup the terms in order to single out the different δ_D dependencies so that we end up with Eq. (4.52), i.e.

$$
\begin{aligned}
&(2\pi)^3\delta_\mathrm{D}(\vec{k}_1+\vec{k}_2)\left[-\mathrm{i}\tilde{G}_{\rho\mathcal{F}}(k_1;t_1,t_2)+\underline{\tilde{\Delta}^{(1)}_{12}(k_1;t_1,t_2)}-\mathrm{i}\int_{t_{\bar{1}}}\underline{\tilde{\Delta}^{(1)}_{12}(k_1;t_1,t_{\bar{1}})}\tilde{G}_{\rho\mathcal{F}}(k_1;t_{\bar{1}},t_2)\right]\dots\\
&\dots+\tfrac{\delta_\mathrm{D}(t_2-t)}{\sigma^2}\Big[\tilde{G}_{\rho\rho}(k_1;t_1,t)+\int_{t_{\bar{1}'}}\tilde{G}_{\rho\rho}(k_1;t_1,t_{\bar{1}'})\tilde{\Delta}_\mathrm{A}(k_1;t_{\bar{1}'},t)+\int_{t_{\bar{1}}}\underline{\tilde{\Delta}^{(1)}_{12}(k_1;t_1,t_{\bar{1}})}\tilde{G}_{\rho\rho}(k_1;t_{\bar{1}},t)\dots\\
&\qquad\dots+\int_{t_{\bar{1}}}\int_{t_{\bar{1}'}}\underline{\tilde{\Delta}^{(1)}_{12}(k_1;t_1,t_{\bar{1}})}\tilde{G}_{\rho\rho}(k_1;t_{\bar{1}},t_{\bar{1}'})\tilde{\Delta}_\mathrm{A}(k_1;t_{\bar{1}'},t)+\sigma^2\underline{\tilde{\Delta}^{(2)}_{12}(k_1,k_2;t_1;t)}\dots\\
&\qquad\dots+\int_{k_{\bar{1}}}\underline{\tilde{\Delta}^{(2)}_{12}(k_1,k_{\bar{1}};t_1;t)}\tilde{G}_{\rho\rho}(-k_{\bar{1}};t,t)+\int_{k_{\bar{1}}}\underline{\tilde{\Delta}^{(2)}_{12}(k_1,k_{\bar{1}};t_1;t)}\int_{t_{\bar{1}'}}\tilde{G}_{\rho\rho}(-k_{\bar{1}};t,t_{\bar{1}'})\tilde{\Delta}_\mathrm{A}(-k_{\bar{1}};t_{\bar{1}'},t)\dots\\
&\qquad\dots+\int_{k_{\bar{1}}}\int_{t_{\bar{1}}}\underline{\tilde{\Delta}^{(3)}_{12}(k_1,k_{\bar{1}};t_1,t_{\bar{1}};t)}\tilde{G}_{\rho\rho}(-k_{\bar{1}};t_{\bar{1}},t)+\int_{k_{\bar{1}}}\int_{t_{\bar{1}}}\underline{\tilde{\Delta}^{(3)}_{12}(k_1,k_{\bar{1}};t_1,t_{\bar{1}};t)}\int_{t_{\bar{1}'}}\tilde{G}_{\rho\rho}(-k_{\bar{1}};t_{\bar{1}},t_{\bar{1}'})\tilde{\Delta}_\mathrm{A}(-k_{\bar{1}};t_{\bar{1}'},t)\Big]\dots\\
&\dots-\mathrm{i}\underline{\tilde{\Delta}^{(2)}_{12}(k_1,k_2;t_1;t)}\tilde{G}_{\rho\mathcal{F}}(-k_2;t,t_2)+\underline{\tilde{\Delta}^{(3)}_{12}(k_1,k_2;t_1,t_2;t)}-\mathrm{i}(2\pi)^3\underline{\tilde{\Delta}^{(3)}_{12}(k_1,k_{\bar{1}};t_1,t_{\bar{1}};t)}\cdot\delta_\mathrm{D}(-\vec{k}_{\bar{1}}+\vec{k}_2)\tilde{G}_{\rho\mathcal{F}}(-k_{\bar{1}};t_{\bar{1}},t_2)\overset{!}{=}0\,.
\end{aligned}
\tag{B.13}
$$

B.3 DERIVING $\tilde{\Delta}_{12}^{(3)}$

We continue with showing the steps for deriving $\tilde{\Delta}_{12}^{(3)}$. We start with Eq. (4.55)

$$\begin{aligned}\tilde{\Delta}_{12}^{(3)}(k_1,k_2;t_1,t_2;t) &= \mathrm{i}\,\underline{\tilde{\Delta}_{12}^{(2)}}(k_1,\underline{k_2};t_1;t)\,\underline{\tilde{G}_{\rho\mathcal{F}}}(-k_2;t,t_2)\ldots \\ &\quad \ldots + \mathrm{i}\,\tilde{\Delta}_{12}^{(3)}(k_1,k_2;t_1,t_{\bar{1}};t)\cdot \underbrace{(2\pi)^3\delta_{\mathrm{D}}(-k_{\bar{1}}+k_2)\tilde{G}_{\rho\mathcal{F}}(-k_2;t_{\bar{1}},t_2)}_{=G_{\rho\mathcal{F}}(\bar{1},2)}\,,\end{aligned} \tag{B.14}$$

where we reintroduce $G_{\rho\mathcal{F}}$ in the last term in order to bring it to the left side

$$\tilde{\Delta}_{12}^{(3)}(k_1,k_{\bar{1}};t_1,t_{\bar{1}};t)\cdot \underbrace{\left(\mathcal{I}(\bar{1},2)-\mathrm{i}G_{\rho\mathcal{F}}(\bar{1},2)\right)}_{=\Delta_{\mathrm{R}}^{-1}(\bar{1},2)} = \mathrm{i}\,\underline{\tilde{\Delta}_{12}^{(2)}}(k_1,\underline{k_2};t_1;t)\,\underline{\tilde{G}_{\rho\mathcal{F}}}(-k_2;t,t_2)\,. \tag{B.15}$$

This allows us to identify the second factor on the left-hand side with the definition of the inverse retarded propagator from Lilow (2018), see also Eq. (4.65). This finally leads to

$$\tilde{\Delta}_{12}^{(3)}(k_1,k_{\bar{1}};t_1,t_{\bar{1}};t) = \mathrm{i}\,\underline{\tilde{\Delta}_{12}^{(2)}}(k_1,\underline{k_2};t_1;t)\,\underline{\tilde{G}_{\rho\mathcal{F}}}(-k_2;t,t_2)\cdot\Delta_{\mathrm{R}}(2,\bar{1})\,. \tag{B.16}$$

Renaming and plugging in Robert's ansatz for Δ_{R} (i.e. Eq. 4.51)

$$\begin{aligned}\tilde{\Delta}_{12}^{(3)}(k_1,k_2;t_1,t_2;t) &= \mathrm{i}\,\underline{\tilde{\Delta}_{12}^{(2)}}(k_1,\underline{k_{\bar{1}}};t_1;t)\,\underline{\tilde{G}_{\rho\mathcal{F}}}(-k_{\bar{1}};t,t_{\bar{1}})\cdot\ldots \\ &\quad \ldots\left(\mathcal{I}(-\bar{1},2)+(2\pi)^3\delta_{\mathrm{D}}(-\vec{k}_{\bar{1}}+\vec{k}_2)\tilde{\Delta}_{\mathrm{R}}(-k_{\bar{1}};t_{\bar{1}},t_2)\right)\,,\end{aligned} \tag{B.17}$$

which can be simplified to

$$\tilde{\Delta}_{12}^{(3)}(k_1,k_2;t_1,t_2;t) = \mathrm{i}\,\underline{\tilde{\Delta}_{12}^{(2)}}(k_1,\underline{k_2};t_1;t)\left(\tilde{G}_{\rho\mathcal{F}}(-k_2;t,t_2)+\int_{t_1}\tilde{G}_{\rho\mathcal{F}}(-k_2;t,t_{\bar{1}})\tilde{\Delta}_{\mathrm{R}}(-k_2;t_{\bar{1}},t_2)\right)\,. \tag{B.18}$$

Since $\tilde{\Delta}_{\mathrm{R}}$ is an infinite series of convolutions of $\tilde{G}_{\rho\mathcal{F}}$, the term in brackets just gives $-\mathrm{i}\tilde{\Delta}_{\mathrm{R}}$

$$\tilde{\Delta}_{12}^{(3)}(k_1,k_2;t_1,t_2;t) = \underline{\tilde{\Delta}_{12}^{(2)}}(k_1,\underline{k_2};t_1;t)\,\tilde{\Delta}_{\mathrm{R}}(-k_2;t,t_2)\,, \tag{B.19}$$

which is the result presented in Eq. (4.57).

B.4 DERIVING Δ_{11}

Here, we present the steps for deriving Δ_{11}. We will start with Eq. (4.64)

$$\Delta_{11}(1,2) = -C^{-1}(1,\bar{1}) \cdot D(-\bar{1},\bar{1}') \cdot \Delta_{21}(-\bar{1}',2) \tag{B.20}$$

and use that we can write C^{-1} in terms of the retarded propagator from Lilow (2018) (see Eq. 4.66)

$$C^{-1}(-\bar{1}',\bar{1}'') = -\mathrm{i}\left[\mathcal{I} - \mathrm{i}G_{\rho\mathcal{F}}\right]^{-1}(-\bar{1}',\bar{1}'') = -\mathrm{i}\Delta_{\mathrm{R}}(-\bar{1}',\bar{1}'') \tag{B.21}$$

$$= -\mathrm{i}\left(\mathcal{I}(-\bar{1}',\bar{1}'') + (2\pi)^3\delta_{\mathrm{D}}(-\vec{k}_{\bar{1}'} + \vec{k}_{\bar{1}''})\tilde{\Delta}_{\mathrm{R}}(-k_{\bar{1}'};t_{\bar{1}'},t_{\bar{1}''})\right). \tag{B.22}$$

Inserting this result together with D (Eq. 4.38) and Δ_{21} (Eq. 4.43) into Eq. (4.64) leads to

$$\begin{aligned}
\Delta_{11}(1,2) &= -C^{-1}(1,\bar{1}) \cdot D(-\bar{1},\bar{1}') \cdot \Delta_{21}(-\bar{1}',2) \\
&= -C^{-1}(1,\bar{1}) \cdot D(-\bar{1},\bar{1}') \cdot \Delta_{12}(2,-\bar{1}') \\
&= \mathrm{i}\left(\mathcal{I}(1,\bar{1}) + (2\pi)^3\delta_{\mathrm{D}}(\vec{k}_1 + \vec{k}_{\bar{1}})\tilde{\Delta}_{\mathrm{R}}(k_1;t_1,t_{\bar{1}})\right) \cdot (2\pi)^3\delta_{\mathrm{D}}(-\vec{k}_{\bar{1}} + \vec{k}_{\bar{1}'})\tilde{G}_{\rho\rho}(k_{\bar{1}};t_{\bar{1}},t_{\bar{1}'}) \dots \\
&\quad \dots \cdot (-\mathrm{i})\left(\mathcal{I}(2,-\bar{1}') + (2\pi)^3\delta_{\mathrm{D}}(-\vec{k}_{\bar{1}'} + \vec{k}_2)\tilde{\Delta}^{(1)}_{12}(k_2;t_2,t_{\bar{1}'}) + \delta_{\mathrm{D}}(t_{\bar{1}'} - t)\tilde{\Delta}^{(2)}_{12}(k_2,-k_{\bar{1}'};t_2;t) + \tilde{\Delta}^{(3)}_{12}(k_2,-k_{\bar{1}'};t_2,t_{\bar{1}'};t)\right) \\
&= \left((2\pi)^3\delta_{\mathrm{D}}(\vec{k}_1 + \vec{k}_{\bar{1}})\delta_{\mathrm{D}}(t_1 - t_{\bar{1}}) + (2\pi)^3\delta_{\mathrm{D}}(\vec{k}_1 + \vec{k}_{\bar{1}})\tilde{\Delta}_{\mathrm{R}}(k_1;t_1,t_{\bar{1}})\right) \cdot \left((2\pi)^3\delta_{\mathrm{D}}(-\vec{k}_{\bar{1}} + \vec{k}_2)\tilde{G}_{\rho\rho}(k_{\bar{1}};t_{\bar{1}},t_2) \dots\right. \\
&\quad \dots + (2\pi)^3\delta_{\mathrm{D}}(-\vec{k}_{\bar{1}} + \vec{k}_2)\int_{t_{\bar{1}'}} \tilde{G}_{\rho\rho}(k_{\bar{1}};t_{\bar{1}},t_{\bar{1}'})\tilde{\Delta}^{(1)}_{12}(k_2;t_2,t_{\bar{1}'}) + \tilde{G}_{\rho\rho}(k_{\bar{1}};t_{\bar{1}},t)\tilde{\Delta}^{(2)}_{12}(k_2,-k_{\bar{1}};t_2;t) \dots \\
&\quad \left. \dots + \int_{t_{\bar{1}'}} \tilde{G}_{\rho\rho}(k_{\bar{1}};t_{\bar{1}},t_{\bar{1}'})\tilde{\Delta}^{(3)}_{12}(k_2,-k_{\bar{1}};t_2,t_{\bar{1}'};t)\right) \\
&= \int_{t_{\bar{1}}}\left[(\delta_{\mathrm{D}}(t_1 - t_{\bar{1}}) + \tilde{\Delta}_{\mathrm{R}}(k_1;t_1,t_{\bar{1}}))\int_{\vec{k}_{\bar{1}}}(2\pi)^3\delta_{\mathrm{D}}(\vec{k}_1 + \vec{k}_{\bar{1}})\left((2\pi)^3\delta_{\mathrm{D}}(-\vec{k}_{\bar{1}} + \vec{k}_2)\tilde{G}_{\rho\rho}(k_{\bar{1}};t_{\bar{1}},t_2) \dots\right.\right. \\
&\quad \dots + (2\pi)^3\delta_{\mathrm{D}}(-\vec{k}_{\bar{1}} + \vec{k}_2)\int_{t_{\bar{1}'}} \tilde{G}_{\rho\rho}(k_{\bar{1}};t_{\bar{1}},t_{\bar{1}'})\tilde{\Delta}^{(1)}_{12}(k_2;t_2,t_{\bar{1}'}) + \tilde{G}_{\rho\rho}(k_{\bar{1}};t_{\bar{1}},t)\tilde{\Delta}^{(2)}_{12}(k_2,-k_{\bar{1}};t_2;t) \dots \\
&\quad \left.\left. \dots + \int_{t_{\bar{1}'}} \tilde{G}_{\rho\rho}(k_{\bar{1}};t_{\bar{1}},t_{\bar{1}'})\tilde{\Delta}^{(3)}_{12}(k_2,-k_{\bar{1}};t_2,t_{\bar{1}'};t)\right)\right] \\
&= \int_{t_{\bar{1}}}\left[(\delta_{\mathrm{D}}(t_{\bar{1}} - t_1) + \tilde{\Delta}_{\mathrm{R}}(k_1;t_1,t_{\bar{1}}))\left((2\pi)^3\delta_{\mathrm{D}}(\vec{k}_1 + \vec{k}_2)\tilde{G}_{\rho\rho}(k_2;t_{\bar{1}},t_2) \dots\right.\right. \\
&\quad \dots + (2\pi)^3\delta_{\mathrm{D}}(\vec{k}_1 + \vec{k}_2)\int_{t_{\bar{1}'}} \tilde{G}_{\rho\rho}(k_2;t_{\bar{1}},t_{\bar{1}'})\tilde{\Delta}^{(1)}_{12}(k_2;t_2,t_{\bar{1}'}) \dots \\
&\quad \left.\left. \dots + \tilde{G}_{\rho\rho}(-k_1;t_{\bar{1}},t)\tilde{\Delta}^{(2)}_{12}(k_2,k_1;t_2;t) + \int_{t_{\bar{1}'}} \tilde{G}_{\rho\rho}(-k_1;t_{\bar{1}},t_{\bar{1}'})\tilde{\Delta}^{(3)}_{12}(k_2,k_1;t_2,t_{\bar{1}'};t)\right)\right],
\end{aligned} \tag{B.23}$$

which is the result presented in Eq. (4.67).

B.5 DERIVING Δ_{22}

We continue with the steps to derive Δ_{22}. Inserting B^{-1} (Eq. 4.51), A (Eq. 4.38) and Δ_{21} (Eq. (4.42)) into Eq. (4.44) results in

$$\begin{aligned}
\Delta_{22}(1,2) &= -B^{-1}(1,\bar{1}) \cdot A(-\bar{1},\bar{1}') \cdot \Delta_{12}(-\bar{1}',2) \\
&= \mathrm{i}\left(\mathcal{I}(1,\bar{1}) + (2\pi)^3\delta_{\mathrm{D}}(\vec{k}_1+\vec{k}_{\bar{1}})\tilde{\Delta}_{\mathrm{A}}(k_1;t_1,t_{\bar{1}})\right)\cdot\frac{\delta_{\mathrm{D}}(t_{\bar{1}}-t)\delta_{\mathrm{D}}(t_{\bar{1}'}-t)}{\sigma^2}\dots \\
&\quad \dots\cdot(-\mathrm{i})\left(\mathcal{I}(-\bar{1}',2) + (2\pi)^3\delta_{\mathrm{D}}(-\vec{k}_{\bar{1}'}+\vec{k}_2)\tilde{\Delta}^{(1)}_{12}(-k_{\bar{1}'};t_{\bar{1}'},t_2) + \delta_{\mathrm{D}}(t_2-t)\tilde{\Delta}^{(2)}_{12}(-k_{\bar{1}'},k_2;t_{\bar{1}'};t) + \tilde{\Delta}^{(3)}_{12}(-k_{\bar{1}'},k_2;t_{\bar{1}'},t_2;t)\right) \\
&= \left(\mathcal{I}(1,\bar{1}) + (2\pi)^3\delta_{\mathrm{D}}(\vec{k}_1+\vec{k}_{\bar{1}})\tilde{\Delta}_{\mathrm{A}}(k_1;t_1,t_{\bar{1}})\right)\cdot\frac{\delta_{\mathrm{D}}(t_{\bar{1}}-t)}{\sigma^2}\dots \\
&\quad \dots\left(\delta_{\mathrm{D}}(t_2-t) + \tilde{\Delta}^{(1)}_{12}(-k_2;t,t_2) + \delta_{\mathrm{D}}(t_2-t)\int_{k_{\bar{1}'}}\tilde{\Delta}^{(2)}_{12}(-k_{\bar{1}'},k_2;t;t) + \int_{k_{\bar{1}'}}\tilde{\Delta}^{(3)}_{12}(-k_{\bar{1}'},k_2;t,t_2;t)\right) \\
&= \frac{\delta_{\mathrm{D}}(t_1-t)+\tilde{\Delta}_{\mathrm{A}}(k_1;t_1,t)}{\sigma^2}\left(\delta_{\mathrm{D}}(t_2-t) + \tilde{\Delta}^{(1)}_{12}(-k_2;t,t_2) + \delta_{\mathrm{D}}(t_2-t)\int_{k_{\bar{1}'}}\tilde{\Delta}^{(2)}_{12}(-k_{\bar{1}'},k_2;t;t) + \int_{k_{\bar{1}'}}\tilde{\Delta}^{(3)}_{12}(-k_{\bar{1}'},k_2;t,t_2;t)\right),
\end{aligned} \tag{B.24}$$

which is the result shown in Eq. (4.69).

B.6 CALCULATING THE TERMS I TO IV OF THE SECOND ORDER APPROXIMATION TO THE PDF

We show here the detailed steps for obtaining the terms I to IV defined in Eq. (4.70). We will make use of the definition

$$\sigma^2_{\mathrm{lin}} := \int_{k_{\bar{1}}}\tilde{\Delta}_{\rho\rho}(k_{\bar{1}};t,t)\,, \tag{B.25}$$

defined in the paragraph preceding Eq. (4.62). Using this definition we can obtain the identity

$$\begin{aligned}
1 + \int_{k_{\bar{1}'}}\tilde{\Delta}^{(2)}_{12}(k_{\bar{1}'};t,t) &= 1 - \int_{k_{\bar{1}'}}\tilde{\Delta}_{\rho\rho}(k_{\bar{1}'};t,t)\left(\sigma^2 + \int_{k_{\bar{1}}}\tilde{\Delta}_{\rho\rho}(-k_{\bar{1}};t,t)\right)^{-1} \\
&= 1 - \frac{\sigma^2_{\mathrm{lin}}}{\sigma^2+\sigma^2_{\mathrm{lin}}} \\
&= \frac{\sigma^2}{\sigma^2+\sigma^2_{\mathrm{lin}}}\,.
\end{aligned} \tag{B.26}$$

We now proceed to solve the terms I to IV. We obtain for the first term

$$
\begin{aligned}
\mathrm{I} &= \mathcal{V}_1 \cdot \Delta_{11} \cdot \mathcal{V}_1 \\
&= \frac{\tilde{\rho}}{\sigma^2}\delta_\mathrm{D}(t_1 - t) \cdot \Delta_{11} \cdot \frac{\tilde{\rho}}{\sigma^2}\delta_\mathrm{D}(t_2 - t) \\
&= \frac{\tilde{\rho}}{\sigma^2}\delta_\mathrm{D}(t_1 - t) \cdot \int_{t_{\bar{1}}} \Big[\big(\delta_\mathrm{D}(t_{\bar{1}} - t_1) + \tilde{\Delta}_\mathrm{R}(-k_1; t_1, t_{\bar{1}})\big) \Big((2\pi)^3 \delta_\mathrm{D}(-\vec{k}_1 + \vec{k}_2) \tilde{G}_{\rho\rho}(k_2; t_{\bar{1}}, t_2) \dots \\
&\qquad \dots + (2\pi)^3 \delta_\mathrm{D}(-\vec{k}_1 + \vec{k}_2) \int_{t_{\bar{1}'}} \tilde{G}_{\rho\rho}(k_2; t_{\bar{1}}, t_{\bar{1}'}) \tilde{\Delta}^{(1)}_{12}(k_2; t_2, t_{\bar{1}'}) \dots \\
&\qquad \dots + \tilde{G}_{\rho\rho}(k_1; t_{\bar{1}}, t) \tilde{\Delta}^{(2)}_{12}(k_2, k_1; t_2; t) + \int_{t_{\bar{1}'}} \tilde{G}_{\rho\rho}(k_1; t_{\bar{1}}, t_{\bar{1}'}) \tilde{\Delta}^{(3)}_{12}(k_2, k_1; t_2, t_{\bar{1}'}; t) \Big) \Big] \cdot \frac{\tilde{\rho}}{\sigma^2}\delta_\mathrm{D}(t_2 - t) \\
&= \frac{\tilde{\rho}^2}{\sigma^4} \int_{k_1} \int_{t_{\bar{1}}} \Big[\big(\delta_\mathrm{D}(t_{\bar{1}} - t) + \tilde{\Delta}_\mathrm{R}(k_1; t, t_{\bar{1}})\big) \Big(\tilde{G}_{\rho\rho}(k_1; t_{\bar{1}}, t) + \int_{t_{\bar{1}'}} \tilde{G}_{\rho\rho}(k_1; t_{\bar{1}}, t_{\bar{1}'}) \tilde{\Delta}_\mathrm{R}(k_1; t, t_{\bar{1}'}) \dots \\
&\qquad \dots + \int_{k_2} \tilde{G}_{\rho\rho}(k_1; t_{\bar{1}}, t) \tilde{\Delta}^{(2)}_{12}(k_2; t; t) + \int_{k_2} \int_{t_{\bar{1}'}} \tilde{G}_{\rho\rho}(k_1; t_{\bar{1}}, t_{\bar{1}'}) \tilde{\Delta}^{(2)}_{12}(k_2; t; t) \tilde{\Delta}_\mathrm{R}(-k_1; t, t_{\bar{1}'}) \Big) \Big] \\
&= \frac{\tilde{\rho}^2}{\sigma^4} \int_{k_1} \Big[\tilde{G}_{\rho\rho}(k_1; t, t) + \int_{t_{\bar{1}'}} \tilde{G}_{\rho\rho}(k_1; t, t_{\bar{1}'}) \tilde{\Delta}_\mathrm{R}(k_1; t, t_{\bar{1}'}) + \int_{k_2} \tilde{\Delta}^{(2)}_{12}(k_2; t; t) \Big[\tilde{G}_{\rho\rho}(k_1; t, t) + \int_{t_{\bar{1}'}} \tilde{G}_{\rho\rho}(k_1; t, t_{\bar{1}'}) \tilde{\Delta}_\mathrm{R}(-k_1; t, t_{\bar{1}'}) \Big] \\
&\qquad \dots + \int_{t_{\bar{1}}} \tilde{\Delta}_\mathrm{R}(k_1; t, t_{\bar{1}}) \tilde{G}_{\rho\rho}(k_1; t_{\bar{1}}, t) + \int_{t_{\bar{1}}} \int_{t_{\bar{1}'}} \tilde{\Delta}_\mathrm{R}(k_1; t, t_{\bar{1}}) \tilde{G}_{\rho\rho}(k_1; t_{\bar{1}}, t_{\bar{1}'}) \tilde{\Delta}_\mathrm{R}(k_1; t, t_{\bar{1}'}) \dots \\
&\qquad \dots + \int_{k_2} \tilde{\Delta}^{(2)}_{12}(k_2; t; t) \Big[\int_{t_{\bar{1}}} \tilde{\Delta}_\mathrm{R}(k_1; t, t_{\bar{1}}) \tilde{G}_{\rho\rho}(k_1; t_{\bar{1}}, t) + \int_{t_{\bar{1}}} \int_{t_{\bar{1}'}} \tilde{\Delta}_\mathrm{R}(k_1; t, t_{\bar{1}}) \tilde{G}_{\rho\rho}(k_1; t_{\bar{1}}, t_{\bar{1}'}) \tilde{\Delta}_\mathrm{R}(-k_1; t, t_{\bar{1}'}) \Big] \Big) \Big] \\
&= \frac{\tilde{\rho}^2}{\sigma^4} \int_{k_1} \tilde{\Delta}_{\rho\rho}(k_{\bar{1}}; t, t) \left(1 + \int_{k_2} \tilde{\Delta}^{(2)}_{12}(k_2; t; t) \right) = \frac{\tilde{\rho}^2 \sigma^2_\mathrm{lin}}{\sigma^4} \frac{\sigma^2}{\sigma^2 + \sigma^2_\mathrm{lin}} \,.
\end{aligned}
\tag{B.27}
$$

For the second term we get

$$
\begin{aligned}
\mathrm{II} &= (2\pi)^3 \delta_\mathrm{D}(-\vec{k}_1) \bar{\rho} \cdot (-\mathrm{i}) \Big(\mathcal{I}_{(2,-1)} + (2\pi)^3 \delta_\mathrm{D}(-\vec{k}_2 + \vec{k}_1) \tilde{\Delta}^{(1)}_{12}(k_2; t_2, t_1) \dots \\
&\qquad + \delta_\mathrm{D}(t_1 - t) \tilde{\Delta}^{(2)}_{12}(k_2, -k_1; t_2; t) + \tilde{\Delta}^{(3)}_{12}(k_2, -k_1; t_2, t_1; t) \Big) \cdot \mathrm{i} \frac{\tilde{\rho}}{\sigma^2} \delta_\mathrm{D}(t_2 - t) \\
&= \frac{\bar{\rho}\tilde{\rho}}{\sigma^2} \delta_\mathrm{D}(-\vec{k}_1) \cdot \Big(\delta_\mathrm{D}(t_1 - t) + \tilde{\Delta}_\mathrm{R}(k_1; t, t_1) + \delta_\mathrm{D}(t_1 - t) \int_{k_2} \tilde{\Delta}^{(2)}_{12}(k_2; t; t) + \int_{k_2} \tilde{\Delta}^{(2)}_{12}(k_2; t; t) \tilde{\Delta}_\mathrm{R}(k_1; t, t_1) \Big) \\
&= \frac{\bar{\rho}\tilde{\rho}}{\sigma^2} \left(1 + \int_{t_1} \tilde{\Delta}_\mathrm{R}(0; t, t_1) + \int_{k_2} \tilde{\Delta}^{(2)}_{12}(k_2; t, t) + \int_{t_1} \int_{k_2} \tilde{\Delta}^{(2)}_{12}(k_2; t; t) \tilde{\Delta}_\mathrm{R}(0; t, t_1) \right) \\
&= \frac{\bar{\rho}\tilde{\rho}}{\sigma^2} \left(1 + \int_{k_2} \tilde{\Delta}^{(2)}_{12}(k_2; t, t) \right) = \frac{\bar{\rho}\tilde{\rho}}{\sigma^2} \frac{\sigma^2}{\sigma^2 + \sigma^2_\mathrm{lin}} \,,
\end{aligned}
\tag{B.28}
$$

we used in the fourth line that $\tilde{\Delta}_\mathrm{R}(k = 0; t, t) = 0$, since the propagator vanishes for $k = 0$.

We proceed with the third term

$$\begin{aligned}
\mathrm{III} &= \mathrm{i}\frac{\tilde{\rho}}{\sigma^2}\delta_\mathrm{D}(t_1-t)\cdot(-\mathrm{i})\Big(\mathcal{I}_{(-1,2)} + (2\pi)^3\delta_\mathrm{D}(-\vec{k}_1+\vec{k}_2)\tilde{\Delta}^{(1)}_{12}(-k_1;t_1,t_2)\ldots \\
&\qquad +\delta_\mathrm{D}(t_2-t)\tilde{\Delta}^{(2)}_{12}(-k_1,k_2;t_1;t) + \tilde{\Delta}^{(3)}_{12}(-k_1,k_2;t_1,t_2;t)\Big)\cdot(2\pi)^3\delta_\mathrm{D}(-\vec{k}_2)\bar{\rho} \\
&= \frac{\tilde{\rho}}{\sigma^2}\delta_\mathrm{D}(t_1-t)\cdot\left((2\pi)^3\delta_\mathrm{D}(-\vec{k}_1)\bar{\rho} + (2\pi)^3\delta_\mathrm{D}(-\vec{k}_1)\int_{t_2}\tilde{\Delta}_\mathrm{R}(-k_1;t_1,t_2)\bar{\rho}\ldots\right. \\
&\qquad \left. +\tilde{\Delta}^{(2)}_{12}(-k_1;t_1;t)\bar{\rho} + \int_{t_2}\tilde{\Delta}^{(2)}_{12}(-k_1;t_1;t)\tilde{\Delta}_\mathrm{R}(0;t,t_2)\bar{\rho}\right) \qquad \text{(B.29)} \\
&= \frac{\tilde{\rho}\bar{\rho}}{\sigma^2}\left(1+\int_{t_2}\tilde{\Delta}_\mathrm{R}(0;t,t_2) + \int_{k_1}\tilde{\Delta}^{(2)}_{12}(-k_1;t,t) + \int_{k_1}\int_{t_2}\tilde{\Delta}^{(2)}_{12}(-k_1;t;t)\tilde{\Delta}_\mathrm{R}(0;t,t_2)\right) \\
&= \frac{\tilde{\rho}\bar{\rho}}{\sigma^2}\left(1+\int_{k_2}\tilde{\Delta}^{(2)}_{12}(k_2;t,t)\right) = \frac{\tilde{\rho}\bar{\rho}}{\sigma^2}\frac{\sigma^2}{\sigma^2+\sigma^2_\mathrm{lin}} = \mathrm{II}\,,
\end{aligned}$$

which is exactly the same as the second term. Finally the fourth term gives

$$\begin{aligned}
\mathrm{IV} &= (2\pi)^3\delta_\mathrm{D}(\vec{k}_1)\bar{\rho}\cdot\frac{\delta_\mathrm{D}(t_1-t)+\tilde{\Delta}_\mathrm{A}(-k_1;t_1,t)}{\sigma^2}\left(\delta_\mathrm{D}(t_2-t)+\tilde{\Delta}^{(1)}_{12}(-k_2;t,t_2)\ldots\right. \\
&\qquad \left. +\delta_\mathrm{D}(t_2-t)\int_{k_{\bar{1}'}}\tilde{\Delta}^{(2)}_{12}(-k_{\bar{1}'},k_2;t;t) + \int_{k_{\bar{1}'}}\tilde{\Delta}^{(3)}_{12}(-k_{\bar{1}'},k_2;t,t_2;t)\right)\cdot(2\pi)^3\delta_\mathrm{D}(-\vec{k}_2)\bar{\rho} \\
&= (2\pi)^3\delta_\mathrm{D}(\vec{k}_1)\bar{\rho}^2\cdot\frac{\delta_\mathrm{D}(t_1-t)+\tilde{\Delta}_\mathrm{A}(-k_1;t_1,t)}{\sigma^2}\left(1+\int_{t_2}\tilde{\Delta}_\mathrm{R}(0;t,t_2)\ldots\right. \qquad \text{(B.30)} \\
&\qquad \left. +\int_{k_{\bar{1}'}}\tilde{\Delta}^{(2)}_{12}(k_{\bar{1}'};t,t) + \int_{t_2}\int_{k_{\bar{1}'}}\tilde{\Delta}^{(2)}_{12}(k_{\bar{1}'};t;t)\tilde{\Delta}_\mathrm{R}(0;t,t_2)\right) \\
&= \frac{\bar{\rho}^2}{\sigma^2}\left(1+\int_{t_1}\tilde{\Delta}_\mathrm{A}(0;t_1,t)\right)\left(1+\int_{k_{\bar{1}'}}\tilde{\Delta}^{(2)}_{12}(k_{\bar{1}'};t,t)\right) = \frac{\bar{\rho}^2}{\sigma^2}\frac{\sigma^2}{\sigma^2+\sigma^2_\mathrm{lin}}\,.
\end{aligned}$$

we used in the fourth line that $\tilde{\Delta}_\mathrm{A}(k=0;t_1,t)=0$, since the advanced propagator vanishes for $k=0$.

C

CALCULATIONS FOR THE FIRST CROSSING DISTRIBUTION WITH STRONGLY CORRELATED STEPS

We show here some additional calculations to those of Chapter 6. The calculations presented here are reproduced from unpublished work of M. Feix.

C.1 MEAN AND COVARIANCE MATRIX OF THE TRANSFORMED LOGNORMAL DISTRIBUTION

In Section 6.1.3, we transformed the weighted lognormal distribution

$$\begin{aligned}\tilde{p}_{\mathrm{LN}}(\delta_R) &= (1+\delta_R)p_{\mathrm{LN}}(\delta_R) \\ &= \frac{1}{\sqrt{2\pi}\tilde{\sigma}_R\,(1+\delta_R)}\exp\left[-\frac{\left(\ln(1+\delta_R)-\tilde{\sigma}_R^2/2\right)^2}{2\tilde{\sigma}_R^2}\right].\end{aligned} \tag{C.1}$$

into a normal distribution by change of variable

$$x = \ln(1+\delta_R)\,. \tag{C.2}$$

This allowed us to obtain the joint distribution p(x,x'), which takes the form of a bivariate normal distribution. We derive here the mean and covariance matrix of this bivariate normal distribution

$$p(x,x') = \frac{1}{2\pi|C|^{\frac{1}{2}}}\exp\left[-\frac{1}{2}\begin{pmatrix}x-\langle x\rangle\\ x'-\langle x'\rangle\end{pmatrix}^{\mathrm{T}} C^{-1}\begin{pmatrix}x-\langle x\rangle\\ x'-\langle x'\rangle\end{pmatrix}\right], \tag{C.3}$$

with

$$C = \begin{pmatrix}\langle xx\rangle & \langle xx'\rangle\\ \langle x'x\rangle & \langle x'x'\rangle\end{pmatrix}. \tag{C.4}$$

It is our aim to express the mean and covariance matrix in terms of δ_R and δ'_R. The derivative of x with respect to the smoothing scale R can be expressed in terms of δ_R and δ'_R as

$$x' = \frac{\delta'_R}{1+\delta_R}\,. \tag{C.5}$$

From Eq. (C.1), we can easily identify $\langle x \rangle$ and $\langle x^2 \rangle$ by comparing with the definition of the normal distribution,

$$\langle x \rangle = \frac{\tilde{\sigma}_R^2}{2}\,, \tag{C.6}$$

$$\langle x^2 \rangle = \tilde{\sigma}_R^2\,. \tag{C.7}$$

We then can make use of the following three simple identities

$$\langle e^x x' \rangle = \left\langle (1+\delta_R)\frac{\delta'_R}{1+\delta_R} \right\rangle = \langle \delta'_R \rangle = 0\,, \tag{C.8}$$

where we used that the mean slope of random walks $\langle \delta'_R \rangle$ should be zero,

$$\langle e^{2x} x' \rangle = \langle \delta'_R + \delta_R \delta'_R \rangle = \langle \delta_R \delta'_R \rangle \tag{C.9}$$

and

$$\langle e^{2x} x'^2 \rangle = \langle \delta'^2_R \rangle\,, \tag{C.10}$$

which we obtain by plugging in the relations from Eqns. (C.2) and (C.5). The mean values of Eqns. (C.8) – (C.10) can also be calculated explicitly by integrating over the PDF (i.e. Eq. C.3). This leads for the first identity to

$$\begin{aligned} \langle e^x x' \rangle &= \langle x' \rangle + \langle x x' \rangle \overset{(C.8)}{=} 0 \\ \Rightarrow \qquad \langle x' \rangle &= -\langle x x' \rangle\,, \end{aligned} \tag{C.11}$$

for the second to

$$\begin{aligned} \langle e^{2x} x' \rangle &= \left(1 + \langle \delta_R^2 \rangle\right) \langle x x' \rangle \overset{(C.9)}{=} \langle \delta_R \delta'_R \rangle \\ \Rightarrow \qquad \langle x x' \rangle &= \frac{\langle \delta_R \delta'_R \rangle}{1 + \langle \delta_R^2 \rangle}\,, \end{aligned} \tag{C.12}$$

and for the third to

$$\begin{aligned} \langle e^{2x} x'^2 \rangle &= \left(1 + \langle \delta_R^2 \rangle\right) \left[\left(\langle x' \rangle + 2 \langle x x' \rangle \right)^2 + \langle x'^2 \rangle \right] \\ &= \left(1 + \langle \delta_R^2 \rangle\right) \left[\left(\langle x x' \rangle + 2 \langle x'^2 \rangle \right) \right] \overset{(C.10)}{=} \langle \delta'_R \rangle \\ \Rightarrow \qquad \langle x'^2 \rangle + \langle x x' \rangle^2 &= -\frac{\delta'^2_R}{1 + \langle \delta_R^2 \rangle} \\ \Rightarrow \qquad \langle x'^2 \rangle &= \frac{\delta'^2_R}{1 + \langle \delta_R^2 \rangle} - \frac{\delta'^2_R}{1 + \langle \delta_R^2 \rangle}\,, \end{aligned} \tag{C.13}$$

which we obtain by plugging in the result for $\langle xx' \rangle$ from Eq. (C.12) in the last line. We can therefore summarise our results as

$$\begin{aligned} \langle x \rangle &= \frac{1}{2}\tilde{\sigma}_R^2, & \langle x' \rangle &= 0, \\ \langle x^2 \rangle &= \tilde{\sigma}_R^2, & \langle xx' \rangle &= \frac{\langle \delta_R \delta_R' \rangle}{1+\sigma_R^2}, \\ \langle x'^2 \rangle &= \frac{\langle \delta_R'^2 \rangle}{1+\sigma_R^2} - \left(\frac{\langle \delta_R \delta_R' \rangle}{1+\sigma_R^2} \right)^2, \end{aligned} \tag{C.14}$$

which corresponds to Eq. (6.16).

C.2 MEAN AND COVARIANCE MATRIX OF THE TRANSFORMED GENERALISED NORMAL DISTRIBUTION

We can apply the same procedure to obtain the mean and covariance matrix for the transformed generalised normal distribution. Although we are interested in the weighted generalised normal distribution in Section 6.1, we will start first with the unweighted distribution since we can use these results to simplify the calculations when the weighting is applied.

C.2.1 *Unweighted generalised normal distribution*

We start with the unweighted generalised normal distribution (c.f. Eq. 4.2)

$$p_{\mathrm{GN}}(\delta_R) = \frac{1}{\sqrt{2\pi}} \frac{1}{\alpha - \beta(\delta_R - \mu)} \times \exp\left[-\frac{1}{2\beta^2} \left(\ln\left[1 - \frac{\beta(\delta_R - \mu)}{\alpha} \right] \right)^2 \right]. \tag{C.15}$$

We can now transform the variable

$$x = -\ln\left[1 - \frac{\beta\,(\delta_R - \tilde{\mu})}{\alpha} \right]. \tag{C.16}$$

Analogous to the previous section, this allows us to write the joint PDF $p(x, x')$ in the form of Eq. (C.3). The derivative of x with respect to smoothing scale R can be expressed in terms of δ_R and δ_R' as

$$x' = \frac{(\beta/\alpha)'\,\delta_R + (\beta/\alpha)\,\delta_R' - (\beta\tilde{\mu}/\alpha)'}{1 - \beta\,(\delta_R - \tilde{\mu})\,/\alpha}. \tag{C.17}$$

As in the case of the lognormal distribution, we can easily identify $\langle x \rangle$ and $\langle x^2 \rangle$ by comparing Eq. (C.15) with the definition of the normal distribution

$$\langle x \rangle = 0\,, \tag{C.18}$$

$$\langle x^2 \rangle = \beta^2\,. \tag{C.19}$$

By definition, we know that $\langle \delta_R \rangle = 0$ and $\langle \delta_R^2 \rangle = \sigma_R^2$. By calculating the mean and variance of δ_R using the PDF directly (i.e. from Eq. C.15) we get

$$\begin{aligned} \langle \delta_R \rangle &= \tilde{\mu} - \frac{\alpha}{\beta}\left(e^{\frac{\beta^2}{2}} - 1\right) \stackrel{!}{=} 0 \\ \Rightarrow \qquad \tilde{\mu} &= \frac{\alpha}{\beta}\left(e^{\frac{\beta^2}{2}} - 1\right) \end{aligned} \tag{C.20}$$

and

$$\langle \delta_R^2 \rangle = \frac{\alpha^2}{\beta^2} e^{\beta^2}\left(e^{\beta^2} - 1\right) \stackrel{!}{=} \sigma_R^2 \,. \tag{C.21}$$

Note that $\beta < 0$, such that $\beta = -\sqrt{\beta^2}$.

We can again make use of three identities, which are

$$\begin{aligned} \langle e^{-x} x' \rangle &= -\left(\frac{\mathrm{d}}{\mathrm{d}R}\sqrt{\frac{\beta^2}{\alpha^2}}\right)\langle \delta_R \rangle - \left(\sqrt{\frac{\beta^2}{\alpha^2}}\right)\langle \delta_R' \rangle - \frac{\mathrm{d}}{\mathrm{d}R}\left(\frac{\beta\tilde{\mu}}{\alpha}\right) \,, \\ &= -\frac{\mathrm{d}}{\mathrm{d}R}\left(\frac{\beta\tilde{\mu}}{\alpha}\right) \,, \end{aligned} \tag{C.22}$$

$$\langle e^{-2x} x' \rangle = -\sqrt{\frac{\beta^2}{\alpha^2}}\left(\frac{\mathrm{d}}{\mathrm{d}R}\sqrt{\frac{\beta^2}{\alpha^2}}\right)\langle \delta_R^2 \rangle - \frac{\beta^2}{\alpha^2}\langle \delta_R \delta_R' \rangle - \left(1 + \frac{\beta\tilde{\mu}}{\alpha}\right)\frac{\mathrm{d}}{\mathrm{d}R}\left(\frac{\beta\tilde{\mu}}{\alpha}\right) \tag{C.23}$$

and

$$\begin{aligned} \langle e^{-2x} x'^2 \rangle = \left(\frac{\mathrm{d}}{\mathrm{d}R}\sqrt{\frac{\beta^2}{\alpha^2}}\right)^2 \langle \delta_R^2 \rangle + 2\sqrt{\frac{\beta^2}{\alpha^2}}\left(\frac{\mathrm{d}}{\mathrm{d}R}\sqrt{\frac{\beta^2}{\alpha^2}}\right)\langle \delta_R \delta_R' \rangle \\ + \frac{\beta^2}{\alpha^2}\left\langle \delta_R'^{\,2} \right\rangle + \left[\frac{\mathrm{d}}{\mathrm{d}R}\left(\frac{\beta\tilde{\mu}}{\alpha}\right)\right]^2 \,, \end{aligned} \tag{C.24}$$

which we obtain by inserting Eqns. (C.16) and (C.30). The mean values of Eqns. (C.22) – (C.24) can also be calculated explicitly by integrating over the PDF (i.e. Eq. C.3). This leads for the first identity to

$$\langle e^{-x} x' \rangle = \exp\left(\frac{\beta^2}{2}\right)\left(\langle x' \rangle - \langle x x' \rangle\right) \stackrel{(C.22)}{=} -\frac{\mathrm{d}}{\mathrm{d}R}\left(\frac{\beta\tilde{\mu}}{\alpha}\right) \,, \tag{C.25}$$

for the second to

$$\begin{aligned} \langle e^{-2x} x' \rangle &= \exp\left(2\beta^2\right)\left(\langle x' \rangle - 2\langle x x' \rangle\right) \\ &\stackrel{(C.25)}{=} -\exp\left(\frac{3}{2}\beta^2\right)\frac{\mathrm{d}}{\mathrm{d}R}\left(\frac{\beta\tilde{\mu}}{\alpha}\right) - \exp\left(2\beta^2\right)\langle x x' \rangle \end{aligned} \tag{C.26}$$

and for the third to

$$\left\langle e^{-2x} x'^2 \right\rangle = \exp\left(2\beta^2\right) \left[\left(\left\langle x' \right\rangle - 2 \left\langle x x' \right\rangle \right)^2 + \left\langle x'^2 \right\rangle \right] . \tag{C.27}$$

With this at hand, we could now write down the mean and the covariance matrix. Since we are interested in the weighted version of the PDF, however, and just need these results to simplify our calculations in the next section, we will proceed with the weighted PDF straight away.

C.2.2 *Weighted generalised normal distribution*

We now consider the weighted generalised normal distribution (c.f. Eq. 6.7)

$$\begin{aligned} \tilde{p}_{\mathrm{GN}}(\delta_R) &= \left(\left| \tilde{\mu} + \frac{\alpha}{\beta} \right| + \delta_R \right) p_{\mathrm{GN}}(\delta_R) \\ &= \frac{1}{\sqrt{2\pi}} \frac{1}{\tilde{\alpha} - \beta(\delta_R - \tilde{\nu})} \exp\left[-\frac{1}{2\beta^2} \left(\ln\left[1 - \frac{\beta(\delta_R - \tilde{\nu})}{\tilde{\alpha}} \right] \right)^2 \right] \end{aligned} \tag{C.28}$$

and apply the change of variable

$$x = -\ln\left[1 - \frac{\beta\left(\delta_R - \tilde{\nu}\right)}{\tilde{\alpha}} \right] . \tag{C.29}$$

We again write the joint PDF $p(x, x')$ in the form of Eq. (C.3). The derivative of x with respect to smoothing scale R can be expressed in terms of δ_R and δ'_R as

$$x' = \frac{\left(\beta/\tilde{\alpha}\right)' \delta_R + \left(\beta/\tilde{\alpha}\right) \delta'_R - \left(\beta\tilde{\nu}/\tilde{\alpha}\right)'}{1 - \beta\left(\delta_R - \tilde{\nu}\right)/\tilde{\alpha}} . \tag{C.30}$$

Once more, we identify $\langle x \rangle$ and $\langle x^2 \rangle$ by comparing Eq. (C.28) with the definition of the normal distribution

$$\langle x \rangle = 0 , \tag{C.31}$$

$$\langle x^2 \rangle = \beta^2 . \tag{C.32}$$

We furthermore can calculate from Eq. (C.28)

$$\begin{aligned} \langle \delta_R \rangle &= \tilde{\nu} - \frac{\tilde{\alpha}}{\beta} \left(e^{\frac{\beta^2}{2}} - 1 \right) = \frac{\alpha}{\beta} e^{\frac{\beta^2}{2}} \left(1 - e^{\beta^2} \right) , \\ \langle \delta_R^2 \rangle &= \frac{\tilde{\alpha}^2}{\beta^2} e^{\beta^2} \left(e^{\beta^2} - 1 \right) = e^{2\beta^2} \sigma_R^2 , \end{aligned} \tag{C.33}$$

Note also here that $\beta < 0$, such that $\beta = -\sqrt{\beta^2}$.

We can now use a trick to derive again three identities for mean values of combinations of e^{-x} and x'. For this, we realise that the weighting factor gives exactly a factor of $(\tilde{\alpha}/\beta)e^{-x}$, which can be seen by inserting Eq. (C.29) the definitions of $\tilde{\nu}$ and $\tilde{\alpha}$ (c.f. Eqns. 6.5 and 6.6)

$$\begin{aligned} e^{-x} &= 1 - \frac{\beta(\delta_R - \tilde{\nu})}{\tilde{\alpha}} = \frac{1}{\tilde{\alpha}}\left[\tilde{\alpha} - \beta(\delta_R - \tilde{\nu})\right] \\ &= \frac{1}{\tilde{\alpha}}\left[\tilde{\alpha} - \beta\left(\delta_R - \tilde{\mu} + \frac{\tilde{\alpha}}{\beta} - \frac{\alpha}{\beta}\right)\right] = \frac{1}{\tilde{\alpha}}\left[\tilde{\alpha} - \tilde{\alpha} + \beta\left(\delta_R - \tilde{\mu} - \frac{\alpha}{\beta}\right)\right] \\ &= \frac{\beta}{\tilde{\alpha}}\left(\delta_R - \tilde{\mu} - \frac{\alpha}{\beta}\right), \end{aligned} \tag{C.34}$$

where the second factor is exactly our weighting factor in Eq. (C.28). We can therefore use the results of the unweighted PDF (i.e. Eqns. C.22 – C.24), by rewriting the weighting factor as shown above[1]. However, we still have to take into account that the parameters have been shifted due to the weighting, which means that we have to replace $\tilde{\mu} \to \tilde{\nu}$ and $\tilde{\alpha} \to \tilde{\alpha}$ when taking the results from the unweighted case. This then leads to

$$\langle x' \rangle = \frac{\tilde{\alpha}}{\beta} \langle x' \rangle_{\text{unweighted}} \overset{\text{(C.22)}}{=} \frac{\tilde{\alpha}}{\beta}\left(\frac{\mathrm{d}}{\mathrm{d}R}\frac{\beta\tilde{\nu}}{\tilde{\alpha}}\right), \tag{C.35}$$

$$\langle e^{-x} x' \rangle \overset{\text{(C.23)}}{=} -\left(\frac{\mathrm{d}}{\mathrm{d}R}\sqrt{\frac{\beta^2}{\tilde{\alpha}^2}}\right)\langle \delta_R^2 \rangle - \sqrt{\frac{\beta^2}{\tilde{\alpha}^2}}\langle \delta_R \delta_R' \rangle + \left(\frac{\tilde{\alpha}}{\beta} + \tilde{\nu}\right)\frac{\mathrm{d}}{\mathrm{d}R}\left(\frac{\beta\tilde{\nu}}{\tilde{\alpha}}\right) \tag{C.36}$$

and

$$\begin{aligned} \langle e^{-x} x'^2 \rangle \overset{\text{(C.24)}}{=} -\frac{\tilde{\alpha}}{\beta}\Bigg[&\left(\frac{\mathrm{d}}{\mathrm{d}R}\sqrt{\frac{\beta^2}{\tilde{\alpha}^2}}\right)^2 \langle \delta_R^2 \rangle + 2\sqrt{\frac{\beta^2}{\tilde{\alpha}^2}}\left(\frac{\mathrm{d}}{\mathrm{d}R}\sqrt{\frac{\beta^2}{\tilde{\alpha}^2}}\right)\langle \delta_R \delta_R' \rangle \dots \\ &+ \frac{\beta^2}{\tilde{\alpha}^2}\langle \delta_R'^2 \rangle + \left[\frac{\mathrm{d}}{\mathrm{d}R}\left(\frac{\beta\tilde{\nu}}{\tilde{\alpha}}\right)\right]^2\Bigg]. \end{aligned} \tag{C.37}$$

The first identity, Eqns. (C.35), already yields $\langle x' \rangle$. As shown in the previous section, the values of Eqns. (C.36) and (C.37) can also be calculated explicitly by integrating over the PDF (i.e. Eq. C.3). We state the results here again for completeness

$$\langle e^{-x} x' \rangle = \exp\left(\frac{\beta^2}{2}\right)\left(\langle x' \rangle - \langle x x' \rangle\right), \tag{C.38}$$

$$\langle e^{-x} x'^2 \rangle = \exp\left(\frac{\beta^2}{2}\right)\left[\left(\langle x' \rangle - \langle x x' \rangle\right)^2 + \langle x'^2 \rangle\right]. \tag{C.39}$$

1 e.g. $\langle x' \rangle = \frac{\tilde{\alpha}}{\beta}\langle e^{-x} x' \rangle_{\text{unweighted}}$, where the unweighted formula needs to be evaluated with the shifted parameters $\tilde{\nu}$ and $\tilde{\alpha}$.

Combining Eqns. (C.35) – (C.37) with Eqns. (C.38) and (C.39) leads then to the desired results for the mean and covariance matrix

$$\begin{aligned}
\langle x \rangle &= 0, \qquad \langle x^2 \rangle = \beta^2, \qquad \langle x' \rangle = \frac{\tilde{\alpha}}{\beta} \left(\frac{\beta \tilde{\nu}}{\tilde{\alpha}} \right)', \\
\frac{\langle x' \rangle - \langle x x' \rangle}{e^{-\beta^2/2}} &= \left(\frac{\beta}{\tilde{\alpha}} \right)' \langle \delta_R^2 \rangle + \frac{\beta}{\tilde{\alpha}} \langle \delta_R \delta_R' \rangle + \left(\tilde{\nu} + \frac{\tilde{\alpha}}{\beta} \right) \left(\frac{\beta \tilde{\nu}}{\tilde{\alpha}} \right)', \\
\frac{\left[\langle x' \rangle - \langle x x' \rangle \right]^2 + \langle x'^2 \rangle}{-\tilde{\alpha} e^{-\beta^2/2}/\beta} &= \left(\frac{\beta}{\tilde{\alpha}} \right)'^2 \langle \delta_R^2 \rangle + 2 \frac{\beta}{\tilde{\alpha}} \left(\frac{\beta}{\tilde{\alpha}} \right)' \langle \delta_R \delta_R' \rangle \dots \\
&\quad + \left(\frac{\beta}{\tilde{\alpha}} \right)^2 \langle \delta_R'^2 \rangle + \left(\frac{\beta \tilde{\nu}}{\tilde{\alpha}} \right)'^2 .
\end{aligned} \tag{C.40}$$

C.3 STRONGLY CORRELATED REGIME FOR THE GENERALISED NORMAL DISTRIBUTION

We now derive the halo mass function for the generalised normal model in the strongly correlated regime. The completely correlated regime has already been derived in Section 6.1.2. The steps presented here are analogous to those of Section 6.1.3, where the lognormal model was used.

We start with the joint distribution $\tilde{p}_x(x, x')$ derived above (Section C.2.2). Reexpressing the PDF in terms of δ_R and δ_R' then gives

$$\tilde{p}(\delta_R, \delta_R') = \left(\frac{\beta}{\tilde{\alpha} - \beta \left(\delta_R - \tilde{\nu} \right)} \right)^2 \tilde{p}_x(x, x'). \tag{C.41}$$

This expression can now be inserted into Eq. (6.14) to obtain the first-crossing distribution

$$\begin{aligned}
f_{\mathrm{sc,GN}} = \frac{1}{2\pi\beta^2} \exp\left[-\frac{x_\Delta^2}{2\beta^2} \right] \Bigg(& -\beta \sqrt{\left(1 - \gamma^2\right) \langle x'^2 \rangle} \exp\left[\frac{-\eta^2}{2\beta^2 \left(1 - \gamma^2\right) \langle x'^2 \rangle} \right] \\
& + \eta \sqrt{\frac{\pi}{2}} \operatorname{erfc}\left[\frac{\eta}{\beta \sqrt{2 \left(1 - \gamma^2\right) \langle x'^2 \rangle}} \right] \Bigg),
\end{aligned} \tag{C.42}$$

where $\gamma = \langle \delta_R \delta'_R \rangle^2 / (\langle \delta_R \delta_R \rangle \langle \delta'_R \delta'_R \rangle)$ as before and we defined the short-hand notations

$$\begin{aligned} x_\Delta &:= -\ln\left[1 - \beta\left(\Delta - \tilde{\nu}\right)/\tilde{\alpha}\right], \\ \eta &:= \gamma x_\Delta \sqrt{\langle x'^2 \rangle} + \beta\left[\epsilon - \langle x' \rangle\right], \\ \epsilon &:= \frac{\left(\beta/\tilde{\alpha}\right)' \Delta - \left(\beta\tilde{\nu}/\tilde{\alpha}\right)'}{1 - \beta\left(\Delta - \tilde{\nu}\right)/\tilde{\alpha}}. \end{aligned} \tag{C.43}$$

Inserting this first crossing distribution into Eq. (5.18) results in the halo mass functions shown in Fig. 6.1 for redshift $z = 0$ and Fig. 6.3 for $z = 1$.

D

RESULTS FOR THE LOGNORMAL MODEL

For completeness, we add in this part of the appendix the plots (see Fig. D.1) corresponding to the calculations of the halo mass function with the lognormal model in Sections 6.1.2 and 6.1.3. This figure is analogous to Fig. 6.1, which was obtained using the generalised normal model instead. The mass functions in the upper panel were calculated using excursion set statistics in the completely correlated regime (Eq. 6.10). Those in the lower panel represent the results for random walks in the strongly correlated regime (Eq. 6.20).

We find a fairly good agreement in the mass range from 10^{10} to 10^{16} $h^{-1}\mathrm{M}_{\odot}$ for both regimes when the overdensity threshold is set to $\Delta = 3.7$. However, comparing the results to those from the generalised normal model (Fig. 6.1), we find that the agreement with the fit to N-body simulations is slightly worse – especially in the knee of the function and the slope of the high mass tail. This is indeed expected, since the lognormal model describes the cosmic density field less accurately than the generalised normal model. For the *maximally correlated* case, shown in Fig. D.1a, higher values for the density threshold Δ lead to an agreement with the Press-Schechter mass function in the low mass regime and a substantial underprediction in the high mass tail. Setting the threshold to $\Delta = 2.0$ leads to a better agreement with the Tinker mass function in the low mass regime, but a significant overprediction in the high mass tail. The *strongly correlated random walk*, shown in Fig. D.1b leads to slightly lower values of the halo mass functions. For masses smaller than 10^{13} $h^{-1}\mathrm{M}_{\odot}$, all curves shown lie below the Tinker mass function if the overdensity is set to $\Delta = 3.7$. It is interesting to note that for the generalised normal model this behaviour is reversed (see Fig. 6.1). There the strongly correlated random walk leads to a slightly higher halo mass function. As mentioned above the worse agreement with the Tinker mass function in comparison to the generalised normal model is caused by the lognormal model describing less accurately the cosmic density field. The relative deviations of our halo mass functions based on the lognormal model as compared to the Tinker fit are shown in Fig. D.2.

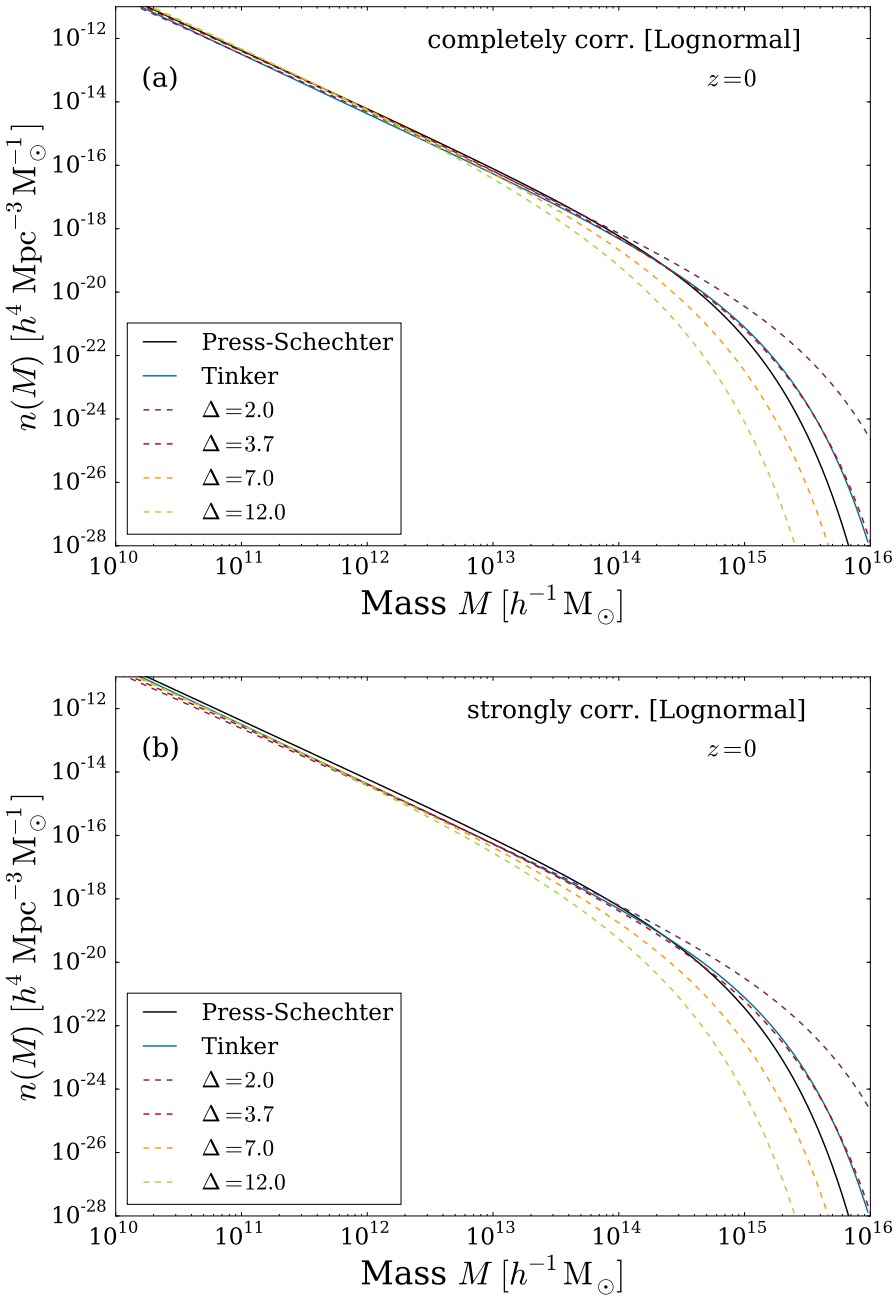

Figure D.1: Halo mass function predictions using a lognormal model for the PDF of the density field (*dashed lines*). The colour coding was chosen analogously to Fig. 6.1. The upper panel (a) shows the completely correlated case (Eq. 6.10). The lower panel (b) shows the results for a strongly correlated random walk (Eq. 6.20).

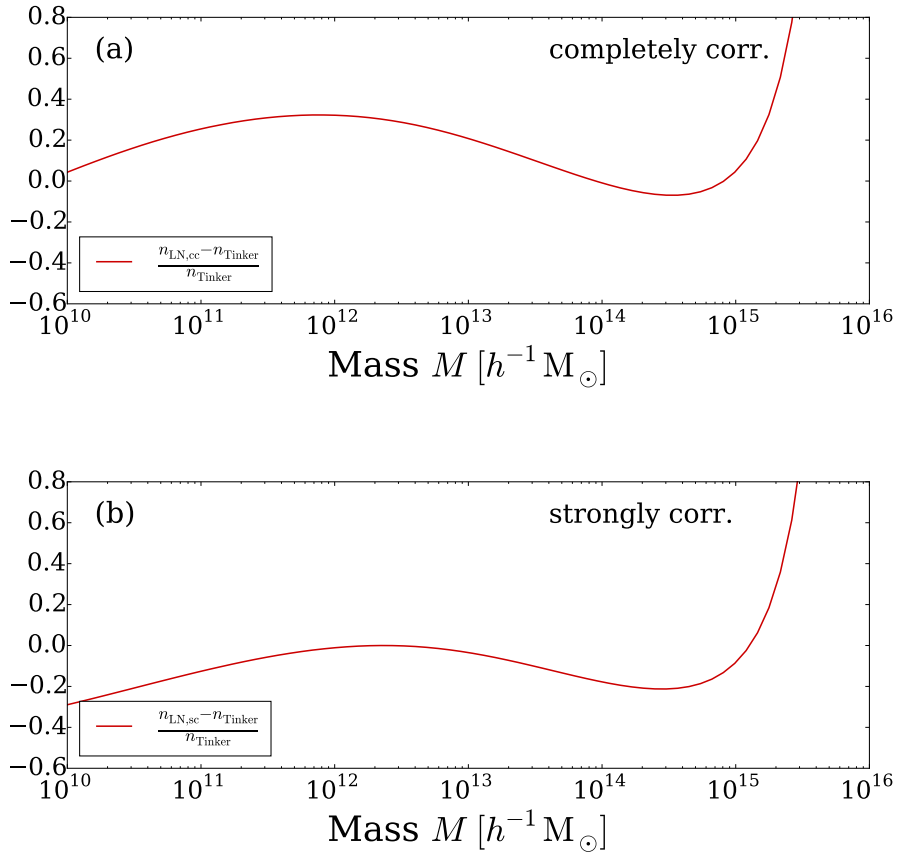

Figure D.2: The relative deviation of our halo mass function based on the lognormal model as compared to the Tinker fit. The density threshold was set in our model to $\Delta = 3.7$ (corresponding to the *red dashed* line in Fig. D.1). The upper panel (a) shows the completely correlated case and the lower panel (b) the a strongly correlated regime.

E

OBSERVATIONAL DATA OF ABELL 2744

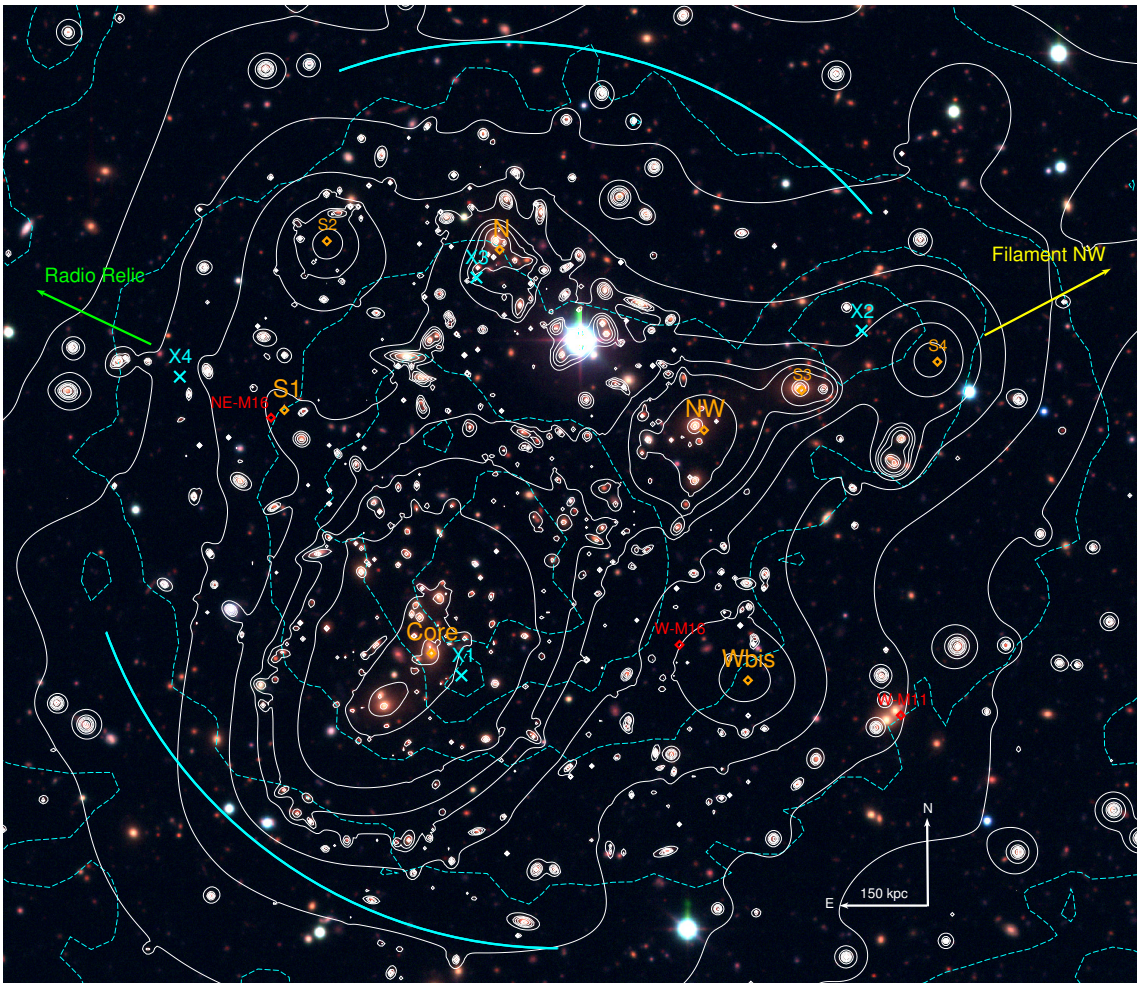

Figure E.1: The gravitational potential of Abell 2744 taken from Jauzac et al. (2016). The *solid white* contours show the potential obtained from a combined strong and weak lensing analysis. The *dashed cyan* contours show the X-ray luminosity of the cluster. The *cyan arcs* highlight the positions of two X-ray shocks. The *cyan crosses* mark the positions of remnant cores. The positions of the all eight detected substructures are shown as *orange diamonds*. In case their position differs from the position shown in Merten et al. (2011) and Medezinski et al. (2016), the previous positions are highlighted as *red diamonds*. The *yellow arrow* denotes the direction of a filament as reported in Eckert et al. (2015) and the *green arrow* shows the direction of a radio relic discussed in Eckert et al. (2016). This figure was taken from Jauzac et al. (2016).

BIBLIOGRAPHY

Abbott, T. M. C. et al. (2018). *Dark Energy Survey year 1 results: Cosmological constraints from galaxy clustering and weak lensing*. In: Physical Review D **98**.4, 043526. arXiv: 1708.01530.

Adamek, J., D. Daverio, R. Durrer, and M. Kunz (2013). *General relativistic N-body simulations in the weak field limit*. In: Physical Review D **88**.10, 103527. arXiv: 1308.6524.

Angrick, C. and M. Bartelmann (2009). *Statistics of gravitational potential perturbations: A novel approach to deriving the X-ray temperature function*. In: Astronomy and Astrophysics **494**.2, 461. arXiv: 0802.1680.

Angulo, R. E. et al. (2012). *Scaling relations for galaxy clusters in the Millennium-XXL simulation*. In: Monthly Notices of the Royal Astronomical Society **426**.3, 2046. arXiv: 1203.3216.

Angulo, R. E., S. Foreman, M. Schmittfull, and L. Senatore (2015). *The one-loop matter bispectrum in the Effective Field Theory of Large Scale Structures*. In: Journal of Cosmology and Astroparticle Physics **2015**.10, 39. arXiv: 1406.4143.

Bardeen, J. M., J. R. Bond, N. Kaiser, and A. S. Szalay (1986). *The statistics of peaks of Gaussian random fields*. In: The Astrophysical Journal **304**, 15.

Bartelmann, M. (2015). *Trajectories of point particles in cosmology and the Zel'dovich approximation*. In: Physical Review D **91**.8, 083524. arXiv: 1411.0805.

Bartelmann, M. et al. (2016). *A microscopic, non-equilibrium, statistical field theory for cosmic structure formation*. In: New Journal of Physics **18**.4, 043020. arXiv: 1411.0806.

Bartelmann, M. et al. (2019). *Cosmic Structure Formation with Kinetic Field Theory*. In: Annalen der Physik **531**.11, 1800446. arXiv: 1905.01179.

Baumann, D., A. Nicolis, L. Senatore, and M. Zaldarriaga (2012). *Cosmological nonlinearities as an effective fluid*. In: Journal of Cosmology and Astroparticle Physics **2012**.07, 51. arXiv: 1004.2488.

Bennett, C. L. et al. (1994). *Cosmic temperature fluctuations from two years of COBE differential microwave radiometers observations*. In: The Astrophysical Journal **436**, 423. arXiv: astro-ph/9401012.

Bernardeau, F. (1994a). *Skewness and kurtosis in large-scale cosmic fields*. In: The Astrophysical Journal **433**, 1. arXiv: astro-ph/9312026.

Bernardeau, F. (1994b). *The effects of smoothing on the statistical properties of large-scale cosmic fields*. In: Astronomy and Astrophysics **291**, 697. arXiv: astro-ph/9403020.

Bernardeau, F. and P. Reimberg (2016). *Large deviation principle at play in large scale structure cosmology*. In: Physical Review D **94**.6, 063520. arXiv: 1511.08641.

Bernardeau, F., S Colombi, E Gaztañaga, and R Scoccimarro (2002). *Large-scale structure of the Universe and cosmological perturbation theory*. In: Physics Reports **367**.1-3, 1. arXiv: astro-ph/0112551.

Bernardeau, F., C. Pichon, and S. Codis (2014). *Statistics of cosmic density profiles from perturbation theory*. In: Physical Review D **90**.10, 1. arXiv: 1310.8134.

Bieringer, S. G. (2018). *Application of the one-particle probability density function from Large Deviation Theory for Kinetic Field Theory*. In: B.Sc. thesis (Heidelberg University).

Bolejko, K. and M. Korzyński (2017). *Inhomogeneous cosmology and backreaction: Current status and future prospects*. In: International Journal of Modern Physics D **26**.06, 1730011. arXiv: 1612.08222.

Bond, J. R., S. Cole, G. Efstathiou, and N. Kaiser (1991). *Excursion set mass functions for hierarchical Gaussian fluctuations*. In: The Astrophysical Journal **379**, 440.

Bonnor, W. B. (1957). *Jeans' Formula for Gravitational Instability*. In: Monthly Notices of the Royal Astronomical Society **117**.1, 104.

Boughn, S. P., E. S. Cheng, and D. T. Wilkinson (1981). *Dipole and quadrupole anisotropy of the 2.7 K radiation*. In: The Astrophysical Journal **243**.9, L113.

Boylan-Kolchin, M., V. Springel, S. D. M. White, A. Jenkins, and G. Lemson (2009). *Resolving cosmic structure formation with the Millennium-II Simulation*. In: Monthly Notices of the Royal Astronomical Society **398**.3, 1150. arXiv: 0903.3041.

Buchert, T. et al. (2015). *Is there proof that backreaction of inhomogeneities is irrelevant in cosmology?* In: Classical and Quantum Gravity **32**.21, 215021. arXiv: 1505.07800.

Bull, P., T. Clifton, and P. G. Ferreira (2012). *Kinematic Sunyaev-Zel'dovich effect as a test of general radial inhomogeneity in Lemaître-Tolman-Bondi cosmology*. In: Physical Review D **85**.2, 024002. arXiv: 1108.2222.

Carrasco, J. J. M., M. P. Hertzberg, and L. Senatore (2012). *The effective field theory of cosmological large scale structures*. In: Journal of High Energy Physics **2012**.9, 82. arXiv: arXiv:1206.2926.

Carroll, S. M., W. H. Press, and E. L. Turner (1992). *The Cosmological Constant*. In: Annual Review of Astronomy and Astrophysics **30**.1, 499.

Carron, J. and M. C. Neyrinck (2012). *On the inadequacy of N-point correlation functions to describe nonlinear cosmological fields: explicit examples and connection to simulations*. In: The Astrophysical Journal **750**.1, 28. arXiv: 1201.1444.

Castro, T. et al. (2020). *On the impact of baryons on the halo mass function, bias, and cluster cosmology*. In: Monthly Notices of the Royal Astronomical Society **500**.2, 2316. arXiv: 2009.01775.

Chandrasekhar, S. (1943). *Stochastic Problems in Physics and Astronomy*. In: Reviews of Modern Physics **15**.1, 1.

Clowe, D. et al. (2006). *A Direct Empirical Proof of the Existence of Dark Matter*. In: The Astrophysical Journal **648**.2, L109. arXiv: astro-ph/0608407.

Cole, S. et al. (2005). *The 2dF Galaxy Redshift Survey: power-spectrum analysis of the final data set and cosmological implications*. In: Monthly Notices of the Royal Astronomical Society **362**, 505. arXiv: astro-ph/0501174.

Coles, P. and B. Jones (1991). *A lognormal model for the cosmological mass distribution*. In: Monthly Notices of the Royal Astronomical Society **248**.1, 1.

Corasaniti, P. S. and I. Achitouv (2011). *Excursion set halo mass function and bias in a stochastic barrier model of ellipsoidal collapse*. In: Physical Review D **84**.2, 023009. arXiv: 1107.1251.

Das, S. P. and G. F. Mazenko (2012). *Field Theoretic Formulation of Kinetic Theory: Basic Development*. In: Journal of Statistical Physics **149**.4, 643. arXiv: 1111.0571.

Das, S. P. and G. F. Mazenko (2013). *Newtonian Kinetic Theory and the Ergodic-Nonergodic Transition*. In: Journal of Statistical Physics **152**.1, 159. arXiv: 1303.1627.

Daubechies, I. (1988). *Orthonormal bases of compactly supported wavelets*. In: Communications on Pure and Applied Mathematics **41**.7, 909.

Daubechies, I. (1992). *Ten Lectures on Wavelets*. Philadelphia: Society for Industrial and Applied Mathematics.

Davis, M., G. Efstathiou, C. S. Frenk, and S. D. M. White (1985). *The evolution of large-scale structure in a universe dominated by cold dark matter*. In: The Astrophysical Journal **292**, 371.

de Jong, J. T. A. et al. (2017). *The third data release of the Kilo-Degree Survey and associated data products*. In: Astronomy and Astrophysics **604**, A134, A134. arXiv: 1703.02991.

Dehnen, W. (2001). *Towards optimal softening in three-dimensional N-body codes - I. Minimizing the force error*. In: Monthly Notices of the Royal Astronomical Society **324**.2, 273. arXiv: astro-ph/0011568.

Desjacques, V., D. Jeong, and F. Schmidt (2018). *Large-scale galaxy bias*. In: Physics Reports **733**, 1. arXiv: 1611.09787.

Doroshkevich, A. G. (1970). *Spatial structure of perturbations and origin of galactic rotation in fluctuation theory*. In: Astrophysics **6**.4, 320.

Dyson, F. W., A. S. Eddington, and C. Davidson (1920). *A Determination of the Deflection of Light by the Sun's Gravitational Field, from Observations Made at the Total Eclipse of May 29, 1919*. In: Philosophical Transactions of the Royal Society A **220**, 291. e-print: e-print.

eBOSS Collaboration (2020). *The Completed SDSS-IV extended Baryon Oscillation Spectroscopic Survey: Cosmological Implications from two Decades of Spectroscopic Surveys at the Apache Point observatory*. In: arXiv E-prints. arXiv: 2007.08991.

Eckert, D. et al. (2015). *Warm-hot baryons comprise 5-10 per cent of filaments in the cosmic web*. In: Nature **528**.7580, 105. arXiv: 1512.00454.

Eckert, D. et al. (2016). *A shock front at the radio relic of Abell 2744*. In: Monthly Notices of the Royal Astronomical Society **461**.2, 1302. arXiv: 1603.02272.

Einstein, A. and E. G. Straus (1946). *Corrections and Additional Remarks to our Paper: The Influence of the Expansion of Space on the Gravitation Fields Surrounding the Individual Stars*. In: Reviews of Modern Physics **18**.1, 148.

Einstein, A. (1915). *Die Feldgleichungen der Gravitation*. In: Sitzungsberichte der Königlich Preußischen Akademie der Wissenschaften, 844. e-print: e-print.

Eisenstein, D. J. and W. Hu (1998). *Small-Scale Perturbations in a General Mixed Dark Matter Cosmology*. In: The Astrophysical Journal **498**.2, 497. arXiv: astro-ph/9710216.

Escalera, E. and A. Mazure (1992). *Wavelet analysis of subclustering - an illustration, Abell 754*. In: The Astrophysical Journal **388**, 23. e-print: e-print.

Fabis, F. (2015). *A statistical field theory for classical particles - foundations and applications in cosmological structure formation*. In: PhD thesis (Heidelberg University).

Flin, P. and J. Krywult (2006). *Substructures in Abell clusters of galaxies*. In: Astronomy and Astrophysics **450**.1, 9.

Floerchinger, S., M. Garny, N. Tetradis, and U. A. Wiedemann (2017). *Renormalization-group flow of the effective action of cosmological large-scale structures*. In: Journal of Cosmology and Astroparticle Physics **2017**.01, 048. arXiv: 1607.03453.

Gao, L. et al. (2012). *The Phoenix Project: the dark side of rich Galaxy clusters*. In: Monthly Notices of the Royal Astronomical Society **425**.3, 2169. arXiv: 1201.1940.

Geiger, N. (2020). *Excursion sets, halos, and the mass function*. In: B.Sc. thesis (Heidelberg University).

Geiss, D., I. Kostyuk, R. Lilow, and M. Bartelmann (2020). *Resummed Kinetic Field Theory: a model of coupled baryonic and dark matter*. In: arXiv E-prints. arXiv: 2007.09484.

Green, S. R. and R. M. Wald (2014). *How well is our Universe described by an FLRW model?* In: Classical and Quantum Gravity **31**.23, 234003. arXiv: 1407.8084.

Gunn, J. E. and J. R. I. Gott (1972). *On the Infall of Matter Into Clusters of Galaxies and Some Effects on Their Evolution*. In: The Astrophysical Journal **176**.1, 1.

Hagstotz, S., M. Costanzi, M. Baldi, and J. Weller (2019). *Joint halo-mass function for modified gravity and massive neutrinos - I. Simulations and cosmological forecasts*. In: Monthly Notices of the Royal Astronomical Society **486**.3, 3927. arXiv: 1806.07400.

Han, J. (2017). *Observing Interstellar and Intergalactic Magnetic Fields*. In: Annual Review of Astronomy and Astrophysics **55**.1, 111.

Han, J., S. Cole, C. S. Frenk, A. Benitez-Llambay, and J. Helly (2017). *HBT+: an improved code for finding subhalos and building merger trees in cosmological simulations*. In: Monthly Notices of the Royal Astronomical Society **474**, 604. arXiv: 1708.03646.

Hiotelis, N. and A. D. Popolo (2017). *Mass functions from the excursion set model*. In: Astronomy and Astrophysics **607**, A47. arXiv: 1802.07343.

Hogg, D. W. et al. (2005). *Cosmic Homogeneity Demonstrated with Luminous Red Galaxies*. In: The Astrophysical Journal **624**.1, 54. arXiv: astro-ph/0411197.

Hu, W., R. Barkana, and A. Gruzinov (2000). *Fuzzy Cold Dark Matter: The Wave Properties of Ultralight Particles*. In: Physical Review Letters **85**.6, 1158. arXiv: astro-ph/0003365.

Hubble, E. (1934). *The Distribution of Extra-Galactic Nebulae*. In: The Astrophysical Journal **79**.485, 8.

Ivezić, Ž. et al. (2019). *LSST: From Science Drivers to Reference Design and Anticipated Data Products*. In: The Astrophysical Journal **873**.2, 111. arXiv: 0805.2366.

Jauzac, M. et al. (2015). *Hubble Frontier Fields : a high-precision strong-lensing analysis of the massive galaxy cluster Abell 2744 using 180 multiple images*. In: Monthly Notices of the Royal Astronomical Society **452**.2, 1437. arXiv: 1409.8663.

Jauzac, M. et al. (2018). *Growing a 'cosmic beast': observations and simulations of MACS J0717.5+3745*. In: Monthly Notices of the Royal Astronomical Society **481**.3, 2901. arXiv: 1711.01324.

Jauzac, M. et al. (2016). *The extraordinary amount of substructure in the Hubble Frontier Fields cluster Abell 2744*. In: Monthly Notices of the Royal Astronomical Society **463**.4, 3876. arXiv: 1606.04527.

Jones, B. (2009). *The Sea of Wavelets*. In: *Data Analysis in Cosmology*. Ed. by Martínez, V., E Saar, E Martfinez-González, and M.-J. Pons-Bordería. Vol. 665. Lecture Notes in Physics. Berlin: Springer. 3.

Joudaki, S. et al. (2017). *CFHTLenS revisited: assessing concordance with Planck including astrophysical systematics*. In: Monthly Notices of the Royal Astronomical Society **465**, 2033. arXiv: 1601.05786.

Juszkiewicz, R., D. H. Weinberg, P. Amsterdamski, M. Chodorowski, and F. Bouchet (1995). *Weakly nonlinear Gaussian fluctuations and the edgeworth expansion*. In: The Astrophysical Journal **442**, 39. arXiv: astro-ph/9308012.

Kampen, E. van (2000). *Overmerging in N-body simulations*. In: arXiv E-prints. arXiv: astro-ph/0002027.

Kayo, I., A. Taruya, and Y. Suto (2001). *Probability Distribution Function of Cosmological Density Fluctuations from a Gaussian Initial Condition: Comparison of One-Point and Two-Point Lognormal Model Predictions with N-Body Simulations*. In: The Astrophysical Journal **561**, 22. arXiv: astro-ph/0105218.

Knebe, A. and V. Mueller (2000). *Quantifying Substructure in Galaxy Clusters*. In: Astronomy and Astrophysics **354**.3, 761. arXiv: astro-ph/9912534.

Köhlinger, F. et al. (2017). *KiDS-450: the tomographic weak lensing power spectrum and constraints on cosmological parameters*. In: Monthly Notices of the Royal Astronomical Society **471**, 4412. arXiv: 1706.02892.

Kozlikin, E. (2018). *Structure formation under different interaction laws*. In: PhD thesis (Heidelberg University).

Krywult, J, H. T. MacGillivray, and P Flin (1999). *Investigation of subclustering in 18 rich clusters of galaxies using wavelet analysis*. In: Astronomy and Astrophysics **351**, 883. e-print: e-print.

LIGO-Collaboration et al. (2016). *Observation of Gravitational Waves from a Binary Black Hole Merger*. In: Physical Review Letters **116**.6, 061102. arXiv: 1602.03837.

Lacey, C. and S. Cole (1993). *Merger rates in hierarchical models of galaxy formation*. In: Monthly Notices of the Royal Astronomical Society **262**.3, 627.

Lacey, C. and S. Cole (1994). *Merger Rates in Hierarchical Models of Galaxy Formation - Part Two - Comparison with N-Body Simulations*. In: Monthly Notices of the Royal Astronomical Society **271**, 676.

Lahav, O., P. B. Lilje, J. R. Primack, and M. J. Rees (1991). *Dynamical effects of the cosmological constant*. In: Monthly Notices of the Royal Astronomical Society **251**.1, 128.

Lam, T. Y. and R. K. Sheth (2008). *Perturbation theory and excursion set estimates of the probability distribution function of dark matter, and a method for reconstructing the initial distribution function*. In: Monthly Notices of the Royal Astronomical Society **386**.1, 407. arXiv: 0711.5029.

Lapi, A. and L. Danese (2014). *Statistics of dark matter halos in the excursion set peak framework*. In: Journal of Cosmology and Astroparticle Physics **2014**.07, 44. arXiv: 1407.1137.

Lapi, A. and L. Danese (2020). *A Stochastic Theory of the Hierarchical Clustering. I. Halo Mass Function*. In: The Astrophysical Journal **903**.2, 117. arXiv: 2009.07023.

Laureijs, R. et al. (2011). *Euclid Definition Study Report*. In: arXiv E-prints. arXiv: 1110.3193.

Lazanu, A. and M. Liguori (2018). *The two and three-loop matter bispectrum in perturbation theories*. In: Journal of Cosmology and Astroparticle Physics **2018**.04, 55. arXiv: 1803.03184.

Lemaître, A. G. (1931). *A Homogeneous Universe of Constant Mass and Increasing Radius accounting for the Radial Velocity of Extra-galactic Nebulae*. In: Monthly Notices of the Royal Astronomical Society **91**.5, 483.

Lifshitz, E. M. (1946). *On the gravitational stability of the expanding universe*. In: Journal of Physics (U.S.S.R) **10**.

Lilow, R. (2018). *Structure Formation in Dark and Baryonic Matter within Resummed Kinetic Field Theory*. In: PhD thesis (Heidelberg University).

Lilow, R., F. Fabis, E. Kozlikin, C. Viermann, and M. Bartelmann (2019). *Resummed Kinetic Field Theory: general formalism and linear structure growth from Newtonian particle dynamics*. In: Journal of Cosmology and Astroparticle Physics **2019**.04, 1. arXiv: 1809.06942.

Lin, G. D. (2017). *Recent developments on the moment problem*. In: Journal of Statistical Distributions and Applications **4**.1, 5. arXiv: 1703.01027.

Linke, L. M. (2017). *Going beyond simulations – analytical approaches to the distribution of the cosmic density field and the halo mass function with the kinetic field theory*. In: M.Sc. thesis (Heidelberg University).

Livermore, R. C., S. L. Finkelstein, and J. M. Lotz (2017). *Directly Observing the Galaxies Likely Responsible for Reionization*. In: The Astrophysical Journal **835**.2, 113. arXiv: 1604.06799.

Lotz, J. M. et al. (2017). *The Frontier Fields: Survey Design and Initial Results*. In: The Astrophysical Journal **837**.1, 97. arXiv: 1605.06567.

Maartens, R., F. B. Abdalla, M. Jarvis, and M. G. Santos (2015). *Cosmology with the SKA – overview*. In: arXiv E-prints. arXiv: 1501.04076.

Maggiore, M. and A. Riotto (2010a). *The Halo Mass Function from Excursion Set Theory. I. Gaussian fluctuations with non-markovian dependence on the smoothing scale*. In: The Astrophysical Journal **711**.2, 907–927. arXiv: 0903.1249.

Maggiore, M. and A. Riotto (2010b). *The Halo Mass Function from Excursion Set Theory. II. The Diffusing Barrier*. In: The Astrophysical Journal **717**.1, 515. arXiv: 0903.1250.

Maggiore, M. and A. Riotto (2010c). *The Halo Mass Function from Excursion Set Theory. III. Non-Gaussian Fluctuations*. In: The Astrophysical Journal **717**.1, 526. arXiv: 0903.1251.

Mallat, S. G. (1989). *Multiresolution approximations and wavelet orthonormal bases of L2*. In: Trans. Amer. Math. Soc. **315**.1, 69. e-print: e-print.

Mallat, S. G. (2009). *A wavelet tour of signal processing. the sparse way*. 3rd. Previous ed.: 1999. Amsterdam: Academic Press Elsevier.

Mao, T.-X. et al. (2018). *Resolution of the apparent discrepancy between the number of massive subhaloes in Abell 2744 and ΛCDM*. In: Monthly Notices of the Royal Astronomical SocietyL **478**.1, L34. arXiv: 1708.01400.

Marriage, T. A. et al. (2011). *The Atacama Cosmology Telescope: Sunyaev Zel'dovich Selected Galaxy Clusters at 148 GHz in the 2008 Survey*. In: The Astrophysical Journal **737**.2, 61. arXiv: 1010.1065.

Mazenko, G. F. (2010). *Fundamental theory of statistical particle dynamics*. In: Physical Review E **81**.6, 061102. arXiv: 0905.4904.

Mazenko, G. F. (2011). *Smoluchowski dynamics and the ergodic-nonergodic transition*. In: Physical Review E **83**.4, 041125. arXiv: 1009.3008.

McCullagh, N., D. Jeong, and A. S. Szalay (2016). *Toward accurate modelling of the non-linear matter bispectrum: standard perturbation theory and transients from initial conditions*. In: Monthly Notices of the Royal Astronomical Society **455**.3, 2945. arXiv: 1507.07824.

Medezinski, E. et al. (2016). *Frontier Fields: Subaru Weak-Lensing Analysis of the Merging Galaxy Cluster A2744*. In: The Astrophysical Journal **817**.1, 24. arXiv: 1507.03992.

Melchiorri, F., C. Ceccarelli, L. Pietranera, and B. O. Melchiorri (1981). *Fluctuations in the microwave background at intermediate angular scales*. In: The Astrophysical Journal **250**.1, L1.

Menanteau, F. et al. (2012). *The Atacama Cosmology Telescope: ACT-CL J0102-4915 "El Gordo," a Massive Merging Cluster at Redshift 0.87*. In: The Astrophysical Journal **748**.1, 7. arXiv: 1109.0953.

Merten, J. et al. (2011). *Creation of cosmic structure in the complex galaxy cluster merger Abell 2744*. In: Monthly Notices of the Royal Astronomical Society **417**.1, 333. arXiv: 1103.2772.

Meyer, Y. (1989). *Wavelets and operators*. In: Analysis at Urbana. Ed. by Berkson, E. and Peck, T. and Uhl, J. Cambridge: Cambridge University Press. 1989. pp. 256–365.

Misner, C. W., K. S. Thorne, and J. A. Wheeler (1973). *Gravitation*. San Francisco: Freeman.

Mo, H., F. Van den Bosch, and S. D. M. White (2011). *Galaxy formation and evolution*. 3. print. with corr. Cambridge: Cambridge University Press.

More, S., A. V. Kravtsov, N. Dalal, and S. Gottlöber (2011). *The overdensity and masses of the friends-of-friends halos and universality of the halo mass function*. In: The Astrophysical Journal Supplement Series **195**.1, 4. arXiv: 1103.0005.

Morlet, J., G. Arens, E. Fourgeau, and D. Glard (1982). *Wave propagation and sampling theory—Part I: Complex signal and scattering in multilayered media*. In: Geophysics **47**.2, 203.

Muldrew, S. I., F. R. Pearce, and C. Power (2011). *The accuracy of subhalo detection*. In: Monthly Notices of the Royal Astronomical Society **410**.4, 2617. arXiv: 1008.2903.

Munari, E. et al. (2016). *Numerical simulations challenged on the prediction of massive subhalo abundance in galaxy clusters: the case of Abell 2142*. In: The Astrophysical Journal **827**.1, L5. arXiv: 1607.01023.

Murray, S. G., C. Power, and A. S. G. Robotham (2013a). *How well do we know the halo mass function?* In: Monthly Notices of the Royal Astronomical Society: Letters **434**.1, L61. arXiv: 1306.5140.

Murray, S. G., C. Power, and A. S. G. Robotham (2013b). *HMFcalc: An online tool for calculating dark matter halo mass functions*. In: Astronomy and Computing **3**, 23. arXiv: 1306.6721.

Musso, M. and R. K. Sheth (2012). *One step beyond: the excursion set approach with correlated steps*. In: Monthly Notices of the Royal Astronomical Society **423**, L102. arXiv: 1201.3876.

Musso, M. and R. K. Sheth (2014a). *The importance of stepping up in the excursion set approach*. In: Monthly Notices of the Royal Astronomical Society **438**, 2683. arXiv: 1306.0551.

Musso, M. and R. K. Sheth (2014b). *The excursion set approach in non-Gaussian random fields*. In: Monthly Notices of the Royal Astronomical Society **439**, 3051. arXiv: 1305.0724.

Natarajan, P., G. De Lucia, and V. Springel (2007). *Substructure in lensing clusters and simulations*. In: Monthly Notices of the Royal Astronomical Society **376**.1, 180. arXiv: astro-ph/0604414.

Natarajan, P. et al. (2017). *Mapping substructure in the HST Frontier Fields cluster lenses and in cosmological simulations*. In: Monthly Notices of the Royal Astronomical Society **468**.2, 1962. arXiv: 1702.04348.

Navarro, J. F., C. S. Frenk, and S. D. M. White (1996). *The Structure of Cold Dark Matter Halos*. In: The Astrophysical Journal **462**, 563. arXiv: astro-ph/9508025.

Neto, A. F. et al. (2007). *The statistics of ΛCDM halo concentrations*. In: Monthly Notices of the Royal Astronomical Society **381**.4, 1450. arXiv: 0706.2919.

Novi Inverardi, P., A. Petri, G. Pontuale, and A. Tagliani (2005). *Stieltjes moment problem via fractional moments*. In: Applied Mathematics and Computation **166**.3, 664.

Ntelis, P. (2016). *The Homogeneity Scale of the universe*. In: arXiv E-prints. arXiv: 1607.03418.

Owers, M. S. et al. (2011). *The Dissection of Abell 2744: A Rich Cluster Growing Through Major and Minor Mergers*. In: The Astrophysical Journal **728**.1, 27. arXiv: 1012.1315.

Paranjape, A., T. Y. Lam, and R. K. Sheth (2012). *Halo abundances and counts-in-cells: the excursion set approach with correlated steps*. In: Monthly Notices of the Royal Astronomical Society **420**.2, 1429. arXiv: 1105.1990.

Peacock, J. A. and A. F. Heavens (1990). *Alternatives to the Press–Schechter cosmological mass function*. In: Monthly Notices of the Royal Astronomical Society **243**.1, 133.

Peebles, P. J. E. (1965). *The Black-Body Radiation Content of the Universe and the Formation of Galaxies*. In: The Astrophysical Journal **142**.39, 1317.

Peebles, P. J. E. (1980). *The large-scale structure of the universe*. Princeton series in physics. Princeton: Princeton Univ. Press.

Peebles, P. J. E. (1982). *Large-scale background temperature and mass fluctuations due to scale-invariant primeval perturbations*. In: The Astrophysical Journal **263**.1981, L1.

Peebles, P. J. E. (1993). *Principles of physical cosmology*. eng. Princeton series in physics. Princeton: Princeton Univ. Press.

Peebles, P. J. E. and J. T. Yu (1970). *Primeval Adiabatic Perturbation in an Expanding Universe*. In: The Astrophysical Journal **162**, 815.

Penco, R and D Mauro (2006). *Perturbation theory via Feynman diagrams in classical mechanics*. In: European Journal of Physics **27**.5, 1241–1249. arXiv: hep-th/0605061.

Perlmutter, S. et al. (1999). *Measurements of Ω and Λ from 42 High-Redshift Supernovae*. In: The Astrophysical Journal **517**.2, 565. arXiv: astro-ph/9812133.

Peskin, M. E. and D. V. Schroeder (1997). *An introduction to quantum field theory*. Boulder, Colo. [u.a.]: Westview Press.

Planck Collaboration (2020a). *Planck 2018 results. VI. Cosmological parameters*. In: Astronomy and Astrophysics **641**, A7. arXiv: 1807.06209.

Planck Collaboration (2020b). *Planck 2018 results. VII. Isotropy and Statistics of the CMB*. In: Astronomy and Astrophysics **641**, A7. arXiv: 1906.02552.

Pound, R. V. and G. A. Rebka (1959). *Gravitational Red-Shift in Nuclear Resonance*. In: Physical Review Letters **3**.9, 439. e-print: e-print.

Power, C. et al. (2003). *The inner structure of CDM haloes – I. A numerical convergence study*. In: Monthly Notices of the Royal Astronomical Society **338**.1, 14. arXiv: astro-ph/0201544.

Press, W. H. and P. Schechter (1974). *Formation of Galaxies and Clusters of Galaxies by Self-Similar Gravitational Condensation*. In: The Astrophysical Journal **187**, 425. e-print: e-print.

Räsänen, S. (2006). *Accelerated expansion from structure formation*. In: Journal of Cosmology and Astroparticle Physics **2006**.11, 3. arXiv: astro-ph/0607626.

Redlich, M., K. Bolejko, S. Meyer, G. F. Lewis, and M. Bartelmann (2014a). *Probing spatial homogeneity with LTB models: a detailed discussion*. In: Astronomy and Astrophysics **570**, A63. arXiv: 1408.1872.

Refregier, A. (2003). *Weak Gravitational Lensing by Large-Scale Structure*. In: Annual Review of Astronomy and Astrophysics **41**.1, 645. arXiv: astro-ph/0307212.

Riess, A. G. et al. (1998). *Observational Evidence from Supernovae for an Accelerating Universe and a Cosmological Constant*. In: The Astrophysical Journal **116**.3, 1009. arXiv: astro-ph/9805201.

Rioul, O. and M. Vetterli (1991). *Wavelets and signal processing*. In: IEEE Signal Processing Magazine **8**.4, 14.

Robertson, B. E., A. V. Kravtsov, J. Tinker, and A. R. Zentner (2009). *Collapse Barriers and Halo Abundance: Testing the Excursion Set Ansatz*. In: The Astrophysical Journal **696**.1, 636. arXiv: 0812.3148.

Rubin, V. C., N. Thonnard, and J. Ford, W. K. (1978). *Extended rotation curves of high-luminosity spiral galaxies. IV - Systematic dynamical properties, SA through SC*. In: The Astrophysical Journal **225**, L107.

Schmidt, C. (2020). *in prep.* In: M.Sc. thesis (Heidelberg University).

Schwinn, J., C. M. Baugh, M. Jauzac, M. Bartelmann, and D. Eckert (2018). *Uncovering substructure with wavelets:proof of concept using Abell 2744*. In: Monthly Notices of the Royal Astronomical Society **481**.4, 4300. arXiv: 1804.07401.

Schwinn, J. et al. (2017). *Abell 2744: too much substructure for ΛCDM?* In: Monthly Notices of the Royal Astronomical Society **467**.3, 2913. arXiv: 1611.02790.

Sellentin, E., A. H. Jaffe, and A. F. Heavens (2017). *On the use of the Edgeworth expansion in cosmology I: how to foresee and evade its pitfalls*. In: arXiv E-prints. arXiv: 1709.03452.

Sellentin, E. (2015). *A fast, always positive definite and normalizable approximation of non-Gaussian likelihoods*. In: Monthly Notices of the Royal Astronomical Society **453**.1, 893. arXiv: 1506.04866.

Shapiro, I. I. (1964). *Fourth Test of General Relativity*. In: Physical Review Letters **13**.26, 789.

Sheth, R. K. (1998). *An excursion set model for the distribution of dark matter and dark matter haloes*. In: Monthly Notices of the Royal Astronomical Society **300**, 1057. arXiv: astro-ph/9805319.

Sheth, R. K., H. J. Mo, and G. Tormen (2001). *Ellipsoidal collapse and an improved model for the number and spatial distribution of dark matter haloes*. In: Monthly Notices of the Royal Astronomical Society **323**, 1. arXiv: astro-ph/9907024.

Sheth, R. K. and G. Tormen (1999). *Large-scale bias and the peak background split*. In: Monthly Notices of the Royal Astronomical Society **308**.1, 119. arXiv: astro-ph/9901122.

Shin, J., J. Kim, C. Pichon, D. Jeong, and C. Park (2017). *New Fitting Formula for Cosmic Nonlinear Density Distribution*. In: The Astrophysical Journal **843**.1, 73. arXiv: 1705.06863.

Shirasaki, M., E. T. Lau, and D. Nagai (2018). *Modelling baryonic effects on galaxy cluster mass profiles*. In: Monthly Notices of the Royal Astronomical Society **477**.2, 2804. arXiv: 1711.06366.

Smith, R. E. et al. (2003). *Stable clustering, the halo model and non-linear cosmological power spectra*. In: Monthly Notices of the Royal Astronomical Society **341**.4, 1311. arXiv: astro-ph/0207664.

Springel, V., S. D. M. White, G. Tormen, and G. Kauffmann (2001). *Populating a cluster of galaxies - I. Results at $z = 0$*. In: Monthly Notices of the Royal Astronomical Society **328**.3, 726. arXiv: astro-ph/0012055.

Springel, V. et al. (2005). *Simulations of the formation, evolution and clustering of galaxies and quasars*. In: Nature **435**.7042, 629. arXiv: astro-ph/0504097.

Springel, V., C. S. Frenk, and S. D. M. White (2006). *The large-scale structure of the Universe*. In: Nature **440**.7088, 1137. arXiv: astro-ph/0604561.

Stieltjes, T. J. (1894). *Recherches sur les fractions continues*. In: Annales de la Faculté des sciences de Toulouse : Mathématiques **1e série 8**.4. English version contained in T.J.

Stieltjes, Collected Papers, G. van Dijk (Ed.),Vol. II, Springer, Berlin, 1993, J1. e-print: e-print.

Taylor, A. N., S. Dye, T. J. Broadhurst, N. Benitez, and E. van Kampen (1998). *Gravitational Lens Magnification and the Mass of Abell 1689*. In: The Astrophysical Journal **501**.2, 539. arXiv: astro-ph/9801158.

Tinker, J. et al. (2008). *Toward a Halo Mass Function for Precision Cosmology: The Limits of Universality*. In: The Astrophysical Journal **688**, 709-728, 709. arXiv: 0803.2706.

Touchette, H. (2009). *The large deviation approach to statistical mechanics*. In: Physics Reports **478**.1-3, 1. arXiv: 0804.0327.

Troxel, M. A. et al. (2018). *Dark Energy Survey Year 1 results: Cosmological constraints from cosmic shear*. In: Physical Review D **98**.4, 43528. arXiv: 1708.01538.

Uhlemann, C., S. Codis, C. Pichon, F. Bernardeau, and P. Reimberg (2016). *Back in the saddle: large-deviation statistics of the cosmic log-density field*. In: Monthly Notices of the Royal Astronomical Society **460**.2, 1529. arXiv: 1512.05793.

Valageas, P. (2002). *Dynamics of gravitational clustering. II. Steepest-descent method for the quasi-linear regime*. In: Astronomy and Astrophysics **382**.2, 412. arXiv: astro-ph/0107126.

Valageas, P. (2009). *Mass functions and bias of dark matter halos*. In: Astronomy and Astrophysics **508**.1, 93. arXiv: 0905.2277.

van den Bosch, Frank C and Ogiya, Go (2018). *Dark matter substructure in numerical simulations: a tale of discreteness noise, runaway instabilities, and artificial disruption*. In: Monthly Notices of the Royal Astronomical Society **475**.3, 4066. arXiv: 1801.05427.

Viermann, C., F. Fabis, E. Kozlikin, R. Lilow, and M. Bartelmann (2015). *Nonequilibrium statistical field theory for classical particles: Basic kinetic theory*. In: Physical Review E **91**.6, 062120. arXiv: 1411.2809.

Vogelsberger, M et al. (2014). *Properties of galaxies reproduced by a hydrodynamic simulation*. In: Nature **509**.7499, 177. arXiv: 1405.1418.

Weigand, T. (2013). *Quantum Field Theory II*. In: Lecture notes, Heidelberg University.

Weinberg, S. (2008). *Cosmology*. Oxford: Oxford University Press.

Zel'dovich, Y. B. (1970). *Gravitational Instability: An Approximate Theory for Large Density Perturbations*. In: Astronomy and Astrophysics **5**, 84. e-print: e-print.

Zel'dovich, Y. B. (1972). *A Hypothesis, Unifying the Structure and the Entropy of the Universe*. In: Monthly Notices of the Royal Astronomical Society **160**.1, 1P.

Zentner, A. R. (2007). *The Excursion Set Theory of Halo Mass Functions, Halo Clustering, and Halo Growth*. In: International Journal of Modern Physics D **16**.05, 763. arXiv: astro-ph/0611454.

Zwicky, F. (1933). *Die Rotverschiebung von extragalaktischen Nebeln*. In: Helvetica Physica Acta **6**, 110. e-print: e-print.

Figure Credits

2.1 Reprinted by permission from Springer Nature:
V. Springel et al. 2006, Nature 440, p. 1137

3.1 Reprinted by permission from John Wiley and Sons:
M. Bartelmann et al. 2019, Annalen der Physik, 531, p. 1800446

7.1 Reprinted by permission from MNRAS:
J. Schwinn et al. 2018, MNRAS 481(4), p. 4300

7.2 Reprinted by permission from MNRAS:
J. Schwinn et al. 2018, MNRAS 481(4), p. 4300

7.3 Reprinted by permission from MNRAS:
J. Schwinn et al. 2018, MNRAS 481(4), p. 4300

7.4 Reprinted by permission from MNRAS:
J. Schwinn et al. 2018, MNRAS 481(4), p. 4300

7.5 Reprinted by permission from MNRAS:
J. Schwinn et al. 2018, MNRAS 481(4), p. 4300

E.1 Reprinted by permission from MNRAS:
M. Jauzac et al. 2016, MNRAS 463(4), p. 3883

ACKNOWLEDGMENTS

It is a pleasant task to spend these last paragraphs thanking all those people who were involved in this thesis, who shared their thoughts, insights or advice and supported me in the past years.

First of all, I would like to thank Matthias Bartelmann not only for the opportunity to write this thesis under his guidance, but also for having had the chance to spend over seven years in his group now. I am very grateful for him always having an open door for all my questions and problems, for his support and kind advice as well as for his great influence on the way I see and understand Physics and science. Thank you so much!

I also cannot thank enough Björn Malte Schäfer for his support, his sympathetic ear, his deep insights about Physics and for envisioning what would have happened if I had won the HGFSP poster price.

Furthermore, I would like to thank Dr. Annalisa Pillepich for being part of my thesis committee and her kind and helpful advice during the thesis committee meetings. I would like to thank as well Prof. Ulrich Uwer and Dr. Stefan Flörchinger for agreeing to be my examiners in the disputation.

I am also much indebted to Martin Feix and Robert Lilow for so many extended and fruitful discussions, which brought many insights and new ideas. Thank you so much and I hope I will see you soon again! I am also especially grateful to Robert Lilow for proofreading the KFT and PDF chapters of this thesis. Furthermore, I would like to thank Sara, Christophe, Martina, Christian, Stefan, Eduardo and Laila for many discussions about KFT and the one point distribution.

I would also like to thank the HGFSP and Prof. Sandra Klevansky for the generous financial support and the excellence cluster STRUCTURES for funding our Schöntal workshop.

Moreover, I would like to thank Anna Zacheus a lot for taking care of all the bureaucratic and organisational work to keep this off our shoulders.

The last seven years would not have been half as pleasant without the warm and welcoming atmosphere of the combined cosmology group at Philosophenweg 12. Thank you for all the nice lunch and coffee breaks, extended discussions, Monty Python quotes, random shifts of topic towards Star Trek and silly jokes. It was very unfortunate that this was somewhat disturbed by the pandemic. However, it is still a great pleasure whenever I get the chance to speak to any of you and if it is only virtually.

Last but not least, I would like to thank my family and my friends for their love and support, the shared moments, the dinners, the weekends and the long conversations, which gave me so much strength and positivity.

COLOPHON

This document was typeset using the typographical look-and-feel `classicthesis` developed by André Miede and Ivo Pletikosić. The style was inspired by Robert Bringhurst's seminal book on typography "*The Elements of Typographic Style*". `classicthesis` is available for both LaTeX and LyX:

https://bitbucket.org/amiede/classicthesis/

Final Version as of November 26, 2020 (classicthesis v4.6).